AGARD-CP-542

AD-A-276 919

AGARD

## ADVISORY GROUP FOR AEROSPACE RESEARCH & DEVELOPMENT

7 RUE ANCELLE 92200 NEUILLY SUR SEINE FRANCE

AGARD CONFERENCE PROCEEDINGS 542

Atmospheric Propagation Effects through Natural and Man-Made Obscurants for Visible to MM-Wave Radiation

(Les Effets des Conditions Défavorables de
Propagation sur les Systèmes Optiques,
IR et à Ondes Millimétriques)

*Papers presented at the Electromagnetic Wave Propagation Panel Symposium,
held in Palma de Mallorca, Spain, 17th—20th May 1993.*

NORTH ATLANTIC TREATY ORGANIZATION

Published November 1993

Distribution and Availability on Back Cover

AGARD-CP-542

AGARD

ADVISORY GROUP FOR AEROSPACE RESEARCH & DEVELOPMENT

7 RUE ANCELLE 92200 NEUILLY SUR SEINE FRANCE

AGARD CONFERENCE PROCEEDINGS 542

Atmospheric Propagation Effects through Natural and Man-Made Obscurants for Visible to MM-Wave Radiation

(Les Effets des Conditions Défavorables de
Propagation sur les Systèmes Optiques,
IR et à Ondes Millimétriques)

Papers presented at the Electromagnetic Wave Propagation Panel Symposium,
held in Palma de Mallorca, Spain, 17th—20th May 1993.

North Atlantic Treaty Organization
Organisation du Traité de l'Atlantique Nord

The Mission of AGARD

According to its Charter, the mission of AGARD is to bring together the leading personalities of the NATO nations in the fields of science and technology relating to aerospace for the following purposes:

— Recommending effective ways for the member nations to use their research and development capabilities for the common benefit of the NATO community;

— Providing scientific and technical advice and assistance to the Military Committee in the field of aerospace research and development (with particular regard to its military application);

— Continuously stimulating advances in the aerospace sciences relevant to strengthening the common defence posture;

— Improving the co-operation among member nations in aerospace research and development;

— Exchange of scientific and technical information;

— Providing assistance to member nations for the purpose of increasing their scientific and technical potential;

— Rendering scientific and technical assistance, as requested, to other NATO bodies and to member nations in connection with research and development problems in the aerospace field.

The highest authority within AGARD is the National Delegates Board consisting of officially appointed senior representatives from each member nation. The mission of AGARD is carried out through the Panels which are composed of experts appointed by the National Delegates, the Consultant and Exchange Programme and the Aerospace Applications Studies Programme. The results of AGARD work are reported to the member nations and the NATO Authorities through the AGARD series of publications of which this is one.

Participation in AGARD activities is by invitation only and is normally limited to citizens of the NATO nations.

Theme

Modern, precision-guided weapons require that guidance and target acquisition/recognition systems take into account the effects of the propagation environment. Successful performance must be obtained under adverse weather conditions such as haze, clouds, fog, rain, snow and under adverse battlefield conditions such as dust, smoke and man-made obscurants.

Sensors operate at wavelengths ranging across the millimetre, IR and the visible regions of the electromagnetic spectrum. Propagation effects vary drastically over this wavelength span and systems may employ a combination of sensors to mitigate adverse environmental conditions. The effectiveness of countermeasures such as multispectral obscurants and multispectral camouflage also depends on atmospheric properties.

System performance is measured in terms of probability of detection, probability of recognition and, ultimately, in terms of probability of a kill. A partial listing of the processes that affect these probabilities and, in turn, are affected by the propagation environment includes extinction, angles and amplitude scintillation, target to background contrast, contrast transmission and clutter characteristics.

The Symposium will address the following topics:

- Natural Obscurants
- Multispectral Camouflage
- Man-made Obscurants and Battlefield-induced Phenomena
- Target and Background Signatures.

Thème

La mise en oeuvre des systèmes d'armes modernes à guidage de précision exige que les systèmes d'acquisition/reconnaissance de l'objectif tiennent compte des conditions de propagation. Les performances requises doivent être réalisées dans des conditions météorologiques défavorables telles que brume, nuages, brouillard, pluie, neige et dans des conditions hostiles de combat telles que poussière, fumée et obscurcissants artificiels.

De nombreux capteurs fonctionnent à des longueurs d'onde du spectre électromagnétique allant des ondes millimétriques aux rayonnements visibles en passant par l'infrarouge. Les conditions de propagation varient de façon considérable dans ces gammes de longueurs d'onde, de sorte que les systèmes peuvent faire appel à des combinaisons de capteurs afin d'atténuer l'influence des facteurs défavorables de propagation. L'efficacité des contremesures telles que les obscurcissants multispectraux et le camouflage multispectral dépend également des caractéristiques atmosphériques.

Les performances des systèmes sont exprimées par la probabilité de détection, la probabilité de reconnaissance et, en dernier ressort, par la probabilité d'anéantissement. Une liste non exhaustive des concepts ayant une incidence sur ces probabilités, influencées à leur tour par les conditions de propagation, comporte l'extinction, le contraste entre la cible et son arrière-plan, la scintillation angulaire et la scintillation d'amplitude, la transmission du contraste et les caractéristiques du fouillis.

Les sujets suivants seront abordés:

- Les obscurcissants naturels
- Le camouflage multispectral
- Les obscurcissants artificiels et les phénomènes liés au champs de bataille
- Les signatures de la cible et de l'arrière-plan.

Electromagnetic Wave Propagation Panel

Chairman: Dr J.H. Richter
Naval Command, Control and Ocean
   Surveillance Center
RDT&E Division, Code 54
San Diego, CA 92152-5320
United States

Deputy Chairman: Dr D.H. Höhn, apl. Prof.
FGAN
Forschungsinstitut für Optik
Schloss Kressbach
D-7400 Tübingen
Germany

TECHNICAL PROGRAMME COMMITTEE

Co-Chairmen

Prof. Dr E. Schweicher
Ecole Royale Militaire
Chaire OM
Avenue de la Renaissance, 30
B-1040 Bruxelles
Belgium

Mr J. Rogge
Royal Military Academy
PO Box 90154
4800 RG Breda
The Netherlands

Members

Dipl. Ing. P. Baars
FGAN
Neuenahrerstrasse 20
W-5307 Wachtberg-Werthhoven
Germany

Col. IMM R. de Bleyser
TDLM/CT
Quartier Major Housiau
Martelarenstraat 181
B-1800 Peutie
Belgium

Dr D. Clement
Forschungsinstitut für Optik
FGAN
Schloss Kressbach
D-7400 Tübingen
Germany

Dr W.A. Flood
Director, Geosciences Division
US Army Research Office
PO Box 12211
Research Triangle Park, NC 27709-2211
United States

Dr U. Lammers
RL/EECP
Hanscom Air Force Base
MA 01731-5000
United States

Mr M. Lizot
DGA/DRET/SDR
26, Boulevard Victor, Paris 15^e
F-00460 Armées
France

Dr Roper
RSRE, (EOM Group)
South Site, St Andrews Road
Malvern, Worcs WR14 3PS
United Kingdom

Dr E. Spitz
Directeur Général Adjoint
Thomson SA — Cedex 67
92045 Paris la Défense
France

PANEL EXECUTIVE

Lt-Col. R. Cariglia

Mail from Europe:
AGARD—OTAN
Attn: EPP Executive
7, rue Ancelle
F-92200 Neuilly-sur-Seine
France

Mail from US and Canada:
AGARD—NATO
Attn: EPP Executive
Unit 21551
APO AE 09777

Tel: 33(1)47 38 57 68
Telex: 610176 (France)
Telefax: 33 (1) 47 38 57 99

Preface

The Symposium on Atmospheric Propagation Effects through Natural and Man-Made Obscurants for Visible to MM-Wave Radiation, was a good Symposium in the way that it brought together experts in the area of optical/infrared as well as millimetre wave propagation and propagation related system aspects.

Many papers addressed the subject of the transmission of electromagnetic radiation through the natural (adverse) atmosphere and through man-made obscurants (smokes) and the degradation effects on acquisition and surveillance systems. This results in a decreased situational awareness and less flexibility to deploy armed forces in unfavourable climatological conditions. The development of methods and/or systems to overcome this strongly depends on a fundamental knowledge of the mechanisms involved.

Modelling of those effects is the basis of simulation techniques that can be used on the one hand to improve training techniques for operations under adverse atmospheric conditions and on the other hand for a visualisation of the problems though computer simulation.

Knowledge of target and background signatures, as they depend on environmental conditions, including the propagation characteristics of the atmosphere, is essential for the development of countermeasures such as camouflage systems and decoy systems. In several papers both the modelling and measurement of target signatures, background signatures, camouflage methods and camouflage effectiveness were addressed. It was encouraging to see that development really goes into the direction of true multispectral systems, operating in the optical, infrared and millimetre wavelength regions.

The presentations at the Symposium exhibited a balance between the optical/infrared and millimetre wavelength bands, between pure propagation effects and systems degradation and mitigation effects, between acquisition systems and countermeasures, between national research projects and international (NATO) cooperative programmes.

In the area of atmospheric battlefield effects (propagation and systems related) there is strong competition with other conferences. It was therefore encouraging to note that the numerous participants acknowledged the quality of the presentations and enjoyed the discussions. The fact that detailed and interesting results can be revealed during a classified session has proven to be an advantage.

In short, AGARD/EPP demonstrated at the Symposium the quality that people expect. This was to a large extent due to the authors, but also to the members of the Technical Programme Committee, the local Spanish Coordinators and the EPP Staff.

We thank everyone who contributed to the success of the Symposium.

J. Rogge and E. Schweicher

Contents

---

* Published in classified volume CP-542 (Supplement).

SESSION IV — MAN-MADE OBSCURANTS AND BATTLEFIELD PHENOMENA
Session Chairman: Colonel Imm R. de Bleyser

---

* Published in classified volume CP-542 (Supplement).

* Published in classified volume CP-542 (Supplement).

Evaluation of Dual Polarization Attenuation of Millimeter Frequencies through a Meteorological Radar

D. Giuli, L. Baldini, L. Facheris, P. Mazzetti

Dipartimento di Ingegneria Elettronica
Università di Firenze
via di Santa Marta, 3
50139 Florence
Italy

SUMMARY
In this paper the possibility of exploiting measurements obtained through a C-band dual polarization radar is examined, as an auxiliary tool for the planning of radio relays operating at millimeter frequencies. C-band weather radars, though featuring several advantages related to their cost and reduced size, provide partially attenuated rainfall measurements with respect to their S-band counterparts. However, good reliability of rainfall rates based on C-band dual polarization measurement is achieved after proper processing based on iterative procedures for propagation attenuation due to rain. A simulation program has been utilized here to provide synthetic rainfall and C-band dual polarization reflectivity data related to several storms, corresponding to different meteorological conditions. Simulated data, after proper correction of radar data, have been utilized to evaluate path attenuation statistics useful to predict fading at millimeter frequencies and related outage probability. Results show that a C-band radar can be profitably exploited for the purpose, prediction being feasible under different space-time rain patterns. On the other hand, the analysis has shown that differential reflectivity is not so essential for the aforementioned purpose as absolute reflectivity, even if it could be utilized with success in real contexts for the identifications of hydrometeors (hail, graupels, wet snow) other than rain, which may be responsible for more pronounced scattering and absorption phenomena.

1. INTRODUCTION
The increasing interest in the use of frequencies above 30 GHz in line of sight radio links, dictated by wider bandwidth occupancy availability for digital transmission, asks for detailed studies of attenuation of e.m. waves propagation in atmosphere along terrestrial paths. Besides the problem of multipath fading, inducing selective frequency attenuation, major problems in terms of outage probability computed on a given temporal basis are caused to this kind of systems by flat fading induced by heavy precipitation phenomena crossing the radio link. In consideration of the high sensitivity of millimeter waves to the meteorological condition of the interposed medium, proper strategies to combat rainfall induced path attenuation must be taken into account both on a planning and a system design basis, in order to reduce the probability of outage. Such strategies require knowledge of the attenuation statistics in the area of interest. In particular, in the planning phase seasonal and monthly rainfall statistics are needed to individuate those zones in the selected area where heaviest rainfall activity is more likely to occur. To this respect, utilization of radar-derived rainfall estimates is significant, since data are characterized by high spatial resolution, which

can be of valuable help in individuating also intense though limited in space and time events, as may typically happen during summer thunderstorms, since usually, outages in a radio link are caused by heavy rain cells averaging 5 to 7 Km in diameter and 5-10 min in duration.

The other advantage of using radar data, consisting in the possibility for them to be updated on a very short time basis (e.g. some minutes), can be profitably exploited in the management phase for a simple outage forecast or, more efficiently, for the optimal selection of one of the available alternating links for transmission, possibly subject to lower path attenuation.

Recent advances in the technology of meteorological radars, especially those connected with the use of polarimetric information, allow accurate measurement of precipitation and investigation of the microstructure of different kind of precipitation, such as rain, hail, snow, mixed-phase particles. In particular, dual-polarization radars allow discrimination and classification of the different precipitating particles and, in the case of rainfall, allow one to determine parameters defining the drop size distribution, which is the basis of a physical model which relates path attenuation to dual polarization meteorological radar measurements. For this kind of applications, it would be preferable to utilize weather radars operating at non-attenuating frequencies. Under this respect, the typical choice in radar meteorology is S-band, since at this band, effects of precipitation-induced attenuation are practically negligible (Ref 1, and Ref 2). In many European countries, however, C-band weather radars are widely employed. In fact, such systems can provide sufficiently reliable rainfall measurments, with the advantage of a lower cost and a reduced dimension antenna, with respect to a S-band systems. On the other hand, at these wavelengths, radar measuraments are affected by attenuation due to precipitation itself. This problem was first addressed for single-polarization radar measurements by Hitschfield and Bordan (Ref 3), Sims et al. (Ref 4), and Hildebrand (Ref 5). Successively, the same problem was examined for the case of C-band radars utilizing the differential reflectivity technique for measuring rainfall (Ref 6). Here an additional problem is posed by the different specific attenuation experienced by horizontally and vertically polarized waves, propagating through the rainfall medium which is characterized by a strong polarization anisotropy. As a consequence, procedures for correcting attenuation effects on reflectivity factors estimates, especially in the presence of heavy rainfall, are necessary for C-band radar systems utilizing either single polarization or dual polarization, in order to

provide rainfall rate estimates with a sufficient degree of reliability, so that they can be utilized to predict attenuation at higher frequencies.

This matter is dealt with in this paper, on the purpose of focusing on the ~~tential operational employment of a C-band dual polarization radar to assess the percentage of availability of a radio link. After having briefly recalled the basic methods and relationships adopted to retrieve specific attenuation estimates from rainfall rates, we describe the simulation program that has been uti!'ₓ a to provide synthetic rainfall and related C-band ःₓ ' polarization reflectivity data corresponding to ⁓ əral storms and different meteorological conditions. Simulated radar data, after proper correction of both absolute and differential propagation attenuation, are conveɪted to rainfall rates through both conventional reflectivity-rainfall rate conversion formulae, and empirically derived on the basis of radar and ground rainfall data, the latter being provided by an hypothetical raingauge placed amid the radio link. "True" rainfall data simultaneously provided by the simulation model are converted into specific attenuation data at a given frequency; due to the way they are derived, such data are considered as the "true" specific attenuation experienced by e.m. waves along their path.

Rainfall estimates obtained from radar data are on turn converted to predict specific attenuation at the given frequency, and subsequently utilized to evaluate path attenuation. Comparisons are finally performed to assess the accuracy of the path attenuation estimate, utilizing "true" specific attenuation as the basis for such comparisons. Results show that a C-band radar can be profitably exploited for the purpose, prediction being in good agreement with the "true" reference under different conditions of space-time rain patterns.

2. RELATIONSHIP BETWEEN REFLECTIVITY, SPECIFIC ATTENUATION AND RAINFALL RATE

In this section, we recall definitions of dual linear incoherent radar measurables, rainfall rate and the specific attenuation due to propagation through rainfall and discuss methods for determining attenuation along a path through the knowledge of rainfall rate.

A rainfall event that occurs over a certain area can be described, at each time step, by a function of two variables $R(x,y)$ defined over a two-dimensional surface representing rainfall intensity at the spatial coordinates (x,y). Rainfall intensity R is defined as the depth of fallen water per time unit and it depends on the terminal velocity of drops $V(D)$ (cm s^{-1}) and on the drop size distribution $N(D)$ (cm^{-1} m^{-3}) through the integral relation (Ref 7)

$$R = 6\pi \times 10^{-3} \int_0^{D_{max}} D^3 V(D) N(D) dD \qquad (mm\ h^{-1}) \qquad (1)$$

where D(cm) is the equivalent drop diameter, and D_{max} is the maximum equivalent drop diameter. The dual-polarization radar measurables, namely the reflectivity factors at horizontal and vertical polarization (Z_H and Z_V, respectively) are given by

$$Z_{H,V} = \frac{\lambda^4}{\pi^5 k^2} \int_0^{D_{max}} \sigma_{H,V}(D) N(D) dD \qquad (mm^6\ m^{-3}) \qquad (2)$$

where λ is the wavelength, k, depending on the refractivity index, at C-band frequencies, equals 0.965, and $\sigma_H(D)$ and $\sigma_V(D)$ (cm^2) at H and V polarization, respectively, are the backscattering cross sections. Ratio between reflectivity factors defines the differential reflectivity

$$Z_{DR} = 10 \log (Z_H/Z_V) \qquad (dB) \qquad (3).$$

Reflectivity factors are evaluated through the received power, according to

$$Z_{H,V} = \frac{P_{H,V}}{C \cdot \gamma_{H,V}} r^2 \qquad (mm^6\ m^{-3}) \qquad (4)$$

where C includes radar parameters, the parameter $\gamma_{H,V}$, in general unknown, accounts for the 2 way attenuation, and r is the distance from radar of the scattering volume. An estimate of rainfall rate is generally obtained by means of a semi-empirical relationship between reflectivity and rainfall rate. For instance, the relationship

$$Z = a R^b \qquad (5)$$

is used for single polarization (generally H) measurements and

$$R = A Z_H Z_{DR}^{\ B} \qquad (6)$$

for dual polarization estimates.

The electromagnetic wave propagating through rainfall undergoes a power loss per unit length $K_{H,V}$ given by

$$K_{H,V} = 434 \times 10^{-3} \int_0^{D_{max}} \sigma_{eH,V}(D) N(D) dD \qquad (dB\ km^{-1})$$
$$(7)$$

where $\sigma_{eH}(D)$ and $\sigma_{eV}(D)$ (cm^2) are the total extinction cross sections at H and V polarizations, respectively, that take into account the whole power loss, due to both absorption and scattering by a raindrop of equivalent diameter D.

As it is well known, the specific attenuation coefficient K, (subscript indicating the polarization is omitted) can be related to the rainfall rate R by the following approximate equation:

$$K = \alpha R^\beta \qquad (8)$$

where K and R are expressed in dBKm^{-1} and mmh^{-1} respectively, while α and β, which obviously depend on the employed polarization, are evaluated through a regression fit for each value of frequency and temperature, and different rain conditions as shown by Olsen (Ref 8).

Based on (8), propagation attenuation along a given link can be expressed as a function of rainfall rate along the path:

$$p = \int_{r_1}^{r_2} K(x,y) dr = \int_{r_1}^{r_2} \alpha [R(x,y)]^\beta dr \quad (dB) \qquad (9)$$

where the geometric vectors r_1 and r_2 represent the coordinates of the receiver and transmitter respectively, and r is the distance along the line path between r_1 and r_2.

The relationship (8) is approximate. Usually, it is determined through a model proposed by Atlas and Ulbrich (Ref 9), which allows to select the numerical values of the parameters α and β. However, such a model assumes that the drop size distribution (DSD) be exponential and known, as well as it assumes that turbulence and local winds associated with the real meteorological conditions do not affect the drop fall velocity law. Furthermore, such parameters depend on temperature and relative humidity.

3. SIMULATION PROCEDURES FOR GENERATING RAINFALL, REFLECTIVITY AND ATTENUATION DATA

In this section we describe the model utilized for the joint simulation of rainfall fields and dual polarization radar measured reflectivity fields. The procedure adopted in the different steps of the simulation process, which are here briefly recalled, are described in Ref. 10. The importance of the model for the application which is the object of this paper is first of all related to the congruency between synthesized rainfall and measured reflectivity fields, and secondly to the possibility that it provides to simulate rainfall events with different statistical behavior.

Congruency between "true" rainfall and "measured" radar data is a consequence of the procedure followed to prepare the simulation environment where radar sampling is then performed. A basic rainfall field is first generated according to a stochastic process (Ref 11). Every rainfall event is obtained as cumulative result of the contributions of a random number of rain cells. Their centers are spatially distributed according to a two-dimensional homogeneous Poisson process of parameter Λ and their instants of birth follow an exponential probability distribution of parameter μ. For each cell, the rainfall intensity in the center has a value i_0 and it is considered exponentially decaying in time and quadratically exponential in space. The spatial extent of the cell ϕ and wind components v_x and v_y are considered. The time history of each cell is thus kept functionally separated from its shape and spatial extension, and the dynamics of the whole rainfall event is driven by the above five parameters, which may be computed in order to obtain the desired statistical characteristics for rainfall depth at a given time. By varying such parameters, it is possible to generate rain events with different typologies, such that a sufficiently differentiate case studies can be simulated.

The generation of the reflectivity environment where radar sampling is successively simulated follows two steps, the first defining a scheme allowing to derive two two-dimensional (Z_H and Z_{DR}) reflectivity fields consistent with the "true" rainfall fields at ground ("reflectivity fields at ground").

The second step in the reflectivity fields generation process requires that the two-dimensional reflectivity fields at ground, obtained as described before, develop themselves along a vertical coordinate axis in order that a couple of volumetric fields be generated. In this context, the Z_H and Z_{DR} fields at ground serve as a reference, in the sense that their use in (7) would directly lead to the "true" rainfall field. Each one of the

three-dimensional fields is made up by cubic cells (called "spatial resolution cells") supposed to be uniform in reflectivity. Their volume was fixed as 10^{-3} Km^3, two orders of magnitude below the typical dimension of the resolution cell of the radar measured fields. This allows to take into account the small scale variations of reflectivity during the simulation of the radar acquisition process, independently of the type of storm that is being generated.

The vertical reflectivity profiles that were simulated fit a basic pattern ("medium profile") evidencing the presence of a precipitation melting layer at an altitude varying from one medium profile to another, with the height of the Z_H peak at the typical altitude of 1.3 Km.

The volumetric radar integration process requires first of all that each spatial resolution cell be identified within each radar sample volume. Fluctuations of reflectivities in each resolution cell follow an exponential distributions whose mean values are the previously computed Z_H and Z_V (Ref 7). Beam smoothing effect is then taken into account by polynomial interpolation of real antenna patterns at horizontal and vertical polarizations relative to the POLAR 55C radar placed in Montagnana Florence (Ref 12). The integration of N_i pulses sequentially acquired by each polarization channel is then simulated.

The parameters needed by the radar acquisition model are the radar site height h_s, the beam elevation e, the azimuth beam-width Φ_1, the elevation beam-width Φ_r, the range resolution Δ r, and the distance d_r between radar and the reflectivity data volume.

The effects of propagation attenuation at C-band are simulated by introducing the specific attenuation at horizontal and vertical polarizations expressed as functions of both Z_H and Z_V according to Aydin et al. (Ref. 6). Specific attenuations at H and V polarization as empirical relationships derived by least squares fifth order polynomial fit of data provided disdrometer measurements. Then, radar measured reflectivities were simulated in each gate n according to the following relationships:

$$Z'_{Hn} = Z_{Hn} - 2\Delta r \sum_{i=k}^{n-1} K_{Hi} - \Delta r K_{Hn} + N_{ZHn} + B_{ZH} \qquad (10a)$$

$$Z'_{DRn} = Z_{DRn} - 2\Delta r \sum_{i=k}^{n-1} K_i - \Delta r K_n + N_{ZDRn} + B_{ZDR} \qquad (10b)$$

where k is the nearest range gate to the radar in which rainfall is present, B_{ZH} and B_{ZDR} are biases (expressed in dB) due to calibration errors, N_{ZHn} and N_{ZDRn} (in dB) are measurement errors, considered as a zero-mean Gaussian noise, $\Delta K_n = K_{Hn} - K_{Vn}$ is the differential attenuation at the n-th gate.

The above described procedure allows one to derive, from a "true" rainfall field, two measured reflectivity (horizontal and differential) fields, which can be converted through relationship as (5) and (6) to determine a radar estimated rainfall field. Comparisons between the two rainfall fields, once the radar estimated rainfall field is referenced with respect to the ground, have given the opportunity to test some

radar data correction procedures and also an hydrological models (Ref. 13). A rather similar scheme is here adopted to set a "true" path attenuation and a radar derived path attenuation at the required frequency. In this case, the path attenuation between two points, has been obtained based on (8), where parameters α and β have been chosen according to values listed in Ref 8. In order to introduce a plausible criterion for evaluating the goodness of correction and prediction, we will consider as "true" the attenuation as obtained by using in such relationships the "true" rainfall field, and as predicted, the attenuation as obtained by using the radar measured rainfall field.

4. APPLICATION OF THE SIMULATION MODEL

In the simulation, we consider 8 rainfall events, obtained varying the three most significative parameters of the model, in order to generate events characterized by different average long term intensity, as well as by different space-time features. Translation velocity components v_x and v_y are always set to 5 and 8 kmh^{-1}, respectively. Parameters ϕ, and v assume the same values (3 km and 0.025 min^{-1}, respectively) for each generated event. Values adopted for Λ, μ, and i_0, are listed in Table 1.

Table 1

event	1	2	3	4	5	6	7	8
Λ(cells/km²)	.03	.03	.06	.06	.03	.03	.06	.06
μ(cells/min)	.02	.02	.02	.02	.04	.04	.04	.04
i_0(mm/h)	10	50	10	50	10	50	10	50

Such events last 200 minutes each, and a 70km×70km area is considered, a sufficient space-time extension to permit a meaningful analysis of the generated data, while maintaining the computing time within acceptable limits. The link is supposed to be along the direction of a ray path. This allow us to better evidentiate the effect due to the distance from radar of the radar sample volume. The geometry of the link is shown in Fig. 1.
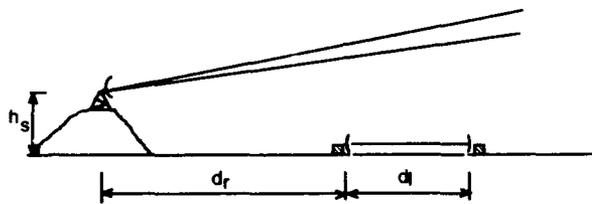
Figure 1:Geometrical sketch of the simulation

The radar data generation process, produces reflectivity data in a circular sector covering the area where "true" rainfall data are available. In Table 2, radar and geometrical adopted parameters are listed. Such parameters reflect typical operational environment of a weather radar system used for hydro-meteorological applications. So, we supposed that the radar is installed on a hill at an altitude of 235m, and operates with an elevation angle greater than zero, supposing that the

antenna beam must avoid to intercept some orographic relieves have to be crossed in order to assure a sufficiently wide coverage area.

Table 2

h_s(m)	d_r (Km)	e(deg)	Φ_l (deg)	Φ_r (deg)	Δr (m)	N_i
235	40	0.5	1.1	0.9	150	64

Supposing that "true" rainfall data refer to the sea level, and that the radio link lies at the same level, radar will sample rainfall at a considerable higher level than that of rainfall disturbing the radio link. The area over which data are generated is at 40 km far away from the radar site and the quote of center of the radar beam varies approximately from 585 and 760 meters over the level of the radio link.

Measured radar reflectivity data are converted into rainfall data by using relationships as of the kind (5) and (6), for a single polarization and dual polarization measurements respectively. Once such data are referenced to the ground, path attenuation data are obtained by substituting R in the (8), where $\alpha=0.121$ and $\beta=1.074$, according to the relationship used in Ref 8 for the frequency of 25 GHz for a Marshall-Palmer DSD. The quality of path attenuation estimate is evaluated through as

$$P_a = \frac{(\text{storm duration}) - (\text{outage time})}{(\text{storm duration})} \cdot 100 \quad (11)$$

where the outage time is the period of time during which path attenuation is exceeding a given threshold. The resulting path attenuation estimates are affected from errors arising from different sources, which are due to the uncertainty on the adopted K-R relationship, to the vertical profile of precipitation (including the presence of bright band) and to the effect of C-band attenuation due to the intercepted rain. It is thus important to individuate what kind of data processing could be performed to enhance the reliability of estimate. Here we analyze the effects and eventually, benefits brought by the correction of the attenuation due to rain propagation and by a simple correction for the effect of vertical profile of precipitation.

4.1 A procedure for correction of C-band rain induced attenuation

The effects that C-band attenuation propagation has on both measured Z_H and Z_{DR} data must be corrected to obtain sufficiently reliable radar rainfall estimates. The algorithm used here has been described by Aydin et al. (Ref. 6). Such algorithm is essentially an extension of the procedure devised by Hildebrand (Ref.) to the dual polarization case. First order estimates of Z_H(dBZ) and Z_{DR}(dB) at the n-th gate are given by

$$Z_{Hn}^{\cdot} = Z_{Hn}^{\cdot} - 2\Delta r \sum_{i=k}^{n-1} K_{Hi} \quad (12a)$$

$$Z_{V_n}^* = Z_{V_n}^{**} - 2\Delta r \sum_{i=k}^{n-1} K_{V_i} \qquad (12b)$$

$$Z_{DRn}^* = Z_{Hn}^* - Z_{V_n}^* \qquad (12c)$$

where meaning of symbol is the same as in (10a) and (10b), and the specific attenuations are computed on the basis of reflectivity values obtained at the preceding gate. After that, an iterative process starts at the n-th gate, which progressively gives higher-order estimates by recalculating the specific attenuations by means of the lower-order ones, and so on, until the absolute differences between two consecutive estimates are less than 0.1 dB for Z_{Hn} and 0.05 for Z_{DRn}, or the convergence have not obtained after six iterations. This method has been applied setting standard deviations of the calibration errors N_{ZH_n} and N_{ZDR_n}, as 0.3 and 0.05 dB, respectively, and the biases due to the same errors B_{ZH} and B_{ZDR}, as 0.3dB and 0.03 dB respectively. Performance of the algorithm is usually satisfying, while the major error cause relies on the initial bias.

4.2 Assessment of rainfall estimates by raingauge calibration

The effect of the vertical profile of the precipitation could be mitigated if the rainfall radar estimate is compared with an accurate point rainfall estimate at ground, as that available from one or more raingauges. The reflectivity-rainfall relationship can be used by simply substituting standard values for the pairs a, b and A, B. Otherwise, such parameters could be estimated by resorting to the information obtainable from a raingauge. Here we utilize as standard relationships that by Marshall-Palmer for single polarization measurements (Ref. 14)

$$a = 200 \qquad (13a)$$
$$b = 1.6 \qquad (13b)$$

and that by Ulbrich and Atlas for dual polarization measurements (Ref. 15)

$$A = 1.69 \times 10^{-3} \qquad (14a)$$
$$B = -1.55 \qquad (14b)$$

Supposing that a raingauge is located in a position corresponding to the middle of the radio link path, such coefficients are computed through a regression method, performed on data available during the storm duration. This situation is not compatible with real time processing requirements, since the adopted regression procedure require the knowledge of data of the entire or part of event. This approach is instead feasible if operating off-line on a database of radar reflectivity data and raingauge data. Instead, that of having a raingauge available in such a favorable position is an optimistic hypothesis, indeed. Results obtained are discussed in the next section.

5. ANALYSIS OF RESULTS

Results refer to different processing procedures applied to the reflectivity data. Two different path lengths (d_l) 10 and 20 Km., have been considered, in order to take into account the effect of the increasing distance from radar and to evaluate its influence on the path attenuation and on the effectiveness of adopted correction procedure for C-band rain induced

attenuation. In Figure 2, path attenuation is shown as a function of time, for the rainfall event numbered 1 and $d_l = 20$ Km. Different processing schemes have been tested for rainfall rate estimation and subsequent prediction of specific attenuation: Figs. 2a and 2b refer to a radar providing absolute reflectivity data only, while Figs. 2c and 2d refer to a radar exploiting both absolute and differential reflectivity. Furthermore, solid curves represent "true" attenuation, dotted one refer to the case that no C-band attenuation correction be performed, and the dashed lines refer to the case that such correction be performed. In plotting Figs. 2a and 2c, standard relationship with parameters given in (13) and (14) have been employed, while in plotting Figs. 2b and 2d parameters of the reflectivity-rainfall relationships have been computed according to the regression procedure described in section 4.2. A merely qualitative analysis of the results, seems to indicate that a main source of error is related to the effect of the vertical reflectivity profiles, since the bias in the attenuation estimate, visible in Figs. 2a and 2c, is not removed by the C-band attenuation correction procedure. A similar observation can be made also to the plots shown in Fig. 3, obtained under the same hypothesis adopted for plots of Fig. 2, but with a 10km path length. A more accurate and quantitative analysis of the results, can be done referring to the scatter plots shown in Figs. 4 and 5. Here a 20 dB path attenuation threshold was selected as a basis for evaluation of both "true" and predicted Percentage Availability as defined in Section 3, for both cases of 10 km and 20 km path length. Subplot indexing and curve codes are the same adopted for Figs. 2 and 3. Each points refers to the "true" and estimated attenuation for each event. Circle marks refer to the case of uncorrected C-band attenuation effects. The beneficial effect provided by the calibration procedure is quite evident, since regression line closely approaches the diagonal. Although less evident, we point out a noticeable reduction of the spreading effect of single points around the regression line, when the C-band attenuation correction procedure is applied, when both single or dual polarization radar measurements are used. Such benefits are more evident in Fig 5, referring to a case for which rainfall sampled by radar is on the average, closer to the radar site and thus at a lower altitude. The main disadvantage in using the procedure described in Section 4, is related to the iterative nature on which the correction algorithm is based: in fact, correction tends to be less effective as distance from radar increases, especially when some anomalous value of Z_{DR}, due to a partial interception of the melting layer, are detected. This means that it is not convenient to devise processing techniques that completely separate the effect of vertical profile from that due to propagation attenuation. Even if Figure 5d presents a lower number of points than in the corresponding subplot of Fig. 4, because of the severe attenuation that causes for some events, the set threshold to be exceeded for the whole event duration, advantages carried out by the joint use of the correction and calibration technique, in terms of bias and dispersion are evident.

6. CONCLUSIONS

The problem of planning radio relays operating at millimeter frequencies with the aid of historical reflectivity data available from a C-band dual linear polarization radar measurements, has been analyzed. The need of adopting procedures for correcting the propagation attenuation due to rain and the effects of vertical profiles of reflectivity are underlined, by

comparing results obtained during some synthetic rainfall events. Some limits in the use of such estimates for an increasing distance from radar have been pointed out. The advantages of the use of dual polarization, especially when the dual polarization information is not conveniently processed seem to be, for this specific application, scarce. Such advantages would indeed be evident when trying to assess the probability of occurrence of precipitation other than rain (hail, graupels, wet snow) which may be responsible for more pronounced scattering and absorption phenomena.

7.   REFERENCES

1.   Leitao, M. J. and P. A. Watson, "Application of dual linearly polarized radar data to prediction of microwave path attenuation at 10-30 GHz", Radio Science, 19, 5, 1984, pp 209-221.

2.   Leitao, M. J. and P. A. Watson, "Method for prediction of attenuation on earth-space links based on radar measurements of the physical structure of rainfall", IEE Proceedings Pt. F, 4, July 1986, pp 429-440.

3.   Hitschfeld W. and J. Bordan, "Errors inherent in the radar measurement of rainfall at attenuating wavelengths", J. Meteorol, 11, 1954, pp 58-67.

4.   Sims, A.L., Mueller, E.A., Stout, G.E. and T.E. Larson, "Investigation of the quantitative determination of point and areal precipitation by radar echo measurements", 9th Tech. Rep., U.S. Army Electronics Research and Development Lab., Ft. Monmouth, NJ, 1964.

5.   Hildebrand, P.H., "Iterative correction for attenuation due to rain for C-band dual linear polarization radars", J. Appl. Meteorol., 17, 1978, pp. 508-514.

6.   Aydin, K., Zhao, Y., and T.A. Seliga, "Rain-induced attenuation effects on C-Band dual-polarization meteorological radars", IEEE Trans. Geosci. Remore Sensing, GE-27, 1, Jan. 1989, pp. 57-66.

7.   Doviak, R. J., and D. S. Zrnic, "Doppler Radar and Weather Observation", Academic Press, 1984, 458 pp.

8.   Olsen, R.L., Roger, D.V., and D. B. Hodge, "The aR b relation in the calculation of rain attenuation", IEEE Trans. Ant. Prop., AP-26, 1978, pp. 318-329.

9.   Atlas, D., and C. Ulbrich, "Path -and area- Integrated Rainfall Measurement by Microwave Attenuation in the 1-3 cm Band", J. Appl. Meteor, 16, pp. 1322-1331.

10.   Giuli, D., Facheris L., and Freni, A., "An integrated model for simulation of dual linear polarization radar measurement fields", to be published on IEE Proceedings, part F.

11.   Rodriguez-Iturbe, I. and P. S. Eagleson, "Mathematical models of rainstorm events in space and time", Water Resources Res, 23 , 1987, pp. 181-190.

12.   Scarchilli, G., Gorgucci, E., Giuli, D., Facheris, L., and A. Freni, "Arno Project: Radar system and objectives", in "Proc. 25th Conf. on Radar Meteorology", Amer. Meteor. Soc., Boston, 1991, pp. 805-808.

13.   Giuli, D., Baldini, L., Facheris, L., and M. Gherardelli, "Arno Project: evolution of data processing techniques in dual polarization radar", in "Proc. 25th Conf. on Radar Meteorology", Amer. Meteor. Soc., Boston, 1991, pp. 579-582.

14.   Marshall, J.S. and Palmer, W.M.K, "The distribution of raindrops with size", J. Meteor., 5, 1948, pp. 165-166.

15.   Ulbrich, C. W. and D., Atlas, "Assesment of the contribution of differential polarization to improved rainfall measurements", Radio Sci., 19, 1984, pp. 49-57.
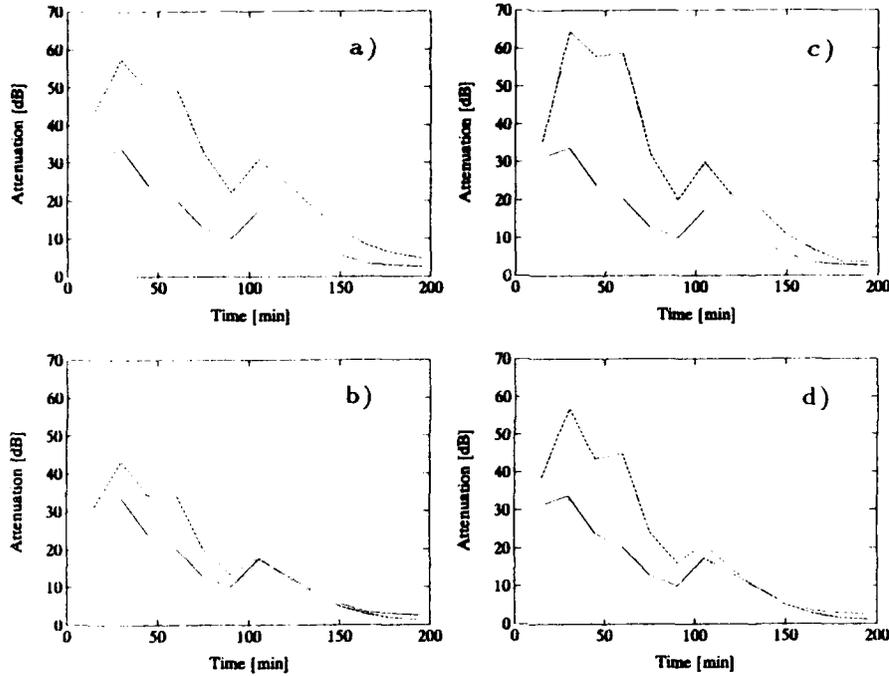
Figure 2: Path attenuation (dB) versus time for the event number 1. Solid line: True attenuation; Dotted line: Predicted path attenuation (C-band attenuation correction not performed); Dashed line: Predicted path attenuation (with C-band attenuation correction); d_{i_1}=20 km

a) Single (H) polarization, standard Z_H-R relationship;   b) Single (H) polarization, calibrated Z_H-R relationship
c) Dual (H) polarization, standard (Z_{DR})-R relationship;   d) Dual (HV) polarization, calibrated (Z_{DR})-R relationship
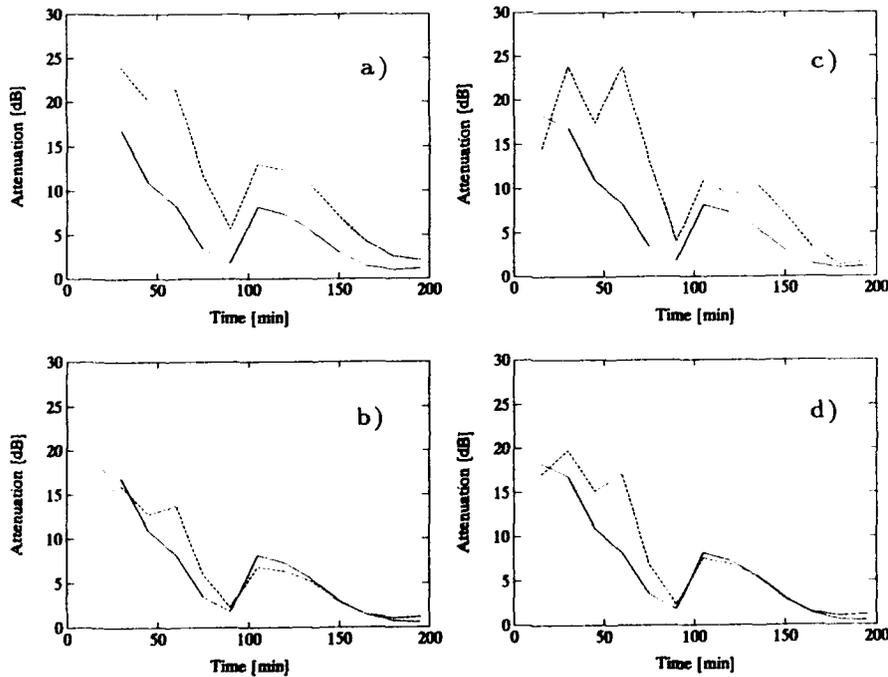
Figure 3: Path attenuation (dB) versus time for the event number 1. Solid line: True attenuation; Dotted line: Predicted path attenuation (C-band attenuation correction not performed); Dashed line: Predicted path attenuation (with C-band attenuation correction); d_{i_1}=10 km

a) Single (H) polarization, standard Z_H-R relationship;   b) Single (H) polarization, calibrated Z_H-R relationship
c) Dual (H) polarization, standard (Z_{DR})-R relationship;   d) Dual (HV) polarization, calibrated (Z_{DR})-R relationship
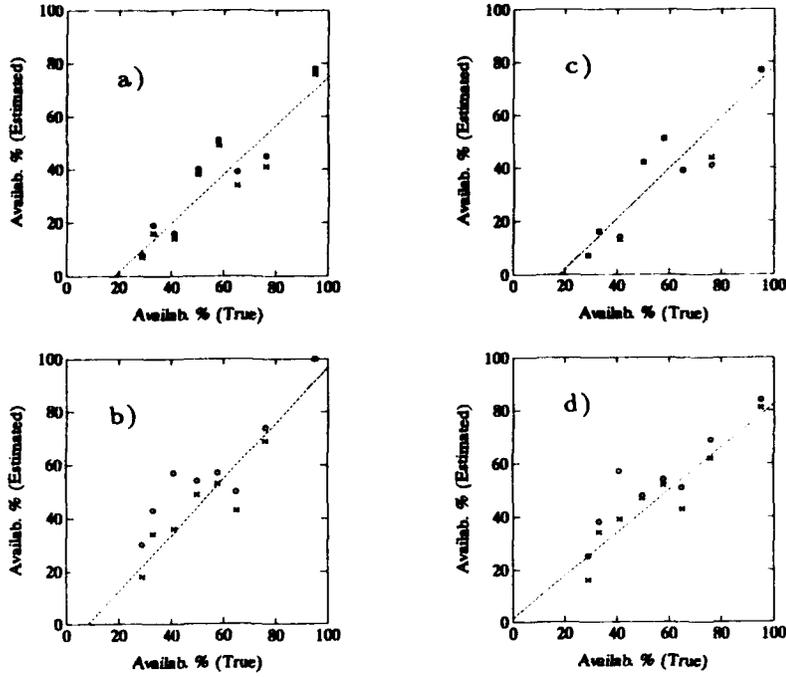
Figure 4: Scatterplot of true Percentage availability of a link, versus the predicted one.; Dotted line and circles: Predicted path attenuation (C-band attenuation correction not performed); Dashed line and "x": Predicted path attenuation (with C-band attenuation correction); d_{i_1}= 20 km

a) Single (H) polarization, standard Z_H-R relationship; b) Single (H) polarization, calibrated Z_H-R relationship

c) Dual (H) polarization, standard (Z_{DR})-R relationship; d) Dual (HV) polarization, calibrated (Z_{DR})-R relationship
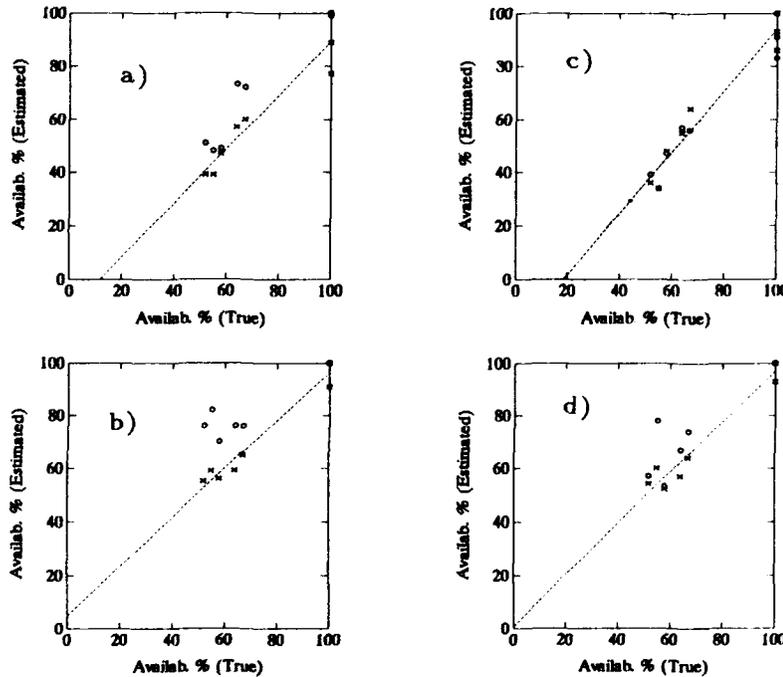
Figure 5: Scatterplot of true Percentage availability of a link, versus the predicted one.; Dotted line and circles: Predicted path attenuation (C-band attenuation correction not performed); Dashed line and "x": Predicted path attenuation (with C-band attenuation correction); d_{i_1}= 10 km

a) Single (H) polarization, standard Z_H-R relationship; b) Single (H) polarization, calibrated Z_H-R relationship

c) Dual (H) polarization, standard (Z_{DR})-R relationship; d) Dual (HV) polarization, calibrated (Z_{DR})-R relationship

Discussion

Discussor's name :   W. Flood, USA

Comment/Question :

You had raingauge data to calibrate both single polarization reflectivity and differential reflectivity with rainfall rate on the ground. You used these calibrations to estimate MMW attenuation along the paths. Just what is the advantage of the differential reflectivity technique over a single polarization reflectivity estimate?

Author/Presenter's reply :

At the present stage of analysis no particular advantage emerged in using the different reflectivity techniques for this application.

Discussor's name :   U. Lammers, US

Comment/Question :

Did you actually compare radar-derived slant path attenuation with measured slant path attenuation?

Author/Presenter's reply :

No such a comparison has been made yet. At the present stage we are analysing possible causes of errors, through simulation models suitable for statistical analysis of performance. Some experimental radar data and raingage measurements have been analysed to check the robustness of the slant path attenuation estimate with respect to the raingage displacement, which can affect the raingage/radar calibration process.

PROPAGATION MODELING OF MOIST AIR AND SUSPENDED WATER/ICE PARTICLES AT FREQUENCIES BELOW 1000 GHz

H. J. Liebe
G. A. Hufford
M. G. Cotton
National Telecommunications and Information Administration
Institute for Telecommunication Sciences
325 Broadway, Boulder, CO 80303
U.S.A

SUMMARY

Propagation characteristics of the atmosphere are modeled for the frequency range from 1 to 1000 GHz (1 THz) by the modular millimeter-wave propagation model MPM. Refractivity spectra of the main natural absorbers (i.e., oxygen, water-vapor, suspended droplets and ice particles) are computed from known meteorological variables. The primary contributions of dry air come from 44 O_2 lines. Results from extensive 60-GHz laboratory measurements of the pressure-broadened O_2 spectrum were applied to update the line data base. The water-vapor module considers 34 local H_2O lines plus continuum contributions from the H_2O spectrum above 1 THz, which are formulated as wing response of a pseudo-line centered at 1.8 THz. Cloud/fog effects are treated with the Rayleigh approximation employing revised formulations for the permittivities of water and ice.

The influence of the Earth's magnetic field on O_2 absorption lines becomes noticeable at altitudes between 30 and 120 km. Anisotropic medium properties result, which are computed by the Zeeman propagation model ZPM. Here the elements of a complex refractivity tensor are determined in the vicinity (± 10 MHz) of O_2 line centers and their effect on the propagation of plane, polarized radiowaves is evaluated.

A spherically stratified (0 - 130 km) atmosphere provides the input for the codes MPM and ZPM in order to analyze transmission and emission properties of radio paths. Height profiles of air and water vapor densities and of the geocoded magnetic field are specified. ZPM predicts polarization- and direction-dependent propagation through the mesosphere. Emission spectra of the 9^+ line (61150 ± 3 MHz) for paths with tangential heights ranging from 30 to 125 km are consistent with data measured by the shuttle-based millimeter-wave limb sounder MAS.

1. INTRODUCTION

The natural atmospheric absorbers of oxygen, water vapor, and suspended water-droplets or ice-crystals, determine the propagation properties of the nonprecipitating atmosphere. The spectral characteristics of these absorbers are predicted up to 1000 GHz based on the physical conditions at altitudes from sea level to 130 km. Both phase and amplitude response of a plane radio wave propagating the distance z at frequency ν are described by a field strength,

$$E(z) = \exp[\, i \, k \, z(\, 1 + N \times 10^{-6}\,)]\, E(0),$$

where $E(0)$ is the initial value, $k = 2\pi\nu/c$ is the free space wave number, and c is the speed of light in vacuum. The spectral characteristics of the atmospheric medium are expressed by a complex refractivity,

$$N = N_o + N' + i\, N'' \quad \text{ppm} \qquad (1)$$

The real part changes the propagation velocity (refraction) and consists of a frequency-independent term, N_o, plus the dispersive refraction $N'(\nu)$. The imaginary part quantifies the loss of radiation energy (absorption). Refractivity N determines the specific quantities of power attenuation α and phase dispersion β or delay rate τ. Assuming frequency ν in GHz, one obtains

$$
\begin{aligned}
\alpha &= 0.1820\,\nu\, N'' && \text{dB/km,} \\
\beta &= 1.2008\,\nu\,(N_o + N') && \text{deg/km,} \\
\tau &= 3.3356\,(N_o + N') && \text{ps/km.}
\end{aligned}
$$

Under special circumstances the refractivity N can exhibit *anisotropic* properties (e.g., mesospheric O_2 Zeeman effect). In such a case the propagation of plane, polarized waves is characterized by a two-dimensional field vector $E^*(z)$ which is affected perpendicular to the direction of propagation by a 2×2 refractivity matrix N.

2. ATMOSPHERIC REFRACTIVITY

2.1 Input Variables

Complex refractivity N is the central quantity computed by the Millimeter-wave Propagation Model MPM.[1,2] Here, the opportunity is taken to update MPM89 [2] with the latest spectroscopic information. The model considers 44 O_2 and 34 H_2O local lines (centered below 1000 GHz), nonresonant spectra for dry air, and an empirical water vapor continuum which reconciles experimental discrepancies. Model formulations for dry air and water vapor spectra follow closely the theory of absorption by atmospheric gases that is reviewed in detail by Rosenkranz.[3] The refractivity of suspended water and ice particles is computed with the Rayleigh absorption approximation.[4] Atmospheric conditions in MPM are characterized by the input variables:

			Typical Range	
- barometric pressure	p		10^{-5} - 1013	mb
- ambient temperature	t		-100 - 50	°C
- relative humidity	u		0 - 100	%
- water droplet density	w		0 - 5	g/m^3
- ice particle density	w_i		0 - 1	g/m^3
- magnetic field strength	B		20 - 65	μT.

For modeling purposes, a reciprocal temperature variable is introduced, $\theta = 300/(t + 273.15)$, and the barometric pressure p (1 mb = 100 Pa) is separated into partial pressures for dry air (p_d) and water vapor (e); i.e.,

$$p = p_d + e \quad \text{mb.}$$

2.2 Dry-Air Module

Refractivity of dry air is expressed by

$$N_D = N_d + \sum_k S_k F_k + N_n \quad ppm, \qquad (2)$$

where the nondispersive term is

$$N_d = 0.2588 \, p_d \, \theta .$$

2.2.1 Oxygen Line Terms

The main contributions to N_D come from 44 O_2 spectral lines (k = line index). Each line strength,

$$S_k = (a_1 / \nu_k) \, p_d \, \theta^3 \exp[a_2 (1 - \theta)] \quad ppm,$$

is multiplied by the complex shape function,

$$F(\nu) = \nu \left[\frac{1 - i\delta_k}{\nu_k - \nu - i\gamma_k} - \frac{1 + i\delta_k}{\nu_k + \nu + i\gamma_k} \right] \qquad (3)$$

The Van Vleck-Weisskopf function $F(\nu)$ was modified by Rosenkranz[3] to include line overlap effects. Width (γ) and overlap (δ) parameters of pressure-broadened O_2 lines in air are

$$\gamma_k = a_3 \times 10^{-3} \, (p_d \, \theta^{0.8} + 1.10 \, e \, \theta) \quad GHz$$

and

$$\delta_k = (a_5 + a_6 \, \theta) \, p \, \theta^{0.8} .$$

A rough estimate of line behavior in the mesosphere can be obtained by replacing γ_k with

$$\gamma_h = (\gamma_k^2 + 625 \, B^2)^{1/2} ,$$

where B is the magnetic field strength (22 - 65 μT) depending on the geographic location and altitude (see Sect. 2.3).

Extensive laboratory measurements of 60-GHz absorption by dry air have been reported recently.[5] A best fit to these data established new coefficients a_5 and a_6 for the microwave lines. Still, the values listed for a_3 and $a_{5,6}$ in Table 1 are different from Ref. 5. Indirect evidence from the data suggests that all microwave widths γ_k are multiplied by 1.05.


Dry Air   6°C
- MPM93

- 1013 mb
- 701
- 472
- 308
- 195
- 121
- 76

Attenuation α, dB/km

Frequency f, GHz
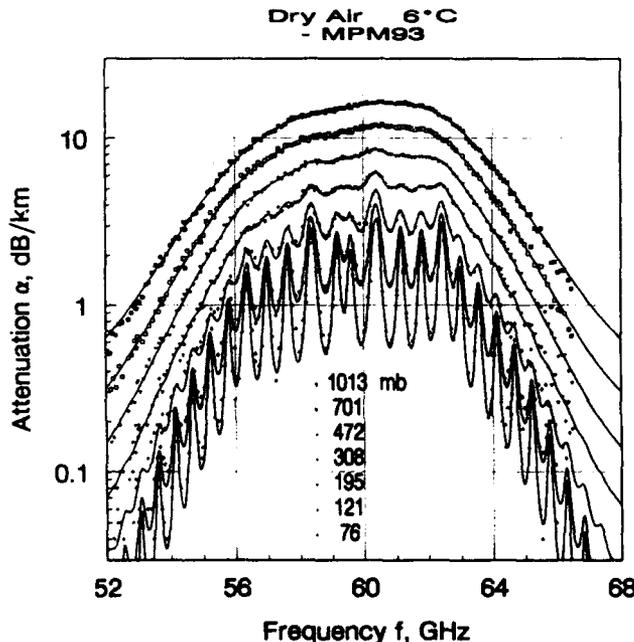
Figure 1. Dry air attenuation α from 52 to 68 GHz at 6°C for pressures from 1013 to 76 mb: MPM93 (lines), measured data [5] (symbols).

This correction reduced on the average by 7 percent the rms error of the residuals for all 5400 data points when, in addition, the δ_k's were raised by a factor of 1.15.[5] Center frequencies ν_k and spectroscopic coefficients a_1 to a_6 are listed in Table 1.

The good fit between predicted attenuation rates and measured data points is illustrated in Fig. 1. Some of the very first attenuation rates (14 values, 49 - 59 GHz) for sea-level conditions were reported in 1956.[6] These field-measured data agree well with predictions based on Eq. (2).

2.2.2 Nonresonant Terms

Nonresonant refractivity,

$$N_n = S_o F_o(\nu) + i \, S_n F_n''(\nu) \quad ppm,$$

consists (a) of the nonresonant O_2 spectrum,

$$S_o = 6.14 \times 10^{-5} \, p_d \, \theta^2 ,$$

$$F_o = -\nu / (\nu + i \gamma_o),$$

where the relaxation frequency is $\gamma_o = 0.56 \times 10^{-3} \, p \, \theta^{0.8}$; and (b) of small contributions above 100 GHz by pressure-induced N_2 absorption,

$$S_n = 1.40 \times 10^{-12} \, p_d^2 \, \theta^{3.5} ,$$

$$F_n'' \approx \nu / (1 + 1.9 \times 10^{-5} \, \nu^{1.5}).$$

2.3 Zeeman-Effect of O_2 Lines

In the mesosphere, oxygen line absorption is complicated.[7-9] Three separate complex-valued Zeeman refractivity patterns, $N_{\sigma\pm}$ and N_{π}, are brought out by the geomagnetic field vector B^*. The refractivity that influences the field components of a plane wave is expressed in matrix form,[8]

$$N = \begin{vmatrix} N_\pi \sin^2 \phi + (N_{\sigma+} + N_{\sigma-})\cos^2\phi & -i(N_{\sigma+} - N_{\sigma-})\cos\phi \\ i(N_{\sigma+} + N_{\sigma-})\cos\phi & N_{\sigma+} + N_{\sigma-} \end{vmatrix}$$

where ϕ is the angle between the direction of propagation and the magnetic vector B^*. The refractivity elements of an isolated line are represented by

$$N_{\sigma\pm, \pi} = N_d + S_k \sum_M \xi_M F_M \quad ppm, \qquad (4)$$

where ξ_M is a relative strength factor defined in such a way that the sum of the Zeeman components equals the strength value (a_1) of the unsplit (B = 0) line. The center frequency of individual lines within a pattern is determined by

$$\nu_M = \nu_k + 28.03 \times 10^{-6} \, \eta_M \, B \quad GHz,$$

where the relative shift factor η_M lies between + 1 and - 1. The index M stands for the azimuthal quantum number M, which controls the structure of a Zeeman pattern.[9] The scheme for determining ξ_M and η_M hinges on the quantum number identification of a particular O_2 line and can be found in Refs. 8, 9. The correct shape function is a Voigt profile,[3] which was approximated by a Lorentzian profile,

$$F_M = \nu / (\nu_M - \nu - i \gamma_h),$$

where the transition to Doppler-broadening at h $\geq$ 50 km ($p \leq 0.8$ mb) is given for each Zeeman component by

$$\gamma_h = 0.535 \, \gamma_k + (0.217 \, \gamma_k^2 + \gamma_D^2)^{1/2} \quad GHz.$$

The Doppler width is $\gamma_D = 1.096 \times 10^{-6} \, \nu_M \, \theta^{1/2} .$

2.4 Water-Vapor Module

The MPM-input for water vapor is relative humidity u, which is converted to vapor pressure $e = (u/100) e_s$ by way of the saturation pressure e_s over water (or ice) [10] at temperature t. A useful approximation for saturation over water is given by

$$e_s = 2.408 \times 10^{11} \theta^5 \exp(-22.644 \theta) \quad \text{mb}.$$

Absolute humidity (water-vapor density) follows from

$$q = 0.7223 e \theta \quad \text{g/m}^3.$$

Refractivity of atmospheric water vapor is written in the form

$$N_V = N_v + \sum_\ell S_\ell F_\ell + N_c \quad \text{ppm}, \quad (5)$$

where the nondispersive term is

$$N_v = (4.163 \theta + 0.239) e \theta .$$

2.4.1 H_2O Line Spectrum

Line refractivity results from 34 local H_2O resonances (ℓ = line index). The individual line strength is

$$S_\ell = (b_1/\nu_\ell) e \theta^{3.5} \exp[b_2(1 - \theta)] \quad \text{ppm};$$

the shape function is that of Eq. (3). The width of a pressure-broadened H_2O line is formulated by [11]

$$\gamma_\ell = b_3 \times 10^{-3} (b_4 e \theta^{b6} + p_d \theta^{b5}) \quad \text{GHz}.$$

Line overlap is neglected ($\delta_\ell = 0$) and Doppler-broadening is approximated for pressures below 0.7 mb (h $\geq$ 60 km) by

$$\gamma_\ell^* = 0.535 \gamma_\ell + (0.217 \gamma_\ell^2 + \gamma_D^2)^{\frac{1}{2}},$$

where the Doppler width is $\gamma_D = 1.46 \times 10^{-6} \nu_\ell \theta^{\frac{1}{2}}$.

2.4.2 H_2O Continuum Spectrum

The contributions of local lines in Eq. (5) are not sufficient to match measured data. In particular, absorption data in the window ranges between spectral lines reflect a magnitude up to five times larger than predicted values. The excess is taken into account by a continuum spectrum N_c, which originates in the strong lines centered in the rotational H_2O spectrum above 1 THz.[14, 20] Absolute absorption data from controlled experiments [15 - 19] provide the basis for formulating a physical model of N_c. Pure water vapor and foreign-gas (air or N_2) mixtures were studied at 18 - 40 GHz [15], 138 GHz [16], 186 - 194 GHz [17], 213.5 GHz [18], and 160 - 920 GHz [19].

At 137.8 GHz, pressure and temperature dependences of moist air absorption data were fitted with 10% rms to [16]

$$N_c'' = e (k_s e + k_f p_d) 10^{-6} \nu \quad \text{ppm}, \quad (6)$$

where $k_s = 0.357 \theta^{7.5}$ and $k_f = 0.0113 \theta^3$. This equation was then applied to define the continuum for MPM89.[2]

At 213.5 GHz, new absorption data of moist nitrogen have been reported,[18] which fitted with an oxygen-free MPM exceptionally well to Eq. (6):

$$k_s = 0.444 \theta^{7.5} \quad (0.4\% \text{ rms}) \quad \text{and}$$

$$k_f = 0.0145 \theta^{4.5} \quad (1.0\% \text{ rms}).$$

Similar data closer to the 183-GHz line center [17] yielded initially a fitting error of 14.6% rms, which improved to 4.5% rms when the theoretical [12] strength value b_1 was increased by 5 percent. A theoretical approximation of the real part,[20]

$$N_c' \approx e \theta^{2.5} 0.791 \times 10^{-6} \nu^2 \quad \text{ppm},$$

was also considered in the fitting exercise.

An analytical match of the continuum was considered by means of a *pseudo*-line centered out-of-band above 1 THz. Expanding the line shape, Eq. (3), into a power series and assuming that $\delta = 0$, $\gamma_c \ll \nu_c$, and $\nu \to 0$, leads to:

$$N_c'' \approx 2 S_c \gamma_c[(\nu/\nu_c) + 3 (\nu/\nu_c)^3] \nu_c^{-2} \quad \text{and}$$

$$N_c' \approx 2 S_c [(\nu/\nu_c)^2 + (\nu/\nu_c)^4] \nu_c^{-1} \quad (7)$$

Different fits to Eq. (7) resulted in three sets of parameters for this pseudo-line:

ν_c	b_1	b_2	b_3	b_4	b_5	b_6	Data Ref.
GHz	kHz/mb		MHz/mb				
2200	4210	0.952	17.8	30.5	2	5	15, 18, 19
1780	2230	0.952	17.6	30.5	2	5	15, 18, Table 2
1470	1257	0.952	17.3	30.5	2	5	15, 18, 20

For the "continuum" line N_c centered at $\nu_c = 1780$ GHz and the chosen units one can assert that

$$k_s (\theta = 1) = 2 \times 10^3 b_1 b_3 b_4 \nu_c^{-3} = 0.434 \quad \text{GHz}^{-1} \text{mb}^{-2},$$

which is close to the value found by fitting the 213.5-GHz data alone (see above). The second-order ν-terms of Eq. (7) allow one to "tailor" the fit close to the upper frequency limit of MPM (1 THz) by changing ν_c. An exact fit to both measured absorption data [19] and analytical refraction results [20] around 900 GHz was not possible. Hence, the continuum line parameters ν_c and b_1 in Table 2 are a compromise which is of no consequence to data fits below about 800 GHz. Both the large widths for far-wing self-($b_3 \times b_4$) and air-broadening (b_3) and the strong negative temperature dependence (b_6) have been postulated by theory.[14, 21]

Table 2 lists the present line frequencies ν_ℓ and spectroscopic coefficients b_1 to b_6 (ν_ℓ and b_1 are from Ref. 12). The b_1 values of the 22-GHz line* and 183-GHz [17] lines were increased by 5 percent to fit measured data.

The MPM for moist air is made up by $N = N_D + N_V$. Predictions of N'' are compared with published data in Figs. 2 to 4. The critical temperature dependence of N_c'' is represented in Fig. 2. The frequency dependence of three data sets [15, 17-19] is shown in Figs. 3 and 4. Measured data in Fig. 4 span a range from 160 to 920 GHz.[19] MPM-predicted attenuation rates $\alpha(\nu)$ are plotted in Fig. 5 for sea-level conditions (100% RH) at five temperatures ($\pm$ 40°C).

2.5 Cloud/Fog Module

The interaction of suspended water droplets and ice crystals with radio waves is treated by employing the Rayleigh approximation for Mie extinction,

$$N_W = 1.5 (w/m_{w,i})[(\epsilon_{w,i} - 1)(\epsilon_{w,i} + 2)^{-1}], \quad (8)$$

where $m_{w,i} = 1$ and 0.916 (g/cm^3) are specific weights, and $\epsilon_{w,i}$ complex permittivities of water and ice, respectively.[4] For the size spectra (r $\leq$ 50 μm) of suspended water droplets, Eq. (8) is valid up to about 300 GHz. Fog or cloud conditions are specified by a water mass density w. Water droplets form when the relative humidity exceeds saturation, $u \approx 100 - 101$ percent, whereby t can be as low as - 40°C (supercooled state). Propagation effects caused by ice crystals (needles and plates) are primarily depolarizing and scattering in nature.

---

*The increase in the b_1-coefficient for the 22.2-GHz line was suggested by ground-level emission measurements.[13] Data at 20.6 GHz exhibited a systematic trend which was not apparent in 31.7- and 90-GHz data taken simultaneously. On-site radiosonde recordings of height profiles for p, t, and u furnished independent input to test three prediction models.

3-4
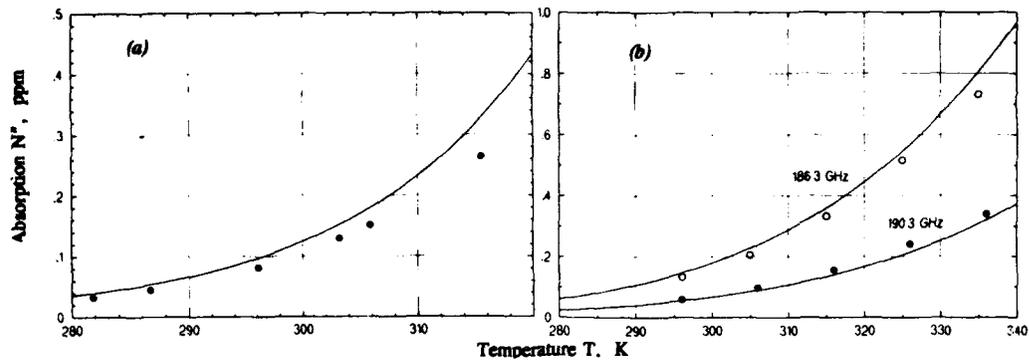
Figure 2. Absorption data N″ versus temperature T in kelvin: (a) moist air at 137.8 GHz (p = 1013 mb, u = 80%) [16], and (b) mixture of water vapor and nitrogen (186.3 and 190.3 GHz, p = 1000 mb, u = 10%) [17]. — MPM93.
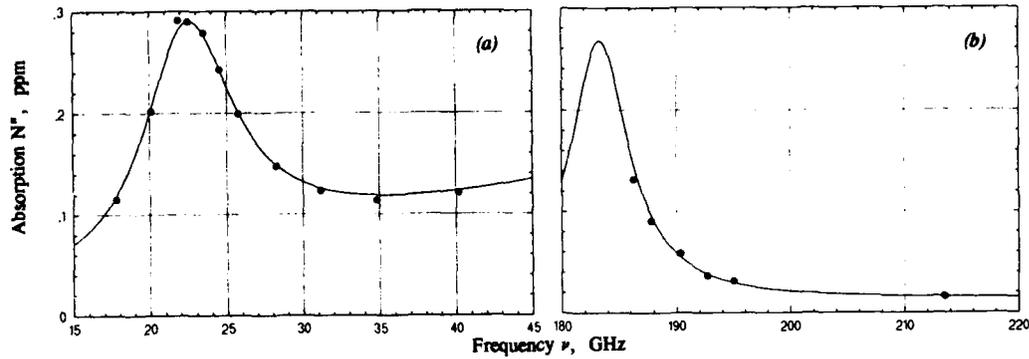
Figure 3. Absorption data N″ over two frequency ranges: (a) moist air (318 K, p = 1013 mb, u = 80%) [15], and (b) mixture of water vapor and nitrogen (296 K, p = 1000 mb, u = 10%) [17, 18]. — MPM93.
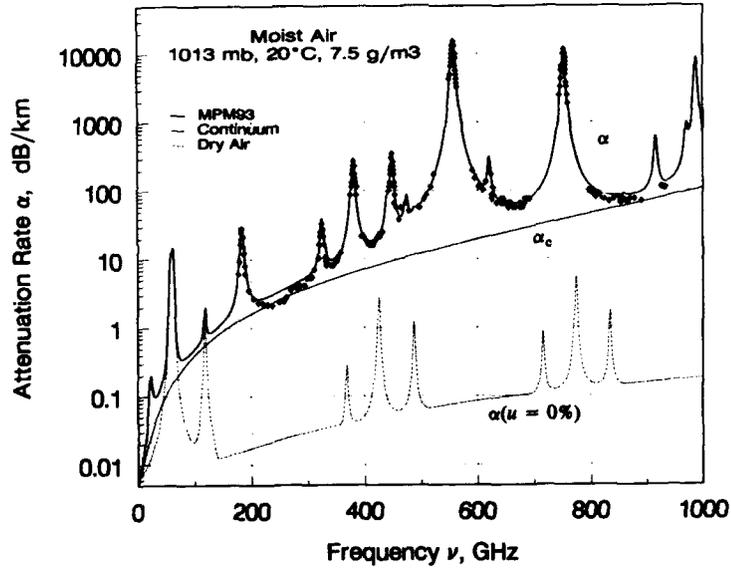

Figure 4. Attenuation rate α and continuum of moist air (u = 43.4%) and of dry air (u = 0) as predicted by MPM93 for standard sea-level conditions (p = 1013 mb, t = 20°C). Data points are from Ref. 19.

4-7

TABLE 1. Spectroscopic Coefficients of O_2 Lines in Air

Center Freq. ν_k	Strength		Width		Overlap	
	a_1	a_2	a_3^*	a_4	a_5^*	a_6^*
GHz	kHz/mb		MHz/mb		10^{-3}/mb	
50.474238	9.400E-08	9.694	0.89	0.8	0.240	0.790
50.987749	2.460E-07	8.694	0.91	0.8	0.220	0.780
51.503350	6.080E-07	7.744	0.94	0.8	0.197	0.774
52.021410	1.414E-06	6.844	0.97	0.8	0.166	0.764
52.542394	3.102E-06	6.004	0.99	0.8	0.136	0.751
53.066907	6.410E-06	5.224	1.02	0.8	0.131	0.714
53.595749	1.247E-05	4.484	1.05	0.8	0.230	0.584
54.130000	2.280E-05	3.814	1.07	0.8	0.335	0.431
54.671159	3.918E-05	3.194	1.10	0.8	0.374	0.305
55.221367	6.316E-05	2.624	1.13	0.8	0.258	0.339
55.783802	9.535E-05	2.119	1.17	0.8	-0.166	0.705
56.264775	5.489E-05	0.015	1.73	0.8	0.390	-0.113
56.363389	1.344E-04	1.660	1.20	0.8	-0.297	0.753
56.968206	1.763E-04	1.260	1.24	0.8	-0.416	0.742
57.612484	2.141E-04	0.915	1.28	0.8	-0.613	0.697
58.323877	2.386E-04	0.626	1.33	0.8	-0.205	0.051
58.446590	1.457E-04	0.084	1.52	0.8	0.748	-0.146
59.164207	2.404E-04	0.391	1.39	0.8	-0.722	0.266
59.590983	2.112E-04	0.212	1.43	0.8	0.765	-0.090
60.306061	2.124E-04	0.212	1.45	0.8	-0.705	0.081
60.434776	2.461E-04	0.391	1.36	0.8	0.697	-0.324
61.150560	2.504E-04	0.626	1.31	0.8	0.104	-0.067
61.800154	2.298E-04	0.915	1.27	0.8	0.570	-0.761
62.411215	1.933E-04	1.260	1.23	0.8	0.360	-0.777
62.486260	1.517E-04	0.083	1.54	0.8	-0.498	0.097
62.997977	1.503E-04	1.665	1.20	0.8	0.239	-0.768
63.568518	1.087E-04	2.115	1.17	0.8	0.108	-0.706
64.127767	7.335E-05	2.620	1.13	0.8	-0.311	-0.332
64.678903	4.635E-05	3.195	1.10	0.8	-0.421	-0.298
65.224071	2.748E-05	3.815	1.07	0.8	-0.375	-0.423
65.764772	1.530E-05	4.485	1.05	0.8	-0.267	-0.575
66.302091	8.009E-06	5.225	1.02	0.8	-0.168	-0.700
66.836830	3.946E-06	6.005	0.99	0.8	-0.169	-0.735
67.369598	1.832E-06	6.845	0.97	0.8	-0.200	-0.744
67.900867	8.010E-07	7.745	0.94	0.8	-0.228	-0.753
68.431005	3.300E-07	8.695	0.92	0.8	-0.240	-0.760
68.960311	1.280E-07	9.695	0.90	0.8	-0.250	-0.765
118.750343	9.450E-05	0.009	1.63	0.8	-0.036	0.009
368.498350	6.790E-06	0.049	1.92	0.2	0	0
424.763124	6.380E-05	0.044	1.93	0.2	0	0
487.249370	2.350E-05	0.049	1.92	0.2	0	0
715.393150	9.960E-06	0.145	1.81	0.2	0	0
773.839675	6.710E-05	0.130	1.82	0.2	0	0
834.145330	1.800E-05	0.147	1.81	0.2	0	0

*Different from MPM89 ^{2}

TABLE 2. Spectroscopic Coefficients of H_2O Lines in Air

| Center Freq. ν_ℓ	Strength		Width			
	b_1^*	b_2	b_3	b_4	b_5	b_6
GHz	kHz/mb		MHz/mb			
22.235080	0.01130+	2.143	2.811	4.80	0.69	1.00
67.803960	0.00012	8.735	2.858	4.93	0.69	0.82
119.995940	0.00008	8.356	2.948	4.78	0.70	0.79
183.310091	0.24200+	0.668	3.050+	5.30	0.64	0.85
321.225644	0.00483	6.181	2.303	4.69	0.64	0.54
325.152919	0.14990	1.540	2.783	4.85	0.67	0.74
336.222601	0.00011	9.829	2.693	4.74	0.68	0.61
380.197372	1.15200	1.048	2.873	5.38	0.69	0.89+
390.134508	0.00046	7.350	2.152	4.81	0.54+	0.55
437.346667	0.00650	5.050	1.845	4.23	0.63	0.48
439.150812	0.09218	3.596	2.100	4.29	0.60	0.52
443.018295	0.01976	5.050	1.860	4.23	0.63	0.50
448.001075	1.03200	1.405	2.632	4.84	0.66	0.67
470.888947	0.03297	3.599	2.152	4.57	0.66	0.65
474.689127	0.12620	2.381	2.355	4.65	0.65	0.64
488.491133	0.02520	2.853	2.602	5.04	0.69	0.72
503.568532	0.00390	6.733	1.612	3.98	0.61	0.43
504.482692	0.00130	6.733	1.612	4.01	0.61	0.45
547.676440*	0.97010	0.114	2.600	4.50	0.70	1.00
552.020960*	1.47700	0.114	2.600	4.50	0.70	1.00
556.936002	48.74000	0.159	3.210	4.11	0.69	1.00
620.700807	0.50120	2.200	2.438	4.68	0.71	0.68
645.866155*	0.00713	8.580	1.800	4.00	0.60	0.50
658.005280	0.03022	7.820	3.210	4.14	0.69	1.00
752.033227	23.96000	0.396	3.060	4.09	0.68	0.84
841.053973	0.00140	8.180	1.590	5.76	0.33	0.45
859.962313	0.01472	7.989	3.060	4.09	0.68	0.84
899.306675	0.00605	7.917	2.985	4.53	0.68	0.90
902.616173	0.00426	8.432	2.865	5.10	0.70	0.95
906.207325	0.01876	5.111	2.408	4.70	0.70	0.53
916.171582*	0.83410	1.442	2.670	4.78	0.70	0.78
913.118427*	0.00869	10.22	2.900	5.00	0.70	0.80
970.315022	0.89720	1.920	2.550	4.94	0.64	0.67
987.926764	13.21000	0.258	2.985	4.55	0.68	0.90
1780*	2230	0.952	17.6	30.5	2	5

*Different from MPM89 ^{2}
$^+$Based on measured data
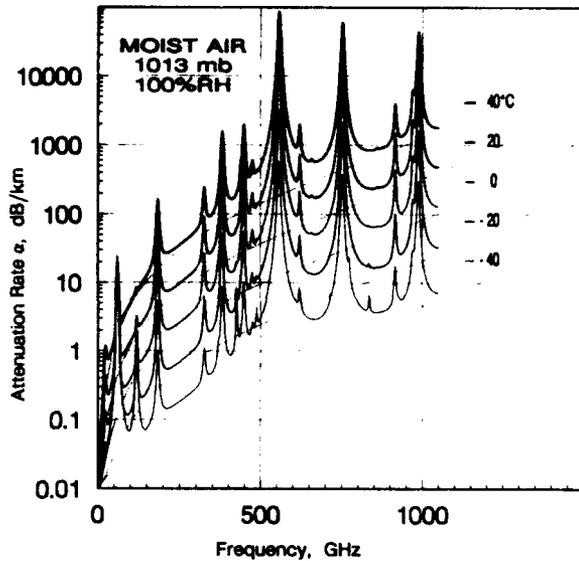
Figure 5. Attenuation α of moist air (u = 100%) for frequencies below 1000 GHz at sea-level (p = 1013 mb) and temperatures ± 40°C:
——— MPM93, ···· Continuum.

Complex permittivity of pure water is expressed by a double--Debye model,[22]

$$\epsilon_w = \epsilon_0 - \nu \left[(\epsilon_0 - \epsilon_1)/(\nu + i\,\gamma_1) + (\epsilon_1 - \epsilon_2)/(\nu + i\,\gamma_2) \right], \quad (9)$$

which provided a best fit to measured ϵ_w data. The static and high-frequency permittivities are

$$\epsilon_0 = 77.66 + 103.3\,(\theta - 1),$$

$$\epsilon_1 = 0.0671\,\epsilon_0, \qquad \epsilon_2 = 3.52\,;$$

and the two relaxation frequencies are

$$\gamma_1 = 20.20 - 146\,(\theta - 1) + 316\,(\theta - 1)^2,$$

$$\gamma_2 = 39.8\,\gamma_1 \quad \text{GHz}.$$

The slight temperature dependence of ϵ_2 (reported in Ref. 22) was eliminated to avoid nonphysical behavior for supercooled (-20 to -40°C) water at frequencies above 100 GHz.

A permittivity model for ice was reported by Hufford,[23]

$$\epsilon_i = 3.15 + i\,(a_i/\nu + b_i\,\nu), \quad (10)$$

where
$$a_i = (\theta - 0.171)\exp(17.0 - 22.1\,\theta)$$
and
$$b_i = \{[0.233/(1 - 0.993/\theta)]^2 + 6.33/\theta - 1.31\}\,10^{-5}.$$

The MPM for fog/cloud cases is $N = N_D + N_V + N_W$. Related attenuation (α) and delay (τ) rates up to 120 GHz are plotted in Fig. 6 for a normalized mass density, $w = 1$ g/m^3 (heavy fog, about 50 m visibility) suspended in saturated, sea-level air (± 30°C). Below freezing, liquid properties were changed to those of ice. Above freezing one notices that the combined attenuation is almost independent of temperature.

3. RADIO-PATH CHARACTERISTICS

The electromagnetic spectrum between 100 and 1000 GHz is available to expand radio services. This band offers favorable alternatives to both microwave and ir/optical systems. Applications in communication, radar, and remote sensing can profit from larger bandwidth, smaller antenna sizes for a

given spatial resolution, high frequency resolution and, in contrast to ir/optical ranges, a favorable performance under fog/cloud conditions. Besides technical difficulties, the attenuating nature of the earth's atmosphere seriously limits usable path lengths. Except for a few window ranges, the medium at ground levels (h ≤ 1 km) is opaque due to strong absorption lines of water vapor. High mountain sites (h ≤ 4 km), airplanes (h ≤ 15 km), and balloons (h ≤ 35 km) are alternative platforms to escape the water-vapor limitations.

A predictive broadband (1 - 1000 GHz) model for radio characteristics of the neutral atmosphere (h ≤ 130 km) was developed to allow prompt evaluations of the highly variable propagation effects from basic data. Performance of established applications (≤ 30 GHz) can be translated to (frequency scaling) or combined with new schemes and economical assessments of feasible trade-offs and adaptive measures can be made.

3.1 Transmission and Emission Formulations

Propagation through the nonscattering and nonturbulent inhomogeneous atmosphere is described by the line integral $\int N\,ds$, where ds is a path differential and the refractivity N was discussed in Sect. 2. Height profiles of N are the basis for calculating delay and loss along the path. Excess delay,

$$D = 3.3356 \int (N_0 + N')ds \quad \text{ps},$$

is linked to the real part and total path attenuation,

$$A = 0.1820\,\nu \int N''\,ds \quad \text{dB}, \quad (11)$$

to the imaginary part.[26] The transmission factor,

$$\Gamma = 10^{-0.1\,A}, \quad (12)$$

evaluates the energy transfer. A path is said to be opaque when less than 0.1% of the original energy is passed ($\Gamma \le 0.001$, $A \ge 30$ dB). The absorbing atmosphere maintains, up to approximately 90 km height, thermal equilibrium and emits noise radiation at the equivalent blackbody temperature,

$$T_B = 4.191 \times 10^{-2}\,\nu \int T(s)\,N''(s)\,\Gamma(s_o,s)\,ds \quad \text{K}. \quad (13)$$

Decreasing transmission leads to increasing emission. The weighting function,

$$W(s) = 4.191 \times 10^{-2}\,\nu\,N''(s)\,\Gamma(s_o,s), \quad (14)$$

determines the height range from where the emission originates. Two cases can be made based on the integration limits for A. In the first one, A is evaluated "upwards", starting at the initial height, h_o; secondly, the start is at the final height, h_∞, and moves "downwards". Reciprocity between path attenuation A_i and brightness $T_{B,\,i}$ was assumed for polarization-sensitive computations based on the matrix N.

3.2 Atmospheric Radio-Path Model

The MPM code (see Sect. 2) is applied in a radio-path model which simulates propagation through an inhomogeneous medium. The atmosphere is spherically stratified in concentric layers between h = 0 and 130 km separated by 1-km increments (Δh). Values for N(h) are enumerated by height profiles of p(h), t(h), and u(h). The U.S. Standard Atmosphere and the mid-latitude mean water-vapor profile[24] are the defaults of the path model. All computed examples given below are for the default case. It is not difficult to implement different model atmospheres or radiosonde data.
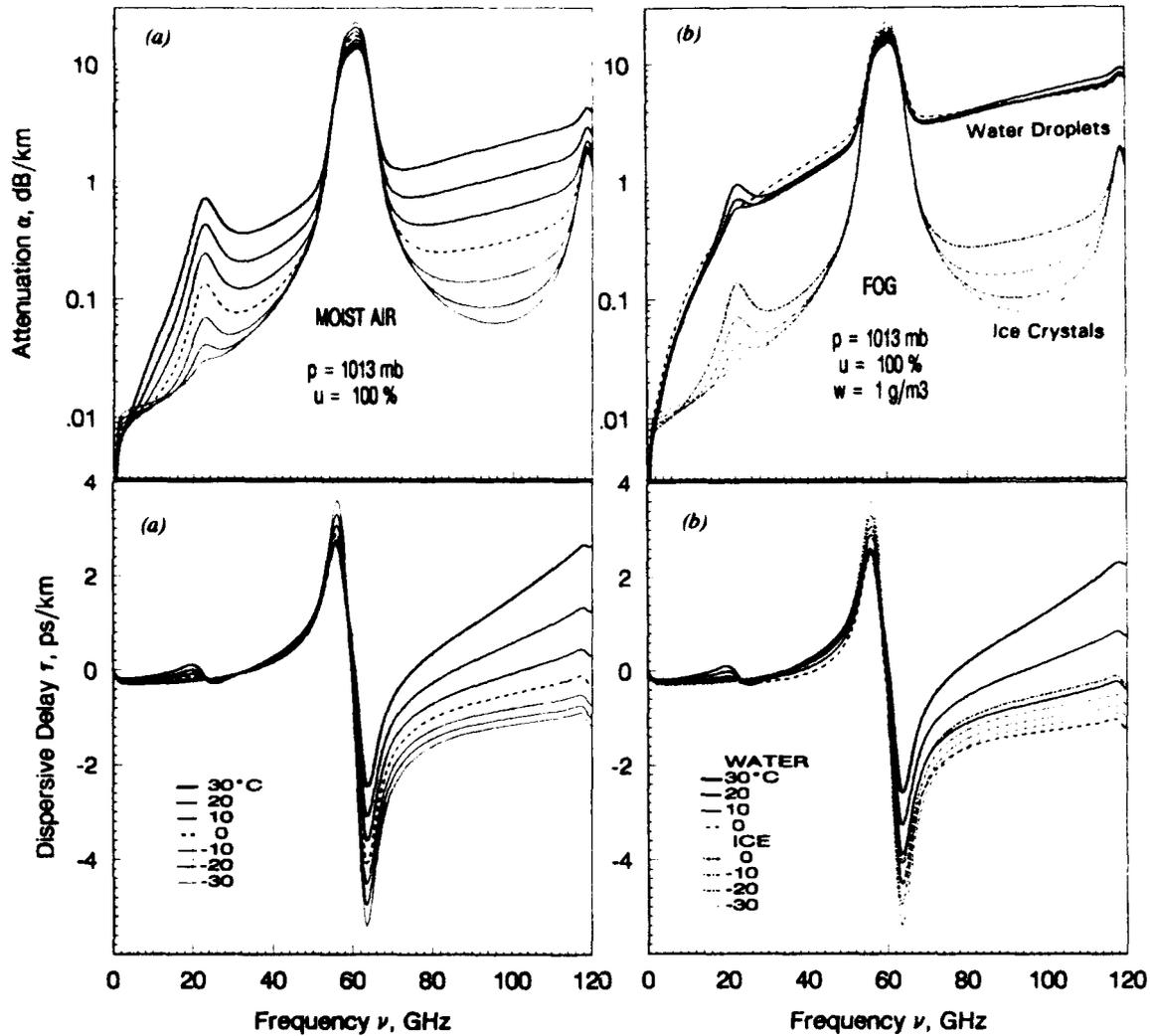
Figure 6. Attenuation rate $\alpha(\nu)$ and delay rate $\tau(\nu)$ up to 120 GHz at temperatures $\pm$ 30°C:
(a) Moist air at sea-level, $u = 100$ %, (b) water droplets or ice crystals, $w = 1$ g/m³ , added to (a).

The path differential ds of a slant path is computed by means of the rules of spherical geometry. For elevation angles, $\varphi \geq 10°$, the secant law ds = $\Delta h / \sin \varphi$ follows. In fact, both the curvature of the Earth and refraction determine the path extension of Δh. At very low elevation angles ($\varphi \to 0$), the height interval Δh is subdivided into 10×0.1-km and further, if needed, into 10×0.01-km groups to approximate more nearly a continuum of N values. When a maximum change of A_h - $A_{h-1} \geq 0.1$ dB is detected across an integration layer, the linear interpolation initiates automatically.

The numerical integration of A (Eq. 11) stops at heights h_∞ when increments ΔA become smaller than 0.01 dB (for a limb path after advancing past the tangential height). The path length L is that between h_0 and h_∞. A numerical integration of T_B (Eq. 13) for emission radiating to the height h_0 follows

$$T_B = 0.2303 \sum_h [\Gamma(h)(A_h - A_{h-1}) \Gamma(h)] + 2.7 \Gamma(\infty), \quad (15)$$

where $2.7 \Gamma(\infty)$ is the cosmic background term. Superfluous computations are stopped when W(h) $\leq 10^{-6}$. The radio-path model operates at any frequency between 1 and 1000 GHz, and Table 3 summarizes results for 21 and 45 GHz. Listed

TABLE 3.
Total Attenuation A and Emission T_B at 21 and 45 GHz Through a Model Atmosphere.[24]

Surface values at h_0: 1013 mb, 15°C, $q = 3.57$ g/m³
($\int$ q(h)dh = 10.6 mm for zenith, $\varphi = 90°$)

ν	A	T_B	φ	h_∞	L
GHz	dB	K	deg	km	km
21.0	0.28	19.2	90	11	11
	0.56	34.9	30	13	26
	0.82	48.5	20	15	44
	1.60	85.1	10	17	94
	15.7	274.4	0	26	577
45.0	0.66	39.2	90	17	17
	1.32	71.1	30	19	38
	1.93	96.4	20	22	64
	3.74	154.9	10	21	115
	32.0	285.6	0	31	650

are the path attenuation of a ground-to-space link and the noise emission received at ground level (e.g., for $\varphi = 0$ and 21 GHz the absorbing air mass is 56 times the zenith value).

3.3 Mesospheric Radio-Path Model

The intensity of O_2 microwave lines under mesospheric conditions ($\geq$ 40 km) is location-, direction-, and polarization-sensitive. Anisotropic transmission and emission effects are recognized. Under these conditions the atmospheric path model program substitutes for N the refractivity matrix $\hat{N}$ ($\nu_k \pm 10$ MHz, Eq. 4), and becomes ZPM (Zeeman Propagation Model).[8, 9] This routine requires numerous additional path parameters to perform a numerical integration of the path attenuation A_i:

- A ray is traced in geodetic coordinates marking altitude h above sea level, LA_titude and LO_ngitude [heights in N-S directions are adjusted to account for the flattening (1/298.25) of the Earth]
- The wave direction is specified by AZ_imuth and elevation angle φ
- Magnitude and direction of the vector B^* are computed using the Int. Geomagnetic Reference Field (IGRF-MAGFIN)[25]
- Polarization of launched wave or emitted noise power is selected (H/V-Linear or R/L-Circular)
- A frequency range is set in terms of deviation from the selected O_2 line center ($\Delta\nu = \nu_k \pm \nu$).

Two characteristic waves are represented by normalized Stokes parameters and combined to produce the initial polarization.[8] This combination is then traced through the propagation distance L. Eigenvalues and eigenvectors of the 2×2 plane-wave refractivity matrix are calculated for the orientation angle ϕ between wave vector E^* and magnetic vector B^*. The propagating field is a linear combination of two characteristic waves.

Individual integration steps of ZPM at the line center, $\nu_k = 61.150$ GHz, are detailed in Table 4: A ray originates at the 300-km orbital height (h, LA, LO, AZ, and φ) and passes through the atmosphere to a minimum, tangential height, $h_t = 90$ km.

Attenuation spectra are plotted in Fig. 7 over the range, $\nu_k \pm 2$ MHz. Path attenuation A_i depends on the initial polarization (i = HL, VL, RC, LC). The main features of the Zeeman effect are exposed when compared with the case $B = 0$.

3.4 Millimeter-Wave Limb Sounding

The microwave limb sounder MLS on the UARS satellite[26] and the millimeter-wave atmospheric sounder MAS[27] on the space-shuttle (ATLAS Missions I, II, ...) both are very refined atmospheric spectrometers. They measure globally thermal emission spectra of atmospheric molecules at altitudes as high as 150 km. The results can be interpreted in profiles of molecular abundances, temperature, pressure, and magnetic field. Line emission is measured against a 3 K background over path lengths which are up to three-orders of magnitude longer than available for laboratory spectroscopy. A previously unknown detection sensitivity brings answers to old problems and raises many new questions.

The MAS radiometers[27] measure thermal emission from O_2 (61.1, 63.0, 63.6 GHz) and H_2O (183 GHz), and from the trace gases O_3 (184 GHz) and ClO (204 GHz). An HL-polarized pencil-beam is scanned downwards from the shuttle orbit (300 km) through the limb. In normal operation, the continuous vertical scan is calibrated (2.7 and 300 K) and repeats every 12.8 seconds. The radiometers are super-heterodyne receivers with double-sideband (DSB) detection. A filter bank follows, which separates the received noise power into 10× 40-MHz, 20× 2-MHz, and 20× 0.2-MHz outputs.

Emission data of the three O_2 lines centered at 61.15, 63.00, and 63.57 GHz have been analyzed.[28] The tangential heights ranged from 125 to 10 km. Two locations were selected: 70°N, 70°W (shuttle at 57°N, antenna looks north) and at the equator. The data are grouped in 5-km height increments and averaged over five scans (1.2 s integration).

The example given here is for the 61.150 GHz line. The upper sideband (image) at 71.630 GHz responds to cosmic background radiation (2.7 K). The measured mean is to first order about half the theoretical single sideband level.

TABLE 4.

Path Attenuation $A_i(h)$ and Noise Emission $T_{B,i}$ for a Limb Path ($h_t = 90$ km) at $\nu_o = 61.15056$ GHz. Antenna is located at 57°N/70°W, h = 300 km and looks down ($\varphi = -14.57°$) towards north (AZ = 0°) to receive linear-polarized radiation (results for i = VL-, RC- and LC-polarizations are also given).

h	LA	LO	AZ	φ	B	ϕ	L	A_{HL}	A_{VL}	W_{HL}	W_{VL}	A_{RC}	A_{LC}
km	deg	deg	deg	deg	μT	deg	km	\multicolumn{2}{c}{dB}	\multicolumn{2}{c}{km^{-1}}	\multicolumn{2}{c}{dB}
300	57.0	-70	0	-14.57			0	T_B(DBS) =	67.8 K (ZPM)			63±2 K	(MAS)
↓							↓	T_B(SSB) =	131.2	174.5		153.0	153.0 K
129	65.2	-70	0	-6.39	55.1	78.4	954	0.00	0.00	.000	.000	0.00	0.00
↓							↓			↑			
91	70.4	-70	0	-1.14	55.4	85.6	1548	1.30	2.92	.060	.094	2.03	2.03
90	71.0	-70	0	-0.53	55.4	86.2	1616	1.97	4.45	.099	.126	3.04	3.04
91	72.1	-70	0	0.53	55.3	87.3	1736	3.39	7.66	.150	.127	5.02	5.02
92	72.7	-70	0	1.14	55.2	88.4	1805	4.06	9.20	.061	.042	5.91	5.91
↓							↓						
129	77.7	-70	0	6.15	53.7	94.9	2371	5.15	11.68	.000	.000	7.29	7.29
130	77.8	-70	0	6.23	53.7	95.0	2380	5.15	11.68	.000	.000	7.29	7.29

Linear Polarization

$\nu_0(9+)=61.15$ GHz; $h_t=90$ km

(a) 2°S, 35°E   (b) 71°N, 70°W

Path Attenuation A, dB

—HL
—VL
··B—O,T

Frequency Deviation $\Delta\nu$, MHz
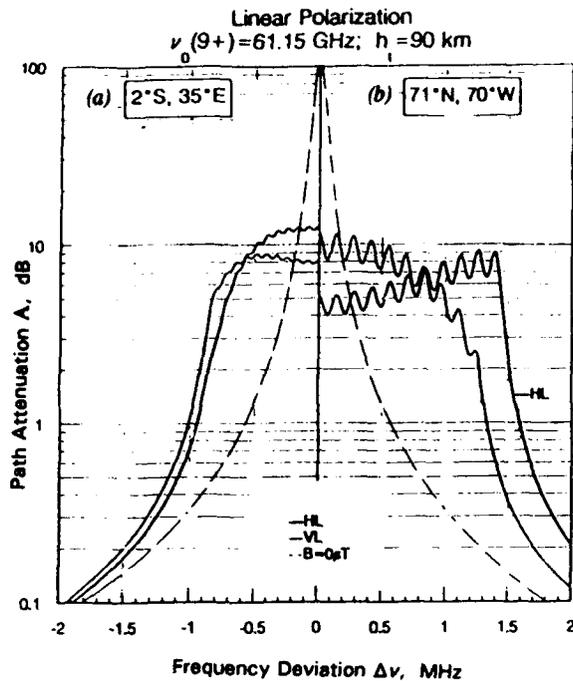
Figure 7.   Spectra ($\nu_0 \pm 2$ MHz) of total attenuations A_i (i = HL, VL) and A_o (B = 0) for a limb path (h_t = 90km) through the U.S. Std. Atm. [24] at two locations marked (a) and (b).

The data are shown in Fig. 8 and serve as a test case for ZPM predictions.[24, 25] Limb-emission was measured for tangential heights ranging from 30 to 120 km at the northern location 71°N/70°W. Table 4 lists the variables that enter a computation of $T_B(\nu_k)$. Very height-selective ($\Delta h \le 1$ km) temperature sounding between 115 and 80 km is indicated by the weighting function W(h), Eq. (14). At $h_t = 78$ km, the path abruptly becomes opaque and T_B assumes about half the physical temperature of the 78-km level (98 K). Below $h_t = 40$ km, the upper sideband at 71.63 GHz "warms up" due to absorption by water vapor and dry air, which is computed by means of MPM.

4.   CONCLUSIONS

Propagation characteristics of the atmosphere are predicted by the general refractivity N, and for Zeeman-broadening by the special refractivity matrix $\bar{N}$. Transmission and emission properties of the inhomogeneous atmosphere (e.g., excess path delay, total attenuation, opacity, sky noise, etc.) were modeled from known path profiles of physical variables.

The new code MPM93 reproduces the spectral characteristics of the clear atmosphere (O_2, H_2O) between 18 and 930 GHz within the uncertainty limits of five reported controlled experiments.[15 - 19]

ZPM reproduces the main features of measured thermal radiation signatures stemming from Zeeman-split oxygen lines. The solution to the forward-transfer problem[8, 9, 28] can serve as a starting point to develop profile inversion algorithms.[7, 13] Validation, error checking of predictions, and incorporation of new research results will continue to be critical and time consuming tasks in the effort to refine understanding and modeling of electromagnetic wave propagation through the neutral atmosphere.

ZPM

9+   (57°N, 70°W) —HL

DSB Brightness Temperature, K

Frequency Deviation, MHz

MAS Data

9+   (57°N, 70°W)

DSB Brightness Temperature, K

Frequency Deviation, MHz
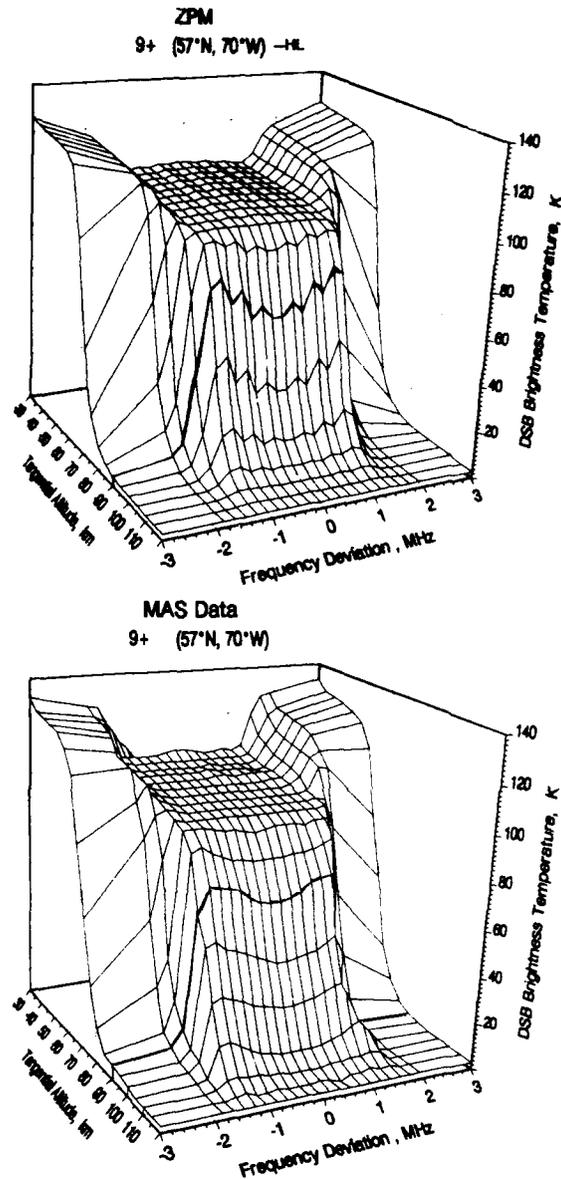
Figure 8.   DSB-emission of the 9[+] line ($\nu_k \pm 3$ MHz) from a limb scan, h_t = 30 to 120 km, approximatly centered over 70°N, 70°W: (a) ZPM predictions for HL polarization and (b) MAS data[**].

5. REFERENCES

1. Liebe, H.J.,"An Updated Model for Millimeter Wave Propagation in Moist Air," Radio Sci., 20, May 1985, pp 1069-1089.

2. Liebe, H.J.,"MPM - An Atmospheric Millimeter-Wave Propagation Model", Int. J. Infrared and Millimeter Waves, 10, July 1989, pp 631-650.

3. Rosenkranz, P.W.,"Absorption of Microwaves by Atmospheric Gases", in "Atmospheric Remote Sensing By Microwave Radiometry"; Janssen, M.A., ed.; J. Wiley & Sons, Inc., 1993 (ISBN 0 471 62891 3), Chapter 2, pp 37-90.

4. Liebe, H.J., Manabe, T. and Hufford, G.A.,"Millimeter-Wave Attenuation and Delay Rates Due to Fog/Cloud Conditions", IEEE Trans. Antennas Propag., AP-37, December 1989, pp 1617-1623.

5. Liebe, H.J., Rosenkranz, P.W. and Hufford, G.A., "Atmospheric 60-GHz Oxygen Spectrum: New Measurements and Line Parameters", J. Quant. Spectr. Radiat. Tr., 48, Nov./Dec. 1992, pp 629-643.

6. Crawford, A.B. and Hogg, D.C.,"Measurement of Atmospheric Attenuation at Millimeter Wavelengths", Bell Syst. Techn. J., 35, July 1956, pp. 907-916.

7. Rosenkranz P.W. and Staelin, D.H.,"Polarized Thermal Emission from Oxygen in the Mesosphere", Radio Sci., 23, May 1988, pp 721-729.

8. Hufford G.A. and Liebe, H.J.,"Millimeter-Wave Propagation In The Mesosphere", NTIA-Report 89-249, U.S. Dept. Commerce, Boulder, CO, 1989; NTIS Order No. PB 90-119868/AF (1989).

9. Liebe, H.J. and Hufford, G.A.," Modeling Millimeter-wave Propagation Effects in the Atmosphere", AGARD CP-454, October 1989, Paper 18.

10. Goff, J.A. and Gratch, S.,"Low-Pressure Properties of Water from -160 to 212°F", Trans. Amer. Soc. Heat. Vent. Eng., 52, 1946, pp 95-121 (also see List, R.J., "Smithonian Meteorological Tables", Washington D.C., Smithonian Inst., 1966).

11. Bauer, A., Godon, M., Kheddar, M. and Hartmann, J.M., "Temperature and Perturber Dependences of Water Vapor Line-Broadening: Experiments at 183 GHz, Calculations Below 1000 GHz", J. Quant. Spectr. Radiat. Tr., 41, 1, 1989, pp 49-54.

12. Poynter, R.L., Pickett, H.M., and Cohen, E., "Submillimeter, Millimeter, and Microwave Spectral Line Catalogue", JPL Publication 80-23, Revision 3, 1991, NASA-JPL, Pasadena, CA.

13. Westwater, Ed.R.,"Groundbased Microwave Radiometry", in "Atmospheric Remote Sensing By Microwave Radiometry", Janssen, M.A., ed.; J. Wiley & Sons, Inc., 1993 (ISBN 0 4710 62891 3), pp 145-213.

14. Ma, Q. and Tipping, R.H.,"Water Vapor Continuum in the Millimeter Spectral Region ", J. Chem. Phys., 93, Sept. 1990, pp 6127-6139.

15. Becker, G.E. and Autler, S.H.,"Water Vapor Absorption of Electromagnetic Radiation in the Cm Wave-length Range", Phys. Rev., 70, Jan. 1946, pp 300-307.

16. Liebe, H.J.," A Contribution to Modeling Atmospheric Millimeter-Wave Properties", Frequenz, 41, Jan./Feb. 1987, pp 31-36.

17. Bauer, A. and Godon, M.,"Temperature Dependence of Water Vapour Absorption in Line-Wings at 190 GHz", J. Quant. Spectr. Rad. Tr., 46, 3, 1991, pp 211-220.

18. Godon, M., Carlier, J. and Bauer, A.,"Laboratory Studies of Water Vapor Absorption in the Atmospheric Window at 213 GHz", J. Quant. Spectr. Radiat. Tr., 47, 4, 1992, pp 275-285.

19. Furashov, N.I., Katkov, V.Yu. and Svertlov, B.A., "Submillimetre Spectrum of the Atmospheric Water Vapor Absorption- Some Experimental Results", ICAP 89, IEE Conf. Publ., No. 301, 1989, pp 310-311.

20. Hill, R.J.,"Dispersion by Atmospheric Water Vapor at Frequencies Less Than 1 THz", IEEE Trans. Antennas Propag., AP-36, 3, March 1988, pp 423-430.

21. Rosenkranz, P.W.,"Pressure Broadening of Rotational Bands.II. Water Vapor from 300 to 1100 cm^{-1} ", J. Chem. Phys., 87, July 1987, pp 163-170.

22. Liebe, H.J., Hufford, G.A. and Manabe, T.,"A Model for the Complex Permittivity of Water at Frequencies Below 1 THz", Int. J. Infrared and Millimeter Waves, 12, July 1991, pp 659-675.

23. Hufford, G.A.,"A Model for the Complex Permittivity of Ice at Frequencies Below 1 THz", Int. J. Infrared and Millimeter Waves, 12, July 1991, pp 677-680.

24. COESA, U.S. Committee on Extension to the Standard Atmosphere,"U.S. Standard Atmosphere 76", NOAA-S/T 76-1562; U.S. Gov. Printing Office, Washington, D.C., 1976.

25. Barraclough, D.R.,"International Geomagnetic Reference Field revision 1985", Pure and Appl. Geophys., 123, 1985, pp 641-645.

26. Waters, J.W.,"Microwave Limb Sounding", in "Atmospheric Remote Sensing By Microwave Radiometry", Janssen, M.A., ed.; J. Wiley & Sons, Inc., 1993 (ISBN 0 4710 62891 3), Chapter 8, pp 383-496.

27. Croskey, C.L. et al., "The Millimeter Wave Atmospheric Sounder (MAS): A Shuttle-Based Remote Sensing Experiment", IEEE Trans. Microw. Theory and Techniques, MTT-40, June 1992, pp 1090-1099.

28. Cotton, M.G., Degenhardt, W., Hartmann, G.K., Hufford, G.A., Liebe, H.J., and Zwick, R.,"Analysis of MAS Emission Signatures from three O$_2$ Microwave Lines", NTIA Report 93-000, in review, 1993.

Discussion

Discussor's name :   U. Lammers, US

Comment/Question :

How did you achieve your 250m measurement path length in the laboratory?

Author/Presenter's reply :

A Fabry-Perot resonator with a loaded Q-value of 400 000 yields by means of multiple reflections over a 30 cm path in semiconfocal arrangement the effective path length.

THE INFLUENCE OF THE EVAPORATION DUCT ON THE ANGLE OF ARRIVAL AND AMPLITUDE OF THE BACKSCATTERED SIGNAL FROM TARGETS LOW ABOVE THE SEA

H. Sittrop
H. Gravesteijn
H.J.M. Heemskerk
Physics and Electronics Laboratory TNO
PO Box 96864
2509 JG The Hague, the Netherlands

ABSTRACT

The impact of multipath and atmospheric refractions on the amplitude, the apparent Radar Cross Section, RCS_a, and the Angle of Arrival, AOA, of low altitude target radar back-scatter at 9.4 GHz, can be described as typical for 3 ranges, and 3 duct height intervals, i.e. respectively 6, 10, and 19 km, and 10 m, 10-18 m and 18-26 m.

The targets are tri-hedrals mounted on poles injected into the sea-bed at the above mentioned ranges. Sensor height is 23 m above normal low sea-tide and the target heights vary from 4.5 m to 8 m depending on the sea-tide.

Whereas the RCS_a and the AOA show opposite behaviour at 10 km and at 19 km, i.e. an RCS_a decrease and an AOA increase at 19 km, and an RCS_a increase and an AOA decrease at 10 km, both for duct heights of 18-26 m, the opposite occurs for duct heights of 10-18 m. However, in this latter case no dramatic differences occur with respect to the AOA.

At the 6 km range the RCS_a is persistently larger (4-8 dB) than the free-space RCS_o, for duct heights < 10 m, whereas the AOA is predominantly negative for all recorded duct heights (0-26 m). On the other hand the RCS_a at this range reduces from circa +6 dB to -6 dB relative to RCS_o for increasing target height and duct heights of 10-26 m.

This characteristic target/duct height behaviour may introduce misleading information about the type of target. Particularly at long ranges (19 km) and target heights of circa 6 m, the RCS_a may be -20 dB with respect to the free-space RCS_o, and the AOA +.6°, for duct heights of 10-26 m. Detection probability reduces significantly, and if the target is detected, the height position is entirely wrong, i.e. circa +200 m, whereas the target is only 6 m above sea.

At duct heights between 10-18 m the RCS_a, and hence the detection probability increases at 19 km. On the other hand this RCS_a can be 10-20 dB lower at 10 km, particularly at target heights between 4-6 m. A lost track at 10 km may therefore be possible, if detection was just feasible at 19 km at these duct heights.

PCPEM predictions and measurements at 5.8 km show in general a fairly comparable trend for target heights between 6-7 m, however, for duct heights of 0-18 m, a too high RCS_a is predicted and for the observed duct heights of 18-25 m a too low RCS_a.

Within the region of transition from a too high to a too low prediction, comparable values are observed.

For target heights between 5.5-6 m PCPEM predicts too large values for all duct heights.

The measurements which provided this information have been supported by both accurate target/sensor height determin-ation, and meteorological profile measurements for duct height computations. All data have been correlated with duct height occurrance probability, and the related target/sensor and duct heights have been used as a basis for the PCPEM predictions.

LIST OF SYMBOLS

RCS	radar cross section in dB's above 1 m^2
RCS_a	apparent radar cross section
RCS_o	free-space radar cross section
AOA	angle of arrival in degrees relative to 0°
PCPEM	personal computer parabolic equation model (a propagation model) (ref. [1])
M	modified refractivity
t_{air}	air temperature
t_{sea}	sea temperature
RH	relative humidity
RF	radio frequency
IR	infrared
ASTD	air to sea temperature difference
DSTD	dew point to sea temperature difference
EVAP	evaporation duct model (ref. [2])

1.0 INTRODUCTION

The implementation of RF and IR sensors on naval platforms to detect and track low altitude targets in a sea environment, leads to a requirement to investigate on the synergism between these two sensor systems. Both are influenced by the propagation properties in a marine environment, hence by the meteorological parameters which determine this propagation.

Superrefraction occurs when the modified refractivity M = N + 0.157z decreases with height from the surface. (N is the refractivity, and z is the height above water.) Then rays are bent towards the surface and targets beyond the geometrical horizon can be observed. The height at which the refraction bending for a horizontal ray equals the earth's curvature defines the duct height. This occurs when dM/dz = 0, i.e. the height at which the gradient of the modified refractivity equals zero.

Subrefraction occurs when the modified refractivity starts to increase with height right at the surface. Under such conditions a duct is non-existent and the duct height has no meaning.

Superrefraction can occur either at RF or at IR frequencies, or simultaneously at both.

Subrefraction, on the other hand, can occur either at RF, or at IR frequencies, but not simultaneously at both frequencies.

This indicates the synergism or the complimentarity of these wavelengths for target detection at long ranges.

For naval applications this is of great importance, hence simultaneous experiments at RF and IR frequencies are strongly supported by the Canadian (Ca) and the Netherlands (Ne) navies, particularly, as at RF frequencies various propagation models have been developed. Hence a tri-lateral experiment has been designed to be performed from the isle of Sylt in Germany. In this paper the Ne contribution is described and the first part of the analysis, i.e. the 9.4 GHz angle of

4-2

arrival (AOA) and the apparent amplitude, RCS_a, of the radar backscattered signals at three critical ranges is presented, together with a validation of the PCPEM (one of the propagation models) with measurements at 5.8 km.

2.0 PLANNING AND DESIGN OF THE EXPERIMENT

The aim of the experiment was the test and improvement of models for radar (RF) and infrared (IR) propagation near the sea surface, which can be used to demonstrate synergism between IR and RF detection systems.

The reason to select the isle of Sylt as the location to perform the experiments is as follows.

The German authorities could provide various facilities required for these measurements.

These authorities are:

- BWB-FE V-4-Koblenz (Bundesamt für Wehrtechnik und Beschaffung, German ministry of procurement)
- ALW-Husum (Amt für Land und Wasserwirtschaft)
- WTD-71-Eckernförde (Wehr Technische Dienststelle)
- STOV-Westerland (Stand Ort Verwaltung).

The following was made available by BWB-FE V-4 and WTD-71:

- At the isle of Sylt, the measurement platform Bunker-Hill, 22 m above normal low sea-tide. All supporting assistance at Sylt and at this platform was performed by STOV-Westerland.
- The jack-up barge Barbara, located 13.5 km SW of Bunker Hill, made available by BWB-FE V-4 and WTD-71, together with a vessel, the TB-1, to provide and support all transport between Bunker Hill and Barbara and all other activities required on the meteo and target poles in the area.
- Sea-tide, wavebuoy and other meteo recordings as well as all other support and advice regarding sea-truth recordings and positioning c.q. retrieval of wavebuoys and target poles in the area was performed by ALW-Husum.
- Manufacturing and injection and retrieval of the target poles I, II, and III, at respectively 5.8, 9.8 and 19 km and the meteorological pole at 2 km from Barbara was performed under contract by a firm in Flensburg. ALW-Husum had an advisory role.

In fig. 1 a general survey is given of the experimental area. Fig. 2 shows the jack-up barge Barbara and fig's 3 and 4 show respectively the target pole with on top an RF tri-hedral and an electro-optics (EO) retro reflector and the meteo-pole for profile measurements.

Coordination of the planning and preparation of the experiments have been performed by the Ne, FEL-TNO. The Ne execution of the experiments was under Ne naval assignment.

Bunker Hill was the centre of RF and IR measurement activities.

Barbara was the centre of meteorological measurements.

Participants in the execution of the experiments are:

Canada - Defence Research Establishment Valcartier - Valcartier (IR)

Germany - Forschungsgesellschaft für angewandte Natur-wissenschaften - FHP - Werthhoven (RF)

The Netherlands - TNO Physics and Electronics Laboratory - (RF and meteo).

3.0 MEASUREMENTS

The Netherlands performed 2-way radar backscatter measurements in four 2.5 minute sequences on the targets located on pole I at 5.8 km, pole II at 19 km and pole III at 9.8 km, and a sea-clutter reference measurement at 3 km. The latter was to verify a correct antenna positioning for the 0-reference of the angle of arrival (AOA).

These four sequences completed a cycle which was continuously repeated, in general during the day between 09.00 and 18.00 local time and once at night time on 8/9 June. The choice of RF frequency was determined on a daily basis, as simultaneous recordings at 9.4 GHz and at 16.5 GHz were unfortunately not possible.

In this paper the analysed 9.4 GHz data are presented. The average RCS_a and AOA over a 90 sec. period were determined and correlated with the actual target and duct height at the moment of recording.

As much as possible these measurements have been synchronized with the German RF recordings.

As Germany could not measure target II at 19 km, Ge made 5 minute sequences on target I and III.

One-way RF recordings have been made as well. The Ne had a 10.5 GHz emitter mounted on an elevator platform at Barbara. Receivers were positioned at Bunker Hill at heights of respectively 13 m and 22 m above normal low sea-tide.

These recordings will be analysed at a later stage. Germany had installed 35 and 95 GHz emitters on the main deck of Barbara and receivers at the same altitude as the Ne 10.5 receiver.

The Ne RF measurements have been made by the Radar Group of the TNO Physics and Electronics Laboratory.

3.1 The Ne radar interferometer system

To be able to measure the angle of arrival the radar receiver has been configured into an interferometer system in the vertical plane. The simple setup as depicted in the schematic diagram of the measuring radar (fig. 5) consists of 2 horn antennas connected to a quadrature hybrid.

The phase comparison is accomplished in the hybrid. The amplitudes of the two output signals a_1 and a_2 are resp. $|e|(cos\frac{1}{2}\theta+sin\frac{1}{2}\theta)$ and $|e|(cos\frac{1}{2}\theta-sin\frac{1}{2}\theta)$, where $|e|$ and θ are the amplitude of resp. the phase difference between the signals at the antennas. The outputs are multiplexed at PRF/2 into the radar single channel receiver system, thus effectively avoiding mismatch errors.

The phase angle θ, as retrieved from the 2 envelope detected and demultiplexed signals, is simply $\theta=arcsin\{(|a_1|^2-|a_2|^2)/(|a_1|^2+|a_2|^2)\}$, while the received power (RCS) is given by $p=(|a_1|^2+|a_2|^2=|e|^2)/2$. From the phase angle the AOA, α, is derived as follows: $\alpha=arcsin(\theta/kd)$, where $k=2\pi/\lambda$ and d is the distance between the antennas.

The maximum angle which can be resolved unambiguously is $\pm1.6°$ at I-band and $\pm1.23°$ at J-band.

4.0 METEOROLOGICAL RECORDINGS

The meteorological measurements were made by the Atmospheric Research Group of the TNO Physics and Electronics Laboratory and by FGAN-FHP. The latter employed a meteo package mounted on pole I, which recorded wind speed, temperature, relative humidity and air pressure, all at a single height of 6-7 m above mean water level. The TNO measurements were made from pole IV (2 km away from Barbara) and from Barbara. The latter measurements were made using equipment mounted on the decks, on a mast rigged up at the helideck, on a rail system fixed to the hull of

the platform, on a pulley system mounted at the helideck, and on buoy systems.

Wave information has been obtained from a wave buoy (close to target I), supervised by the DHI-Hamburg (Deutsche Hydrografische Institut); ALW-Husum was the liaison. TNO performed profile measurements from pole IV. The following was recorded: air temperature t_{air}, and relative humidity RH, at a height of respectively 3.9, 5, 7 and 9.5 m above normal low sea-tide, windspeed with a cup anemometer at 9.7 m, and sea temperature t_{sea} with a thermistor at -0.2 m.

Profiles of air temperature and relative humidity were measured from Barbara with hygrometers (based on wet/dry bulb temperature measurements), Hydrographil Typ G 1463 with semiconductors as sensitive elements. The hygrometers were mounted on a rail system which allowed to situate them at heights of 5.9, 7.2, 10.4, 15.3 and 25.9 m above mean low water level.

Direct measurements of turbulence parameters were made with sonic anemometers and an Ophir hygrometer mounted on a mast rigged up at the helideck at 34.3 m. These yield information on the turbulent fluctuations (20 Hz for the sonic, and 25 Hz for the Ophir) of the temperature and relative humidity. Both these parameters are crucial for the propagation models.

4.1 Meteo data analysis

The TNO profile recordings have been used as a basis for the meteo data analysis.

The following procedure is adopted.
- The modified refractivity is computed vs height above water.
- Then the best parabolic fit is used to determine the duct height (see fig's 6 and 7).

A thorough qualification of the data revealed that the OPHIR recordings at 34.3 m are unreliable. In case only the data from the 4 sensors at pole IV were used for duct height calculation, the best parabolic fit showed to be not reliable since quite often a sudden duct height drop was calculated. However, taking into account the data from the sensor at 25 m, reliable duct heights were obtained.

Hence, it is decided that only results with 5 sensors can be used.

Comparisons are made between a duct height determination with 5 reliable sensors and computations based on the measured data of $t_{air/sea}$, RH and wind speed and the EVAP-Jeske-Paulus model.

A fairly well similar duct height pattern is obtained on 2 days, 3 June and 12 June (see fig's 8 and 9). On 3 June, between 00.00 and 12.00 hours, profile measurements deviate from model predictions.

When observing the ASTD (Air to sea temperature differences) and the RH relationships, a gradual decrease in duct height is to be expected from 00.00-06.00 hours on 3 June.

From 12.00 hours onwards a close relationship between the profile measurements and EVAP predictions is observed.

Between 14.00-16.00 hours, the ASTD remains constant, but the RH first increases and then decreases sharply, resulting in a sudden dip in the duct height, recorded by both the profile measurements and predictions.

A reverse situation occurs between 20.00-21.00 hours. Then the duct height increases when the ASTD is constant and the RH decreases and then increases.

These kind of situations occur any time the ASTD remains stable and the RH varies. They underline the generally accepted theory that the humidity gradients determine the RF refractive properties, whereas the IR refractivity profile is mostly influenced by the temperature gradients. It is decided to use the EVAP model for duct height determination.

The meteorological conditions during the SYLT92 experiments varied strongly, with ASTD's between -3° and +5°C, very dry conditions with RH < 50% to humidities close to 100%, and a range of windspeeds up to 15 m/s.

Windspeed directions were during the first part of the experiments East, which is not normal for this area. These warm, dry, winds caused the great variety of ASTD's during the day time, up to + 5°C.

For radar frequencies (RF) the dew point to sea temperature difference, DSTD, determines superrefraction, which occurs when DSTD < 0. Because the dew point cannot be higher than the air temperature a negative DSTD is more likely than positive ASTD. IR superrefraction occurs when ASTD > 0. Subrefraction occurs at RF frequencies when DSTD > 0 and at IR frequencies when ASTD < 0. Hence, superrefraction at RF is more to be expected than at IR frequencies. However, superrefraction at both RF and IR frequencies is possible, when ASTD > 0 with low RH, resulting in a DSTD < 0. This situation may have occurred quite often during daytime during the first part of the experiments, in the period 1-10 June, when warm dry landwinds caused a rapid increase of t_{air}, with a simultaneous fast drop of RH.

On 11 June the duct height pattern gradually changed. On 12 June the RH pattern increased and decreased rather dramatically and the ASTD's varied relatively little. Hence, the duct heights varied accordingly during the 24 hours period (see fig. 9). In fig's 10, 11 and 12, typical meteorological situations of ASTD, RH and windspeed/direction are given for the periods 1-4 June, 9-12 June, and 13-16 June.

On 13 June, the wind turned to West, Northwest and North. The ASTD's now are predominantly either 0 or < 0, except for some time between 06.00-24.00 hours on 13 June, when they are slightly positive.

Hence, except for this latter timeframe, subrefraction at IR frequencies may have occurred, as the ASTD < 0. Other possibilities of IR subrefraction are in the following time-frames:

day/time	day/time
3/6-12.00	4/6-12.00
9/6 02.00-07.00	
10/6 00.00-12.00	
10/6 22.00	11/6-12.00
12/6 04.00-12.00	
16/6 00.00-	18/6-12.00

Particularly in the last period 16/6-18/6, subrefraction conditions for IR would have been possible during day and night. Then, subrefraction at RF frequencies, requiring a DSTD > 0 is not possible.

The information outlined above will serve as a basis for investigations on synergism or the complimentarity of the use of IR and RF wavelengths for target detection at long ranges.

5.0 RF DATA RECORDING, PROCESSING AND ANALYSIS

5.1 Recording

Two-way backscatter measurements

Radar backscatter data (two-way) have been alternatively recorded at 9.4 GHz and at 16.5 GHz, in four sequences as described in section 3.0.

For each pole at distances of respectively 5.8 km, 19 km and 9.8 km, the average RCS of the tri-hedral was computed over a 90 sec. interval.

Simultaneously the angle of arrival (AOA) in degrees was computed (see section 3.1).

The target height is determined as follows. At a well known sea-tide, the height of the tri-hedral (centre) above water is measured with a tape measure (see fig. 3). Thus the height above normal low-tide could be computed. From this the height above any sea-tide can be determined. The sea-tide in this area varied in general between 2-2.5 m. At rough seas, the lower part of the pole is screened due to sea waves, and the effective target height will be lower. Corrections have been made with 1/2 significant wave height, as recorded by the wave buoys in the area. Also the sensor height above the sea has been corrected for the sea-tide variations.

RF one-way propagation measurements
Continuous RF recordings have been made between the emitters of 10.5 GHz located on the lift platform of Barbara and the receivers positioned at 13 m and 22 m above normal low tide, at Bunker Hill (see sec. 3.0). These data have not yet been processed.

5.2 Processing
The following procedure is adopted.
- All data are accumulated within target height intervals of 0.5 m and 1.0 m.
- Each data point is correlated with the actual duct height at the moment of recording.
- The average RCS in dBsm, the corresponding predicted RCS in dBsm according to PCPEM, the angle of arrival (AOA) in degrees, including their spread within a one meter duct interval, and the duct height are plotted vs duct height occurrence percentage for the above mentioned target height intervals.
- The PCPEM predictions are only performed for target 1 at 5.8 km at I-band.
- J-band data analysis is only partly completed.

When performing the PCPEM predictions, the target height, within the observed target height interval, is corrected with 1/2 significant wave height (1/2 H1/3), to obtain an effective target height. For each data point the corrections are made for the H1/3 recorded at that time frame. The radar sensor height is also corrected for sea-tide.

Because the measurements at the various target positions and height intervals have not been made simultaneously, the duct heights and their percentage of occurrence are not the same for the selected target heights intervals. Due to the long periods of dry warm winds, however, the occurrence of large duct heights was much more frequent than is usual for this area. This has given the advantage that, particularly at these large duct heights, interesting observations were made at all the target distances.

The duct heights are determined by using the data recorded at the meteo pole at 2 km from Barbara, as an input to the EVAP-Jeske-Paulus model. The ASTD, RH and windspeed recorded by the highest sensor were selected after a comparison procedure. Due to the fact that warm dry winds were predominant during a large part of the measuring period a fifth and if possible even a sixth sensor at much larger height are required. Unfortunately, however, these sensors at Barbara did not provide reliable results throughout the whole measuring period. Those which were reliable have been used

to validate the EVAP model (see also sect. 4.1), which proves to be reliable. Hence, to provide uniformity for the data analysis the EVAP-Jeske-Paulus model has been further applied to calculate duct heights.

5.3 Analysis
In order to obtain an overall survey of the processed data, summary diagrams are made for the average RCS_a and the AOA vs target height, using duct height intervals as parameter.

This is done because it became clear that the RCS and AOA behaviour can be considered to be typical for duct height intervals of 0-10 m, 10-18 m, and 18-26 m. The latter is limited to 26 m only because no larger duct heights have been observed (except for some single observations with a maximum of 30 m).

In fig's 13, 14 and 15 I-band diagrams are made for target 1 at 5.8 km, target 2 at 19 km, and target 3 at 9.0 km.

A summary of the characteristics at I-band is given in table 1.

The typical behaviour is as follows.
Target 1 shows in general a decreasing RCS_a with increasing target height for duct heights 10-26 m, whereas target 2 at 19 km shows in general an RCS_a which is larger than RCS_0 for duct heights 0-18 m. However, for duct heights 18-26 the RCS_a rapidly decreases with increasing duct heights.
In fig's 16 and 17 this is illustrated clearly. Fig. 17 shows moreover that after reaching a minimum the RCS_a increases again with duct height if the target height increases.
For target 3 the RCS_a increases with target height, basically for all duct heights. For duct heights < 18 m, however, in general the RCS_a is lower than the RCS_0 (free space).

With regard to the AOA, an interesting behaviour is observed at target 2, 19 km: whereas for a target height between 5-5.5 m the AOA is negative, the AOA becomes strongly positive for a target height between 6-7 m.
In both cases the RCS_a is very small, down to -22 dB with respect to RCS_0. A satisfactory explanation of this typical behaviour can only be obtained by ray-tracing techniques, which so far has not yet been applied.
This characteristic behaviour, that has only been observed at the 19 km range, can lead to a misinterpretation of the type of target. Whereas the real target is at a height between 6-7 m above water, it seems that the target is at a height of 200-300 m above sea and moreover has an RCS_a which is more than 20 dB lower than its real RCS.

5.4 PCPEM predictions
Comparisons have been made with measurements at target 1.
The effective target height and the sensor height corrections for tidal variations have been made for each data recording (see also section 5.2).
In general a similar trend is found for predictions and measurements. However, the results depend strongly on target height. For target heights between 5.5-6 m PCPEM predictions show a larger RCS_a for all duct heights, see fig's 18, 19.
For target heights between 6-6.5 m predictions show a larger RCS for duct heights 6-18 m; a comparable RCS for duct heights between 18-22 m, and a lower RCS for duct heights 722 m, see fig's 20 and 21.
For target heights between 6.5-7 m predictions show a larger RCS for duct heights < 18 m. For duct heights > 18 m predictions are lower than measurements. See fig's 22 and 23.

For target heights between 7-8 m predictions and measurements do not correlate at all. See fig's 24 and 25. An overall survey is given in table 2.

Comparisons between PCPEM predictions for target 2, at 19 km, and target 3, at 9.8 km, have not yet been made, as well as comparisons at J-band.
Further analysis will be performed in the near future.

6 CONCLUSIONS
1) The behaviour of both RCS and AOA v.s. target height, can be described as typical for the 3 ranges (5.8, 9.8 and 19 km) and for duct height intervals < 10 m, 10-18 m and 18-26 m.
2) In general the RCS and AOA show opposite behaviour at 9.8 km and 19.0 km.
   - RCS $\frac{\text{decrease at 19 km}}{\text{increase at 9.8 km}}$, for duct heights 18-26 m
   - The opposite occurs for duct heights 10-18 m
   - AOA $\frac{\text{increase at 19 km}}{\text{decrease at 9.8 km}}$, for duct heights 18-26 m
   - No dramatic differences for duct heights 10-18 m.
3) PCPEM prediction
   In general a fairly comparable trend with measurements is observed, however,
   - for duct heights 0-18 m, a too high RCS is predicted, (2-6) dB
   - for duct heights 18-25 m, a too low RSC is predicted, (2-7) dB.

   Except, on some occasions, fairly comparable comparisons with measurements are obtained, depending on target- and duct height.

7 FOLLOW-UP
- PCPEM validation with measurements will be continued
  at I-band, for target 2 and 3
  at J-band for target 1, 2 and 3.
- Further analysis of J-band data.
- Investigations of RF-IR synergism using I- and J-band data.
- Correlations of RF Netherlands data at 9.4 and 16.5 GHz and RF German data at 35 and 94 GHz.
- Processing and analysis of one-way RF data.

ACKNOWLEDGEMENT
BWB-FE V-4, WTD-71, ALW-Husum and STOV-Westerland provided this support on a pro deo basis. Their support is explicitly acknowledged.

REFERENCES
[1] Craigh K.H., Levy M.F., "Parabolic equation modelling of the effects of multipath and ducting on radar systems", IEE Proc-F, Vol 138, No 2, April 1991.
[2] Paulus R.A., "Specifications for Environmental Measurements to Assess Radar Sensors", NCCOSC TD. 1685, November 1985.

4-6
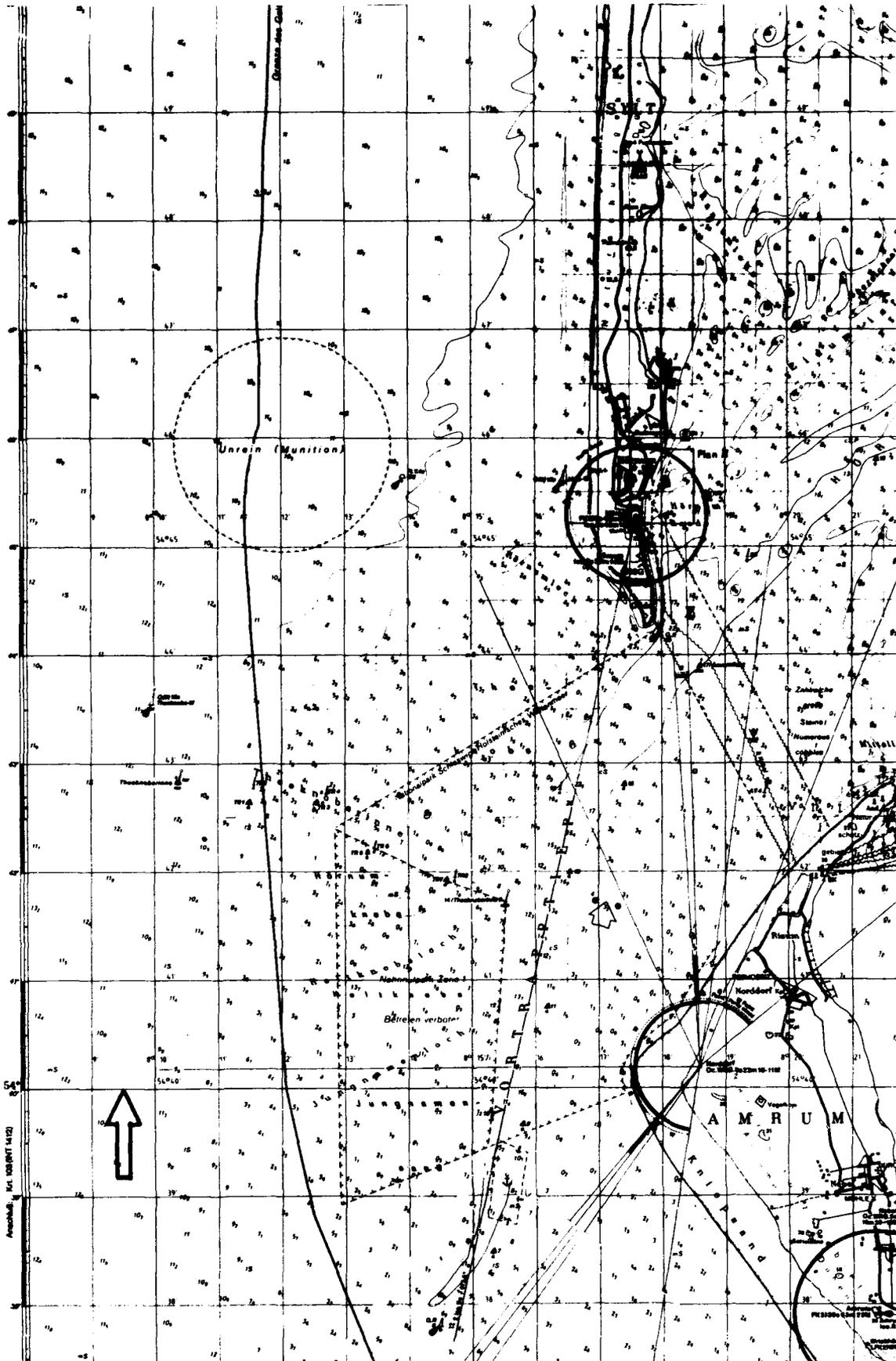


Fig. 1

Fig. 2

Fig. 3

Fig. 4

4-8
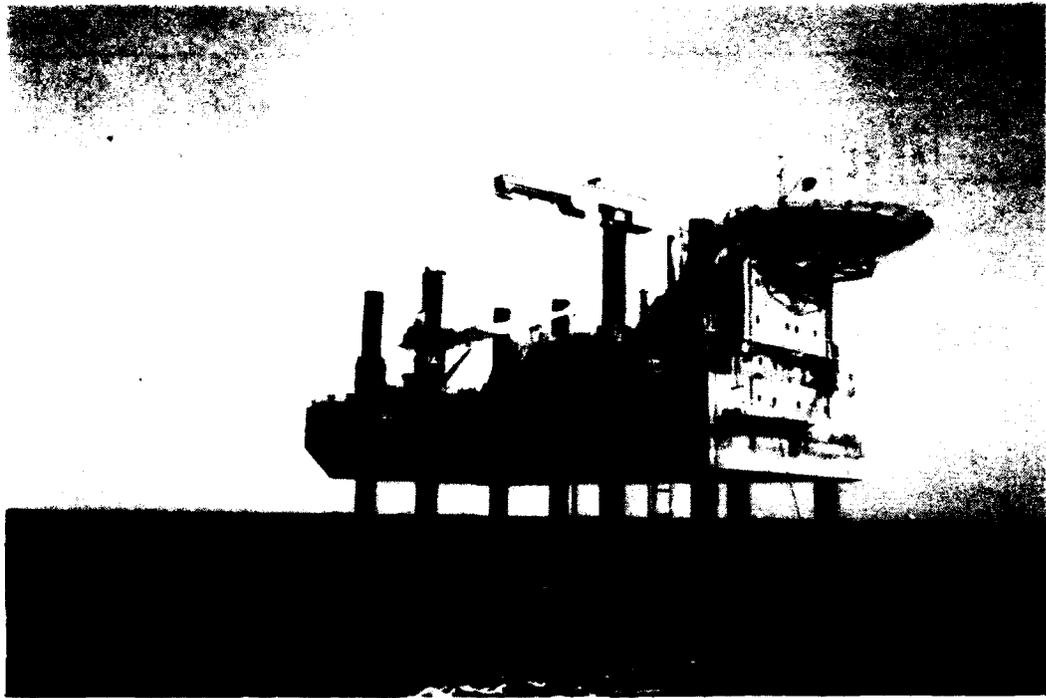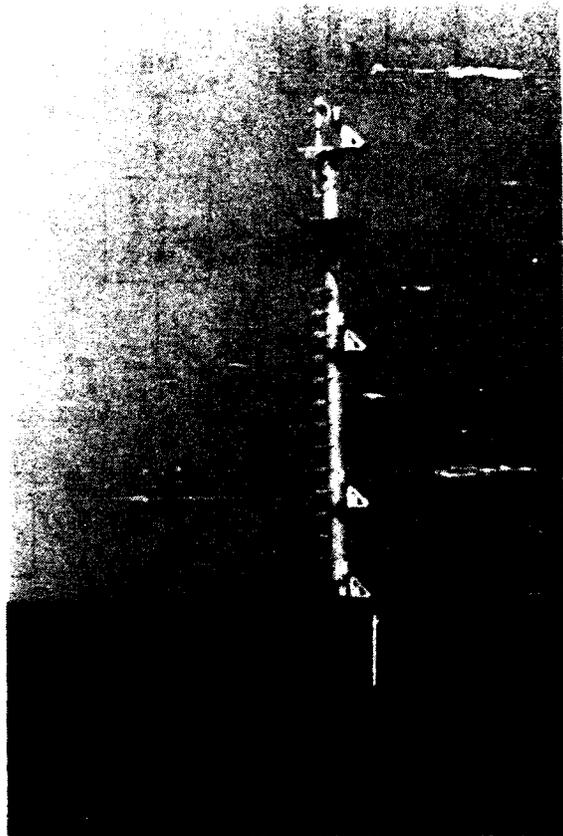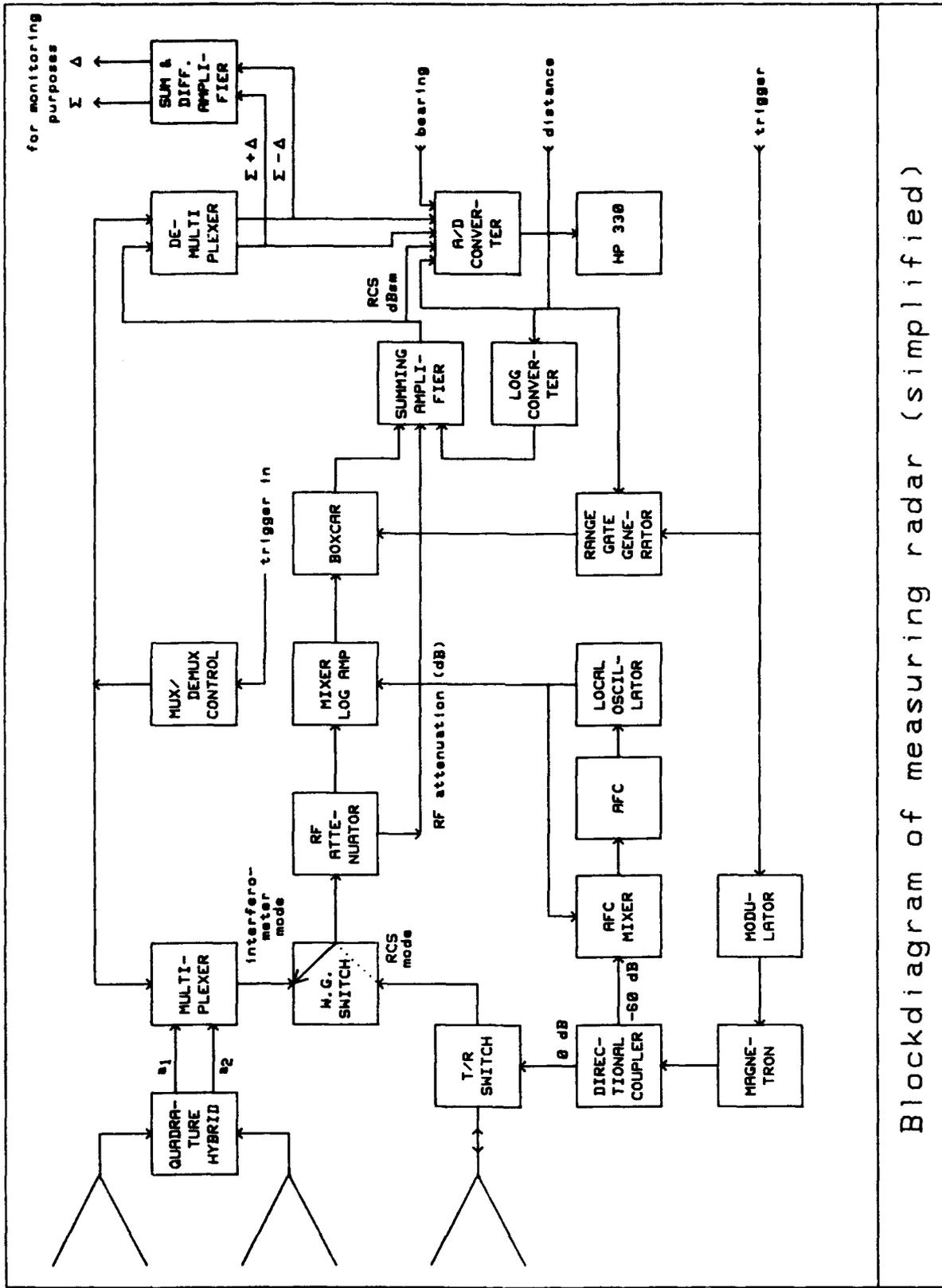
Fig. 5

Blockdiagram of measuring radar (simplified)

Fig. 6

Fig. 7

Fig. 8

Fig. 9

Fig. 10

Fig. 11

Fig. 12

4-10
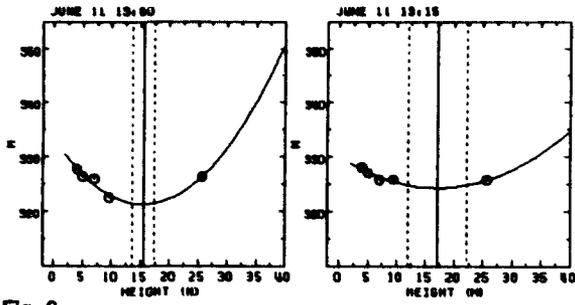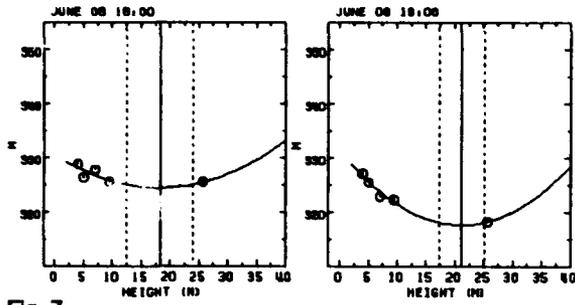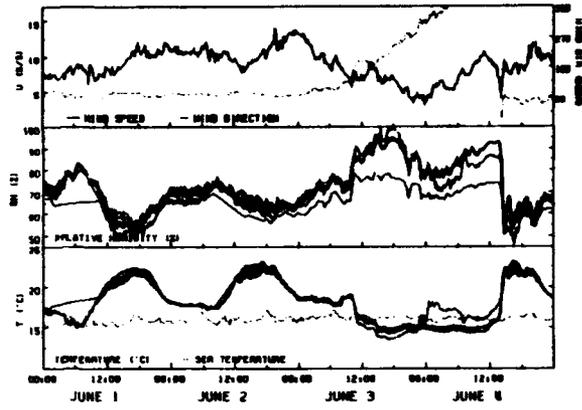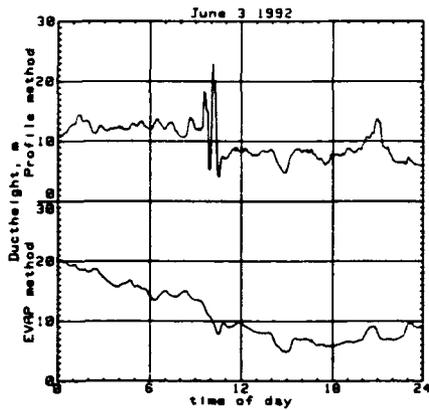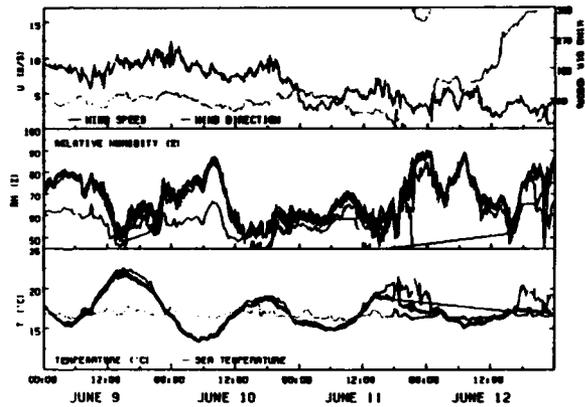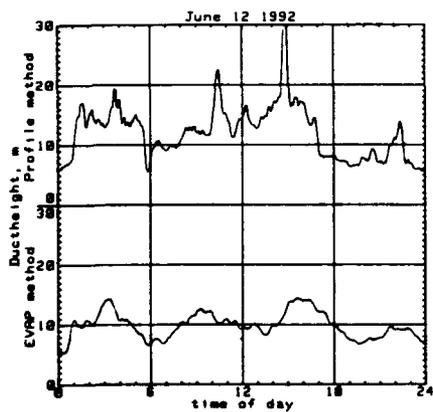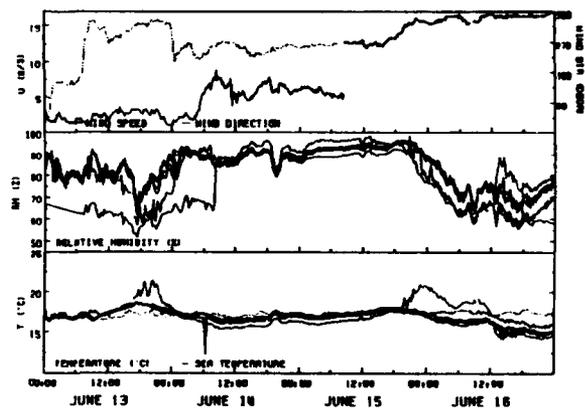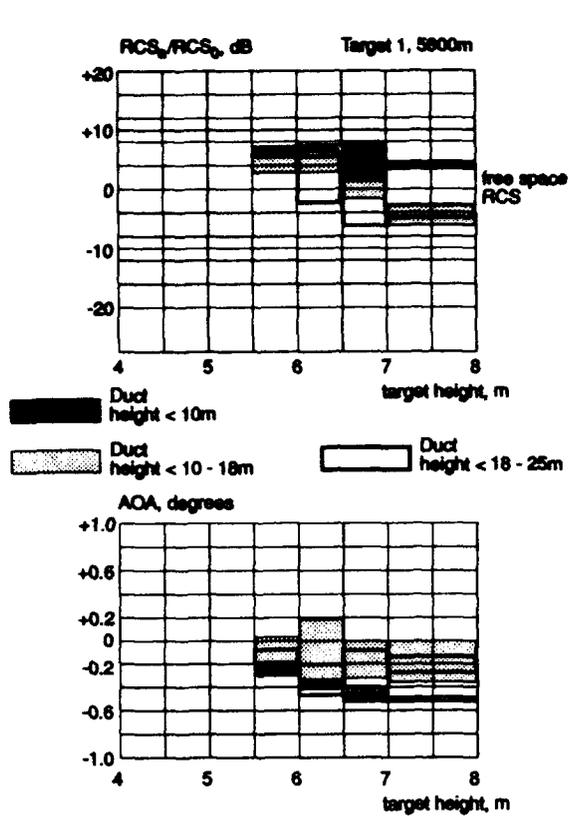
Fig. 13
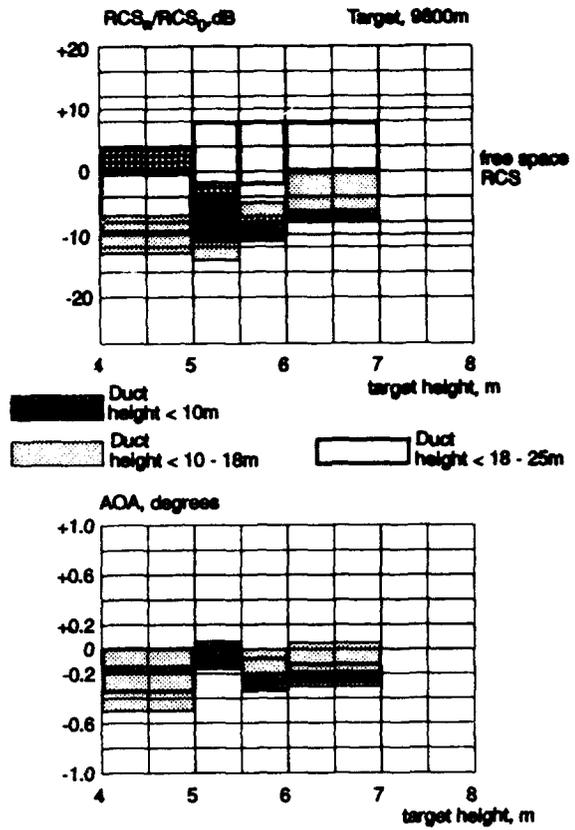

Fig. 15
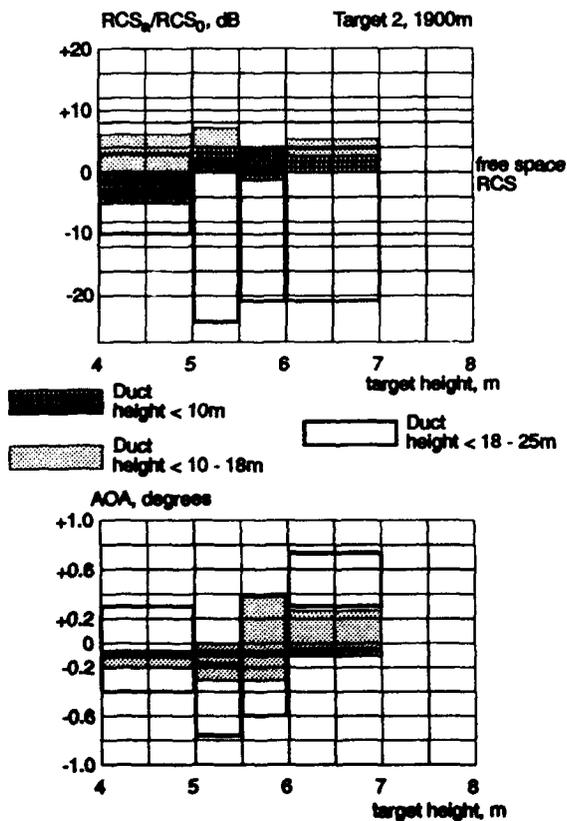
Fig. 14

Fig. 16
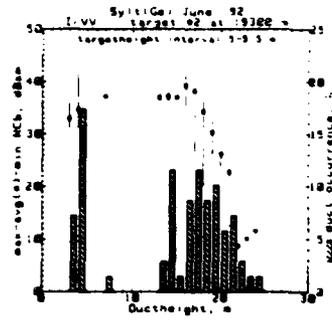
Fig. 17

Fig. 18

Fig. 19

Fig. 20

Fig. 21
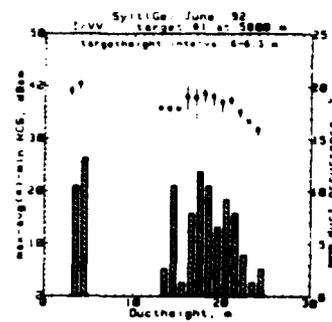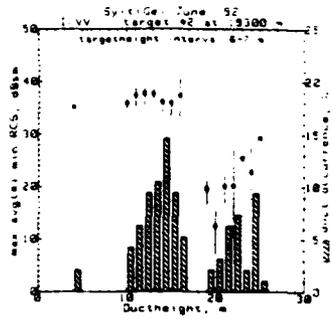
Fig. 22
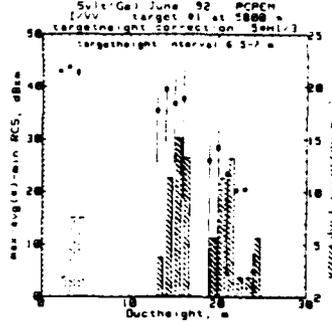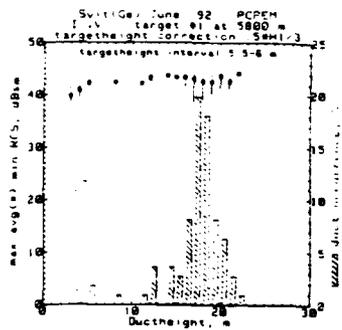
Fig. 23
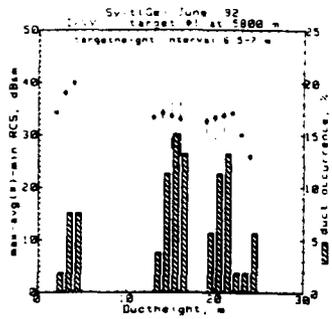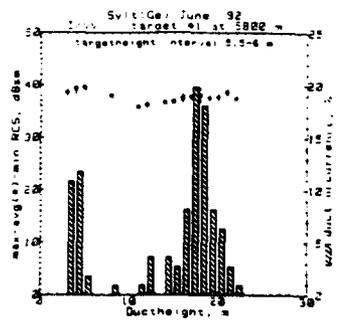
Fig. 24
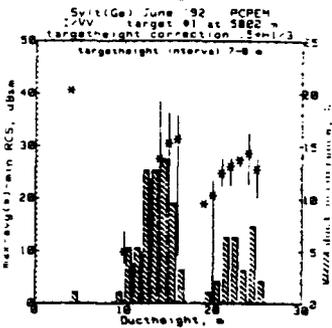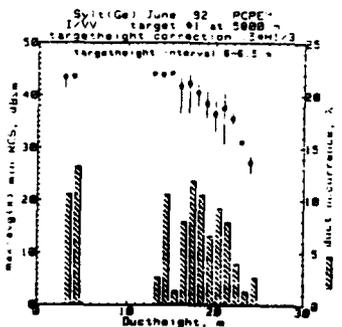
Fig. 25
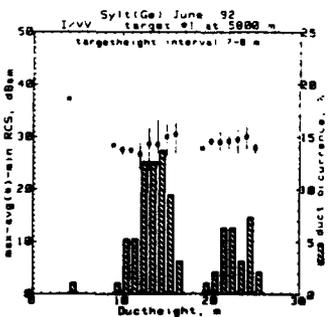
Typical samples at I / VV

Range	Target height,m	Duct height,m	RCS/ free.sp.^{dB}	AOA
Long, 19 km	5 - 5.5	0 - 18	0 → +5	0° → -0.25°
		18 - 26	0 → -24	-0.2°→ -0.75°
	6 - 7	0 - 18	0 → +4	-0.1°→+0.25°
		18 - 26	0 → -22	+0.3°→+0.75°
MID, 9.8 km	5 - 5.5	0 - 18	-2 → -13	-0.1° →+0.05°
		18 - 26	-2 → +9	0° → -0.1°
	6 - 7	0 - 18	0 → -1	-0.3°→ +0.05°
		18 - 26	0 → +8	-0.15° → -0.25°
Short, 5.8 km	5.5 - 6	0 - 23	+2 → +7	0° → -0.25°
	6 - 7	0 - 18	0 → +8	-0.3° → +0.1°
		18 - 26	±5	-0.1° → -0.5°

Table 1

Comparison of PCPEM prediction and measurements at 5.8 km

| Targ.h., m	Duct height, m	PCPEM/meas.	Δ dB
5.5 - 6	< 10	fairly comparible	
	> 10	circa +5	
		similar trend	
6 - 6.5	0 - 18	+ (3 - 5)	too high
	18- 22	comparable	
	22- 25	- (2 - 3)	too low
6.5 - 7	< 10	+ (2 - 9)	too high
	10 - 18	+ (2 - 6)	too high
	18 - 25	- (5 - 7)	too low
7 - 8	15 - 18	comparable	
	other	totally different	
	heights	trend	

Table 2

Discussion

Discussor's name :   F. Christophe, FR

Comment/Question :

You have shown, on one hand, evidence of temporal variation of duct heights, which seems logical for conditions close to the coast. On the other hand, I understand the propagation mode assumes horizontal homogeneity. Are they both coherent?

Author/Presenter's reply :

With sea winds basically predominant in that area, the meteorological and therefore duct conditions are fairly stable in that area. I demonstrated that in my presentation. Due to the dry-warm winds coming from inland, air temperature and RH changed dramatically during day time and therefore also evaporation duct heights. Therefore we obtained duct heights larger than 20m, unusual for the area, but very favourable for our experiments, as we do not only have a great variety of duct heights, but also measured entirely different RCS and AOA values at these large duct heights. This can be of benefit in warm sea areas like the Gulf. Target detection at 20km is degraded strongly at that range and duct heights between 18-26m. Regarding model validation, the meteorological data recording was performed close to the target, for which the validation was performed. Therefore for these validation purposes horizon homogeneity may be assumed.

Discussor's name :   U. Lammers, US

Comment/Question :

In a line-of-sight experiment in the northeastern US at 16GHz on a 100 km over-land path we observed high rates of angle-of-arrival (AOA) fluctuations under disturbed refractive conditions, sometimes higher than the 6sec rate of vertical scan of the receiving antenna. Did you observe similarly high fluctuation rates in your experiment over water?

Author/Presenter's reply :

So far we have averaged the RCS and the angle of arrival over 90 sec., but we do have recorded the data at a sampling rate of more than 500 Hz; we will analyze this further at a later stage. We have observed, however, that the spread of AOA is dependent on target heigth. For a target height between 6-8m above water the spread is significantly larger than for a target height of 4-6m above water, particularly for evaporation duct heights above 10m.

Multispectral Transmittance Measurements
Through Man-made Water Fogs

Young P. Yee
Robert A. Sutherland
James L. Cogan

U.S. Army Research Laboratory
Battlefield Environment Directorate
White Sands Missile Range, NM, USA, 88002-5501

SUMMARY

A fog system capable of producing water droplets with diameters between 5 and 40 micrometers was used for multispectral transmittance measurements. Measurements were conducted at an arid, desert field location on the White Sands Missile Range, New Mexico. The fog system consists of a supply of local tap water, 50 gallon holding barrels, high pressure water pump, water filters, high pressure hoses and connectors, and an array of specially designed spray nozzles. The spray nozzles have precision made .006" diameter orifices. Water under 1000 psi of pressure is forced through the small orifice and impacts onto a curved metal pin causing droplet formation and dispersion. Droplet size distributions of the man-made fog were measured by forward scattering particle measuring instruments. The advantages of using the fog generation system are low energy requirements, high rates of droplet production, environmentally safe dispersion, and commercial availability.

Transmittance measurements were taken by a Multi-Path Transmissometer/Radiometer (MPTR). The MPTR is capable of obtaining transmittances at .4-.7μm, 1.0-1.1μm, 3.5-4.8μm, and 7.9-12.3μm spectral bands. Results will be presented on transmittance comparisons between the different wavelength bands during varying fog density conditions. The transmittance data from the line of sight were tested for optical depth linearity in the various wavelength bands.

1. INTRODUCTION

Mechanical water fog generators were used to create artificial fog for transmissometer measurement studies. The advantages of these artificial fogs include environmentally safe dispersion, high droplet throughput, controlled delivery, and amenability to quantitative characterization. The droplet size spectra indicate a distribution with a mass median diameter of about 20-30μm which is comparable to values reported for natural fog. Under favorable ambient temperature and relative humidity, fog clouds up to 50 meters in length can be realized. A transmissometry system was used to measure transmittances through the generated fog cloud. The transmissometer consists of several light sources, a scanning receiving unit, and a PC based data acquisition system. Results of these experimental investigations to explore the concept of using commercially available water fog generators for transmissometer research are presented. Possible future applications may involve mixing additives in the water supply in order to change the optical properties of the dispersed droplets.

1.1 Background

In the past, measurements of natural occurring fog has been difficult because of the variability and unpredictability of fog formation. Transporting measurement equipment to remote locations is expensive and may be futile if weather conditions are unfavorable for fog during the testing period. Unforseen events such as high winds and radiative heating effects from high clouds can inhibit natural fog development on the ground. The concept of creating a microenvironment for both laboratory and field experimentation is appealing to researchers since they will be able to control, to a certain extent, the dispersion process. In this way, the cost of conducting field experiments will be dramatically reduced since researchers will be able to conduct tests at their local field site.

Significant progress in the generation of artificial fogs came from the agricultural industry who are interested in many environmental control applications such as the prevention of crop freezing. Using existing state-of-the-art commercial fog systems[1] to produce very dense, optically thick, artificial fogs, Sutherland[2] has demonstrated that fogs on the order of a few hundred meters could be produced if meteorological conditions are favorable.

Results from Fourier transform spectrometer measurements[3,4] demonstrated the artificial fog's effective screening over the entire visible to far infrared spectral region. The extinction coefficient was found to be somewhat constant from the visible through mid infrared spectral regions with little structure in the 3-5μm water band absorption region.

2. ARTIFICIAL FOG SYSTEM

The artificial fog system is made up of specially manufactured high pressure direct impaction nozzles. A fine stream of water impacts onto a metal pin (Fig. 1) and causes the water to break up into small droplets. This technique allows significantly higher water throughput than previous evaporation-condensation techniques to generate man-made fogs. Such a system has been used previously for lidar measurements[3] at an emitting wavelength of 535nm.
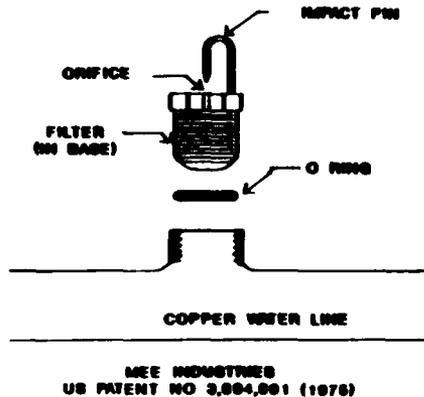

Figure 1. Depiction of a MEE Industries Fog Nozzle.

2.1 Description of Fog System

The fog system is comprised of several 3' x 4' copper frames each consisting of a 5 by 8 array of 40 nozzles total spaced from 8 to 10 centimeters apart. Experiments have been conducted using one, two, or three frames operating simultaneously. When operated at the recommended pressure, the flow rate is approximately 1.2 gallons per 40 nozzle array per minute in the form of a dense white spray very similar in appearance to a natural fog.

The key to the success of the MEE fog system lies in the high pressure direct impaction nozzles that produce both high throughput and small droplets of the about the same size as those found in natural fogs. Water exits through a small, precision machined, orifice under a pressure of 1000 psi and strikes the small (curved) impaction pin center directly in front of the orifice. The initial laminar stream exiting the orifice is first separated into a hollow cone of spray which is then broken up by turbulence into small droplets.

2.2 Components of Fog System

The main components of the artificial fog system is listed as follows:

* 8 HP Gasoline Engine
* Water filters
* Mixing barrel

* Water Tank or Water Outlet
* High Pressure Pump
* High Pressure Hoses
* Manifold Shutoff Valves
* Copper Frames (set of 40 fog nozzles per frame)
* 3 foot support stands for frames
* Single/Dual nozzle mounting

2.3 Advantages of Utilization

The advantage of utilizing this type of artificial fog system is its environment safe dispersion since its product is water. The pump assembly and dispersion equipment is relatively easy to operate and maintain. It is a fast, economical and effective method for instrument calibration, transmissometer measurements in multispectral regions, and sensor performance testing.

Water soluble additives can be mixed with the inlet water supply to provide optically different droplets. Thereby providing some form of validation of scattering and transmission models. Certain parameters can be controlled such as the rate of dispersion and the position of the nozzle frames. This allows some amount of repeatability for investigating theoretical relationships.

3. PARTICLE SIZE DISTRIBUTION

Particle measuring spectrometers were used to count particles between size diameters of .5μm and 47μm. The principle of operation of this type of measuring device is that as an aerosol flows through an illuminated volume of laser light, light is scattered in the forward direction. The intensity of light scattered is measured and used to determine particle size by electronically classifying response pulses according to their magnitude[6]. Measurements of the artificially generated droplet size spectra at the White Sands Missile Range, New Mexico, which is an arid region indicate a bimodal distribution with the mass median diameter varying between 15 to 30 μm which is comparable to values of 10 to 20 μm reported for natural fog. Figure 2 shows an example of one of the droplet
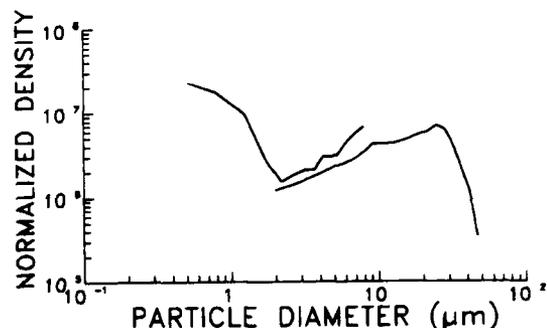
Figure 2. Size distribution of artificial fog. Normalized Density (number of droplets/m^3/μm) versus Droplet Diameter (μm).

size distributions taken with a Particle Measurement System scattering particle counter at the test site. The corresponding normalized mass density assuming spherical particle shape is given in Fig. 3. There are two curves in each figure representing two different instrument size ranges. The lower size range spans .5 to 8μm in diameter. The higher size range covers the larger size droplets of 2 to 47μm in diameter. Fog densities varied throughout the testing period due to many factors such as changing wind conditions, turbulence, and evaporation of droplets.
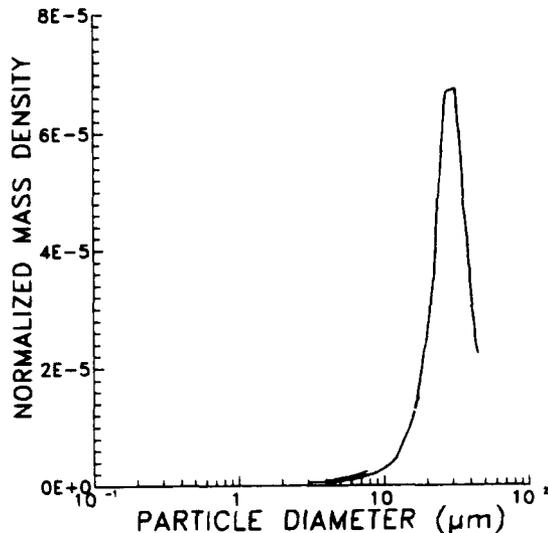

Figure 3. Mass density of artificial fog. Normalized Mass Density (grams/m³/μm) versus Droplet Diameter (μm).

4. MPTR SYSTEM

4.1 Brief Description

The MPTR (Multi-Path Transmissometer/Radiometer)[7,8] developed by the Netherlands is a transmissometry system that is capable of taking measurements along multiple lines of sight scanning a horizontal field of view. The MPTR spectral characteristics cover four spectral bands from the visible region to the infrared region. The source consists of 7 reflectors, two in the near IR and five in the IR with 2 degree beams. The receiver's field of view is 60° in the horizontal position. The instrument is capable of completing a scan every second.

4.2 Transmittance Measurements

The experiment field setup consisted of the MPTR receiver located approximately 100 meters away from the MPTR light sources. The artificial fog system was positioned between the MPTR receiver and source about 20 meters away from the receiver. The line of sight (LOS) was directed approximately 3-5 meters above the ground. There were two man-made fog test trials, Trial 2607 and Trial 2608. Data for Trial 2607 was taken during a 7 minute period and the Trial 2608 period was 15 minutes in duration. Figures 4, 5, 6, and 7 are the MPTR transmittances for Trial 2607 along a single line of sight for the four different spectral bands, respectively: 0.4-0.7μm, 1.0-1.1μm, 3.5-4.8μm, and 7.9-12.3μm.

13:58:00   14:06:59
MPTR2 Transmission LOS 1 Trial 2607 p 0.4- 0.7μ
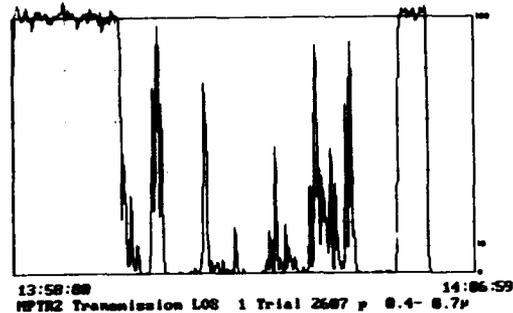
Figure 4. MPTR transmittance measurements versus time. Trial 2607. Spectral Band: .4-.7μm Test Period: 1358 hr - 1407 hr. Ambient Temperature: 25°C

13:58:00   14:06:59
MPTR2 Transmission LOS 1 Trial 2607 p 1.0- 1.1μ
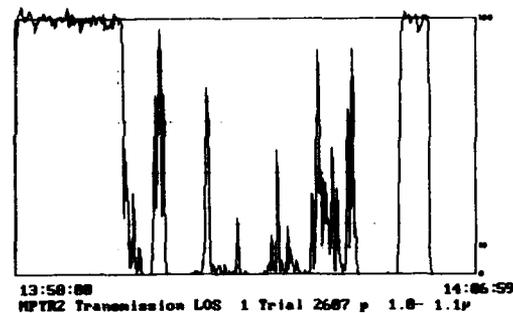
Figure 5. MPTR transmittance measurements versus time. Trial 2607. Spectral Band: 1.0-1.1μm

13:58:00   14:06:59
MPTR2 Transmission LOS 1 Trial 2607 p 3.5- 4.8μ
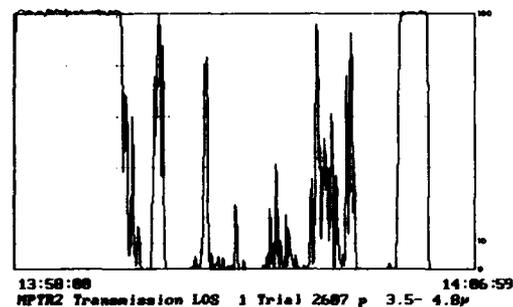
Figure 6. MPTR transmittance measurements versus time. Trial 2607. Spectral Band: 3.5-4.8μm

13:50:00   **14:06:59**
**MPTR2 Transmission LOS 1 Trial 2607 p 7.9-12.3μ**
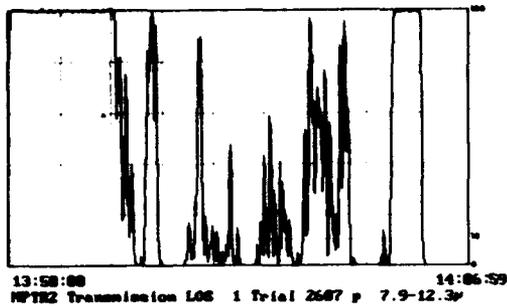
Figure 7. MPTR transmittance
measurements versus time. Trial 2607.
Spectral Band: 7.9-12.3μm

4.3 Optical Depth Comparisons

The obscurant optical depth depends on the
obscurant mass concentration and the mass
extinction coefficient along a line of
sight. In many applications, the mass
extinction coefficient can reasonably be
assumed constant along the path. For
broadband applications, the optical depth
can be integrated over wavelength to yield
a band-averaged optical depth[9].
Furthermore, if the mass extinction
coefficient is assumed independent of
wavelength, relative comparisons can be
made between pairs of spectral bands.
These assumptions were made for the
following optical depth calculations from
transmittance measurements through man-
made fog. One salient feature of the MPTR
system is that spectral bands are measured
along co-linear lines of sight thereby
maintaining equivalent obscurant mass
concentrations during a complete scan
assuming the mass density does not change
dramatically during the scan period. The
design of the system also minimizes
geometrical corrections due to different
receiving optics configurations.

Figures 8, 9, and 10 show the calculated
optical depths from transmittance
measurements made at the .4μm to .7μm
(visible) compared to the corresponding
calculated optical depths at 1.0-1.1μm,
3.5-4.8μm, and 7.9-12.3μm spectral bands,
respectively, for Trial 2607. All the
graphs indicate noticeably less
correlation with optical depths greater
than 5. In general, random scatter in the
data points increases with increasing
optical depths. The ratios of the optical
depths at 3.5-4.8μm over the optical
depths at .4-.7μm are greater than the
ratios of the optical depths at 7.9-12.3μm
over the corresponding optical depths at
.4-.7μm. These ratios essentially
indicate the mass extinction coefficient
ratios. If the obscurant is spectrally
flat for the wavebands plotted, the Beer-
Bougher law should apply and the data
points should fall close to a straight
line. The random scatter at higher
optical depths suggest instrumental noise
as the transmittance signals become very
low. Optical depth comparisons for Trial
2608 are ploted in figures 11, 12, and 13.
These results show similar trends to those
in Trial 2607.
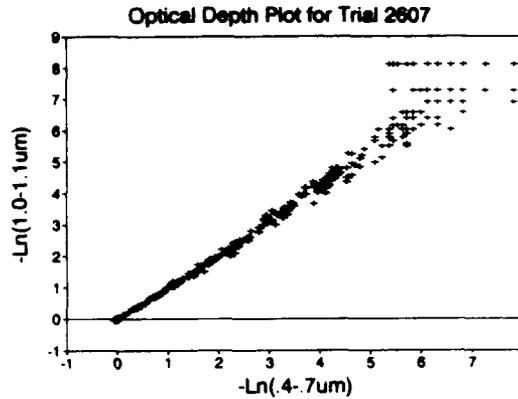
Figure 8. Optical depth comparisons at
visible (.4-.7μm) and 1.0-1.1μm bands.
Trial 2607.
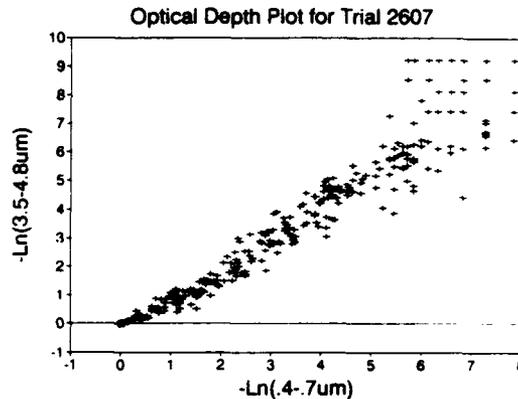
Figure 9. Optical depth comparisons at
visible and 3.5-4.8μm bands.
Trial 2607.
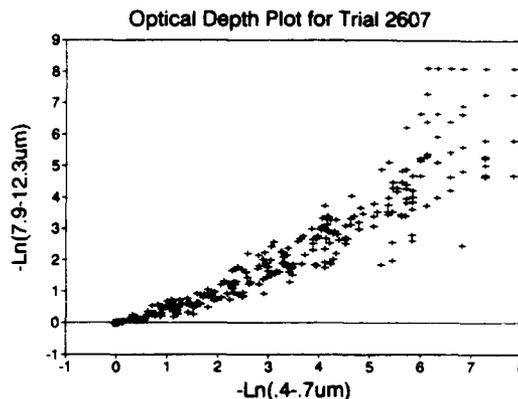
Figure 10. Optical depth comparisons at
visible and 7.9-12.3μm bands.
Trial 2607.

Optical Depth Plot for Trial 2608
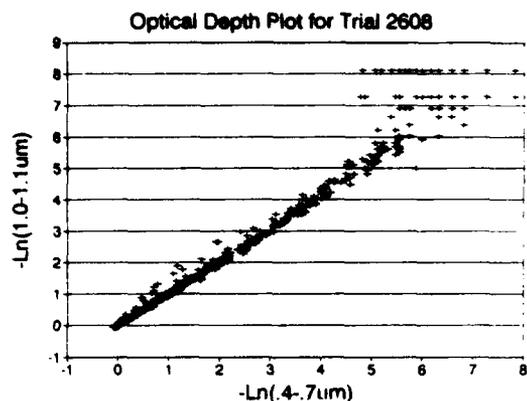
Figure 11. Optical depth comparisons at visible (.4-.7μm) and 1.0-1.1μm bands. Trial 2608.

Optical Depth Plot for Trial 2608
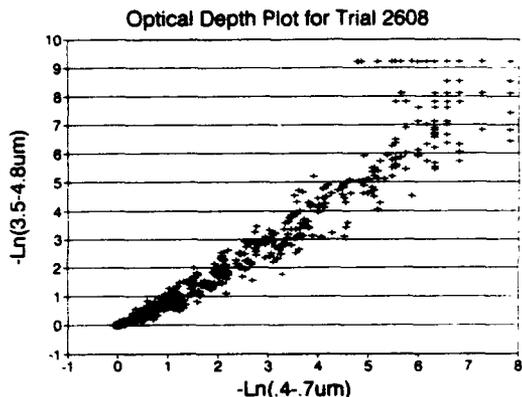
Figure 12. Optical depth comparisons at at visible and 3.5-4.8μm bands. Trial 2608.

**Optical Depth Plot for Trial 2608**
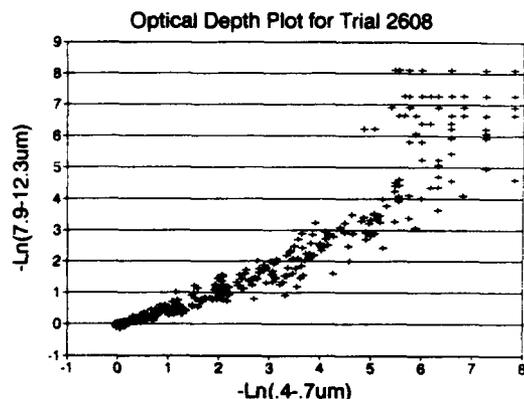
Figure 13. Optical depth comparisons at visible and 7.9-12.3μm bands. Trial 2608.

5. CONCLUSIONS

The artificial fog system has proved to be a useful tool in transmissometry research in which the obscurant is amenable to physical characterization. In this way, experimental measurements can validate theoretical relationships. Future transmissometer field tests will involve REVIRT (Research Visible and Infrared Transmissometers) for longer path, high resolution measurements through the artificially generated fog.

Applications for artificial fogs include fog/cloud simulant, materiel testing, chemical countermeasures, multispectral obscuration, and large area "smoke" screening. Other possible applications may involve mixing additives in the water supply in order to change the optical properties of the dispersed droplets.

The feasibility of using these water fog generators for field research has been demonstrated. These systems are mobile and environmentally safe to operate. They provide a fast, economic and effective method for instrument calibration, transmissometer measurements, and sensor evaluation through fog like conditions.

MPTR transmittance measurements were taken through man-made water fogs and results show that obscuration increased with decreasing wavelengths for the broad spectral bands used. The optical depth plots proved to be a useful tool in the analysis of the transmittance data. The plots can provide qualitative information about instrumental noise, detector/amplifier range, analyses between different wavebands, system linearity, and estimates of mass extinction coefficient ratios from obscurant test data.

6. REFERENCES

1. Mee, T.R., 1977: Man-made Fog for Freeze Protection & Microclimate Control, *Proceedings of the International Society of Citriculture*, 1, 203-208.

2. Sutherland, R.A., R.D. Eaton, S.M. Squires, and M.Z. Kiss, 1990: Properties of Mechanically Generated Water Fogs, *Proceedings of the 11th Annual EOSAEL/TWI Conference*, Physical Sciences Laboratory, New Mexico State University, Las Cruces, NM, 27-30 November 1990.

3. Sutherland, R.A., Y.P. Yee, F.D. Eaton, W.A. Peterson, M.Z. Kiss, and C.E. Foster, 1991: Results of Man-Made Fog Experiments, *Proceedings of the Battlefield Atmospherics Conference*, Hinman Hall, Fort Bliss, Texas, December 1991.

4. Peterson, W.A., D.M. Garvey, and W.M. Gutman, 1991: Spectrally Resolved Transmittance Measurements at Smoke Week XIII, *Proceedings of the 1991 Battlefield Atmospherics Conference*, Hinman Hall, Fort Bliss, Texas, December 1991.

5.   Yee, Y.P., R. Gonzalez, R.A.
Sutherland, J. Thompson, and R.B.
Loveland, 1992: Lidar Measurement Studies
Through Artificially Generated Fog,
*Proceedings of the SMOKE/OBSCURANTS
SYMPOSIUM XVI*, Laurel, Maryland, 14-16
April 1992.

6.   Pinnick, R.G. and H.J. Auvermann,
1979: Response characteristics of
Knollenberg light-scattering aerosol
counters, *Journal of Aerosol Science*, 10,
55-74.

7.   De Jong, A.N., M.J. Roos, and P.J.
Fritz, 1988: Smoke Characterization by
Means of MPTR, IR1988-07, FEL-TNO, The
Netherlands.

8.   Kennedy, B.W., B.A. Locke, W. Klimek,
and R. Laughman, 1990: Large Area and
Self-Screening Smokes and Obscurants
(LASSO) SMOKE WEEK XII, Sponsored by *U.S.*
Army Chemical Research, Development and
Engineering Center, Science and Technology
Corporation Technical Report #4056,
Hampton, Virginia.

9.   AAODL BULLETIN, Vol.8, No.2, September
1990, published by U.S. Army Research
Laboratory and the U.S. Army Chemical
Research, Development, and Engineering
Center (CRDEC), Aberdeen Proving Ground,
Maryland.

Discussion

Discussor's name :   Col. IMM de Bleyser R., BE

Comment/Question :

Is there a possibility to use the MEE water fog installation in tactical applications?

Author/Presenter's reply :

Could be used in a tactical situation if system in a different configuration. Not now suitable for tactical use, but technology involved may have an application. Certainly worth looking into.

Discussor's name :   C. M. Jenden, UK

Comment/Question :

You suggested it was possible that the spectral transmission could be modified by the addition of dyes. Would this not limit the applicability of the system in that these dyes tend to have a serious toxicological impact?

Author/Presenter's reply :

The chemistry of these water soluble dyes is outside my area of expertise. However, if a dye is toxic, its use would be limited. The artificial fog system in such a case would be subject to numerous restrictions. Perhaps the use of dyes needs to be handled on a case by case basis, leading to a set of non-toxic dyes (if any) that would not restrict use of the system.

Discussor's name :   C. M. Jenden, UK

Comment/Question :

Will it be possible to utilize water fogs in a true battlefield environment?

Author/Presenter's reply :

It should be possible to use a variation of the system presented in a battlefield environment, but not in the test configuration shown. The need for a readily available water supply, especially for continuous or repeated use, may be a limitation (e.g. in desert regime). Also, not for temperatures < 0°C, unless use some type of antifreeze (that may change the properties of fog).

ESTIMATION OF TRANSMITTANCE FROM SATELLITE IMAGERY

James Cogan
U.S. Army Research Laboratory
Battlefield Environment Directorate
White Sands Missile Range, New Mexico 88002, USA

and

David Williams
Electrical Engineering Department
University of Texas at El Paso
El Paso, Texas 79968, USA

1. SUMMARY

Transmittance in the visible and thermal infrared may be estimated from a variety of in-situ and remote techniques using ground-based or airborne sensors. However, estimation of transmittance in the troposphere from data gathered by sensors on space platforms remains a problem, especially over land surfaces. This paper presents two preliminary methods: one to compute visibility using changes in contrast from a series of luminance images or measuring changes in the non-zero frequency amplitudes from the associated frequency domain images, and the other to calculate thermal infrared transmittance over a horizontal, vertical, or slant path that uses estimates of precipitable water from satellite data, combined with sounding data from satellite or other sources.

2. INTRODUCTION

The visibility investigation focuses on evaluating techniques that were described in Williams and Cogan (Ref 1). Two algorithms are being investigated: one measuring changes in contrast from a series of luminance images and the other measuring changes in the nonzero frequency amplitudes from the associated frequency domain images. Images from selected areas are taken at designated times and then processed for changes resulting from atmospheric attenuation. In addition, a variation of the method has been specified, in which images from a scene taken at different distances were processed. Both satellite and aircraft images have been processed; however, the results from the aircraft imagery will be predominately discussed, since that work is more advanced.

The second part of this paper presents a preliminary method to compute thermal infrared transmittance over a horizontal, vertical, or slant path that uses estimates of precipitable water from satellite data, combined with sounding data from satellite or other sources. Essentially, profiles of specific humidity are computed from actual atmospheric profiles and adjusted according to satellite estimates of total precipitable water. Temperature and humidity data at each pressure level provide input to equations of the type found in LOWTRAN. These equations yield estimates of thermal infrared transmittance for user specified path lengths.

3. VISUAL RANGE

3.1 Theoretical Overview

With simplifications (Ref 1; Ref 2; Ref 3), the apparent luminance recorded by each pixel within an aircraft or satellite image is

$$B_1(x, y, z_1) = B_0(x, y) T_{01}(z_1) + B_{01}^{\bullet}(z_1) \quad (1)$$

where

B_1 is the apparent luminance recorded at the aircraft or satellite.

B_0 is the inherent luminance of scene described by the pixel.

$B_{01}^{\bullet}$ is the path luminance that represents the light scattered along the path of sight.

T_{01} is the beam transmittance from the scene to the aircraft or satellite.

z_1 denotes the distance between the satellite or aircraft and the scene.

x, y specifies the spatial coordinates of the pixel.

Simplifying assumptions include the following:

* Atmospheric turbulence is neglected.
* The recording sensor records a small band of frequencies approximating the monochromatic case.

* The beam transmittance and the path luminance are assumed constant over the field of view.
* Relative motion between the recording device and the scene is neglected.
* All changes in the scene over time are assu''ed to be due to atmospheric effects only.
* Each scene is recorded such that the zenith and azimuth angles of the sun and the satellite are constant. (Aircraft imagery assumes a constant sun angle.) Different scenes can have different zenith and azimuth angles.

For contrast, a reference pixel value is subtracted from each pixel in the luminance image, forming the measured apparent contrast image (Ref 1):

$$C_1(x,y,z_1) = B_1(x,y,z_1) - B_1(x_{ref},y_{ref},z_1)$$
$$= [B_0(x,y) - B_0(x_{ref},y_{ref})] T_{01}(z_1)$$
$$= C_0(x,y) T_{01}(z_1)$$
$$(2)$$

Taking the Fourier transform of equation (2) with respect to x and y gives the frequency response of the measured apparent contrast image (Ref 1):

$$C_1(f_x,f_y,z_1) = B_1(f_x,f_y,z_1) - B_1(x_{ref},y_{ref},z_1)$$
$$= B_0(f_x,f_y) T_{01} - B_0(x_{ref},y_{ref}) T_{01}(z_1)$$
$$= C_0(f_x,f_y) T_{01}(z_1)$$
$$(3)$$

Note that the first term on the second line of equation (3) consists of the frequency response of the luminance image multiplied by the beam transmittance that acts as a gain factor. Furthermore, the second term on the second line affects only the zero frequency component (Ref 1). Consequently, the frequency response of the measured apparent contrast image differs from the response of the luminance image in that all nonzero frequencies will be reduced equally by the effect of the beam transmittance. Furthermore, areas of an image with sharp differences (high frequency information) do not attenuate faster than areas with little or no changes (low frequency information), so that all nonzero spatial frequencies of the luminance image vary linearly with beam transmittance.

Assuming a beam transmittance of the form (Ref 3),

$$T_{01}(z_1) = \exp[-z_1/L(z)] \qquad (4)$$

where $L(z_1)$ is the equivalent attenuation length, and noting that

$$L(z_1) = v/3.912 \qquad (5)$$

where v is the meteorological range, then the observed visibility (as specified by v) can be directly related to changes in contrast and changes in the nonzero

frequency response of the luminance images. This is accomplished by reverse substitution of equations (5) and (4) into (3) or (2) and by taking a sequence of images of a scene where the images differ in time or differ in distance from the scene. Then the resulting changes in contrast or changes in the nonzero frequency components can be measured to determine the visibility (Ref 1).

3.2. Experimental Results

These measurement techniques were evaluated by using satellite imagery from GOES and TIROS-N satellites and from low altitude aircraft images. Contrast variations and changes in the frequency spectrum amplitude were compared with observed surface visibility measurements and also with simulated values.

3.2.1 Satellite Imagery

Preliminary processing with limited results has been performed on visible channels recorded by GOES and TIROS-N satellites. The GOES satellite is in geosynchronous orbit at approximately 35,000 km and records the visible channel with a grey scale resolution of 6 bits, expanded to 8 bits (256 grey levels). Each pixel has a ground resolution of approximately 0.9 km^2 at nadir. The TIROS-N (NOAA) satellites are in polar orbit at altitudes of 833 to 870 km and record two visible channels with a grey scale resolution of 10 bits, which are normalized to a range of 0 to 100. The maximum ground resolution of each pixel is approximately 1.1 km^2.

Initial testing determined that images from both satellites lack contrast. Although simulations with satellite images support the techniques that are being tested, the experimental results have been, to date, inconclusive. Scenes have been picked with substantial differences in horizontal visibility; however, these changes are not apparent in the images, either by human eye or by machine processing. Consequently, we have no meaningful results to repor* from either the spatial or frequency domain methods.

3.2.2 Aircraft Imagery

Aircraft images were taken using a Cessna 150 flown on a triangular course bounded by El Paso, Texas, and Las Cruces and Deming, New Mexico. The aircraft was flown at a nominal altitude of 1980 m and a nominal speed of 46 ms^{-1}. The images were recorded with a Nikon F2 35-mm camera and Kodak Tmax 100 black and white film and with an inexpensive 35-mm camera using Kodak Ektachrome 200 color film. Except for the first flight, all scenes were photographed through the side window of the aircraft.

Nine test flights were flown between 31 July and 25 November 1992, primarily recording scenes of mountains and sky along the flight path. Images were also recorded of urban scenes as appropriate. Mountains were chosen as targets because their locations are well defined and they

are visible from a wide range of distances.

Commercial processing was used to develop and print the images. Selected scenes were digitized at a nominal resolution of 440 by 450 pixels by using a CCD (charge coupled device) TV camera driving a video digitizer. The gray scale resolution of the digitizer was 8 bits (256 values), with a typical scene being digitized with an intensity range of about 210 out of the possible 256 values.

The images were processed in a variety of ways to obtain the visibility estimates. Currently, this processing is performed with SUN and HP workstations using X Windows. The Florida Mountains near Deming were used for the majority of the work since they are visible over a wide range of distances along the flight path. Images of the Florida Mountains were recorded at distances ranging from 15.8 to 85.7 km. The Florida mountain range is remote from El Paso and Las Cruces and, for the most part, is not obscured by localized smog that collects within the Rio Grande valley.

Spatial domain analysis involved processing images taken at different distances from the mountains during the same flight and images recorded at a constant distance, but taken during different flights. Examples of images taken at different distances are shown in figure 1, and images taken at a constant distance but at different times are shown in figure 2. In both cases, the contrast of each image was measured by using the image histogram and then plotted with the data from other images in the same group. These contrast values were used to calculate the meteorological range, v, as in Reference 1.

Subimages consisting only of mountains and sky were formed of each target, so that each subimage displayed the same scene, regardless of the distance. Consequently, subimages of a scene at the greatest distances were a few hundred pixels in size, while those taken nearest to the mountains were a few hundred thousand pixels.

The contrast was measured in one of two ways, max-min and peak. The max-min process measured contrast by taking the difference between the absolute maximum and minimum pixel intensities within the image. The peak method calculated contrast by taking the difference between the two histogram peaks representing the mountain and sky data. These values are shown in figure 3. In a limited number of cases, an average was taken of the mountain and sky intensities, and then a difference was formed between these averages.
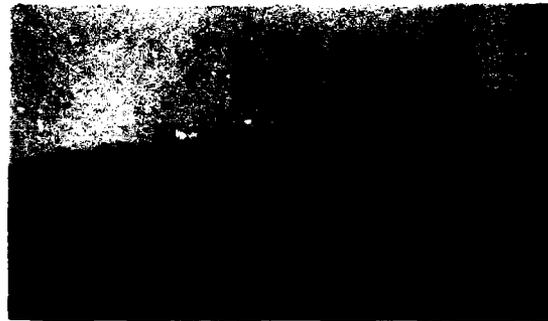
(a) 57.1 km

(b) 25.4 km

Figure 1. Two views of the Florida Mountains at different distances at almost the same time (about 12 minutes apart).

(a) September 25, 1992

(b) October 16, 1992

Figure 2. Two views of the Florida Mountains at a constant distance (about 44 km) at different times.
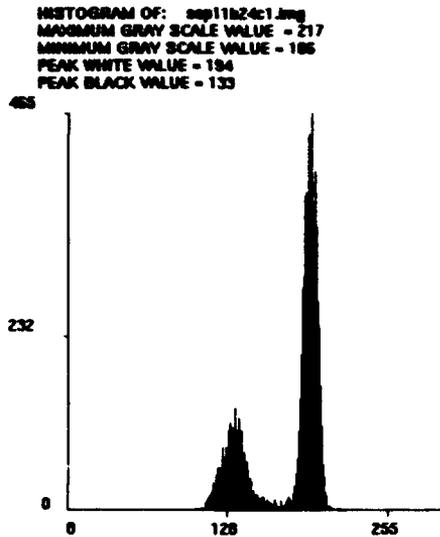
Figure 3. Histogram showing max-min and
peak contrast values for one
subimage.

Selected results from the Florida
Mountain data are shown in tables 1 and
2. The multiple distance results were
calculated from images taken at six
distances from the Florida Mountains and
averaged for each of the specified days.
The observed meteorological range, v, was
then tabulated with the values obtained
from using the max-min and peak contrast
calculation methods. The average (non-
zero) FFT (fast Fourier transform)
frequency amplitude was also calculated.
(The FFT analysis will be discussed
shortly.)

TABLE 1. MULTIPLE DISTANCE RESULTS
(FLORIDA MOUNTAINS)

METHOD	METEOROLOGICAL RANGE, V(km)		
	27 AUG	11 AUG	25 SEP
OBSERVED	80	72	160
MAX-MIN	163	315	279
PEAK	52	88	166

TABLE 2. CONSTANT DISTANCE RESULTS
(DISTANCE TO FLORIDA MOUNTAINS
= 44.4 km)

METHOD	METEOROLOGICAL RANGE, V(km)			
	27 AUG	11 SEP	25 SEP	16 OCT
OBSERVED	80	72	160	160
MAX-MIN	122	122	149	194
PEAK	77	72	97	105

The max-min method generated high
visibility estimates, while the peak
contrast estimates returned values that,
although not perfect, tracked the

observed visibility more closely. This
seems reasonable since the maximum and
minimum pixels may include artifacts such
as bad or saturated pixels that exag-
gerate the contrast range, while the
histogram peaks more closely represent
mean intensity values exhibited by the
mountains and the sky.

The constant distance results in table 2
were calculated from several images
recorded at a distance of approximately
44.4 km from the Florida Mountains. This
distance was chosen because the subimages
exhibited good detail, and yet provided
good variation with changes in visi-
bility. The observed visibility was also
listed. Contrast calculated using the
max-min method tended to generate high
visibility estimates, while contrast
calculated using the peak method returned
close estimates for lower observed visi-
bilities, but were low for higher
observed visibilities. The reason for the
latter case is not yet clear.

There are many sources of error for this
analysis.

* The observed visibility was not
constant along the flight path.
Typically there was substantial smog
over downtown El Paso and Juarez that
usually propagated along the Rio
Grande Valley and the Tularosa Basin.
On some days, the observed visibility
was approximately 32 km within the
Rio Grande Valley, and about 160 km
west of the valley. In such cases, the
Florida Mountains would be indistinct
near Las Cruces, but would become much
more visible just a few miles west of
town. The smog seems to stratify with
respect to altitude, and lie in
patches depending on the wind direc-
tion and speed. On one or two flights,
scattered precipitation caused vari-
ability in the visibility. Since the
test methods assume a constant beam
transmittance between the viewer and
the target scene, application of this
assumption could incur measurable
error over the distances traversed on
the flight path.

* The observed meteorological range was
not precise, particularly at higher
values, because there are no targets
at longer distances. For example,
there are no distinct landmarks at 140
km, 150 km, 160 km, and so on. Conse-
quently, a meteorological range esti-
mate of 160 km could possibly repre-
sent a range of about 120 to 200 km.

* The photographic processing was not
consistent. The print processing
appeared to vary between runs, causing
a noticeable variation in contrast for
days having the same apparent meteoro-
logical range. This variation implies
that it might be better to digitize
the image negatives rather than the
prints.

* Subimages of the same scene cannot be exactly registered with respect to position.

Frequency domain analysis was also performed by taking an FFT of the images. Several methods were tried. The average was taken of all nonzero frequencies, the first 32 harmonics along the positive X axis were tabulated, and the 10 largest nonzero harmonics were sorted and printed. In addition, the frequency response was divided into three regions: low, medium and high, with average frequency amplitudes calculated for each region.

Although the basic theory was verified by using a single image whose contrast was reduced by specified amounts, the results from real data have been inconsistent, using each of the aforementioned methods. We do not know why this is the case. However, aside from the sources of error given above, the following artifacts will also change the results.

* High frequencies exceed the resolution of the film and therefore are rolled off with distance. (Edges are more distinct closer than farther away from the target.)

* Digitization affects the frequency response of the scene. If a digitized scene contains mostly sky, it will have a stronger low frequency response than an image that contains mostly mountains. This difference in response is because the sky is normally constant in appearance while the mountains have edges that are characterized by high frequencies. Thus, image registration is important, and calculating an average frequency amplitude may not be appropriate.

Because of these problems, the frequency domain processing technique is being investigated further.

4. INFRARED TRANSMITTANCE

4.1 Overview

The preliminary technique uses the relation between water vapor and infrared extinction in the atmosphere. Algorithms of the type found in LOWTRAN may be used to compute infrared transmittance in a horizontally stratified atmosphere (Refs 4, 5, 6). Temperature and humidity data at each pressure level of an atmospheric sounding provide input to equations similar to those found in reference 4. That older version of LOWTRAN used standard type variables (for example, vapor pressure in atmospheres). The accuracy in the thermal infrared is virtually the same as in reference 5, and the algorithms are the same as in reference 6 and reference 5. These equations yield estimates of thermal infrared transmittance for user-specified horizontal, vertical, or slant path lengths. The preliminary version assumes a horizontally stratified atmosphere. The simple integration techniques of this approximate method assume constant or

only smoothly varying transmittance over spectral intervals of up to 20 cm^{-1}

Atmospheric soundings from a variety of sources may be used in general, but for applications to distant remote areas the primary sources would be satellite soundings, soundings derived from aircraft or unmanned aerial vehicle (UAV) data, dropsonde profiles, or a combination of the above. The resultant sounding provides temperature (T) and humidity (h) values at given pressure levels, which may be used to compute specific humidity (q). From values of q one may compute precipitable water (W_p) for individual layers or for the entire vertical extent of the sounding (total or integrated W_p). Integrated values of W_p may be compared to values derived from satellite imagery. The sounding amount (not the shape of the distribution curve) is adjusted according to the ratio of the estimate from satellite imagery (herein called satellite estimate or value) to the value computed from the sounding.

Satellite estimates of W_p may be obtained through techniques developed by a number of investigators using, for example, transmittance ratios (total through entire atmosphere). Split window radiances from the visible infrared spin scan radiometer (VISSR) atmospheric sounder (VAS) carried on geostationary operational environmental satellites (GOES) were used by Chesters et al. (Ref 7; Ref 8), while Jedlovic (Ref 9) and Kleepsies and McMillin (Ref 10) developed methods that used data from both the VAS and the advanced very high resolution radiometer (AVHRR) carried by National Oceanographic and Atmospheric Administration (NOAA) satellites. Jedlovic (Ref 9) derived his method by using aircraft data and then applying it to satellite values. Kleepsies and McMillin (Ref 10) reported correlations as high as 0.85 (AVHRR) and 0.92 (VAS) relative to W_p from radiosonde data. Ongoing work in this area by some of the above authors and others can be expected to lead to improved absolute accuracies.

4.2 Transmittance Algorithms

We assumed that an atmospheric sounding provides profiles of T (kelvin), h (percent), and z (meters) at a number of pressure levels where pressure (p) has units of hPa. Values of h are converted to values of absolute humidity q (g m^{-3}) through the standard equations found in references such as Ludlam (Ref 11). From the q profile we compute W_p for each layer (i) in units of grams per square centimeter, and layer values of W_p are summed to obtain the total W_p. The ratio of the satellite measured value of W_p to the total W_p from the sounding is used to scale the values of q for each pressure level or height.

The resultant profile of q is used with equations of the type found in Kneizys et al. (Ref 4) for the computation of transmittance for the mean wavenumber of a narrow spectral interval. Next we

calculate the LOWTRAN water vapor parameter (w), the effective water vapor absorber amount per unit path length in grams per centimeter^{-2} atmospheric kilometers^{-1} at altitude z. The water vapor attenuation coefficient (C_a) in grams^{-1} centimeter^2 atmosphere^{-1}, as defined in Kneizys et al. (Ref 4) for a thermal infrared wavenumber (ν) in the 8- to 14-μm wavelength region at a temperature of 296 K, is given by

$$C_a = 4.18 + 5578 \exp(-0.00787\nu) \quad (6)$$

Finally, the transmittance (τ) for a given thermal infrared wavenumber is computed from $\tau = \exp(-C_a w d_a)$. This procedure should be valid for a narrow wavenumber band in the thermal infrared to a useful accuracy. For example, τ for the mean wavenumber of a 20-cm^{-1} band, as used in LOWTRAN, provides a reasonable estimate of τ for that interval. Transmittance is assumed to be constant or to vary only slowly and fairly smoothly over a 20-cm^{-1} interval. However, the use of LOWTRAN, or this program, to compute monochromatic transmittances (as for a laser) may lead to serious errors (Ref 12).

The equations for carbon dioxide, ozone, and noncontinuum water vapor were derived from LOWTRAN equations for "uniformly mixed gases" (for example, carbon dioxide) and water vapor (Ref 4). Transmittance over an interval of 20 cm^{-1} is computed from an equation of the form $\tau = f(C_a w^* D_a)$, where C_a is a wavenumber dependent absorption coefficient, w^* is an equivalent absorber density, and D_a is the atmospheric path.

$$w^* = w \left[\frac{p(z)}{p_o} \sqrt{\frac{T_o}{T(z)}} \right]^m \quad (7)$$

where p_0 and T_0 correspond to standard pressure and temperature. m has values of 0.9, 0.75, and 0.4 for water vapor, carbon dioxide, and ozone, respectively. In LOWTRAN the form of the function for τ and the parameter m were determined empirically by using laboratory transmittance data and molecular line constants (Ref 4). Curves were computed based on these data and presented in Kneizys et al. (Ref 4) for τ (graphed as log to the base 10 of τ), C_a, and absorber concentrations. The curve of $\log_{10} \tau$ for ozone is different from that for water vapor (noncontinuum) and the uniform mixed gases, but the basic form is similar. The units for the C_a and concentrations differed, but can be converted to "standard" units through the use of relationships given in McClatchey et al (Ref 12).

The approach for aerosols was based on the technique of Kneizys et al. (Ref 4). In this preliminary report only distributions for land aerosols were considered (rural and urban). Later, Kneizys et al. (Ref 5) improved the distribution for the lowest 2 km over land through the use of routines based on Heaps (Ref 13). More

recent updates as noted in Kneizys et al. (Ref 6) should improve matters further, but no documentation was available when this paper was prepared. However, the earlier approach should be sufficiently accurate for the needs of the research described in this paper.

Kneizys et al. (Ref 4) presented profiles of aerosols for a variety of situations, including the rural and urban curves, maritime distributions, and curves for after volcanic eruptions. Seasonal and high humidity differences were included. However, for the preliminary effort described herein we felt that mean curves for the basic profiles for land, rural and urban, would be sufficient. Transmittance was then calculated through an equation of the form τ(aerosol) = $\exp$(-extinction coef * haze scale factor value * distance).

In the program of this report the aforementioned curves were approximated through piecewise linear or power law fits, or a combination of both. Other fits may produce a closer approximation, but the ones chosen gave a sufficiently good fit for the purposes of this initial investigation.

4.3 Comparisons and Simulations

4.3.1 Comparisons

The approximate method of this paper for computation of thermal infrared transmittances was compared with LOWTRAN 7 (PC version) for vertical paths from the surface to 14 km. In particular, the spectral intervals covered by channels 4 and 5 of the AVHRR were chosen for the comparison (885 to 971 and 800 to 870 cm^{-1}). For this comparison the spectral responses of the actual instrument were not considered (that is, step function response used), and a rural aerosol with a 23-km visibility was assumed.

Table 3 shows the results of the comparison for a few of the "standard" atmospheres. The differences in τ were small to moderate except for the much larger difference (over 0.06) for the subarctic winter atmosphere. Transmittances from both LOWTRAN and the program of this paper were compared to those from computations using a line-by-line method (GENLN2) as reported by Saunders and Edwards (Ref 14). Table 4 compares values of τ computed over a vertical path from 0 to 100 km for the U.S. Standard Atmosphere with an urban aerosol by the approximation program of this paper, the PC version of LOWTRAN, and the GENLN2 line-by-line program. The GENLN2 values are listed as presented in Saunders and Edwards (that is, rounded to the nearest 0.01).

Neither LOWTRAN nor the approximate method produced values equal to the GENLN2 results, but the approximation values were closer. A comparison of the results shown in table 3 with those derived from data presented in Saunders and Edwards (Ref 14) suggested that the approximation values were closer to the

GENLN2 output (especially for the subarctic winter case), except for the tropical atmosphere. In all cases the line-by-line calculations led to higher values of τ than either of the lower resolution programs. However, different line-by-line models may not yield the same values. Saunders and Edwards noted that Chedin et al. (Ref 15) reported that for nadir paths in the 15-μm region various transmittance models agree to within only 2 percent in τ.

TABLE 3. RESULTS FROM TRANSMITTANCE
COMPUTATIONS USING LOWTRAN 7
(L) AND THE APPROXIMATE METHOD
(A)*

Atmosphere	Model	Transmittance	
		ch 4	ch 5
Tropical	L	0.516	0.368
	A	0.509	0.363
Mid Latitude Summer	L	0.641	0.522
	A	0.662	0.541
Subarctic Winter	L	0.870	0.850
	A	0.941	0.927

*The atmospheres and AVHRR channels (ch) are indicated in the table. The PC version of LOWTRAN was used.

TABLE 4. TRANSMITTANCE RESULTS USING
GENLN2 (G), LOWTRAN 7 (L) AND
THE APPROXIMATE METHOD (A)*

Model	Transmittance	
	ch 4	ch 5
G	0.85	0.80
L	0.792	0.737
A	0.851	0.792

*The results from GENLN2 (a line-by-line model) were presented in Saunders and Edwards (ref 14). All results were for the 1962 U. S. Standard Atmosphere.

As noted previously, the calculations of this paper did not account for sensor response as did those for the GENLN2. However, sample computations with the U.S. Standard and Tropical atmospheres

suggested that leaving out the response function only led to errors in the approximate and LOWTRAN results that were < 0.002 for channel 4 and $\leq$ 0.01 for channel 5 (all values computed with sensor response higher). Nevertheless, the closeness of the approximate method and GENLN2 results, with the possible "errors" taken into account, may be fortuitous. However, the method apparently can produce useful results for a cloud-free line of sight.

Very preliminary results from ongoing comparisons with the latest version of MODTRAN (2 cm^{-1} spectral resolution) suggest that differences between results from the approximate method and MODTRAN are somewhat smaller than those between LOWTRAN and the approximate method for channels 4 and 5 of the AVHRR.

4.3.2 *Modified Method*

The approximate method was analyzed and compared to the line-by-line model for several atmospheric constituents. The main differences from the line-by-line results were for water vapor, especially continuum absorption. The differences were nonlinear, and they increased with increasing water vapor amount. A minor change to the wavenumber coefficient in equation (1) (from -0.00787 to -0.00817) resulted in significantly closer values for the more moist atmospheres, especially for the tropical one. Table 5 shows some results of the comparison between the GENLN2 and modified approximate method. For channel 5 (800 to 870 cm^{-1}) the two sets of values agreed to within 0.004; and for channel 4 (885 to 971 cm^{-1}), the largest difference was 0.011. Both maximum differences were computed for the subarctic winter atmosphere. The values presented in table 5 may be compared with LOWTRAN and unmodified approximate results in table 3.

Saunders and Edwards (Ref 14) published results by absorber/scatterer for the U.S. Standard Atmosphere that were compared to those computed by the modified method. As seen in table 6 the two methods produced values that agree reasonably well. Certain of the Saunders and Edwards' results were presented to the nearest 0.01 and others to 0.0001; the former values are shown as printed and the latter are rounded to the nearest 0.001, as was the output from the approximate method. The maximum difference apparently did not exceed about 0.01, and may have been smaller if the response curves had been used in the latter method.

TABLE 5. TRANSMITTANCE COMPUTED FOR AVHRR CHANNELS 4 AND 5 FOR THREE MODEL ATMOSPHERES*

| Model | | Atmosphere | | |
		SAW	MLS	TROP
ch 4	A	0.942	0.686	0.542
	G	0.931	0.691	0.552
ch 5	A	0.930	0.579	0.410
	G	0.926	0.580	0.413

*A = approximate model (modified), G = GENLN2 line-by-line model, SAW = subarctic winter, MLS = midlatitude summer, and TROP = tropical. Channel (ch) 4 = 885-971 cm^{-1} and ch 5 = 800-870 cm^{-1}.

TABLE 6. TRANSMITTANCE COMPUTED FOR AVHRR CHANNELS 4 AND 5 FOR IMPORTANT ABSORBERS/SCATTERERS*

| Channel | Model | Absorber/Scatterer | | | | | |
		H2O c	H2O l	CO2	O3	Aerosol	Total
ch 4	A	0.925	0.972	0.988	1.000	0.968	0.860
	G	0.93	0.97	0.985	1.000	0.97	0.85
ch 5	A	0.892	0.935	1.000	1.000	0.968	0.807
	G	0.90	0.94	0.966	1.000	0.97	0.80

*All values computed using the U. S. Standard Atmosphere. A = approximate model (modified), G = GENLN2 line-by-line model, c refers to continuum absorption, and l refers to line absorption.

4.3.3 Simulations

A variety of simulations was made with the approximate method to obtain an idea of the likely errors in τ that would be associated with typical errors in W_p from satellite data. Chesters et al. (Ref 7) reported an overall rms error in total W_p computed from VAS data of about ±1.0 g cm^{-2} over a range of W_p values from 1.7 to 5.5 g cm^{-2}. In a later paper by Chesters et al. (Ref 8) the error was reduced to ±0.6 g cm^{-2}. Kleepsies and McMillin (Ref 10) found a standard difference of around 0.44 g cm^{-2} when their technique was

applied to AVHRR data, and 0.39 g cm^{-2} for VAS data. For all of the above methods, single comparisons with data from individual rawinsondes gave differences of up to around 2 or 3 g cm^{-2}. For this paper τ values were calculated for the tropical and midlatitude summer atmospheres where the total W_p was changed by ±0.5 and ±1.0 g cm^{-2}. The results of those computations for the midlatitude summer are shown in table 7. Figure 4 shows the variation of τ for horizontal paths of 3 km at each level up to 6 km for channel 5 for the same model atmosphere with a W_p variation of ±0.5 g cm^{-2}. As indicated in the figure the differences in horizontal τ at lower levels can be significant for the given "errors" in W_p .

TABLE 7. TRANSMITTANCE COMPUTED WITH THE APPROXIMATE METHOD USING THE MIDLATITUDE SUMMER ATMOSPHERE*

| W_p (g cm^{-2}) | Transmittance | |
	ch 4	ch 5
1.977	0.796	0.718
2.477	0.732	0.631
2.977	0.663	0.545
3.477	0.592	0.458
3.977	0.520	0.377

*W_p in g cm^{-2} was varied by ±0.5 and ±1.0 g cm^{-2} relative to the nominal midlatitude summer value of 2.977 g cm^{-2} (total value from 0 to 14 km).
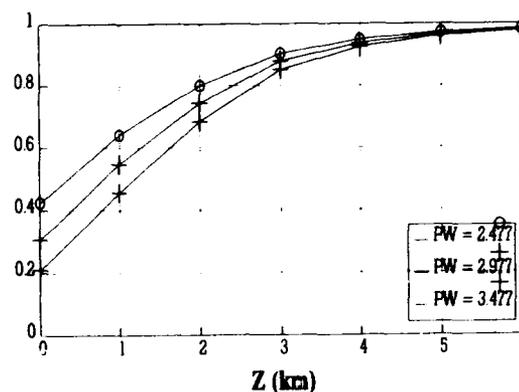

Figure 4. Transmittance (τ) values for channel (ch) 5 computed using the approximate method for the midlatitude summer atmosphere for 3 km horizontal paths at the indicated heights (Z) for the listed values of W_p(WP) in g cm^{-2}.

Curves similar to those of figure 4 were prepared for the subarctic winter (figure 5), tropical (figure 6), and U. S. standard (not shown) atmospheres. Among the standard atmospheres it appeared that the greatest change in τ for a change in W_p of ± 0.5 g cm^{-2} occurred for the fairly moist (W_p = 2.977 g cm^{-2}) midlatitude summer atmosphere. A slightly smaller change occurred for the less moist (W_p = 1.448 g cm^{-2}) U. S. standard atmosphere. Figure 2 was calculated for a real rawinsonde sounding launched at about 16 Z on 26 September 1980 at Dayton, Ohio (Ref 16). A fairly strong subsidence inversion capped a modestly moist layer below 2 km. The values of τ below 2 km exhibit changes greater than those shown by any of the above standard atmospheres when W_p is varied by ± 0.5 g cm^{-2}. This very limited comparison with real data supports the idea that use of climatological data to estimate τ would lead to less accurate results and that actual sounding data should be used whenever possible.
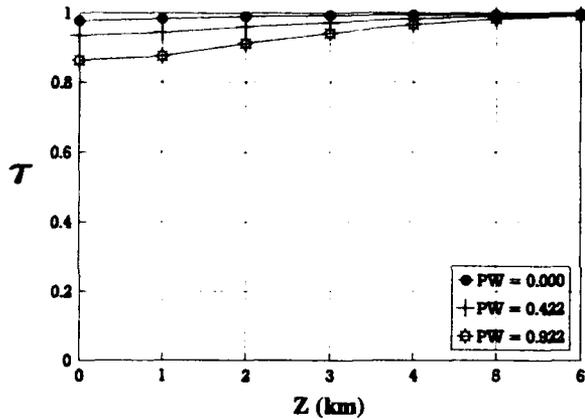

Figure 5. Transmittance (τ) values as in figure 4, but for the subarctic winter atmosphere.
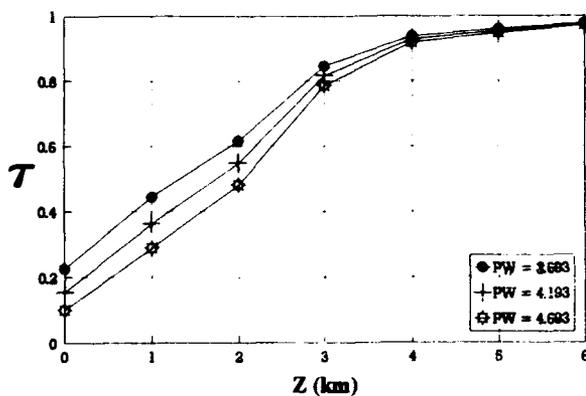
Figure 6. Transmittance (τ) values as in figure 4 but for the tropical atmosphere.

5. CONCLUSION

The techniques specified in Williams and Cogan (Ref 1) have been verified by tests that have manually changed the contrast of a single image. Using these methods with satellite images has proven diffi- cult, however, because of the inherent lack of contrast. Applying the methods to aircraft imagery has proven to be fruitful with spatial domain methods; however, frequency domain techniques have been inconclusive to date.

A preliminary technique was developed for estimation of transmittance in the ther- mal infrared in the troposphere using satellite derived values of W_p along with profile data that are not too distant in space or time. Chesters et al. (Ref 8) noted that relative accuracies are very good when compared to absolute accura- cies. Consequently, adjustment of a coincident satellite derived value of W_p to that extracted from the profile data may allow a useful description of the surrounding moisture field. Furthermore, the apparent accuracy of the approximate method for computing τ of about 0.01 relative to a line-by-line model seems reasonably useful for many cloud-free atmospheres, although further refinement would be worthwhile. However, the pri- mary source of error appears to arise from the satellite estimates of W_p. An error in W_p of ± 0.5 g cm^{-2} can lead to errors in τ for a 3-km horizontal path that may exceed 0.10 (figure 7). There- fore, further work should concentrate more on improving the technique for estimating W_p from satellite imagery.
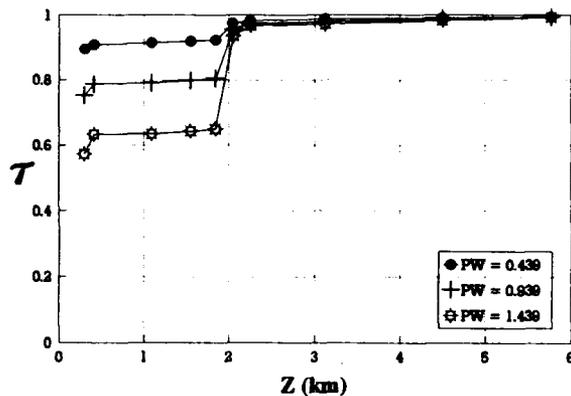

Figure 7. Transmittance (τ) values as in figure 4, but for an actual sounding (see text).

The methods described herein for estimating visibility and infrared transmittance clearly require further research before becoming viable, operationally capable techniques. However, they appear to offer promise for obtaining useful measures of those parameters for remote areas that are distant from ground-based instruments.

6. REFERENCES

1. Williams, D. H., and J.L. Cogan, 1991: "Estimation of Visibility from Satellite Imagery," *Applied Optics*, Vol. 30, 414-419.

2. Duntley S. Q., J. Gordon, J. Taylor, A. Boileau, J. Tyler, R. Austin, and J. Harris, 1964: "Visibility," *Applied Optics*, Vol. 3, 549-598.

3. Duntley, S. Q., A. R. Boileau, and R. W. Preisendorfer, 1957: "Image Transmission by the Troposphere I", *Journal of the Optical Society of America*, Vol. 47, No. 6, 499-506.

4. Kneizys, F. X., E. P. Shettle, W. O. Gallery, J. T. Chetwynd, L. W. Abreu, J. E. A. Selby, R. W. Fenn, and R. A. McClatchey, 1980: *Atmospheric Transmittance/Radiance: Computer Code LOWTRAN 5*, AFGL-TR-80-0067, Air Force Geophysics Laboratory, Hanscom AFB, MA, 233 pp.

5. Kneizys, F. X., E. P. Shettle, W. O. Gallery, J. T. Chetwynd, L. W. Abreu, J. E. A. Selby, S. A. Clough, and R. W. Fenn, 1983: *Atmospheric Transmittance/Radiance: Computer Code LOWTRAN 5*, AFGL-TR-83-0187, Air Force Geophysics Laboratory, Hanscom AFB, MA, 200 pp.

6. Kneizys, F. X., E. P. Shettle, L. W. Abreu, J. T. Chetwynd, G. P. Anderson, W. O. Gallery, J. E. A. Selby, and S. A. Clough, 1988: *Users Guide to LOWTRAN 7*, AFGL-TR-88-0177, Air Force Geophysics Laboratory, Hanscom AFB, MA, 137 pp.

7. Chesters, D., L. W. Uccellini, and W. D. Robinson, 1983: "Low-Level Water Vapor Fields from the VISSR Atmospheric Sounder (VAS) "Split Window" Channels," *J. Clim. Appl. Meteor.*, 725-743.

8. Chesters, D., W. D. Robinson, and L. W. Uccellini, 1987: "Optimized Retrievals of Precipitable Water from the VAS "Split Window"," *J. Clim. Appl. Meteor.*, 1059-1066.

9. Jedlovec, G. J., 1990: "Precipitable Water Estimation from High Resolution Split Window Radiance Measurements," *J. Appl. Meteor.*, 851-865.

10. Kleepsies, T. J., and L. M. McMillin, 1990: "Retrieval of Precipitable Water from Observations in the Split Window over Varying Surface Temperatures," *J. Appl. Meteor.*, 851-862.

11. Ludlam, F. H., 1980: *Clouds and Storms: The Behavior and Effect of Water in the Atmosphere*, The Pennsylvania State University Press, University Park, PA, 468 pp.

12. McClatchey, R. A., R. W. Fenn, J. E. A. Selby, F. E. Volz, and J. S. Garing, 1972: *Opitical (sic) Properties of the Atmosphere (Third Edition)*, AFCRL-72-0497, Air Force Cambridge Research Laboratories, L. G. Hanscom Field, Bedford, MA, 108 pp.

13. Heaps, M. G., 1982: *A Vertical Structure Algorithm for Low Visibility/Low Stratus Conditions*, ASL-TR-0111, U. S. Army Atmospheric Sciences Lab., White Sands Missile Range, NM, 38 pp.

14. Saunders, R. W. and D. P. Edwards, 1989: "Atmospheric transmittances for the AVHRR channels," *Appl. Opt.*, 4154-4160.

15. Chedin, A., H. Fischer, K. Kunzi, D. Spankuch, and N. A. Scott, 1988: *Report on the ITRA Campaign and Workshop*, University of Maryland, 12-14 March 1986.

16. Bradford, G. R., B. P. Sanford, J. R. Stearns, J. A. Conant, and J. Schroeder, 1982: *Airborne Background Measurements in Support of Tactical Decision Aid Development*, AFGL-TR-82-0358, Air Force Geophysics Laboratory, Hanscom AFB, MA, 68pp.

Une méthode expérimentale et globale de mesure de l'émissivité.

R. Marchal
Service d'optique et d'optronique
Arsenal du Matériel Mécanique et de l'Armement
Rue F. Lefèbvre 50, B 4000 Rocourt
Belgium

RESUME.

Dans le cadre de l'évaluation de camouflages multispectraux dans le domaine de l'infrarouge thermique, un paramètre d'importance capitale est l'émissivité des matériaux mis en oeuvre.

Cette émissivité peut être mesurée de deux manières différentes: soit par mesure directe du flux émis et comparaison avec un corps noir de référence, soit par mesure de la réflectivité et application des lois de Kirchoff. Les deux approches présentent des avantages et des inconvénients selon le type d'émissivité concernée.

La méthode présentée dans cet article applique le premier principe, étant donné qu'elle s'adresse à des émissivités relativement élevées (> 0,5), directionnelles et pondérées par un détecteur donné. Afin d'améliorer la précision des mesures, le banc présente les caractéristiques suivantes:

- Diminution du flux parasite résiduel par utilisation de matériaux à faible émissivité et d'un diaphragme refroidi pour la construction d'une enceinte de confinement.

- Prise en compte du flux parasite résiduel par modélisation des échanges radiatifs à l'intérieur de l'enceinte de mesure.

- Maîtrise de l'homogénéité en température de l'échantillon et de la référence.

- Calcul de l'intervalle de confiance en fonction des incertitudes des paramètres de départ.

Cette modélisation poussée et les astuces techniques utilisées ont permis de réaliser un banc à très faible coût, du moins en ce qui concerne les acquisitions spécifiques. De nombreuses mesures comparatives ont montré que la gamme d'émissivités mesurables s'étend de 0,5 à 1 avec une incertitude absolue allant de 0,05 à 0,02 selon le type de matériau. Les meilleures performances sont obtenues avec des matériaux fortement émissifs et bons conducteurs de la chaleur.

1. INTRODUCTION.

Dans le domaine de la discrétion des objectifs militaires, la recherche du contrôle de leur *signature thermique* revêt une importance capitale. Du point de vue de l'observateur, le flux reçu est composé du flux propre émis par l'objet observé, ainsi que d'une partie du flux de l'environnement, réfléchi par l'objet dans la direction de l'observateur.

Le flux propre est essentiellement fonction de deux paramètres: la température des surfaces émissives et leur émissivité. Le flux réfléchi, quant à lui, est fonction de la réflectivité des surfaces de l'objet et du flux incident. A priori, ce dernier aspect échappe à notre contrôle. De même, l'influence de la température, bien que très importante, ne constitue un paramètre abordable qu'au niveau de la conception du matériel, certaines techniques permettant d'assurer une température de surface relativement basse.

Dans le cadre du camouflage thermique, on cherche par des moyens simples et de mise en oeuvre facile (écrans, filets ou peintures) à diminuer et/ou à modifier la signature thermique de l'objet. Le seul paramètre sur lequel on peut agir de manière directe est donc l'*émissivité* (la réflectivité est en effet liée à l'émissivité, comme nous le montrerons plus loin).

Ce travail s'inscrit dans le cadre de recherches menées par le Service Technique de la Force Terrestre de l'Armée Belge, en collaboration avec des firmes industrielles intéressées dans le secteur du camouflage multispectral. La mesure expérimentale de l'émissivité des matériaux fabriqués par ces sociétés constituait une étape fondamentale dans le processus de recherche et développement. Une méthode fut alors mise au point, en respectant les contraintes suivantes:

- un coût le plus bas possible.

- des résultats rapides et assez précis.

- des mesures tenant compte des moyens d'observation potentiels.

- la possibilité de caractériser des échantillons de dimensions et de nature très variées, et non préparés spécifiquement pour les mesures envisagées.

- utiliser au maximum les moyens existants (caméras thermiques, corps noirs, etc...).

La méthode mise en oeuvre est extrêmement simple dans son principe, et est accessible à faible coût à quiconque possède déjà une caméra thermique et un corps noir de référence. Si l'on y ajoute une relativement bonne précision dans la détermination de l'émissivité, on se rend compte de l'intérêt que peut susciter la méthode décrite ci-dessous.

2. EMISSIVITE ET REFLECTIVITE.

2.1. Emissivités: définitions.

D'une manière générale, l'émissivité d'une surface est définie comme le rapport de la luminance de cette surface à celle du corps noir à la même température. Elle est fonction de la longueur d'onde et de la direction du flux concerné, ainsi que de la température de la surface. Cependant, cette définition peut être précisée en fonction

des paramètres directionnels et spectraux. Ainsi, la grandeur de base est l'émissivité spectrale directionnelle, qui est le rapport entre la luminance spectrale d'une surface à celle du corps noir à la même température et à la même longueur d'onde:

$$\varepsilon'_\lambda(\lambda, T, D) = \frac{L_\lambda(\lambda, T, D)}{L^0_\lambda(T, D)}$$

D'autres émissivités peuvent alors en être déduites: si l'on intègre les luminances spectrales sur tout le spectre, on parlera d'émissivité *totale*. Si, d'autre part, on intègre sur une demi-sphère (les luminances deviennent des émittances encore appelées exitances), on parle d'émissivité *hémisphérique*. En outre, nous attribuerons le qualificatif de "*spectrique*" à des grandeurs pondérées par la réponse spectrale d'un détecteur donné.

2.2. Cas particuliers.

Un *corps gris* possède une émissivité spectrale indépendante de la longueur d'onde. Ses émissivités spectrales, spectriques ou totales sont donc identiques. Si les corps réels ne sont jamais parfaitement gris sur tout le spectre, ils le sont souvent sur un intervalle spectral limité. Comme nous allons le voir plus loin, les intervalles spectraux qui nous intéressent étant compris respectivement entre 3 et 5 µm et entre 8 et 12 µm, l'hypothèse de corps gris est tout à fait légitime.

Un *corps lambertien* possède une luminance indépendante de la direction. Il s'ensuit que pour un tel corps, les émissivités directionnelles et hémisphériques sont identiques. Les corps réels montrent une variation directionnelle de l'émissivité relativement limitée jusqu'à des incidences de l'ordre de 40°. Au delà, de fortes variations peuvent survenir, conduisant à une différence entre l'émissivité hémisphérique et l'émissivité directionnelle (incidence normale), bien que cette différence reste peu marquée pour les diélectriques.

Les *surfaces à la fois grises et lambertiennes* ont toutes leurs émissivités égales, et fonctions uniquement de la température. Cependant, pour les matériaux réels (surtout les diélectriques), la dépendance en température est en général très peu marquée si l'on reste dans un domaine de température raisonnable (quelques dizaines de degrés), de sorte que l'on pourra, en première approximation, estimer que les émissivités sont également indépendantes de la température.

2.3. Réflectivités.

De manière analogue aux émissivités, on peut définir plusieurs sortes de réflectivités, selon les paramètres suivants:

- géométrie des flux incidents et réfléchis: flux selon une direction déterminée ou intégré dans un hémisphère. On parle alors de réflectivités bidirectionnelle, directionnelle-hémisphérique, hémisphérique-directionnelle ou hémisphérique tout court selon les géométries respectives des flux incidents et réfléchis considérés.

- grandeur spectrale, spectrique ou totale.

Ainsi, la réflectivité la plus élémentaire est la réflectivité spectrale bidirectionnelle, rapport entre la luminance réfléchie et le flux incident. Si les luminances sont du même ordre de grandeur, cette réflectivité bidirectionnelle peut être bien plus grande que 1. Elle est donnée par:

$$\rho''_\lambda(\lambda, T, D_i, D_r) = \frac{L''_{\lambda r}(\lambda, T, D_i, D_r)}{L_{\lambda i}(\lambda, D_i) \cdot \cos\beta_i \cdot d\Omega_i}$$

avec:

$L_{\lambda i}(\lambda, D_i)$ = luminance incidente dans la direction Di..

$L''_{\lambda r}(\lambda, T, D_i, D_r)$ = part de la luminance réfléchie dans la direction Dr et due à la luminance incidente selon Di.

La géométrie est reprise dans le schéma ci-dessous.
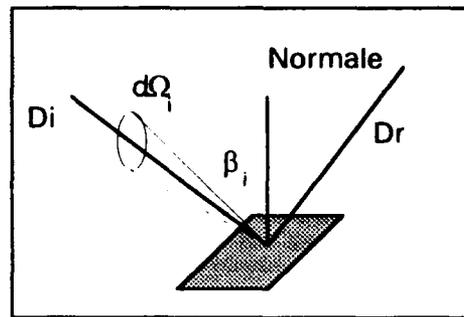
Figure 1: Géométrie de la réflectivité.

Les autres réflectivités présentant un certain intérêt sont la réflectivité directionnelle-hémisphérique et la réflectivité hémisphérique-directionnelle et la réflectivité hémisphérique.

2.4. Loi de Kirchoff.

La loi de Kirchoff exprime la relation existant entre l'absorptivité α' et l'émissivité ε' d'un corps en équilibre thermodynamique:

$$\varepsilon'_\lambda(\lambda, T, D) = \alpha'_\lambda(\lambda, T, D)$$

Cette relation n'est vraie que pour les grandeurs spectrales directionnelles. Pour pouvoir l'appliquer aux grandeurs totales, il faut qu'une des conditions suivantes soit remplie:

- soit le rayonnement incident a une distribution spectrale proportionnelle à celle du corps noir à la température de la surface.

- soit la surface est grise.

Pour pouvoir l'appliquer aux grandeurs totales, il faut qu'une des conditions suivantes soit remplie:

- *soit le rayonnement incident a une distribution angulaire uniforme.*

- soit la surface est lambertienne.

Un simple bilan énergétique sur un corps opaque (transmittivité nulle) en équilibre thermodynamique permet d'établir les relations suivantes:

$$\alpha'_\lambda(\lambda,T,D_i)+\rho'_\lambda(\lambda,T,D_i)=1$$
$$\varepsilon'_\lambda(\lambda,T,D_i)+\rho'_\lambda(\lambda,T,D_i)=1$$

Sous les conditions énoncées ci-dessus, il est possible d'étendre ces relations aux grandeurs totales ou hémisphériques. Dans le cas particulier d'un corps gris et lambertien, on peut dire, sans précautions quant au contenu spectral, que les deux relations suivantes sont vérifiées:

$$\varepsilon'(T,D_i)+\rho'(T,D_i)=1$$
$$\varepsilon(T)+\rho(T)=1$$

Cette mise au point théorique était cependant nécessaire avant de pouvoir aborder la description des méthodes de mesure d'émissivité.

3. METHODES DE MESURE DES EMISSIVITES.

Il est possible de mesurer l'émissivité des matériaux de différentes manières. On peut classer ces méthodes en deux catégories.

3.1. Mesure du flux réfléchi.

La mesure de la réflectivité spectrale directionnelle-hémisphérique et l'application de la loi de Kirchoff permettent de déterminer l'émissivité spectrale directionnelle, à partir de laquelle les autres grandeurs peuvent être déduites. De plus, la maîtrise rigoureuse de la température de la surface n'est pas requise. Cependant, les moyens mis en oeuvre sont spécifiques et relativement complexes et coûteux.

Des méthodes apparentées permettent de mesurer directement les émissivités spectriques et/ou hémisphériques, mais donnent en général des résultats moins précis et imposent de faire des hypothèses de corps gris ou lambertien.

3.2. Mesure du flux émis.

La mesure de l'émission propre du corps permet de déterminer l'émissivité par comparaison avec le flux d'un corps noir de référence. Cependant, le rayonnement perçu est composé de la superposition des flux propres et réfléchis, et ce dernier constitue une source d'erreur de mesure d'autant plus grande que l'émissivité est faible (donc réflectivité forte). Comme en général la réflectivité est en partie spéculaire et en partie diffuse, la modélisation du flux réfléchi est très difficile (il dépend également du rayonnement incident).

Cette méthode est tout de même intéressante pour la mesure de l'émissivité directionnelle (en fait, normale) spectrique, pour les raisons suivantes:

- le senseur utilisé pour la mesure est le même que celui utilisé pour l'observation, ce qui rend les résultats directement exploitables et limite les investissements, dans la mesure où le senseur est déjà acquis.

- l'écart par rapport aux hypothèses de modélisation n'est pas aussi critique que dans le cas de la mesure en réflexion.

Bien que le principe en soit simple, la réalisation pratique pose quelques problèmes, dans le plus important concerne la maîtrise des températures de surface de l'échantillon et de la référence (homogénéité, stabilisation et mesure précise des températures).

4. METHODE CHOISIE.

La méthode retenue utilise le flux émis par la surface pour la mesure de l'émissivité. Afin d'atteindre un niveau de précision suffisant, certaines précautions s'imposent.

4.1. Diminution et modélisation du flux parasite.

On cherchera à réduire au maximum le flux parasite d'une part par utilisation de matériaux à faible émissivité, et d'autre part par abaissement de certaines températures de surface. De plus, le flux parasite résiduel sera modélisé mathématiquement de manière à pouvoir déduire sa contribution au flux perçu par le senseur.

4.2. Maîtrise des températures de surface.

Les échantillons seront chauffés de telle manière que leur température de surface soit la plus élevée possible. Le rapport signal/bruit (flux propre/flux réfléchi) sera ainsi amélioré. La température sera homogène et mesurée avec précision avec un thermomètre de contact.

4.3. Détermination de l'incertitude sur la mesure.

La modélisation mathématique permettra en outre de déterminer, à partir des imprécisions sur les paramètres du dispositifs de mesure, l'imprécision maximale sur l'émissivité de l'échantillon. Parmi les paramètres jouant un rôle majeur, on peut citer les températures (du corps noir de référence, de l'échantillon, mais également des corps environnants) et les émissivités (du corps noir de référence et des corps environnants).
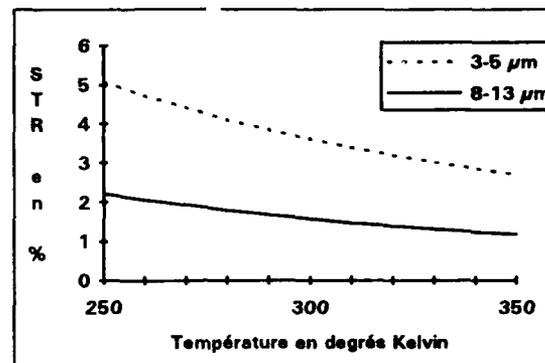

Figure 2: Sensibilité thermique relative.

La courbe ci-dessus donne la sensibilité thermique relative de la luminance émise (variation relative de luminance pour $\Delta T = 1$ degré) pour les deux fenêtres 3-5 μm et 8-1? μm. En admettant que l'imprécision sur la température est de l'ordre de 0,5 °C, on voit que l'erreur sur le flux est de l'ordre de 1%.

L'influence de l'émissivité est plus facile à déterminer. On peut montrer que la sensibilité relative à l'émissivité est indépendante de la température et est égale à l'inverse de l'émissivité:

$$SRE\,(\lambda, T, \varepsilon) = \frac{\partial L_\lambda}{\partial \varepsilon_\lambda} \cdot \frac{1}{\varepsilon_\lambda \cdot L_\lambda^0} = \frac{1}{\varepsilon_\lambda}$$

Cela signifie qu'une précision de l'ordre de 1% sur l'émissivité du corps noir de référence aura pour conséquence une erreur du même ordre sur le flux. On est donc en droit d'attendre une précision de l'ordre de quelques pourcents sur les mesures finales d'émissivité.

5. RÉALISATION.

En pratique, le banc de mesure se compose des éléments suivants, représentés dans le schéma ci-dessous:

(1) le porte-échantillon et son dispositif de chauffage.

(2) le corps noir de référence.

(3) le senseur infrarouge (caméra thermique).

(4) la structure de limitation du flux parasite (enceinte de confinement) avec diaphragme froid (4').

(5) le thermomètre.

(6) l'ordinateur servant à la mesure et au calcul.
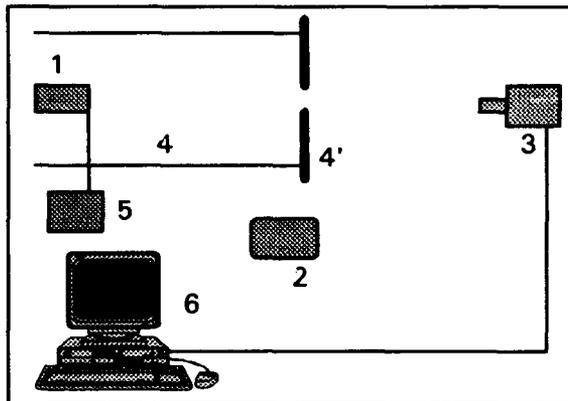
Figure 3: Dispositif de test.

5.1. Le porte échantillon.

La porte-échantillon est réalisé en acier chromé, avec possibilité de chauffage par l'arrière (conduction) ou par l'avant (flux d'air chaud), cette dernière solution nécessitant l'interposition d'une fenêtre diathermane en germanium traité antireflet, mais étant nécessaire pour les échantillons mauvais conducteurs de la chaleur. Dans les deux cas, la source de chaleur est un flux d'air chaud

thermostatisé. La température de chauffe est limitée à 100°C, afin d'éviter les dégradations de l'échantillon (peintures, etc.), mais également à cause du comportement thermique du germanium (qui s'opacifie aux hautes températures). Le schéma ci-dessous montre la réalisation.
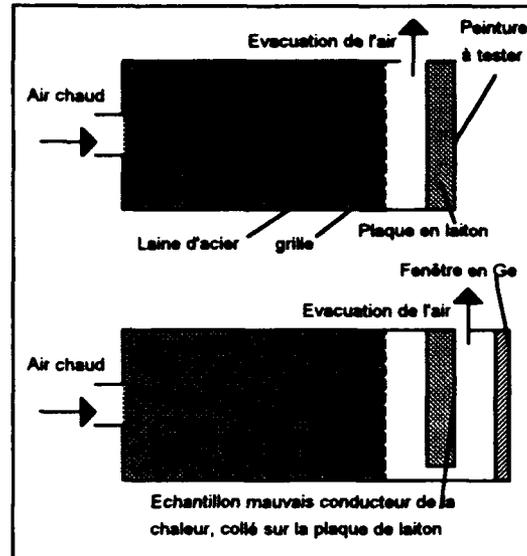
Figure 4: Le porte échantillon.

5.2. La structure de limitation du flux.

Afin de contrôler et de limiter le flux parasite, l'échantillon et le porte-échantillon seront placés dans une structure mécanique composée de parois réfléchissantes (émissivité théoriquement nulle) et d'un diaphragme noir qui est refroidi par circulation d'un fluide. Une température de surface de moins 10°C peut ainsi être atteinte, ce qui correspond, par rapport au flux parasite à 20°C, à une diminution de moitié dans la bande 8-13μm, et même des deux tiers dans la bande 3-5 μm.

5.3. Instruments de mesure.

Les caméras thermiques utilisées sont toutes à détecteur HgCdTe.

- Dans la bande 3-5 μm: AGEMA Thermovision 870 (refroidissement par effet Peltier).

- Dans la bande 8-13 μm: INFRAMETRICS 525 (refroidissement par azote liquide) et GEC TICM2 (refroidissement par cycle cryogénique). En pratique, c'est surtout avec la caméra INFRAMETRICS que les mesures ont été effectués, la facilité d'emploi et les possibilités de cette caméra la destinant plus particulièrement aux mesures de flux et de températures.

Bien que certaines caméras possèdent des références internes, les références ont été prises sur des corps noirs externes, plus précis. Deux méthodes de mesure comparative seront dès lors possibles:

- Dans la méthode isotherme, les températures de surface des deux corps sont identiques. Les valeurs de gris des caméras doivent être reliées aux flux par une

calibration. En pratique, cette méthode n'est pas utilisable avec la TICM2, dépourvue de calibration.

- Dans la méthode isoflux, la température de l'échantillon étant fixe, on règle la température du corps noir de manière à égaler les flux perçus. Cette méthode suppose que l'émissivité soit constante dans les intervalles spectraux et de température considérés. De plus, comme les températures sont différentes, il faut calculer les flux spectriques, et donc connaître le réponse spectrale du senseur utilisé. Pour pouvoir utiliser cette méthode avec la TICM2, dépourvue de fonctions de mesure et comportant en outre 8 détecteurs distincts, l'image est numérisée par un ordinateur, qui traite effectue les comparaisons entre deux champs de l'image, ligne par ligne.

La température de surface des échantillons est déterminée à l'aide d'un thermomètre de contact TECHNOTHERM 9500, donnant une précision de l'ordre de 0,2°C. La température du flux d'air de chauffe est également mesurée (sonde FLUKE 51) et une corrélation est établie entre ces deux températures.

6. LA MODELISATION.

La modélisation mathématique des échanges radiatifs à l'intérieur de l'enceinte de confinement permet de déterminer quelle est la part de flux propre et de flux parasite.

6.1. Les surfaces radiatives.

L'enceinte du banc de mesure a été décomposée en une série de surfaces homogènes, schématisées ci-dessous.
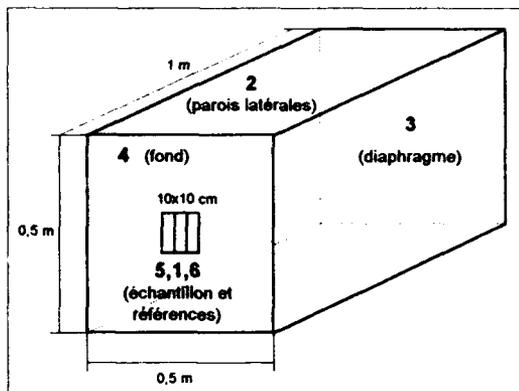

Figure 5: Modélisation des surfaces du banc.

Le porte-échantillon est soit entièrement couvert par l'échantillon (surface #1) dans le cas de la méthode isoflux (comparaison avec une référence externe), soit par l'échantillon et deux références (#5 et #6) d'émissivités connues et choisies pour encadrer celle de l'échantillon. Dans ce dernier cas, il est clair que seule la méthode isotherme est applicable.

Le fond est la surface fictive entre les parois latérales et l'échantillon. Il sera considéré comme un corps noir à température ordinaire.

Le diaphragme froid possède une bonne homogénéité en température (< 2°C) et sera considéré comme un corps noir, vu son excellente émissivité (> 0,99).

Les parois latérales, en acier chromé, possèdent une réflectivité de 0,95. Elles seront considérées, du point de vue de l'émission, comme des corps gris lambertiens d'émissivité 0,05. Leur réflectivité est, quant à elle, considérée comme parfaitement spéculaire.

Les réflexions seront prises en compte lors de la détermination des échanges radiatifs. Du fait de la géométrie du système et des hypothèses faites, on peut en déduire que le flux parasite sur l'échantillon est composé uniquement du rayonnement des parois latérales, et de celui du diaphragme froid, soit directement, soit après réflexion sur les parois latérales.

6.2. Les échanges radiatifs.

Les échanges radiatifs entre surfaces grises lambertiennes à réflexion diffuse peuvent facilement être modélisés par l'intermédiaire du concept de facteur d'angle, à la condition toutefois que chaque surface soit de température et d'émissivité homogènes, et soit de plus soumise à un rayonnement uniforme.

6.2.1. Facteur d'angle.

Le facteur d'angle entre une surface émettrice A et une surface réceptrice B est la fraction de flux quittant A et interceptée par B. Le facteur d'angle entre les deux surfaces élémentaires représentées dans le schéma ci-dessous, est par définition égal à:

$$d\Phi_{AB} = \frac{\cos\beta_A \cdot \cos\beta_B \cdot dS_B}{\pi \cdot d^2}$$
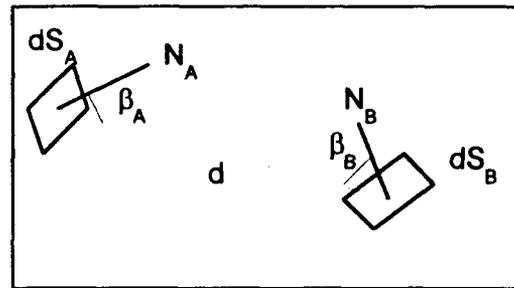

Figure 6: Géométrie des facteurs d'angle.

Pour obtenir le facteur d'angle de deux surfaces A et B de grandeur finie, il suffit d'intégrer sur les deux surfaces et de diviser par le flux issu de A. De plus, la somme des facteurs d'angle d'une surface vers toutes les surfaces d'une enceinte fermée est égale à l'unité. Il existe également une relation de réciprocité:

$$\Phi_{AB} \cdot S_A = \Phi_{BA} \cdot S_B$$

Dans le cas particulier de l'enceinte susmentionnée, composée de n surfaces (n=4 ou 6), il faudra calculer n^2 facteurs d'angle. Toutefois, comme il n'existe aucune surface concave, les Φ_{ii} sont nuls. De plus, seuls sont à

calculer des facteurs d'angle relatifs à des surfaces planes soit parallèles, soit perpenduculaires entre elles.Comme les surfaces sont rectangulaires, il est possible d'exprimer les facteurs d'angle par une intégrale quadruple d'une fonction analytique de paramètres géométriques. La relation de réciprocité permet une réduction supplémentaire du volume de calcul.

Une attention particulière doit être portée au facteur d'angle entre le diaphragme et l'échantillon. Il faut en effet tenir compte des réflexions spéculaires sur les parois latérales. On peut tenir compte de ces réflexions en remplaçant le facteur d'angle Φ_{31} par (cas de trois réflexions):

$$\Phi_{31}^{3} = \Phi_{31} + \rho_4 \cdot \Phi'_{31} + \rho_4^2 \cdot \Phi''_{31} + \rho_4^3 \cdot \Phi'''_{31}$$

Dans notre modèle, nous nous sommes limités à quatre réflexions.

6.2.2. *Echanges radiatifs.*

Soit une enceinte composée de n surfaces de température T_i et d'émissivité ε_i connues. Chaque surface émet un flux (spectrique) F_{ai} constitué du flux propre F_{pi} et du flux réfléchi F_{ri}:

$$F_{pi} = \varepsilon_i \cdot M_i^0 \cdot S_i$$

$$F_{ri} = \rho_i \cdot F_{xi} = (1 - \varepsilon_i) \cdot F_{xi}$$

Dans ces équations, M^0 représente l'émittance du corps noir à la température de la surface et F_{xi} le flux incident sur la surface i en provenance de toutes les autres surfaces. Il s'exprime en fonction des facteurs d'angle:

$$F_{xi} = \sum_{j=1}^{n} \left[\Phi_{ji} \cdot F_{aj} \right]$$

En combinant ces équations, on trouve le système de n équations à n inconnues (les F_{ai}):

$$F_{ai} = \varepsilon_i . M_i^0 \cdot S_i + \rho_i \cdot \sum_{j=1}^{n} \left[\Phi_{ji} \cdot F_{aj} \right]$$

La résolution de ce système linéaire fourni les flux apparents issus de chaque surface. Toutefois, dans le cas où une émissivité (ε_1) est inconnue, et que l'on connaît la luminance apparente L_{a1}, le système d'équations peut d'abord être résolu pour les (n-1) flux restant, et la première équation permet alors de déterminer l'émissivité par:

$$\varepsilon_1 = \frac{(1 - \Phi_{11})F_{a1} - \sum_{j=2}^{n} \left[\Phi_{j1} \cdot F_{aj} \right]}{M_1^0 \cdot S_1 - \sum_{j=1}^{n} \left[\Phi_{j1} \cdot F_{aj} \right]}$$

Il est à noter que tous les échanges radiatifs sont calculés en tenant compte de la répartition spectrale des flux, et en les intégrant après pondération avec la réponse de la caméra, puisque seules ces grandeurs nous intéressent.

7. RESULTATS.

De nombreuses mesures ont été effectuées, visant dans un premier temps à qualifier la méthode (homogénéité des températures, influence de la fenêtre en germanium, facteurs correctifs à apporter lors des mesures de température, etc.). Ensuite des mesures d'émissivités dans des conditions différentes (avec et sans refroidissement du diaphragme, avec différentes températures de l'échantillon, etc.) et des calculs de sensibilités aux erreurs basés sur des simulations ont été faits afin de prouver d'une part la validité des hypothèses, et de déterminer d'autre part le domaine d'application de la méthode.

Les simulations ont montré que les grandeurs dont la variation est la plus critique sont la température de l'échantillon ainsi que de la référence, et l'émissivité de cette dernière. Dès lors, compte tenu d'incertitudes-types de 0,5°C sur la température de l'échantillon, 0,2°C sur celle du corps noir, et de 1% sur son émissivité, nous obtenons une incertitude sur l'émissivité de 2% pour les bons émetteurs ($\varepsilon > 0,9$). Si l'on tolère une incertitude de 0,1, il est possible de descendre à des valeurs avoisinant 0,2. En pratique cependant, la validité de la méthode est limitée à des émissivités de 0,5 (erreur d'environ 0,05).

8. CONCLUSIONS.

Au vu des résultats obtenus, cette méthode permet, pour un très faible coût, d'effectuer des mesures d'émissivités sur des matériaux très variés et dans une large gamme. La précision atteinte est suffisante pour une première approche des problèmes de diminution de signature thermique.

Néanmoins, ces avantages se payent par une certaine lourdeur dans les manipulations, surtout due au refroidissement progressif du diaphragme. Une miniaturisation du banc permettrait sans doute de réduire cet inconvénient. Toutefois, pour des mesures plus précises ou répétitives, on donnera la préférence aux mesures par réflexion.

9. BIBLIOGRAPHIE.

1. **J-L Gardner, T.P Jones:** *Multi-wavelenght radiation pyrometry where reflectance is measured to estimate emissivity.* J. Phys. E: Sci. Instrum., Vol 13, 1980, pp 306-310.

2. **You-Wen Zhang, Cai-Gen Zhang, V. Klemas:** *Quantitative measurements of ambient radiation, emissivity and truth temperature of a greybody: methods and experimental results.* Applied optics, Vol 25, N° 20, 15 Oct 86, pp 3683-3688.

3. **F. E. Nicomedus:** *Directionnal reflectance and emissivity of an opaque surface.* Aplied optics, Vol 4, N° 7, July 65, pp 767-773.

4. C. Martin et P. Fauchais: *Mesure par thermographie infrarouge de l'émissivité de matériaux bons conducteurs de la chaleur. Influence de l'état de surface, de l'oxydation et de la température.* Revue Phys. Appl. 15, Septembre 80, pp 1469-1478.

5. C. Martin: *Contribution à l'utilisation de la thermographie infrarouge pour la mesure de flux, de températures et de divers paramètres.* Université de Limoges, 1978, thèse de doctorat.

6. R. Marchal: *Application des caméras infrarouges thermiques à la mesure d'émissivité.* Université de Liège, 1989, thèse de maîtrise en physique (optoélectronique).

7. A. B. De Vriendt: *La transmission de la chaleur, Vol 2: Introduction au rayonnement thermique.* Gaëtan Morin, éditeur, 1984 (deuxième édition).

8. A. Gouffé: *Transmission de la chaleur par rayonnement.* Eyrolles, Gauthier-Villars, 1968.

9. Dean Baker, Ryder: *Temperature measurement in engineering, Vol 2: Various methods.* Omega Press, 1975.

10. G. Gaussorgues: *La thermographie infrarouge.* Technique et documentation Lavoisier, 1984 (2° édition).

10. BIOGRAPHIE.

Richard Marchal *est né à Namur (Belgique) le 7 mai 1960. Il obtient un diplôme d'ingénieur civil (spécialisation télé- communications et armement-balistique) sanctionnant des études suivies à l'Ecole Royale Militaire de Bruxelles (Belgique), au sein de la 133° promotion polytechnique. En 1989, il obtient une maîtrise en physique (spécialisation optoélectronique) à l'université de Liège (Belgique).*
Il dirige depuis quatre ans les services d'optique et d'optronique de l'Arsenal du Matériel Mécanique et de l'Armement (As MECA) à Rocourt, près de Liège.

****

Discussion

Discussor's name :   D. B. Webb, UK

Comment/Question :

Did the measurement make the appropriate correction for the self emission of the germanium window you used in some experiments?

Author/Presenter's reply :

Initially not fully. Only the loss of the germanium window was taken into account. No correction was made for the radiance from the germanium window.

EXPERIMENTAL EVALUATION OF CAMOUFLAGE EFFECTIVENESS IN THE THERMAL INFRARED

Pieter A. M. Jacobs, Ph.D.

Physics and Electronics Laboratory TNO
PO BOX 96864
2509 JG The Hague
The Netherlands

1. SUMMARY

The detectability of a target in the infrared spectral region is determined by differences between the radiative signatures of the target and the local background. This implies that both, the difference in surface temperature and emissivity ΔT resp. $\Delta \varepsilon$ and the distribution of these differences over the target area and the background, are of major importance. Therefore camouflage measures have to address both issues in order to achieve maximum signature adaptation to the background.

To determine the ability of a camouflage material to follow temperature changes in the background, measurements of camouflage and background temperatures have to be performed under a variety of meteorological conditions. Measurements of representative weather- and background conditions are needed to determine those situations, where the camouflage material effectively reduces the target signature. The degree of temperature reduction depends on the required level of protection, that is for detection, recognition and identification. Statistical analyses are given for various camouflage materials in relation to a number of background elements. Camouflage effectiveness is expressed in the percentage of time for which the apparent temperature contrast between the camouflage material and a background element is 1°C, 2°C or 5°C. Analyses are performed for five consecutive weeks of measurements in summer and winter, using data which were taken during a measurement campaign at Gilze Rijen air force base in 1990.

2.0 INTRODUCTION

The success of the use of infrared (IR) equipment to locate an object in a background, is determined by system performance, atmospheric propagation and the intrinsic radiation contrast between the object and the background.

In relation to the background signature, detection radiance contrast and the distribution of these contrasts (grey levels) in the background (clutter).

To prevent targets from being detected or recognized at an early stage (at far range), the target signature can be manipulated by camouflage measures in such a way that it adapts better to the local background.

For camouflage measures to be effective in the thermal infrared, two conditions have to be fulfilled:

Temperature similarity

The camouflage measure must shift the range of apparent temperatures on the target within, or at least to be very close to, the temperature envelope of the background. Since in many occasions, targets are warmer than the background, this means that camouflage measures most of the time have to reduce target temperatures.

Spatial similarity

The shape of the camouflage measures has to be such, that the resulting temperature distribution over the target is similar to that of the local background. In practice this means that camouflage measures also have to create thermal patterns on the target.

Camouflage requirements are determined by the threat for a specific target. This threat generally can be differentiated into (aided) human perception and/or missile seeker algorithms. Furthermore, the level of camouflage depends on the desired degree of protection, that is for detection, recognition or identification. In the detection phase the target normally is not more than a white spot in the background, while in the recognition and identification phase, more target details are required. For detection, for instance, camouflage measures should emphasise the adjustment of the average target signature (temperature similarity), combined with shape distortion. For recognition, however, camouflage measures have to adjust the target signature in more detail to the background clutter (spatial similarity).

Therefore camouflage effectiveness should also be expressed in terms of a reduction of the detection and/or recognition range. These ranges are

determined by observer experiments (photo simulations) or by seeker calculations. Operational models are then used to convert these ranges to battle related parameters, like the kill probability.

The first step, however, to determine the potential of a material to be an effective camouflage measure, is to determine the dynamics of the apparent surface temperature under the most prevailing weather conditions in relation to the dynamics of the most likely backgrounds under the same weather conditions.

The temperature of the camouflage measures has to be studied in relation to the thermal behaviour of the various background elements, like grass, trees, soil, etc.. Backgrounds are difficult to model due to their very complex geometrical structure and by the fact that the mathematical description for some physical processes, which exist in a vegetation layer, are not yet accurate enough.

This also is the problem when modelling light weight (small thermal mass) and textured camouflage materials, like nets and thermal screens, which are very sensitive to small variations in some input parameters. Models can be used to evaluate the general trend of the temperature behaviour of prototype camouflage measures. Especially, models are very helpful to determine the effect of material properties on the apparent temperature and to define optimum values.

The great advantage of measurements over calculations is the fact that the desired quantity, i.e. the apparent emittance or the apparent temperature of a background element is measured directly in relation to the prevailing weather conditions. Ideally, the signatures of targets, camouflage measures and backgrounds are measured simultaneously under various conditions and over long periods of time.

3.0 DATA COLLECTION

To evaluate the thermal behaviour, camouflage measures of a number of prototype materials were installed in a measurement facility at Gilze Rijen Air force base and were measured simultaneously with a large number of background elements. The camouflage measures which were used are shown in figure 1. In spite of the fact that there were no · targets behind the camouflage measures, a direct comparison between camouflage- and background temperatures still is very useful. The materials can be described as follows:

a   A green carpet type material (Danish texture mat)
b   A black version of the same texture mat
c   Black-grey tar paper
d   A conventional camouflage net*)
e   A camouflage net, sprayed with a Low Emissivity Paint (LEP) with an emissivity of ε = 0.75**)
f   A grey coloured LEP (ε = 0.60) on concrete**)

*)   the nets were applied horizontally 0.50 cm above a grass area
**)   in both 3-5 and 8-12 μm

The CARABAS radiometer [1] autonomously and automatically measures the selected elements every preset time interval. Two external black body sources, positioned at 1m from the entrance pupil, are incorporated in the measurement cycle to check system performance continuously.

Figure 1 Camouflage materials in place at Gilze Rijen AFB

The following background elements were measured in conjunction with the camouflage materials:

1 different types of grass
2 deciduous trees at various orientations and at different ranges, 2-7m in height having different type of foliage and leaf density
3 coniferous trees, 4m height at 100m range
4 agricultural field (seasonal plant growing)
5 bare soil (ploughed rough surface)
6 concrete surface
7 Water surface (small pond, 1m depth)
8 Up- and down hill slopes (bare soil and grass covered), North and South facing.

At regular intervals, the physical condition of most background elements, was recorded, like height, emission coefficient and possible mud/snow coverage.

Figure 1 also gives an impression of the type and variety of background elements which are found at the Gilze-Rijen site (51°3'N, 5°5'E). The photograph of the measuring facility is taken in the summer of 1990. The radiometer is placed on an elevated platform (7m in height), next to measurement cabin. A synoptic weather station is placed south-east of the cabin at 50m. The camouflage materials are laid out over the grass

area due east of the platform. The grey area on the concrete, North of the cabin is the LEP.

Table 1 gives an example of the format of the data as it has been stored on disk.

4.0 DATA ANALYSES AND RESULTS

Since camouflage materials only can have a limited number of characteristics, designed, for instance, for winter/summer, desert/woodland, rural/urban conditions, its physical properties, like colour, temperature and texture, have to be based on statistics.

The measurement campaign at Gilze-Rijen produced a database of more than a full year of data of 25 background elements and camouflage materials, taken at 15 min interval.

Before a search through the database is made, the time period (season) and the desired weather conditions are defined, like wind- and/or sunlit, dry conditions and a given limit for the solar irradiance $100 < Q_{sun} < 200$ (W m^{-2}). Then, the database is searched and at every event where the selected and actual weather conditions do match, the apparent temperatures of all selected elements are stored. This way, the thermal behaviour during specific weather conditions as well as statistical analyses over longer periods of time can be studied.

TARGET CODE 02818319158	DATE 13-08-1990			SHORT DESCRIPTION GRASS			ELEVATION HORIZONTAL		AZIMUTH 315°	
TIME	T_3 °C	T_8 °C	T_a °C	RH %	Q_g W m^{-2}	Q_p W m^{-2}	v m s^{-1}	Φ_v (°)	PR mm	p hPa
00:30	18.7	19.5	20.6	83.3	0.0	392.9	2.2	27.7	0.0	1011.5
00:45	18.6	19.0	20.3	86.7	0.0	398.5	1.3	32.4	0.0	1011.3
01:00	18.0	18.7	19.9	89.2	0.0	391.3	1.5	28.6	0.0	1011.2
01:15	18.1	19.0	19.8	91.3	0.0	393.1	1.6	16.5	0.0	1011.0
01:30	17.6	18.3	19.8	92.1	0.0	396.2	1.5	8.9	0.0	1011.0
01:45	17.4	18.2	19.8	92.5	0.0	389.0	1.4	43.8	0.0	1011.1
02:00	16.8	17.3	19.1	93.1	0.0	389.7	1.3	20.3	0.0	1010.6

T_3, T_8 : Apparent temperature in 3-5 resp. 8-12mm

T_a : Air temperature

RH   : Relative humidity

Q_g : Global irradiance

Q_p : Longwave sky irradiance

v   : Wind speed

Φ_v : Wind direction

PR : Precipitation

p   : Atmospheric pressure

Table 1   Database example of collected background data
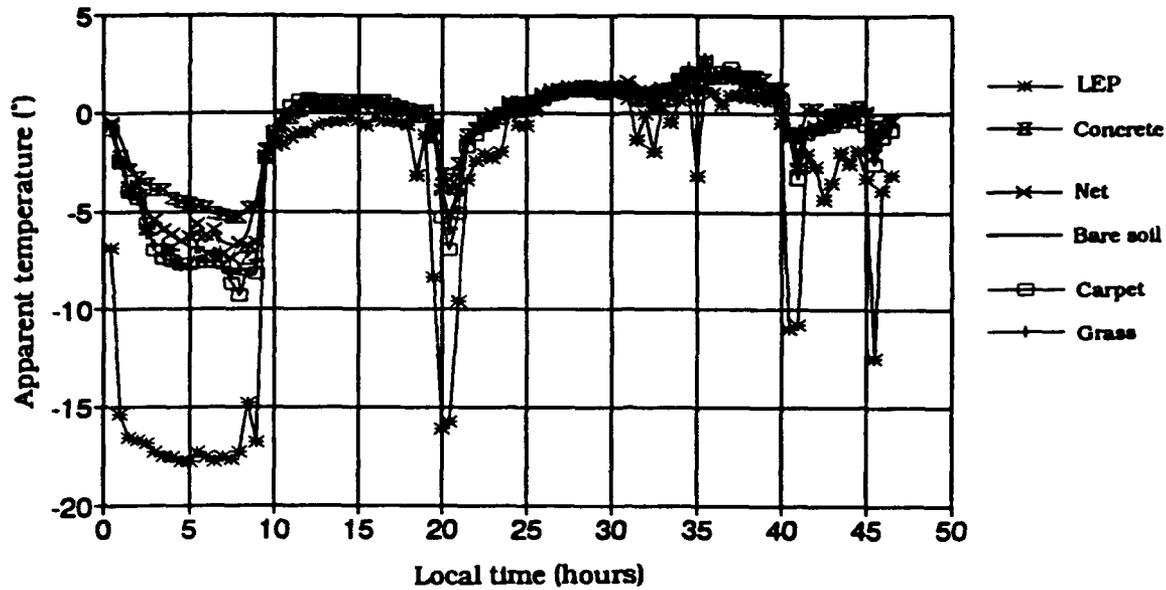
Figure 2 Temperature of camouflage materials and background elements on 16 and 17 December 1990
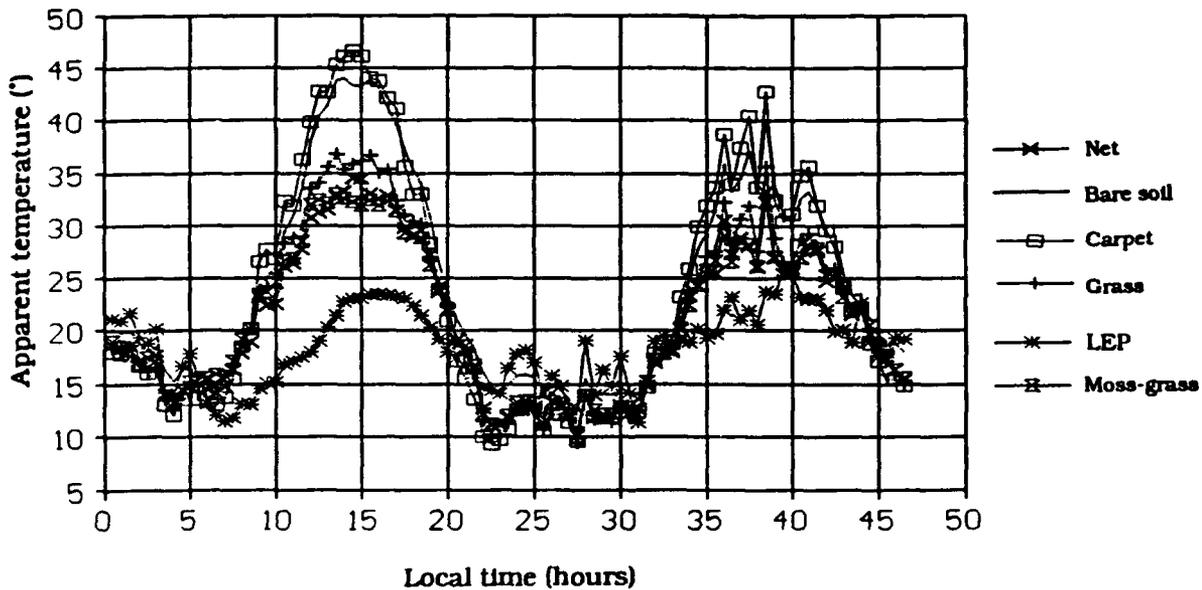
Figure 3 Temperature of camouflage materials and background elements on 13 and 14 August 1990

4.1 Temporal behaviour

The temporal behaviour of background and camouflage temperatures is needed to study camouflage performane under specific weather conditions. Figure 2 shows the measured apparent temperatures (in 8-12μm) of various background elements in relation to some camouflage materials on two cold days in December 1990. Figure 3 shows the temperature variation of similar background elements in relation to the same camouflage materials on two hot days in August.

The effect of the low emission coefficient of the camouflage net is spectacular (very negative apparent temperature) during the clear night of 16 December. Generally, it can be concluded that the temperature differences during wintery conditions are quite small. This is due to the fact that

vegetation behaves like 'dead' material in winter time and therefore is not different than other materials with constant physical properties, like camouflage materials.

During sunny conditions, the temperature differences may become very large, for instance, the difference between the net and the carpet exceeds 25°C!, at 15:00 hours on August 13.

4.2 Temperature statistics

For statistical analyses, two time periods are used, being 19 July - 28 August 1990 (period A) and 10 November - 19 December 1990 (period B). These periods should be representative for a summer season and a fall/winter season in NW Europe.

Table 2 and 3 show the average apparent temperature and RMS variance of some background elements for the summer and winter period. The RMS variance σ is calculated as:

$$\sigma = \left[\frac{1}{N} \sum_{i=1}^{N} (T_i - T_m)^2 \right]^{0.5}$$

T_i : Momentary temperature (°C)
T_m : Average temperature (°C)
N : Total number of measurements

The tables show that in winter time the temperatures of the background elements are quite close. The trees are colder than the air temperature because, since leaves are missing,

part of the measurement area on the trees is filled with sky background. During day time in summer the temperature spreading is more pronounced and materials with a large thermal mass, like concrete, remain warm during night time.

Statistical analyses of the temperature differences between background elements them selfs and between camouflage materials and background elements, are carried out for each period. As was to be expected, the temperature differences in the background and between the camouflage materials are very moderate in winter time.

The situation during the summer period is quite different from that in winter time. Due to the temperature controlling mechanism of the vegetation (by evaporation and condensation), the contrast with non-vegetated surfaces can become quite big. Figure 4 and figure 5 show a comparison of the temperature difference distributions for the summer and winter period during day and night time. The distributions are very wide (20-30°C), showing a variance up to 9°C. The figures show the long 'warm tail' in the distributions for the texture mat during day time in summer, indicating that it gets much too hot. The LEP net, which is placed horizontally, is much cooler than the (vertical) tree line during night time.

Whether a given (intrinsic) temperature contrast can be detected, depends on the performance of the IR sensor and on the atmospheric propagation in the optical path.

	DAY TIME				NIGHT TIME			
	3 - 5μm		8 - 12μm		3 - 5μm		8 - 12μm	
Element	T_m	σ	T_m	σ	T_m	σ	T_m	σ
Grass	25.1	9.0	25.8	9.1	12.3	4.1	13.2	4.4
Concrete	28.5	7.4	27.5	7.1	19.9	3.7	19.2	3.9
Soil	26.7	9.7	26.8	9.7	12.0	4.4	13.0	5.2
Trees (S)	24.0	5.1	24.2	5.1	14.1	3.8	14.9	4.2
Trees (NE)	20.1	5.5	20.2	5.5	14.1	3.9	14.8	4.2
	T_m	σ			T_m	σ		
air temperature	20.9	5.5			14.0	3.7		

T_m and σ in °C

Table 2   Average background temperatures during the summer period

9-6

	DAY TIME				NIGHT TIME			
	3 - 5μm		8 - 12μm		3 - 5μm		8 - 12μm	
Element	T_m	σ	T_m	σ	T_m	σ	T_m	σ
Grass	5.3	4.1	5.7	4.1	2.3	4.8	2.9	4.8
Concrete	5.0	3.9	4.8	3.9	2.8	4.1	2.9	4.1
Soil	5.1	4.1	5.4	4.0	2.4	4.7	2.9	4.8
Trees (S)	2.3	2.4	2.5	2.2	0.7	2.9	1.0	2.7
Trees (NE)	2.0	2.4	2.4	2.2	0.3	3.1	0.9	2.9
	T_m	σ			T_m	σ		
air temperature	4.8	4.0			3.0	4.4		

T_m and σ in °C

Table 3   Average background temperatures during the winter period

So, a temperature reduction by the camouflage material as such, does not mean so much and its final impact on the detection or recognition process, depends on the momentary situation.

In terms of a **temperature contrast** ΔT, camouflage effectiveness γ can be defined as the percentage of time in which the contrast between the camouflage and a background element is smaller than a temperature X:

$$\gamma = \frac{\{ \Delta T | |\Delta T| \le X \, (°C) \}}{N} \times 100\%$$

N is the total number of contributing sample points

X is determined by the circumstances. For a target at close range, already a small value of X will lead to detection, while for greater ranges the temperature contrast needs to be larger, because of the atmospheric attenuation. Calculations for γ have been performed for values for X of 1°C, 2°C and 5°C, during day (sunrise-sunset) and night time (sunset-sunrise) for the summer and winter period. Calculations have been carried out using apparent temperatures in both spectral regions.
To get an impression of the contrast values, which exist in a natural background scene, contrast values between a few background elements have been included in the calculations. Table 4 and table 5 show the results, in which also the mean contrast ΔT_m and the variance σ have been

incorporated.
The tables again show that during winter time the contrast values are very moderate. The contrast between the LEP and the background elements shows that the LEP has a modest negative effect (i.e. too cold) on the apparent temperature, in both spectral regions. During day time in summer, there are some remarkable differences in temperature behaviour between the two spectral bands. In the 8-12μm region the LEP gives a much lower temperature contrast with the background elements than in the 3-5μm band. This is explained by the fact that the solar reflectance in the 3-5μm region is increased by the enhanced reflectivity of the LEP (ρ = 1 - ε). Furthermore, the reflectance of 'cold' sky radiance is enhanced, because the atmospheric trans-mission coefficient in the 8-12μm is greater than in the 3-5μm region. At night time, the contrast between the concrete and the LEP seems to small (i.e. the LEP temperature is too high), but this is caused by the high surface temperature of the concrete, which largely compensates the effect of the LEP.
Expressed in a percentage of time, the contrasts in winter time are within 2°C for almost 90% of time, that is, 31 days out of 35! (except for the LEP). In summer time the camouflage effectiveness, for both day and night, very much depends on the type of camouflage and the type of background element to which it is compared to. For instance, if concrete has to look like grass, the main camouflage effort will be to match the time response of the concrete with that of the grass.
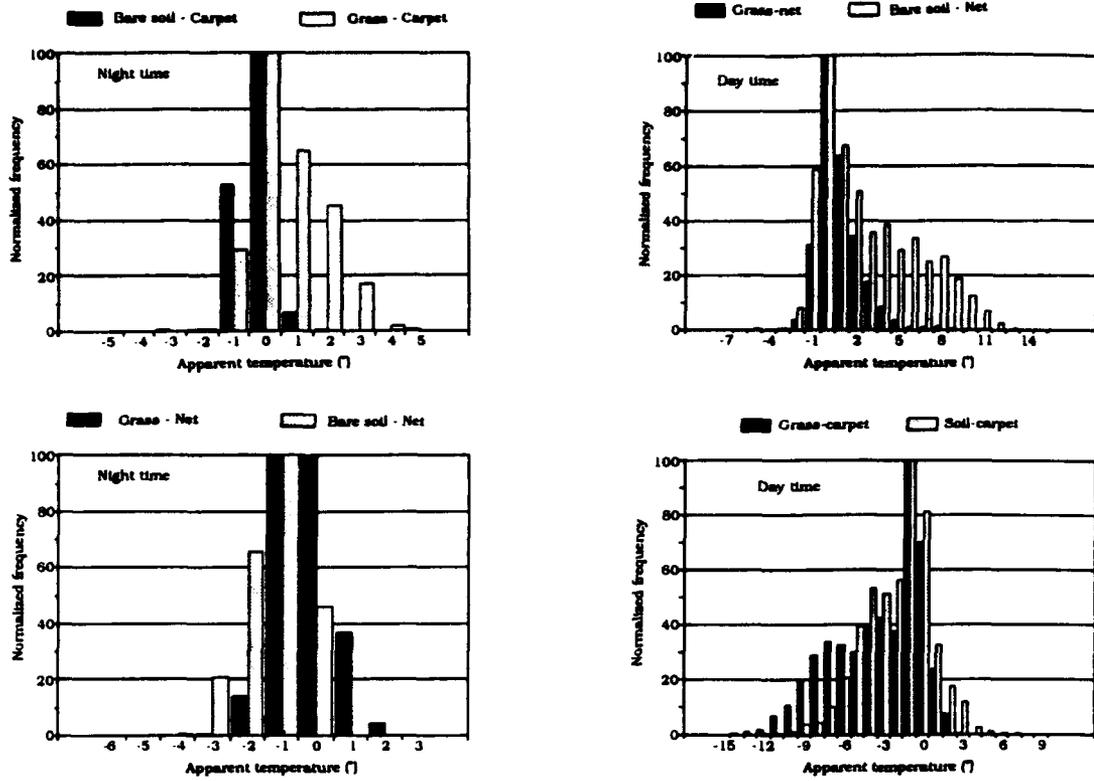
**Figure 4** Temperature difference distributions during day and night time in the summer
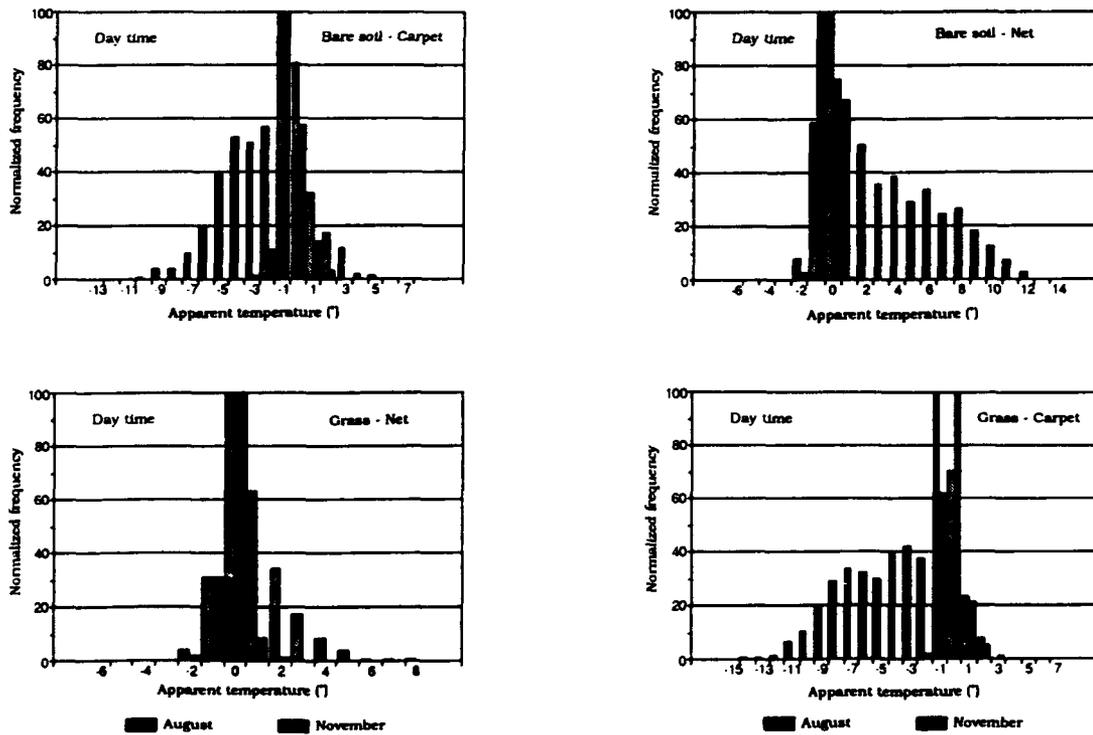
Figure 5 Comparison of temperature difference distributions in summer and winter time

3 - 5 μm										
	DAY TIME					NIGHT TIME				
	Statistics		γ (%)			Statistics		γ (%)		
Contrast	ΔT_m	σ	1°C	2°C	5°C	ΔT_m	σ	1°C	2°C	5°C
Grass-Soil	-1.0	1.8	44	69	98	-0.1	1.9	61	88	96
Grass-Concrete	-2.7	3.1	17	33	77	-7.5	3.0	2	5	23
Trees-Grass*	-4.4	3.9	14	26	57	-2.2	2.1	14	35	94
Grass-Carpet	-1.6	2.4	34	56	89	+1.1	2.2	56	81	94
Grass-LEP	+1.0	3.0	24	45	89	-3.1	2.5	15	28	78
Grass-Net	+1.7	2.5	35	58	89	+0.0	1.9	69	92	96
Soil-Carpet	-0.7	2.4	36	59	96	+1.3	1.5	35	69	99
Soil-Net	+3.1	2.8	27	47	75	+0.3	1.3	66	93	99
Soil-LEP	+1.9	3.1	24	42	82	-3.2	2.2	12	29	75
Concrete-LEP	+3.8	2.2	10	24	69	+4.6	1.4	4	7	56
Trees-Net	-1.7	2.3	28	51	92	+2.4	1.6	17	41	96
8 - 12 μm										
Contrast	ΔT_m	σ	1°C	2°C	5°C	ΔT_m	σ	1°C	2°C	5°C
Grass-Soil	-0.3	1.7	54	78	99	-0.0	1.7	79	94	96
Grass-Concrete	-1.0	3.6	21	39	82	-5.9	3.3	12	16	37
Trees-Grass*	-5.0	4.1	14	26	53	-2.0	1.9	28	45	97
Grass-Carpet	-1.6	2.6	36	57	88	+1.1	2.0	47	83	96
Grass-LEP	+7.9	6.2	12	18	34	+0.6	3.1	34	57	88
Grass-Net	+2.8	3.0	36	51	77	+0.1	1.5	90	95	97
Soil-Carpet	-1.3	2.6	37	56	92	+1.3	2.2	47	69	97
Soil-Net	+3.6	3.5	29	43	67	+0.3	1.2	76	96	99
Soil-LEP	+8.6	6.5	11	17	33	+0.6	2.3	49	67	94
Concrete-LEP	+9.2	4.1	5	7	17	+6.7	4.0	15	20	32
Trees-Net	-1.0	1.9	42	65	98	+2.1	1.9	30	44	96

* South facing tree line, sunlit condition

Table 4   Camouflage effectiveness in summer time, expressed as a percentage of time γ

3 - 5 μm										
	DAY TIME					NIGHT TIME				
	Statistics		γ (%)			Statistics		γ (%)		
Contrast	ΔT_m	σ	1°C	2°C	5°C	ΔT_m	σ	1°C	2°C	5°C
Grass-Soil	+0.1	1.1	63	92	100	-0.1	1.3	57	88	100
Grass-Concrete	+0.3	1.3	59	88	100	-0.5	1.7	48	78	99
Trees-Grass[*]	+0.4	1.2	59	91	100	+1.0	1.6	43	64	100
Grass-Carpet	+0.3	1.1	64	91	100	+0.7	1.4	51	82	99
Grass-LEP	+1.4	1.8	39	70	95	+0.5	2.0	43	72	97
Grass-Net	+0.1	1.1	66	92	100	-0.1	0.4	58	87	100
Soil-Carpet	+0.2	1.2	61	91	100	+0.8	1.4	52	81	99
Soil-Net	-0.1	1.1	65	93	100	-0.0	1.3	60	89	100
Soil-LEP	+1.3	1.9	43	72	95	+0.6	1.8	47	75	98
Concrete-LEP	+1.1	1.8	46	75	96	+1.0	1.8	46	73	96
Trees-Net	+0.2	1.3	58	88	100	+1.0	1.5	46	79	100
8 - 12 μm										
Contrast	ΔT_m	σ	1°C	2°C	5°C	ΔT_m	σ	1°C	2°C	5°C
Grass-Soil	+0.3	0.6	92	99	100	-0.0	0.6	96	99	100
Grass-Concrete	+0.9	1.1	62	86	100	-0.0	1.1	68	94	100
Trees-Grass[*]	+0.2	0.4	97	99	100	+0.6	0.7	82	89	100
Grass-Carpet	+0.3	0.8	88	98	100	+0.5	0.7	87	98	100
Grass-LEP	+2.9	4.4	39	65	85	+2.1	4.0	48	74	85
Grass-Net	+0.2	0.6	94	99	100	-0.1	0.6	95	99	100
Soil-Carpet	-0.0	0.8	90	99	100	+0.4	1.4	85	98	100
Soil-Net	-0.1	0.3	99	100	100	+0.1	0.3	100	100	100
Soil-LEP	+2.6	4.3	49	72	86	+2.1	3.9	54	76	85
Concrete-LEP	+2.1	3.8	65	79	87	+2.1	3.9	67	79	85
Trees-Net	+0.3	0.4	91	100	100	+0.7	0.7	82	93	100

[*] South facing tree line, sunlit condition

Table 5   Camouflage effectiveness in winter time, expressed in a percentage of time γ

5.0 CONCLUSIONS

The experimental quantification of the behaviour of the apparent temperature of background elements and of potential camouflage measures looks promising. Although the efforts to acquire the necessary data are quite substantial, the output of the analyses directly show the potential of a camouflage measure to adapt to the background conditions.

Temporal information can be used to study specific threat conditions, while statistical analyses give the general behaviour during a typical weather period (season).

The camouflage effectiveness percentages for the different contrast values, can directly be used to analyse sensor system performance against camouflaged targets.

To include the thermal interaction between the target and the camouflage measure, targets should be part of a follow up exercise. Especially the treatment of hot spots, like exhaust grids and power generators are of interest. If real targets are not available for longer periods, black body radiators should be used instead.

Preferably, a total camouflage concept is applied in order to determine over all camouflage efficiency, for instance by photosimulation techniques or by using seeker algorithms. This implies that next to spot radiometer data, high quality (thermal and geometrical resolution) imagery is required over statistically significant periods of time.

The study provides a strong argument to investigate the feasibility of using 'adaptive' camouflage materials or systems. A possible way is the variation of a physical property of a material in relation to the variation of the environmental conditions. For instance, coatings which change colour as a function of temperature (thermo-chromes) or electrical current (electro-chromes). Such a new study would largely have to deal with material research.

6.0 REFERENCES

1. Jacobs, P.A.M., "CARABAS, A programmable scanning radiometer for the characterization of backgrounds in the thermal infrared.", Int. J. of Remote Sensing, 13, 1992, pp 2865-2871.

Author/Presenter's reply :

I did not include spatial analysis of the data. I would expect a differenct in texture (clutter) in case the camouflage net is transparent, showing parts of the hot target. But again I did not investigate this during this project.

Discussor's name :   E. Schweicher, BE

Comment/Question :

Could you compare the bands 3-5μm and 8-12μm from the viewpoint of the "decamouflaging effect". What about the solar influence in the 3-5μm band?

Author/Presenter's reply :

There is a contribution of solar reflection in the 3-5μm band which might be of major importance during sunshine.

Discussor's name :   D. B. Webb, UK

Comment/Question :

In assessing camouflage it is useful to separate reflection and emission effects. Were the materials ever draped over compound curved surfaces?

Author/Presenter's reply :

No, materials were laid out over a grass area in a flat, horizontal way; there were also no real targets behind it.
In a following up measurement campaign (1993 --> ...) we will include more realistic use of camouflage measures including vertical placement with real targets or heated plates behind them.

NATO SOCMET TRIALS

C. M. Jenden[†]
Ministry of Defence, Procurement Executive
Chemical & Biological Defence and Pyrotechnics
St Christopher House
Southwark Street
London SE1 0TD
United Kingdom

1. SUMMARY

During 1993, Canada, France, Germany and the United Kingdom will be participating in the Smoke and Obscurants Countermeasures Materials Evaluation Tests (SOCMET). The Tests will be carried out under the auspices of the NATO Army Armaments Group, AC/225, Panel VI, Sub-Panel 7 whose interests include multi-spectral smoke screening systems. The Tests will comprise two sets of trials; one under cold climate conditions in Quebec, Canada during February/March 1993 and the other in temperate conditions in Bourges, France during September 1993. This paper provides an insight into the management and aims of SOCMET.

The evaluations will be seeking to identify candidate materials which create effective obscurant screens in the visible, infrared and millimetric bands of the electromagnetic spectrum. These materials will be disseminated through a range of equipment from vehicle deployment to large area dispersal. A key element of the trials will be the evaluation of field test instrumentation which may eventually lead to the development of standardised evaluation techniques.

Following the trials, a scientific workshop will be held to review the results. A final report will be presented to NATO which will form the basis of future collaborative developments on multi-spectral screening systems leading towards standard NATO documentation on smoke and obscurants systems.

2. KEYWORDS
SOCMET, Smoke, Obscurant, Multi-Spectral, Pyrotechnics, Munitions.

3. INTRODUCTION
The use of smokes and obscurants on the battlefield is well known to be a cost effective countermeasure to many of the most advanced weapon systems. To deny enemy forces these weapons and surveillance and target acquisition devices, smoke materials and delivery systems must be identified which are effective in the visual, infrared and millimetric wavebands. This paper gives a brief overview of the aims and management of the NATO Smoke and Obscurants Countermeasures Materials Evaluation Tests (SOCMET) which are instrumental in the pursuit of this objective.

The Tests will be attended by representatives of the Defence Departments and Pyrotechnics Industries from Canada, France, Germany and the United Kingdom. They have been established under the direction of the NATO Army Armaments Group Sub-Panel which is concerned with multi-spectral smoke screening systems. The Tests will consist of two distinct trials, one in temperate conditions in Bourges, France and the other in a cold climate at Quebec, Canada.

4. SOCMET AND NATO
Six of the NATO nations, Canada, France, Germany, the Netherlands, the United Kingdom and the United States, have been involved in the planning of SOCMET over the last two years. It was spawned from Sub-Panel 6 of the NATO Army Armaments Group Panel VI of Allied Committee (AC)225. The Sub-Panel was specifically concerned with multi-spectral screening smoke and smoke munitions. However, as part of the recent review of NATO NAAG committees, Sub-Panels 6 and 7 merged to form a new Sub-Panel 7 covering countersurveillance

[†] The Author is Chairman of the NATO SOCMET Steering Group

work and, from November 1992, became the NATO focus for SOCMET.

Though SOCMET has been planned within the structure of NATO, the trials will be a collaborative project covered under a Memorandum of Understanding, MOU, between the Governments concerned. The MOU was signed in the summer of 1992 by four nations, Canada, France, Germany and United Kingdom. It is possible that other nations may sign later.

5. SOCMET TIMETABLE

The first Test, the Winter Test, will take place at the Defence Research Establishment Valcartier, DREV, near Quebec Canada during February/March 1993. It will be followed by the Summer Test in temperate conditions at Etablissement Technique de Bourges, ETBS, at Bourges in central France in September 1993. There will be a Workshop in June 1993 to discuss preliminary results of the first Test and in June 1994 a Symposium will be held to discuss the results and conclusions of the trials. A final report will be provided to NATO in November 1994.

It is anticipated that SOCMET will become the basis for cooperative developments in the future on multi-spectral screening systems and help towards getting agreed NATO standards on smoke and obscurant systems.

6. OBJECTIVES OF SOCMET

6.1 Material Identification

Each nation taking part in SOCMET has development materials which aim to obscure in the visual (Vis), infrared (IR) and millimetre wavebands (MMW) and combinations of these bands. The trials will provide an opportunity to evaluate these materials in field test conditions.

6.2 Evaluate Instrumentation

The second objective highlights the need for standard evaluation methodologies using specific field test instrumentation. The aim is to agree methodologies so that a STANAG - a standard NATO agreement - can be drafted which will establish common smoke and obscurant assessment techniques. By developing common techniques that are understood by NATO nations, it will be easier in the future to agree collaborative procurement programmes.

6.3 Simulated Smoke Screens

To simulate, with generators or statically fired munitions, smoke screens that might be produced with candidate materials offering the potential for effective countermeasures to weapon systems employing electro-magnetic wave sensors operating in the visual, infrared and millimetre wave bands.

6.4 Field Test Evaluation

To provide an opportunity for material evaluators and developers to examine material performance for defeating electro-magnetic wave weapon system sensors under realistic field test conditions and at field level concentrations.

6.5 Data Collection

Obscuration and meteorological data will be collected for use in computer models to evaluate the potential effectiveness of materials in full-scale munition delivery systems. No one model is presently used by all NATO nations and consequently each participant will analyze the data they collect from the trials using their own instrumentation and exchange raw or analyzed data to improve their own models.

7. SITES, MATERIALS, TARGETS AND INSTRUMENTATION

7.1 Test Sites

A rectangular area of approximately 1.0 x 1.5 km is required over which to release and observe the smoke screen materials. Health and safety requirements suggest that additional corridors of 0.3 x 0.4 km on either side of the smoke release area be clear for smoke dispersal. Flat or gently rolling terrain is desirable to permit clear lines of sight to targets in the smoke screening area. Ideally test site orientation should be such that the primary line of sight aligns north-south and the most probable wind directions east or west.

The test sites at Valcartier and Bourges both exceed these minimum requirements.

7.2 Candidate Materials

The four nations taking part in SOCMET are fielding a variety of different materials for evaluation. They will be disseminated by AFV grenades, generators and large calibre systems. These are summarised in Table I. Though one of the dissemination methods is labelled artillery munitions, it should be read as "large calibre systems" that will be statically fired simulations of mortars and artillery smoke rounds.

The relative percentages of AFV grenades, generators and large calibre systems provides a rough reflection of the equipment requirements of the participating nations.

Table I
SOCMET Candidate Materials

AFV Grenades	Vis/IR	7 Materials
	MMW	3 Materials
Generators	Vis/IR	6 Materials
	MMW	3 Materials
Artillery	Vis/IR	3 Materials
	MMW	3 Materials

7.3 Targets

Four to six military targets (tanks and armoured personnel carriers) will be placed in a designated target area behind the smoke release zone. These vehicles may or may not be idled according to the requirements of the trial. Other targets, such as corner reflectors, decoys, camouflage materials and flat panels will also be deployed throughout the test grid.

7.4 Instrumentation

Table II summarises the generic types of instrumentation that will be used during SOCMET to evaluate smoke performance.

Table II
SOCMET Instrumentation

Multi-Spectral Transmissometry
Laser Cloud Mapper
MFOV LIDAR
Vis/IR Radiometric Imagery
Millimetre Wave Radiometry
IR Radiometric Spectra
Documentary Video and Photography
Laser Range Finders
Meteorological Station

8. ASSESSMENT CRITERIA

To assess the performance of the candidate materials, nations will employ many of the criteria agreed in an Outline NATO Staff Target for multi-spectral screening smokes[1] and a NATO Staff Target for multi-spectral smoke generator systems[2]. These set out smoke assessment criteria in terms of screen dimensions and duration, its effectiveness in a particular spectral waveband, screen homogeneity and sensitivity to the environment and, also, environmental and toxicity standards. In addition to this scientific assessment of the smoke materials, an assessment will be made from a military viewpoint. The latter will consider the effective obscuration of the smoke and its ability to affect target recognition.

9. TRIAL MANAGEMENT

9.1 SOCMET Steering Group (SG)

The SOCMET SG is responsible for the implementation and management of the MOU and has a representative from each of the participating nations. Its basic function is to formulate policy to achieve this in the most cost effective manner. The work of the SG may be broken down into a number of constituent tasks.

- The SG is under remit to report progress and results to its NATO parent body (NAAG Panel VI, SP.7). Once SOCMET is completed, an executive summary will become available to NATO nations, though details of the data collected and the final report will only be available to participants.

- The SG will not become involved in the detail of running the Tests which will be the responsibility of the Technical Sub-Group for each Test. It will, however, authorise the Summer and Winter Test Plans and provide Security Guidelines for the Tests and the protection of data.

- The SG also has budgetary responsibilities. The overall trial cost, which nations are funding equally, is defined in the MOU but the SG is responsible for agreeing the budget for each Test and approval of payment plans.

9.2 Technical Sub-Groups (TSGs)

Technical Sub-Groups for each Test have been formed by the SG with representatives from all the participating nations. They are responsible for the detailed organisation of the tests including site planning and preparation and report progress to SOCMET SG through their Chairmen. The Chairmen are also the Test Directors for their respective Tests and are nominated by the host nation.

10. CONCLUSIONS

At the time of writing this paper (January 1993) preparations for the Winter Test are at an advanced stage. The Test Plan has been agreed

and the site at Valcartier prepared before the winter snows set in. Each nation's munitions have been manufactured and, together with the instrumentation, have been dispatched to the test site. We now eagerly await set-up week when the trailers and portable laboratory accommodation will be set in place ready for the first firings of the smoke munitions and generators in March.

It is anticipated that the successful operation of SOCMET will provide a forum for future collaborative development of smoke munitions and lead towards the introduction of NATO standards for smokes and obscurants.

11. ACKNOWLEDGEMENTS
The Author would like to acknowledge the valuable contribution of the following members of the SOCMET SG and the TSGs, both past and present, for all their hard work in making SOCMET a reality and to the current SG for their assistance in the preparation of this paper:-

Canadian Delegation: Mr G Couture
Mr G Roy
Mr P Roy

French Delegation: M. J Leblanc
M. J-L Lahaye
Chef de Bat. P Didier
M. G Menard
M. C Hamel
M. C Patron
M. C Cransac
M. F Danielian

German Delegation: Dr W Scheunemann
Dr W Wassmuth
Mr H Schroers

UK Delegation: Maj S C Freeland
Mr P J Strudley
Dr H Edwards
Mrs A Marshall

The SOCMET SG would also like to express their gratitude to the Netherlands Delegation (Messrs J Rogge and A de Jong) and the United States Delegation (Messrs W Klimek and S Gerard) who were instrumental in the initial concept and planning of SOCMET.

12. REFERENCES
1. NATO Document Reference AC/225 (Panel VI/SP.6) D/2 dated 12 April 1989
2. NATO Document Reference AC/225 (Panel VI/SP.6) D/15 dated 8 September 1992

GLOBAL APPROACH TOWARDS THE EVALUATION OF THERMAL INFRARED COUNTERMEASURES

by Patrick Verlinde and Philippe Wilms

Technical Department of the Army (TDLM)
Center for Technological Applications (CT)
Applied Electronics Division (TE)
Martelarenstraat 181, B1801 Peutie, Belgium

ABSTRACT
This paper proposes a procedure for the numerical evaluation of the efficiency of countermeasures in the thermal infrared. This procedure consists of three phases. In the first phase, the characteristics of different thermal camouflage materials are tested on a lab-scale. These tests comprise measurements of the attenuation of the incident infrared energy and/or of the thermal emissivity factor. With respect to the attenuation measurement, a calibrated infrared sensor is used, to determine the radiation patterns of an object. The comparison of these patterns before and after the application of a camouflage system, gives an absolute measure of its attenuation. The result of this measurement is important since the attenuation is closely related to the contrast between the camouflaged object and its background and thus to the probability of detection. Contrast however, is not the only important feature for the detection of an object in a thermal image. That is why in a second phase the countermeasures under evaluation are tested in a real environment. During this phase, a numerical value is given to the efficiency of the considered camouflage in the thermal infrared, using features selected from those which are known to be important for human vision. These include besides contrast other features such as correlation and texture. The third and final phase aims at a verification and a validation of the test results. Indeed, it is of a crucial importance to find a link between the performances obtained in the field and the characteristics measured on a lab-scale. It is also necessary to verify that a good correlation exists between the efficiency as determined by human observers and the result of this numerical evaluation procedure. This will be done using a database of thermal images taken with a GEC Avionics TICM II (8 to 12 μm). Those images are then presented as well to human observers as to the machine in a project called "Psychotest".

1. FOREWORD
One of the primary missions of the Technical Department of the Belgian Army is to assist the project officers of the General Headquarters of the Army during the procurement of new equipment or the modification of existing ones. This assistance mainly consists in a first phase in the translation of operational requirements into technical specifications, in a second phase in the evaluation of the equipment proposed by the different tenders and finally in a third phase in the validation testing of the pre-series production of the equipment, chosen after the evaluation phase. To be able to carry out these tasks in the specific domain of countermeasure technology, TDLM/CT-TE had to acquire knowledge and develop evaluation methods in those parts of the electromagnetic spectrum, which form the most important threat and for which little knowledge, in the *open* literature, was available yet.

The relative threat of different parts of the electromagnetic spectrum is depicted in figure 1 as a function of the evolution of military observation systems. From this figure can be deduced that for the years to come, the two most important parts, next to the visual region and the Near Infrared (or NIR, which includes Image Intensifiers and Low Light Level Television), are the microwave region and the Thermal Infrared (or TIR).

The importance of the use of countermeasures in the visual and NIR parts of the spectrum has been known for a very long time now. This is one of the main reasons why industry nowadays understands (more or less) the phenomena involved and controls the technology sufficiently to produce some countermeasures which are relatively efficient for these spectral regions. On the other hand, for the microwave and the TIR region, this same consideration is certainly not valid, since in this part of the spectrum the technological

developments have only been made very recently. Taking these facts into account, TDLM/CT decided to start up research in the microwave region and to extend it afterwards to the TIR.

This paper however only deals with the thermal infrared part of the spectrum.
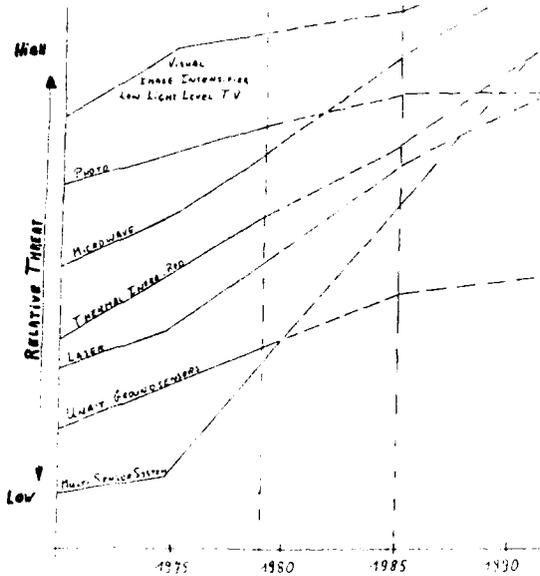
Figure 1: Relative threat as a function of the evolution of military observation systems [8]

2. INTRODUCTION
There are a lot of observation systems using infrared energy which can vary significantly, for example in wavelength range, human/automatic/semi-automatic manipulation, spatial and thermal resolution and so on. Camouflages will be more or less efficient depending on the observing system. They can even be designed to perform specifically against one of those "threats". The one taken into account for this work was *the human observer*. At this moment most of the evaluations of countermeasures are done using human observers. Their efficiency in a specific spectral region and against a specific observation system (spectral response, spatial resolution,...) can be determined through the statistical study of a very large number of observations. The main drawback of this method is the need for a great amount of time, personnel and equipment, which in the case of the TIR happens to be very demanding and costly. To overcome these drawbacks, this section presents a numerical method to evaluate the efficiency of camouflage systems in the thermal infrared.

The proposed evaluation procedure consists of three phases. In the first phase, the

characteristics of different materials are tested on a lab-scale. These tests comprise measurements of the attenuation of the incident infrared energy and/or of the thermal emissivity factor, in the chosen band (3 to 5 μm or 8 to 12 μm). With respect to the attenuation measurement, a calibrated infrared sensor is used, to determine the radiation patterns of that object, in the chosen band. The comparison of these patterns before and after the application of the camouflage (e.g. a camouflage net), gives an absolute measure of this attenuation. The result of this measurement is important as the attenuation is closely related to the contrast between the camouflaged object and its background and thus to the probability of detection, via the intensity of the object in the thermal image. However for characterising the thermal infrared behaviour of certain compound materials which do present very high attenuation characteristics (such as the outer paint layer on a metal sheet), it is not useful to determine the attenuation as described above. In that case a measurement of the thermal emissivity factor is performed instead, on a dedicated installation developed in the TDLM/CT-TE (see paragraph 3.2.).

Contrast as determined above however is not the only important feature for the detection of an object in a thermal image. Indeed, suppose that to reduce the contrast a certain paint is used to reduce the thermal IR emission with a constant factor over the whole surface of a target. In that case, *if* detected (i.e. found in a complex scene) it would be not more difficult to recognise it (i.e. classify in a broad range of possible targets) or to identify it (i.e. specify precisely what kind of target it is), because the *relative* intensities on the target itself would not have changed. On the other hand, if one uses a camouflage net, some kind of cooling, different paints or another thermal countermeasure, then not only the global emission will change, but also the relative emission on the target itself, thereby eliminating some features that allow detection, recognition or identification. That is why in a second phase the countermeasures under evaluation are tested in a real environment. During this phase, a numerical value is given to the efficiency of the considered camouflage in the thermal infrared, using features selected from those which are known to be important for human vision. These include besides contrast other features such as correlation and texture.

Because capabilities differ from observer to observer, what is sought here are numerical

values that have a direct link with probabilities of detection, recognition, identification of a *group* of observers (or average observer). Therefore, the computer program is not asked to find the target itself but rather to give *global* measures depending on the chosen features for the target which position is already given to the computer program through the system operator who took the images and therefore knows exactly the positions.

Although one of the most important features for the detection of a target is its motion in the (static) nature, it will not be used in this study. Indeed, unfortunately enough, to be able to deal with motion is not that easy in image processing. This is one of the reasons why this project has been started only for the evaluation of the efficiency on static targets. Once this is completed and with the knowledge and experience that will have been gathered by then, the problem dealing with the motion of targets will be tackled.

The third and final phase aims at a verification and a validation of the test results. Indeed, it is of a crucial importance to find a link between the performances obtained in the field and the characteristics measured on a lab-scale. It is also necessary to verify that a good correlation exists between the efficiency of the camouflage as determined by human observers and by numerical evaluation. This verification will be done using a database of thermal images taken with a GEC AVIONICS TICM II (8 to 12 μm). Those images are then presented to human observers and to the machine in a project called "Psychotest". The interpretation of the results of these tests should either give confidence in this method or indications on how to correct it.

3. DETERMINATION OF THE ATTENUATION

3.1. Attenuation measurement
Determining "the" attenuation comparing thermal radiation patterns before and after the application cf a camouflage system is not as simple as it seems and certainly not as straightforward as in the case of radar. The quantity of radiant thermal energy collected on a sensor does not only depend on the emission, reflection and transmission factors of the considered object. It also depends on the characteristics of the background, environment and weather conditions of the moment. Consequently the same dependence can be found for the value of the attenuation.

As the separation of the incoming energy in its different parts is practically impossible (the values of the emission, reflection and transmission factors of a (hostile) target will never be known exactly, since dust, mud and other battlefield conditions can modify the original (probably also unknown) factors completely and are not sufficiently predictable themselves either), the attenuation is determined using radiation patterns recorded in a background and an environment which are typical for our purposes. The weather dependency can be dealt with partly by means of models such as the well-known LOWTRAN model for (between other things) the calculation of the transmission factor of the atmosphere.

The measurements of the radiation patterns are performed with a calibrated thermal sensor in the chosen band and with a set-up as shown in figure 2.
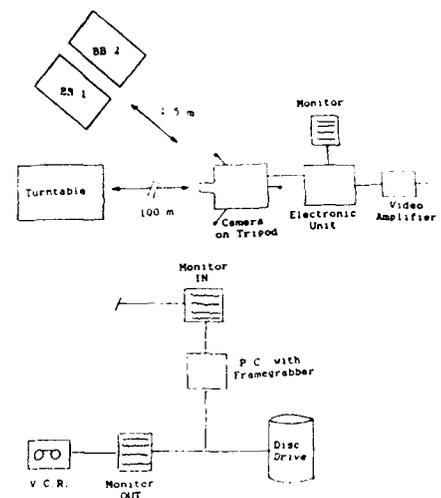
Figure 2: Measurement set-up for radiation patterns

3.2. Measurement of the thermal emissivity factor
To determine the emissivity factor ε of a material, the energy emitted by a reference black body (with a known temperature and an ε close to 1) is compared to that of the material with an unknown ε, but with a known temperature. The ratio of both emitted energies is the unknown emissivity factor.

Especially when dealing with a low ε, the material under test reflects a large amount of energy which it receives from the environment. To quantify this energy, a test bench with known parameters has been constructed in order to calculate the energy arriving on the sample under test, through multiple reflections. In this way it becomes

possible to discriminate between the reflected energy and the energy emitted by the sample under test itself, in the global measurement of the energy arriving at the thermal sensor.

The test bench that TDLM/CT-TE has developed and is using, has the form of a rectangular cube. The finish of the walls is a chromium plated copper alloy with an emissivity factor of 0.03. The side in front of the sample (the diaphragm) is a cooled plate provided with an aperture. Through this aperture the thermal sensor measures the apparent emitted energy from the (uniformly heated) sample, i.e. the sum of the energy emitted by the sample itself and the energy coming from the environment and reflected by the sample.

The program that calculates the emissivity factor is based on the assumption that the sample under test is a Lambertian radiator. Consequently the results of this measurement are only valid for diffuse surfaces and therefore this test bench is not appropriate for specular reflectors. For more information on this test bench, please refer to the paper of R. Marchal which is included in this same session.

4. NUMERICAL EVALUATION OF THE EFFICIENCY

4.1. General
The detection of an object in its environment can be treated using pattern recognition methods [3,4,6]. In the special case of the detection there are only two distinct classes: the target and the background. The general development of a pattern recognition system is given in figure 3.
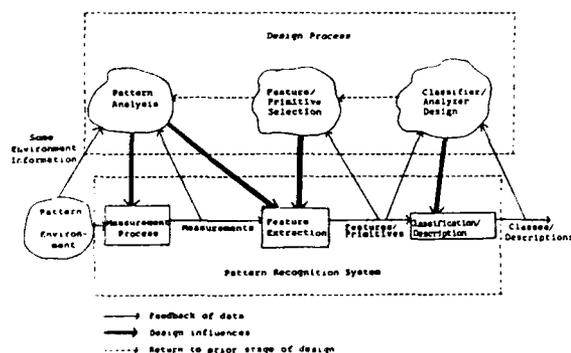
Figure 3: Development of a pattern recognition system [7]

The most important part of the process is the correct selection (which characteristics to chose?) and the efficient extraction (what is the best way to calculate them on an image?) of the features. These must have enough discriminatory power to separate the different classes, and preferably under all possible conditions.

4.2. Feature selection
The German "Forschungsinstitut für Informationsverarbeitung und Mustererkennung (FIM)" has made a considerable effort in determining the most efficient features to distinguish man-made targets from background in a natural environment and for distances which are relevant for the combat. The FIM concluded that in this specific case the features of correlation and texture are the most appropriate [1,2].

4.3. Feature extraction

4.3.1. Correlation algorithm
The normalised correlation has been implemented [2]:

$$ \ldots $$

The normalised correlation K can be seen as the resemblance between the camouflaged target and the rest of the thermal image. This is certainly an important aspect since the more the camouflaged target looks like the rest of the thermal image, the more unlikely it will be detected.

The main problem with the calculation of this feature is to determine the correct contour of the camouflaged target. The algorithm that is being used in this study, has been developed at the TDLM/CT-TE. It is an interactive algorithm, based on a minimum cost path starting from a rough estimate of the contour, determined by the operator.

4.3.2. Texture analysis algorithm [10]
The texture analysis describes a scene by examining the distribution of local differences in radiance by the features Mi as defined by Haralick [5]. He and others have suggested a method to estimate the second order probability densities and they have developed measures based on those densities. The second order statistics are given by $P(i,j,d,\alpha)$,

the probability for a pair of points to have respective intensities i and j if they are separated by a distance d in the direction α. These statistics can be calculated and stored under form of coocurrence matrices, one for each pair (d,α). An element (i,j) of this matrices is the number of pairs of points with the intensities i and j, which can be found separated by the distance d in the direction α.


(a)

(b)
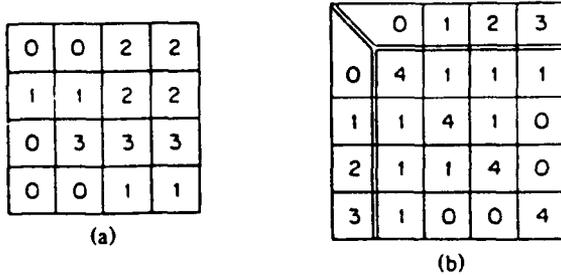
Figure 4: Example of the calculation of a coocurrence matrix

Figure 4 shows a window of an image containing grey levels between 0 and 3. The corresponding coocurrence matrix for a distance d=1 and for a horizontal direction (d is taken as an absolute value i.e. to the left and to the right) is also shown. The coocurrence matrix of figure 4 must still be normalised to represent probabilities.

Note that the complete calculation of the second order statistics requires the calculation of the coocurrence matrices for each direction α and distance d. Normalised, these matrices form second order densities and can as such be representative for the analysed texture (figures 5 and 6).
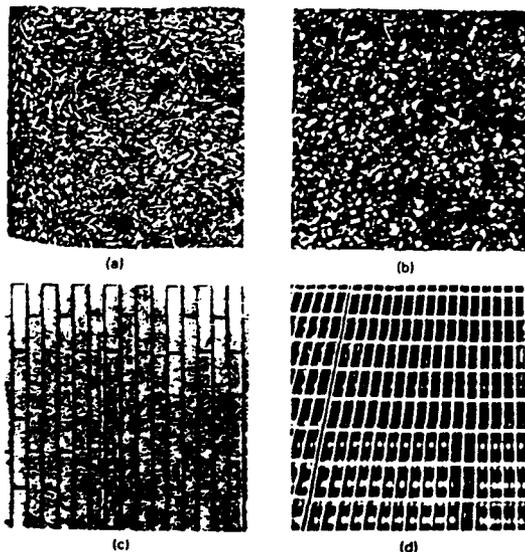
Figure 5: Natural textures (a) Glass, (b) Ivy, (c) Brick, (d) Grill
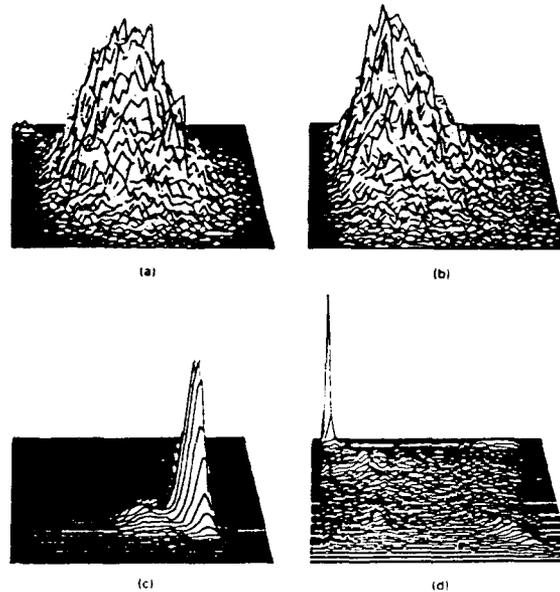
Figure 6: Normalised coocurrence matrices corresponding with the natural textures from figure 5

In the majority of the cases, those matrices are not used like they are but rather reduced to a series of measures (Haralick) such as for example:

M5 = [Local homogenity]

4.4. Separation criterion

The various numerical features needed for the detection of a target in its background form a feature vector X. A necessary condition to detect a target in its background is that the feature vector takes different values in the two cases (camouflaged and not camouflaged). The features however take different values across target and background. In other words they are distributed in feature space. Therefore a necessary condition for detection is that the multivariate feature distributions differ for target and background:

$$p(X/target) \neq p(X/background)$$

The greater the difference between the above conditional probability distributions the greater the chance of detection.

A number of ways of expressing the difference between such distributions are the statistical distance measures. One of these measures, the Bhattacharyya distance is used in this paper [3,4,6]:

$$D_{tb} = -log \int_{-\infty}^{+\infty} [p(X|target).p(X|background)]^{1/2} .dX$$

4.5. The efficiency of a camouflage
The features used to discern between target
and background are contrast, correlation factor
K and texture analysis parameters. The
efficiency γ of a camouflage is then given by:

$$\gamma = \frac{D_{tb}\ (before) - D_{tb}\ (after)}{D_{tb}\ (before) + D_{tb}\ (after)}$$

The Bhattacharyya distances are measured
before and after applying the camouflage. The
effect of the effort is measured by γ, the
relative decrease in Bhattacharyya distance.

To be more correct one should use the
corresponding probabilities instead of the
Bhattacharyya distances, as is explained
hereafter.

5. EVALUATION OF THE CORRELATION MAN/MACHINE
A correct choice of the features used in a
pattern recognition environment is, as already
mentioned, very important. That is the main
reason why it is necessary to have an
evaluation of the choice made with respect to
the detection of military targets in infrared
imagery. Therefore TDLM/CT-TE developed
a test (called Psychotest), which allows to
compare the statistical distance (based on the
chosen features) between target and
background, with the probability of detection,
recognition and identification. For this test a
number of (low resolution) thermal images
had been recorded, in a typical NW-European
background. These images were submitted to
the machine who calculated, for each feature,
the statistical distance between the target and
the background. Afterwards, human observers
had a look at those images and had to point out
targets and classify them. This Psychotest is
very important by itself. Indeed, since the
images are computer recorded, field work (i.e.
manipulating targets with or without
camouflage, thermal cameras and human
resources) is reduced to the time needed for
the recording. Afterwards observation of the
images can be done with as many people as
desired using a lot less resources of all kind.
All these observations lead to *actual measured*
probabilities of detection, recognition and/or
identification. The relative change in
probabilities from the non camouflaged to the
camouflaged target gives the *actual measured*
efficiency. *The purpose of the numerical
evaluation* is to find a numerical measurement
scheme that bears a close resemblance with the
actual probabilities (validation of the

numerical model). If this is found then the
step of the human observers can be skipped,
thereby reducing even more the workload of
determining the efficiency of countermeasures.

From this first experience it has been seen that
a great statistical distance between target and
background (bad camouflage), also implies a
great probability of detection. However, for
statistical distances below a certain threshold
(good camouflage), it is seen that only a few
of the features show a close relationship
between this distance and the probability of
detection. This can be explained by the fact
that the chosen features are not optimal with
respect to the (low resolution) images used. It
seems, for instance, that the quality of the
texture information of these images was very
low, due to the bad resolution. Therefore one
should not expect that texture features perform
well on that kind of imagery. Furthermore, it
is only when a target is well camouflaged that
texture really takes a meaning. In that case
detection probabilities become low and thus
the relative error measuring them increases
(with the same number of observers). It then
makes it more difficult to get a good
relationship between Bhattacharyya distances
and measured probabilities. As a summary it
can be said that a threshold phenomenon
occurs; under a certain (low) statistical
distance (e.g. Bhattacharyya) the detection
probabilities are small and over a (high)
statistical distance, detection probabilities are
high, but no close relationship was obtained so
far.

A further step in this research will be the
creation of a database with higher resolution
thermal imagery (GEC AVIONICS TICM II).

Furthermore, we have to consider the
possibility that some of the features are not
suitable, or that other features have to be
incorporated. Next to intensity and texture
characteristics, experiments with gradient
information, contour characteristics and
shapes, grouping features, etc. are taking
place. A major drawback of the
Bhattacharyya analysis is that it takes the
picture as a whole. If a part of the target is
much more apparent than the rest (e.g. exhaust
gasses or a recently fired gun), detection can
easily be done without using all the
information available in the whole picture.

6. IMPLEMENTATION
The evaluation system is implemented on a
DOMAIN/APOLLO DN4000 and a DN3550
workstation. The software for the
determination of the attenuation has been

written in PASCAL, while the more recently developed software for the numerical evaluation of the efficiency has been written in ADA. This was mainly done to increase the portability and the modularity of the program.

7. PERSPECTIVES
* Verification of the correlation on a high resolution database.
* If necessary, adaptation of the features, the extraction or the separation criterion.
* Study of the performances of artificial neural net (ANN) algorithms versus the classical pattern recognition methods. Analysis of the ANN approach of perception, to find (eventually) more fundamental features.
* Study of the implementation of ANN on massively parallel architectures such as transputers.

8. CONCLUSIONS
The research in the TIR domain is more recent than the research in the radar wavelengths and it is also seems more complex with respect to the interaction of the environment. At this moment the process of validating the performances of our numerical evaluation procedure is still going on. This research will be continued using the high resolution database and Psychotest.

The philosophy used for the development of the numerical evaluation method is in principle independent of the spectral region. The only things that will possibly change are the feature selection and extraction parts.

Another advantage of a completely numerical evaluation system is the possibility to evaluate the performances of automated weapon systems against countermeasures, but only if the used detection algorithms and the characteristics (such as the spectral response, the temperature resolution and the spatial resolution) of the sensor are known.

Another important aspect for the future developments of this project is the study of the performances of artificial neural nets versus classical pattern recognition algorithms. Together with this study, we will investigate the possibilities of implementing ANNs on massively parallel architectures such as transputers.

9. REFERENCES
1. Bargel B., *Automatische Klassifikation von Fernerkundungsdaten durch statische und strukturelle Texturanalyse*, Dissertation zur Erlangung des akademischen Grades eines Doktor-Ingenieurs von der Fakultät für Elektrotechnik der Universität Karlsruhe, Nov. 1982.

2. Bers K.-H. and Holub H., *Automatische Bewertung der Wirksamkeit von Tarnmassnahmen*, Forschungsinstitut für Informationsverarbeitung und Mustererkennung, Bericht Nr. 166, Dezember 1986.

3. Brock-Nannestad L. and Hvedstrup Jensen G., *Pattern Recognition Aspects in the Characterisation of Targets and Backgrounds*, Danish Defence Research Establishment, DDRE 1979/34, Aug. 1979.

4. Brock-Nannestad L., *The Application of Pattern Recognition Methods in Countersurveillance*, Danish Defence Research Establishment, DDRE 1981/6.

5. Haralick R. M. and Shanmugam K., *Textural Features for Image Classification*, IEEE Transactions on Systems, Man and Cybernetics, Vol. SMC-6, Nov. 1973, p. 610-621.

6. Hvedstrup Jensen G. and Dannenberg E., *Evaluation of Camouflage Measures by use of Image Processing Technique*, Danish Defence Research Establishment, DDRE 1981/7, April 1981.

7. Kanal L., *Patterns in Pattern Recognition*, IEEE Transactions on Information Theory, Vol. IT-20, Nr. 6, Nov. 1974, p. 697-722.

8. Van der Plas G. et al., *Studie van de Invloed van Dunne Materialen op de Reflectie en/of Absorptie van Electromagnetische Stralen in het Microgolfgebied*, IWONL-study Nr. 3020/069 from 18 Mar. 1986 until 31 Mar. 1990.

9. Verlinde P., *Numerical Evaluation of the Efficiency of a Camouflage System in the Thermal Infrared*, Eleventh Annual Symposium on Ground Vehicle Signatures, August 22-24 1989.

10. Wilms P., *Evaluation Automatique de camouflages en infrarouge thermique. Modélisation grâce à des mesures de texture tirées de matrices de coocurrence*. Mémoire de maîtrise en physique de l'Université de Liège, Belgium.

11. Ramakant N., *Machine Perception*, Department of Electrical Engineering and Computer Science, University of Southern California, Prentice-Hall Inc., 1982.

10. BIOGRAPHY

Patrick Verlinde was born in Bruges (Belgium) on the 9th September 1960. He obtained a degree of civil engineer (specialisations armament/ ballistics and telecommunications) with the 133rd polytechnic promotion at the Royal Military Academy of Brussels (Belgium) in 1983. In 1989 he obtained the degree of civil electromechanical engineer orientation electronics, specialisation mechatronics at the Catholic University of Leuven (Belgium). He is now working at the General Headquarters of the Belgian Gendarmerie, Higher Direction of the Telematics at Brussels, where he is the technical project manager for the realisation of a nation-wide trunking radio communication network for the use of all the Belgian security and emergency services.

Phillipe Wilms was born in Brussels on the 22nd august 1965. He obtained a degree of civil engineer (specialisation Telecommunications) with the 138th polytechnic promotion at the Royal Military Academy of Brussels in 1988. In 1990 he obtained a M. Sc. in physics at the University of Liège (Belgium). He is now working at the 16th squadron light aviation as a helicopter pilot and aircraft maintenance officer.

Discussion

Discussor's name :   P. Baars, GE

Comment/Question :

1. Can you provide data for comparing the effectiveness of the numerical methods with that of the human operator?

2. You propose AAN methods to be investigated. Can you give reasons and exspectations?

Author/Presenter's reply :

1. Until now, the effectiveness we calculated couldn't be correlated to the observations of human operators, because the resolution of the images was too low. In the future, we shall work with a high resolution database, so that the texture features make sense.

2. I can't answer this question, because I am not the author. I know the state of his research, but I cannot know his intentions. Personally, I don't think AAN is a good way for this purpose.

Discussor's name :   Dr Pfeifer, ISL, GE

Comment/Question :

What are your perspectives on applications of neural networks for your work?

Author/Presenter's reply :

It is difficult for me to answer this question because I did not perform the work since I only present this paper.

The Effects of Man-made Smokes and Battlefield-Induced Smokes on the Propagation of Electromagnetic Radiation

Anthony Van de Wal
Chief, Obscuration Effects Branch
U.S. Army Research Laboratory
Aberdeen Proving Ground, Maryland
MD 21010-5423, United States

1. SUMMARY

This paper provides an unclassified overview of the U.S. Army program that collects and disseminates information about the effects of battlefield smokes and obscurants on weapon system performance. The primary mechanism for collecting field data is an annual exercise called SMOKE WEEK.

In SMOKE WEEK testing, a complete characterization is made of the ambient test conditions, of the electromagnetic radiation propagation in clear and obscured conditions, and of the obscuring cloud and the particles that comprise the cloud. This paper describes the instrumentation and methodology employed to make these field measurements, methods of analysis, and some typical results.

The effects of these realistic battlefield environments on weapons system performance are discussed generically.

2. INTRODUCTION

The propagation of electromagnetic radiation through the atmosphere is a common requirement for many military functions. Among them are (a) combat surveillance and target acquisition; (b) missile or projectile guidance, control and terminal homing; (c) laser range finding and target designation; d) training with systems such as MILES; and (e) remote chemical warfare agent detection.

The sensors and seekers that perform these functions must be capable of operating in realistic battlefield environments at all levels of conflict (tactical, operational, and strategic). In contrast to typical "clear air" conditions, reliable function of military equipment requires that they perform in (a) a diversity of meteorological conditions (rain, snow, fog); (b) dust or debris created by wind, moving vehicles, and explosions; (c) smoke created by fires and explosions; and (d) military-unique smokes such as white phosphorus (WP), red phosphorus (RP), HC and fog oil, and diesel fuel aerosols.

Atmospheric propagation of electromagnetic radiation is a function of two principal characteristics: wavelength of the energy, and the intervening medium.

Modern armies are fully exploiting the electromagnetic spectrum with tactical weapon systems that operate from ultraviolet through millimeter wavelengths. The reliability of operating these weapon systems in complex physical simulations of realistic battlefield environments has been evaluated by the United States and some allied nations in a series of field tests called SMOKE WEEK.

3. SMOKE WEEK

The primary technical requirement for SMOKE WEEK testing is the simultaneous measurement of four groups of variables: (a) ambient conditions; (b) the intervening medium; (c) radiative transfer through the medium; and (d) thresholds of weapon system performance.

Quantification of ambient conditions includes micrometeorology; target and background signatures; dynamic geometry of targets, sensors or seekers, and smoke sources; and soil conditions.

Quantification of the intervening medium includes characterization of the cloud, its physical dimensions, growth, transport and diffusion as a function of time. It also includes characterization of the aerosol particles that comprise the cloud (the mass concentration, number density, particle size, and shape distributions).

Quantification of radiative transfer through the intervening medium will be subject for future discussion. It includes narrow and broad band transmissometry and radiometry of energy from the cloud.

3.1 Determination of Thresholds of System Performance.

Smokes and aerosols normally encountered on the battlefield severely constrain the performance of weapon systems that rely on the propagation of electromagnetic energy for their function. Demonstrations of the ability of smokes and aerosols, both natural and man-made, to limit the use of systems are valuable to military planners and executors of the battle. However, much more use, especially for the hardware developer, results from determining the probabilistic threshold of performance in marginally effective aerosol environments. An acquisition philosophy used by the U.S. Army is to iteratively test, assess, and fix hardware throughout its development cycle. By determining thresholds of system performance, rather than just demonstrating that a system can be defeated, it is possible to quantitatively measure the contribution to enhanced performance made by modifying some hardware or software component of the system.

4. ATMOSPHERIC AEROSOLS AND OPTICS DATA LIBRARY

In addition to the publishing of hard copy reports and analyses of SMOKE WEEK results, the data are incorporated in a contractor-maintained data base called the Atmospheric Aerosols and Optics Data Library (AAODL). This computer-based system contains data from approximately 80 field tests.

A primary concern in managing a data base such as AAODL is the quality control of information it contains. The author's concepts of quality control not only include the typical bookkeeping, monitoring, and assurance of internal consistency within the data sets, but they also concentrated on evaluations of the quality of the measurements made in the field.

5. TRANSMISSOMETRY VALIDATION

Beginning in 1984 with a workshop about transmissometry, an effort to validate the measurements of the propagation of electro-magnetic energy was begun. The goals of the effort were to

1. Intercompare the dozen or so multi-spectral transmissometry systems being used by the U.S. in field tests;

2. Identify sources of variation in results reported from different systems;

3. Develop means to remove or reduce the variation;

4. Model and measure the performance of transmissometers; and

5. Develop standard operating procedures (SOPs) for field measurements.

A significant contribution was to identify a means of intercomparing measurements made by different transmissometers at the same and different wavelengths. The parameter identified for comparison is the negative logarithm of transmission, that is, the optical depth of the medium through which the measurements are made. Scattergrams of measurements of optical depths at two wavelengths or by different systems at the same wavelength quickly revealed when non-correlation of the two systems occurred. Generally, at optical depths greater than 3 or 4, the data were no longer correlated.

The 1984 workshop discussed a variety of potential rationalizations for the lack of agreement: (a) lack of homogeneity of the clouds; (b) differences in lines of sight of the measuring system; (c) aerosol effects such as different mechanisms of attenuation at different wavelengths and multiple scattering; (d) atmospheric effects such as path radiance and turbulence; and (e) system electro-optical engineering.

Based on the discussions at the workshop, a program was developed to investigate and reduce the variation in transmissometry results: (a) laboratory characterization of transmissometry system components; (b) development of a transmissometry system performance model; and (c) field evaluation of the transmissometers.

Component characterization resulted in measurement of (a) spectral responses of 260 filters; (b) dynamic range and

linearity of 31 detectors;
(c) effective aperture and
field of view (FOV) of 14
receivers; (d) source
divergence and intensity
distributions of five sources.

Results of the characterization
measurements can be summarized
with the statement that
anything that filters,
transduces, or amplifies
electromagnetic energy will
produce variance over dynamic
ranges greater than about three
orders of magnitude. Filters,
although sharp and distinct for
their designated wavelength,
allowed 10% of the transmitted
energy to be out of band. In
general terms, the detectors,
although nonlinear spectrally,
met their manufacturer's
specifications. Especially
in trying to measure
propagation through optically
dense media, the logarithmic
amplifiers became essential.
They were a significant source
of error and invalidated a
costly double-ended lidar field
test. In optical
amplification, a significant
source of error was found to be
telescope and mirror
alignments. Significant gains
in dynamic range can be
achieved by minimizing receiver
FOV and source divergence and
by ensuring proper optical
alignment.

A model named integrated
transmissometer modeling system
(ITEMS) was developed and
applied to predict and evaluate
transmissometer performance in
the field.

A dedicated field test called
the comparison, evaluation, and
characterization of Army
transmissometer systems
(CECATS) was conducted during
May of 1988 at White Sands
Missile Range. The test
provided side-by-side
comparisons of six
transmissometer suites over
1.0- or 1.8-kilometer ranges in
56 obscurant trials conducted
both day and night and with
illuminating flares. The
obscurant clouds were fully
characterized with the
atmospheric transmittance large
area analysis system (ATLAS)
and nephelometry. The wide
range of atmospheric stability
conditions that were encoun-
tered during the month were
fully documented.

The results of these analyses,
calibrations, and field trials
have been incorporated into the
AAODL data base and are being
used to validate the
transmissometry measurements
contained in the data base.

6. AEROSOL VALIDATION
For the purposes of SMOKE WEEK
testing, validation of the
various measurement techniques
applied for characterization of
the smoke clouds and the
aerosol particles that comprise
the cloud is the next priority.
Because of restructuring of
organizations within the U.S.
Army and reduced budgets, this
effort has been less structured
and focused. As an individual
initiative, the methodology and
algorithms used in the ATLAS to
quantify cloud dimensions and
transmission profiles were
accredited by independent
audit. Several small scale
intercomparisons of
nephelometry have been made
within SMOKE WEEK, but overall
validation of cloud and aerosol
characterizations remains an
unfilled requirement.

7. EFFECTS ON SYSTEM
PERFORMANCE
Because of proprietary and
system vulnerability
considerations, only generic
effects of natural and man-made
obscurants on systems are dis-
cussed.

Hydrometeors, blowing or
explosively generated dust, and
the common military smokes (WP,
HC, and vaporized or
recondensed petroleum smokes)
are all highly effective in
limiting the propagation of the
visible wavelengths of radia-
tion. The military smokes are
not only effective, but
efficient, having extinction
coefficients an order of
magnitude or more than that of
dust, for example. Such
obscurants obviously will
severely limit the performance
of systems that operate in the
visible portion of the
spectrum.

Because the traditional
military smokes form micron-
sized particles in the
atmosphere, they are effective
in scattering radiation
throughout the near infrared
portion of the electromagnetic
spectrum. Systems that operate
in this portion of the spectrum
may be susceptible to defeat by
these aerosols. Such systems
include image intensifiers used
for combat surveillance and
target acquisition, laser range
finders using ruby, gallium
arsenide, neodymium on glass,
or yttrium aluminum garnet,
common laser designators, many

guided missile beacons, and terminal homing seekers.

For the most part, the traditional military smokes and most of the hydrometeors are transparent for thermal imaging systems, CO_2 range finders, and missile beacons and seekers, which operate at far infrared wavelengths. WP smoke and blowing or explosively generated dust, both of which absorb far infrared radiation, can affect such systems. Although not the atmospheric transmission issue mainly addressed in this paper, the energy emitted by burning WP, pyrotechnics such as HC smoke, and flares, provides scene clutter that can degrade system performance.

Contemporary missile guidance links, missile or projectile seekers, and target acquisition radars, which operate at millimeter wavelengths, are generally immune to typical battlefield obscurants. Hydrometeors, which approach millimeter dimensions, will scatter millimeter wave radiation. Artillery and other explosions, which generate large particle ejecta, have transient effects on millimeter wave propagation. For millimeter wave radars, the transient effect is a nuisance. For seekers and missile guidance links, the transient effect may be enough to break lock.

The smokes that were evaluated in NATO PG 16 trials in the early 1980s and introduced into inventories in the mid to late 1980s are effective and efficient in absorbing radiation from visible through far infrared wavelengths. These far infrared-defeating smokes have the potential to adversely impact target acquisition systems, missile or projectile seekers, and laser range finders, which hitherto have operated with impunity on the battlefield.

The NATO smoke and obscurant countermeasure evaluation trials (SOCMET) that are currently being conducted by NATO Panel VI, Subpanel 6, have the potential of providing NATO forces with a capability of significant control of the electromagnetic spectrum later in this decade.

8. BENEFITS

A complete understanding of the interactions between electromagnetic radiation and the medium through which it is propagating is essential for several important reasons.

8.1 Electro-optical Systems Engineering

The primary determinant of systems performance in realistic battlefield environments is the wavelength selected for the sensor. Generally, the longer the wavelength, the less affected a system's performance will be by atmospheric aerosols. However, the inverse relationship between wavelength and resolution requires trade-offs be made, especially for tactical systems that require high resolution for target identification.

At a given wavelength, both hardware and software considerations determine system performance. Output powers, collection apertures, and signal amplification will determine system performance both optically and electronically. With an understanding of the mechanisms of interaction between radiation and the aerosols, system performance can be improved with signal-processing techniques to reject or reduce false information introduced by the aerosols to the system.

The repetitive test-assess-and-fix cycle allows the system developer and tester to interact to optimize system performance in realistic battlefield environments. Repetitive testing, which quantifies thresholds of system performance, is an essential element in that process. It demonstrates that changes made by the materiel developer contribute to enhanced performance.

8.2 Operational Performance

It is essential that war fighters know the performance limits of the weapon systems they are employing. The data collected during technical and operational testing must be converted into doctrinal information readily available to war fighters. Based upon some notable failures in the 1980s and some notable successes in the 1990s, the United States has not yet fully met the challenge of transferring information from the technical community to the battle captains and war fighters.

8.3 Synergy

NATO policy is evolving, thus placing more and more reliance on "high technology" electro-optical equipment operated by fewer and fewer personnel. Indeed, smart and brilliant weapons systems are combat multipliers. When these new systems are made robust so that they can operate in realistic battlefield environments that limit the performance of the systems of opposing forces, the synergism between smart systems and battlefield obscuration gives our fighting forces unprecedented capability.

9. THE FUTURE

Despite political change, technological innovation, and doctrinal evolution, basic requirements for pursuing ground warfare on any scale will be to acquire and service targets. Those two military functions will require military systems that operate in complex environments that could limit the performance of the systems. Only by continued study, assessment, understanding, and concomitant improvement in system performance will our fighting forces have effective capabilities on future battlefields. The work must continue.

Discussion

Discussor's name :   C. M. Jenden, UK

Comment/Question :

Thank you for an excellent presentation of the work done at SMOKE weeks. Can you say what studies are done to evaluate the environmental impact of smokes during these trials?

Author/Presenter's reply :

The United States laws and regulations controlling the release of potentially hazardous material into the environment are growing exponentially. Until 1990, many exemptions for military activities were available.

Discussor's name :   A. V. Kay, GE

Comment/Question :

How does the data library AAODL differ form the data library EOSAEL?

Author/Presenter's reply :

The primary diffence is taht EOSAEL is a collection of propagation models while AAODL is a multi-media collection of data. For example COMBIC (Combaid Obscuration model for Battlefield Induces Contaminants) is an EOSAEL model. It provides predictions of the transport, diffusion and transmission through smoke clouds. It was validated by the data contained in AAODL.

Discussor's name :   F. T. Ulaby, US

Comment/Question :

Can you provide more details on the type of millimeterwaves systems you are using? What types? What bands?

Author/Presenter's reply :

Frequencies are : 35 and 95 GHz

Procedure to Optimize the Effectiveness of
Man-made Smoke Screens
for Fixed Installations

G. Kollers
Industrieanlagen-Betriebsgesellschaft mbH (IABG)
Dpt. WTU
Einsteinstraße 20
D-85521 Ottobrunn
Germany

1.   Summary

In this presentation a method is described which enables man-made smoke screens to be mixed into realistic backgrounds in any form, size, number and time of release. The background may consist of a single image or a video recording of a complete airborne attack.

The result is a smoke scenario available as image or video film for observer interviews or for automatic image evaluation. By means of this tool the reduction or delay in target acquisition can be evaluated. Comparisons are possible between different smoke scenarios with the same background or with the same scene without smoke.

This procedure is based on a smoke model of the US Army Electro-Optical Systems Atmospheric Effects Library (EOSAEL) of the Atmospheric Sciences Laboratory (ASL) in New Mexico, USA, called COMBIC (Combined Obscuration Model for Battlefield Induced Contaminants).

By means of COMBIC a smoke scenario with numerous familiar smoke sources, their spreading behaviour, their free selectable wind direction and wind speed etc. can be generated. A package developed by IABG visualizes this smoke scenario with a resolution of 512•512 pixel and combines it with a realistic background either black and white or coloured. Various smoke densities may be chosen so that the smoke completely prevents the view on the concealed parts of the background or that the background partly shows through.

This procedure enables to evaluate the tactical effectiveness of smoke when used together with other techniques of CCD at fixed installations under various threat scenarios and meteorological conditions. Investigations can be carried out at low cost which is not possible with field trials.

2.   Introduction

A smoke screen neither is an universal counter-measure against airborne attackers for all targets nor a countermeasure against all kinds of attacking weapon systems.

Mostly, the airborne attacker exactly knows the position of a large-scaled fixed installation (e.g. an air base) and its environment by recon-naissance. During an airborne attack man-made smoke screens makes the mission more difficult for the attacker who has successfully passed the active countermeasures up to this moment.

What is the effect of man-made smoke screens?

For an effective use of many kinds of weapons the global target acquisition of the airborne attacker in the environment of the installation and in addition the point target acquisition in the installation is necessary.

A smoke screen forces the attacker

*   to newly orientate himself in an environment different from reconnaissance and
*   to find the targets in a much more difficult environment where all or most of the characteristic points are concealed.

The probability that weapons are released in time exactly in the target decreases. This increases the survivability of the fixed installation.

increased by radiation from smoke cloud $I_{cloud} \bullet \{1 - \tau(x,y,t)\}$ itself.

The radiation of the cloud is stronger, the denser the smoke, expressed by $\{1 - \tau(x,y,t)\}$. The assumption of $I_{cloud}(t)$ is justified for diffuse illumination and set equal to the brightest cloud pixel value. Depending on the sort of smoke sources the intensity varies from white to dark grey.

The combination of target and smoke scenario implemented by equation (1) is not a simple overlay but a superposition. The images generated have no sharp edges around the cloud and include semi-transparent cloud segments. They offer a very close approximation to actually screened target scenes and are well suited for smoke screen evaluation.

5.1 Target Scenes

Target scenes can easily be obtained. During an simulated airborne attack over an air base one can take pictures or a video film.

5.2 Smoke Scenes

There are a number of computer programs available which calculate cloud size and trans-mission losses for various types of smoke munitions. None of these models present the results as a smoke cloud image.

IABG developed special software to change an existing smoke model with the aim of generating images.

| 155-mm HC M1 canister |
| 155-mm HC M2 canister |
| 105-mm HC canister |
| 155-mm HC M116B1 proj |
| 105-mm HC M84A1 proj |
| Smoke pot, HC M5 |
| Smoke pot, HC M4A2 |
| 60-mm WP M302A1 cart |
| 81-mm WP M375A2 cart |
| 4.2-in WP M328A1 cart |
| 2.75-in WP M156 rocket |
| etc. |

Table 1: COMBIC Model smoke sources

The US Army Electro-Optical Systems Atmospheric Effects Library (EOSAEL) contains a specialized smoke model called COMBIC (Hoock, Sutherland, Clayton) /1/.

COMBIC has two sub modules COMBIC-I and COMBIC-II.

In COMBIC-I a user can specify desired smoke sources, the amount of smoke, the number of smoke sources, the releasing time, wind speed etc. A lot of smoke sources are available. Table 1 shows a few of the available smoke sources.

```
vertical                                 horizontal
     -100          -50          +50        100
 50



                         88
                       876678
 25                   75322357
                      741***1258
                     62*****1478
                    841*****14789
                  8887621****13689
                87665442223478 89
               6766654422234789
                  8887666789

 0
     -100          -50          +50        100
vertical                                 horizontal
```

Fig. 1: Looking at a smoke cloud (155-mm HC M1 canister) in a window scaled from -100 m to +100 m in horizontal width and from 0 m to 50 m in vertical width, ten steps from 0 to 9 indicate the increasing of transmission, * indicates no more trans-mission through the cloud

A user can generate a smoke scenario including the evaluation of this scenario. In COMBIC-II, the transmission through the scenario of clouds for a given line of sight (LOS) is calculated. A parallel bundle of up to 40•80 LOS can be defined depending on the printer paper size and COMBIC provides a print-out of the transmission map for these 40•80 pixels on a 10-step scale like in figure 1.

25-4

5.2.1 Smoke Scenarios

The first adaptation of COMBIC was to increase the spatial resolution from 40•80 to 512•512 (or anyone else) and the grey-scale resolution from 10 to 256 steps. The output was re-routed from the printer to an image processing system, which required rewriting of the output routine because COMBIC stores the data in a form that is not compatible with normal pixel processing. The image processing system converts the transmission fractions to grey values and display the results as an image.

5.2.2 Fixed View Point

It became apparent that bundles of parallel lines of sight are not adequate because a correct perspective view is not obtained. The second adaptation was to define a view point anywhere in space and to run the lines of sight from this view point through the clouds like in an optical lens.

After this second step the superposition described in equation (1) of a smoke scene with a target scene, taken under the same field of view, line of sight etc. is possible.
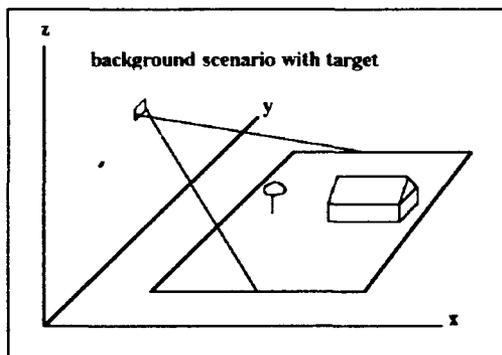
Figure 2: Rough outlines of a background scenario

A demonstration of a superposition with a fixed view point is shown in the first video at the 52nd AGARD EPP Meeting in Palma de Mallorca, Mallorca, Spain at 17-21 May 1993. This video is classified NATO CONFIDENTIAL.

Figure 2 shows a background scenario with a target and figure 3 shows a smoke scenario. Figure 4 shows the superposition of figures 2 and 3.
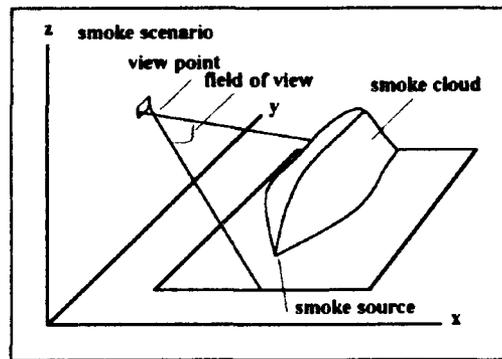

Figure 3: Rough outlines of a smoke scenario with the same line of sight and field of view as the background scenario in figure 2
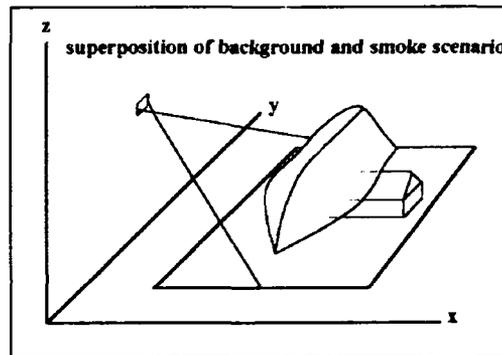

Figure 4: Superposition of a smoke scenario and a background scenario with a partly concealed target

5.2.3 Moving View Point

Chapter 5.2.2 described the superposition of a smoke screen variable in time with a static background scene.

Finally, it was desirable to simulate a moving observer e.g. an observer flying towards the smoke cloud. The third adaptation of COMBIC permits the definition of movement of the view point.

Simulating a moving observer is much more complex: for each frame (25 per second are required), the background scene changes and the smoke clouds are seen under a different perspective.

The procedure to generate a 120-sec-video is as follows: 3000 smoke transmission maps (2•60•25)

were calculated each at a different view point and at a different smoke evaluation time. They are stored on a hard disk. The video film of the attack flight was digitized and stored on a hard disk or magnetical tape. The digitized 3000 backgrounds and transmission maps were superimposed subsequently and written to a video recorder.

For a realistic video the roll and pitch of an aircraft must be known. The flight direction and the pilots line of sight can be different (e.g. the pilot is looking down) and must taken into account. If they are not considered, smoke clouds and background scenario drift against each other without being moved by wind.

If all inputs are correct for one fly over, it is very simple to produce a lot of different smoke scenarios with different meteorological conditions. A demonstration of a smoke scenario with a moving attacker is shown in the second video. This video is classified NATO CONFIDENTIAL.

6. Conclusion

By means of this procedure it is possible to easily generate and evaluate different smoke scenarios for each fixed installation to be camouflaged so that the most effective smoke screen for all weather conditions may be chosen.

7. References

/1/ Hoock, D.W., R. Sutherland and D. Clayton, 1984: "EOSAEL 84 Volume 11 - Combined Obscuration Model for Battlefield Induced Contaminants, COMBIC", ASL-TR-0160-11, US Army Atmospheric Sciences Laboratory, White Sands Missile Range, NM, 88002-5501.

Discussion

Discussor's name : J. Rogge, NE

Comment/Question :

Are the backgrounds that you showed in the video's real backgrounds or were they computer generated?

Author/Presenter's reply :

First movie : real background
Second movie : computer generated background

STRATEGIE DE DETECTION-VISEE ACED EN AMBIANCE METEO, DE TERRAINS ET DE CONTRE-MESURES

par

Pascal Laurend
Thomson Brandt Armements
route d'Ardon
F-45240 La Ferte Saint Aubin
France

1. INTRODUCTION

La présente publication a pour objectif d'exposer une stratégie de détection-visée de cibles blindées, applicable aux munitions et sous-munitions à effet dirigé.

La stratégie présentée est celle retenue par THOMSON BRANDT ARMEMENTS pour ses sous-munitions à effet dirigé ACED, par exemple pour celles de sa munition de mortier de 120 mm ou celles de ses cargos air-sol.

La stratégie retenue confère des capacités tous temps aux sous-munitions, elle leur confère aussi la capacité de fonctionner sur tous type de terrain et d'être durcies face aux contre-mesures naturelles et artificielles.

Enfin, la possibilité de reprogrammer facilement avant les conflits ou pendant ceux-ci, les sous-munitions, donne toute latitude aux utilisateurs pour pallier à l'apparition d'une contre-mesure sophistiquée et répandue. Elle permet aussi de panacher les algorithmes de fusion de données afin de mettre en difficulté par avance la définition des contre-mesures sophistiquées pouvant géner en partie l'efficacité système des salves de munitions.

2. CYCLE de VIE de la MUNITION ACED en 120 mm

Le cycle de vie de la munition rayée de mortier de 120 mm ACED est caractérisé par des phases classiques logistique, tactique, suivies d'une phase opérationnelle décomposée en sous-phases. A l'issue du tir canon, la munition se trouve en vol balistique jusqu'à environ 1000 mètres de l'objectif, en portée et en altitude. Les deux sous-munitions sont alors éjectées vers l'arrière et rentrent dans une phase de séparation freinage qui permet de les disperser dans l'espace et de réduire leurs vitesses axiale et de rotation. L'altimètre ordonne à une altitude de l'ordre de 400 m,

l'ouverture du parachute des sous-munitions. Le détecteur-viseur alors activé scrute les conditions météo et de terrain, au-dessus de l'objectif, afin d'adapter la sensibilité des modes de détection et afin d'accorder la confiance optimum à chacun des modes nourrissant la fusion de données.

Lorsque les sous-munitions se trouvent au-dessous d'une altitude de l'ordre de 100 m, alors que leur cinématique de descente et de rotation s'est stabilisée, permettant un scanning du sol en forme de spirale, l'autorisation de tir est donnée aux sous-munitions qui se trouvent à des portées d'attaque efficace ($\approx$ 120 m).

Le détecteur-viseur multimode analyse en permanence les informations en provenance du sol, il prendra sa décision de tir et visera le centre de la cible lors du premier passage sur une cible reconnue par l'algorithme de maximum de vraisemblance.

3. SOUS-MUNITIONS ACED dans d'AUTRES VECTEURS

Les sous-munitions ACED sont intégrables dans différents vecteurs et dispersables à partir de ces derniers.

Seule une modification du calibre de la charge militaire peut, si nécessaire, être effectuée afin d'adapter aux dimensions du porteur, l'efficacité terminale des sous-munitions.

Les applications considérées sont :

- Mortier de 120 mm
- MLRS
- APACHE
- ATACMS
- CASCAD
- Roquettes hélicoptères
- Roquettes sol-sol
- ADZ/ADW

4. STRATEGIE de DETECTION-VISEE MULTIMODE

4.1 Technique de Détection-Visée et d'agression (ACED)

Les techniques de détection et d'agression retenues pour l'ACED sont des techniques axiales. L'autorotation, la descente de la sous-munition sous parachute et l'inclinaison de la sous-munition font que la trace du balayage au sol est une spirale se refermant sur son centre.

Le détecteur-viseur est en avance sur l'axe de tir de la CGN(Charge Génératrice de Noyau), afin de permettre le traitement des informations issues des senseurs et d'assurer la visée de la CGN sur le centre de la cible. La CGN est déclenchée sur ordre du détecteur-viseur après que ce dernier ait détecté et visé sa cible. La détection multimode permet à la sous-munition d'analyser les conditions météorologiques et les terrains face auxquels elle évolue. Les informations ainsi recueillies permettent à la sous-munition de positionner au mieux ses voies de détection (réglage de seuils, modification de filtres, mise hors service de certains modes...) et aussi de choisir le type de fusion à effectuer.

Chacun des modes est capable d'analyser les contrastes introduits par la cible dans son environnement et les dimensions balayées sur cette dernière, ce qui permet la réjection des fausses cibles de dimensions inférieures ou supérieures aux cibles réelles.

La visée s'effectue sur le centre de la cible grâce à l'analyse dimensionnelle effectuée.

Le tir est déclenché lors du premier passage sur la cible lorsqu'il y a détection et visée correcte. Il n'est pas souhaitable d'attendre un second balayage sur la cible car les vitesses relatives cible/sous-munition dans le vent, sont susceptibles de l'interdire.

Le tir s'effectuant au premier balayage, il est nécessaire de réaliser la fusion des données et de prendre la décision de tir avant que l'axe de la CGN (en retard sur l'axe des faisceaux) ne soit aligné sur le centre de la cible. Pour les altitudes d'attaque les plus hautes, ce temps est de l'ordre de 1 ms.

D'un point de vue technologique, citons la capacité qu'ont les senseurs et le calculateur ACED à tenir les fortes accélérations de lancement des munitions tirées canon et leur forte vitesse de rotation sur trajectoire.

La charge militaire est une CGN équipée d'un revêtement en tantale et d'un explosif insensible à l'agression par balle et à l'incendie.

Son principe de fonctionnement consiste à former par explosion, un projectile empenné (≈ 500 g), qui se trouve à l'avant de la CGN en forme de calotte sphérique ; l'explosion permet sa mise en forme de "flèche" et sa propulsion à des vitesses voisines de 2000 m/s.

L'empennage assure la stabilité de ce projectile dont la précision est en écart-type de l'ordre de 3 mrad.

Une vue de la CGN déclenchée par un détecteur-viseur multimode est donnée dans les supports illustrant cette publication, elle a été réalisée lors des tirs de sous-munitions complètes en première européenne le 9 Octobre 1990 au Centre d'Essais de la Direction des Armements Terrestres à BOURGES dans le centre de la FRANCE.

4.2 Modes de détection d'un véhicule blindé

Un véhicule blindé se distingue sur le sol par un certain nombre de caractéristiques physiques, géométriques ou cinématiques au rang desquelles on peut compter les contrastes de température, de couleur, métallique, de SER, de champ magnétique, de hauteur, sonore, de mouvement. Ces caractéristiques sont détectables par des senseurs embarqués à bord des sous-munitions du type ACED, certains étant actifs, d'autres passifs. Citons respectivement pour les caractéristiques précitées un senseur capable de les détecter ; radiomètre IR, radiomètre visible, radiomètre millimétrique, radar millimétrique, magnéto-mètre, laser, senseur acoustique, radar millimétrique (effet doppler).

Certains de ces senseurs présentent des limites pour les applications à effet dirigé, par exemple les magnétomètres se trouvent confrontés à des problèmes de portée, les senseurs acoustiques à des problèmes de directivité.

4.3 Stratégie de détection multimode

Il convient pour réaliser une détection multimode de retenir un nombre plus grand que 1 d'informations indépendantes caractérisant la cible blindée. Le tir sera déclenché sur ordre d'un algorithme de fusion de donnée pouvant être par exemple du type "maximum de vraisemblance" :

Tir si Σ PROB.DETEC.INFO (i) x (0 ou 1) > α K

ou K = Σ PROB.DETEC.INFO. (i) x (1)

avec α < 1

PROB.DETEC.INFO (i) étant la probabilité de détecter l'information i en fonction des conditions météo et de terrain du jour qui sont mesurées par les senseurs.

4.4 Modes de visée d'un véhicule blindé

Afin d'assurer une visée correcte du projectile autoforgé sur la silhouette de la cible, il est utile de détecter les bords montant et descendant de la cible afin de pouvoir recentrer sur le milieu du véhicule le point visé. Il est aussi utile de s'assurer que le centre du faisceau de détection est bien passé sur une partie importante de la surface projetée de la cible, ce qui conduit à l'utilisation d'au moins un faisceau de petite dimension issu de technologies optiques permettant seules, dans les calibres considérés des sous-munitions, d'assurer un angle solide de visée inférieur à 1°.

Citons pour la détection des bords montants et descendants, des couples mode-senseur ; contraste métal-radiomètre millimétrique, contraste hauteur-laser, contraste mouvement-radar millimétrique.

Citons pour la détection d'une partie importante de la surface projetée de la cible, les couples modes-senseur ; contraste hauteur-laser, contraste température-radiomètre IR, contraste couleur-radiomètre visible.

4.5 Stratégie de visée multimode

Il convient, pour réaliser une visée multimode, de retenir un nombre plus grand que 1 d'informations indépendantes caractérisant les bords montant et descendant du véhicule et s'assurant que le faisceau de détection est bien passé sur une partie importante de sa silhouette projetée.

La visée s'effectue alors sur le centre de la partie interceptée de la cible, si cette partie a une dimension supérieure à une dimension minimale retenue, de l'ordre de 2 m. La mesure de la partie interceptée est rendue possible grâce à la connaissance de l'altitude et de l'angle d'inclinaison de la sous-munition et grâce à la connaissance de la dimension des faisceaux des senseurs.

5. STRATEGIE DE DETECTION-VISEE MULTIMODE EN AMBIANCE METEO, DE TERRAINS ET DE CONTRE-MESURES

5.1 Ambiance météo

Lors de mauvaises conditions météorologiques le détecteur-viseur multimode s'auto-adapte en mesurant les conditions au-dessus de l'objectif et en contribuant à déterminer les PROB.DETECT.INFO (i) pour chaque mode i.

Cette démarche peut conduire par exemple à la mise à 0 d'une PROB.DETECT.INFO (i) en *particulier lors de l'occultation totale d'une longueur d'onde (brouillard en IR et visible par exemple).*

La stratégie retenue pour la détection-visée multimode en ambiance météo est l'utilisation d'au minimum 2 bandes éloignées afin qu'elles ne soient pas occultées simultanément.

En effet, la dimension des particules naturelles obscurantes occultera l'une ou l'autre des bandes, mais pas les deux.

La sagesse veut que parmi les bandes retenues, le millimétrique qui est tous temps aux portées de l'ACED (≈ 100 m) soit l'une d'elles.

5.2 Ambiance de terrains

Le détecteur-.iseur multimode s'auto-adapte en mesurant les conditions de terrain au-dessus de l'objectif et en contribuant à déterminer les PROB.DETECT.INFO (i) pour chaque mode i (par exemple : baisse de la PROB.DETECT.INFO [contraste haute] sur terrain rocheux, augmentation de la PROB.DETECT.INFO [contraste SER] sur terrain à faible SER).

La stratégie retenue pour la détection-visée multimode en ambiance de terrain est l'utilisation d'au moins 2 modes différents en terme de nature de terrain, par exemple [contraste hauteur] et [contraste métal] afin que les contre-mesures naturelles ne soient que très rarement les mêmes dans les deux modes.

5.3 Ambiance de contre-mesures

Les considérations de fonctionnement tous temps et au-dessus de tous terrains conduisent à retenir 2 modes pour chaque cas. Afin d'être peu sensible aux contre-mesures, il est sage de ne pas se contenter de 2 modes mais d'en retenir au moins 4, ce qui est le cas de l'ACED de THOMSON BRANDT ARMEMENTS.

Ainsi les leurres doivent être multimode pour être efficace ce qui est difficilement réalisable pour des pelotons de blindés au combat.

Ainsi les brouilleurs doivent être multimode et directifs pour géner momentanément les sous-munitions. Si ces derniers se trouvent positionnés sur les véhicules, ils aident les sous-munitions à les agresser en forçant à 1 la *détection des modes brouillés.*

Enfin les camouflages doivent être multimode pour protéger les véhicules d'une agression, ce qui est extrêmement difficile car les camouflages de certains modes renforcent souvent la signature d'autres modes.

6. INTEGRATION DES SENSEURS ET DU CALCULATEUR ACED

Les senseurs et le calculateur constituent les sous-ensembles des sous-munitions assurant la détection et la visée des cibles blindées.

Le senseur millimétrique est situé à l'avant de la charge génératrice de noyau, afin d'avoir une vue directe sur la scène à analyser et de profiter au mieux du calibre disponible dans la sous-munition pour intégrer son antenne.

Le senseur infrarouge, de forte densité, ne peut être positionné aussi à l'avant de la CGN car il génerait la formation du projectile autoforgé, c'est pourquoi il se situe à l'arrière de la charge. Il est nécessaire, afin que la CGN prof.te au maximum du calibre des porteurs, de le replier, il sera déployé afin d'avoir une vue directe de la scène dans les dernières phases du cycle de vie au cours desquelles les sous-munitions ne seront plus positionnées dans leur porteur.

Le calculateur est aussi situé à l'arrière de la CGN, il est relié au senseur IR par une connectique flexible et au senseur millimétrique par un guide d'onde.

L'intégration des senseurs et du calculateur, de même que leur conception et leur réalisation, nécessite toute l'attention du munitionnaire habitué à travailler en tenant compte des environnements sévères induits par les lanceurs sur les munitions.

7. POSSIBILITES DE REPROGRAMMATION

Les sous-munitions ACED, accessibles quel que soit le cargo considéré, sont reprogrammables facilement et rapidement afin de parer à une contre-mesure sophistiquée éventuelle ou afin de s'adapter à des théatres d'opération très particuliers, ou encore afin de panacher les algorithmes de fusion de données pour rendre par avance inefficace pour l'adversaire la réalisation de contre-mesures.

8. CONCLUSION

Appliquée aux sous-munitions à effet dirigé du type de l'ACED de THOMSON BRANDT ARMEMENTS, la détection-visée multimode permet un fonctionnement tous temps, sur tous type de terrain et confère une forte insensibilité aux contre-mesures de toutes natures (leurres, brouilleurs, camouflages).

Cette technologie disponible au sein de THOMSON BRANDT ARMEMENTS est intégrable dans les sous-munitions à effet dirigé mais aussi dans d'autres types de munitions intelligentes, elle constitue l'un des axes stratégiques du développement de TBA.

Discussion

Discussor's name :   Dr. Pfeiffer, GE

Comment/Question :

What happens if more than one target is present in the battlefield? Can the submunitions distinguish between these targets?

Author/Presenter's reply :

Si plus d'une cible est présente dans l' empreinte la première cible détectée est attaquée. La strategie retenue est de ne pas distinguer les cibles atteintes des cibles non atteintes afin d'éviter ne simulation d'atteinte de ces dernières, qui interdirait le tir et les protégerait.

Discussor's name :   E. Schweicher, BE

Comment/Question :

Etant donné l'aspect verdatre de la lentille du capteur IR, je suppose qu'il s'agit d'une lentille au Si et que le capteur travaille dans la bande de 3 à 5 microns.

Author/Presenter's reply :

Ceci est vrai, le senseur IR presenté sur la vue considérée possède une lentille au Si et travaille dans la bande II (3 à 5 microns).

Discussor's name :   F. Ulaby, Univ. of Michigan, US

Comment/Question :

What's new in your presentation? The strategy and approach you described have been discussed in the literature for 20 years, how is your strategy different?

Author/Presenter's reply :

La strategie presentée de Detection-Visée est celle retenue par THOMSON BRANDT ARMEMENTS pour ses sous-munitions ACED. Elle est developpée dans l'industrie française depuis peu (quelques années) mais aussi dans l'industrie allemande (SMART du GIWS). Le SADARM Américain à ma connaissance utilise aussi une strategie analogue avec cependant un système de senseur moins evalué et moins efficace; si j'avais à choisir entre le SADARM et l'ACED c'est ce dernier que je choisirai.

Time-Dependent Properties of a Diode Laser Beam after Propagation through Expanding Gun Blast

A.V. Kay
Institut Franco-Allemand de Recherches de Saint-Louis (ISL)
5 rue du Général-Cassagnou
F 68301 Saint-Louis
France

SUMMARY

Laser radiation used to transmit signals from a powder gun system to a high-tech projectile in flight suffers considerable beam quality degradation caused by the muzzle exhaust. This study is to provide some experimental data about the phenomena involved. Two laser beams are adjusted parallel to the barrel axis of a 40 mm-bore gun, at a horizontal distance of about 1.5 m. To make handling easier, diode lasers of 670 nm wavelength are utilized. Two different receivers are installed, accordingly, mounted about 11 m from the muzzle.

The first one comprises a variable diaphragm and a lens focussing the transmitted and the forward scattered radiation on a sensor. The intensity fluctuations generated by the expanding gun blast increase with decreasing free aperture, simulating a sensor at elongated distance in this way, but generally the spectral density of these fluctuations decays rapidly above approximately 2 kHz. Frequency spectra are also determined as criteria for the recognizability of sine wave intensity modulated signals with modulation frequencies between 1 and 40 kHz.

The second receiver consists of a CCD linear array with high spatial resolution. A series of up to 15 consecutive intensity profiles across the second laser beam, with a shortest integration time of 2 ms each, can be stored in a memory device. The following time-dependent properties are determined: beam extinction (down to 0.1), beam broadering, and beam wander (both up to 2 mrad). Probability distributions of the characteristic beam parameters verified 0.5 s after firing are reported. Finally, a simple experimental simulation of some gun blast effects is described, suitable for laboratory tests.

1. INTRODUCTION

Recent progress in the development of infrared diode lasers with improved features like output power, beam quality, ease of intensity modulation, and operation temperature, suggests their application in military communications links. This study considers the particular case of an optical command link between a mobile launching system with a conventional powder gun and a high-tech projectile, the trajectory of which may be corrected appropriately during the terminal phase of its target approach (command guided, modified beam rider system).

Unfortunately, the period of time when corrective signals (pulsed or intensity modulated laser radiation) ought to be transmitted to the projectile in flight coincides with the progressing expansion of the gun blast. For projectiles with initial velocities between 1 and 2 km/s the first two seconds after firing are concerned. The interaction of a laser beam traversing the muzzle exhaust may cause distortions of the beam quality which by far exceed those resulting from long-distance propagation through the natural atmosphere.

The propagation of laser beams through the atmosphere under a variety of meteorological conditions is very well documented in the literature (e.g. Refs 1 to 5) and can be described by computer codes with sufficient accuracy (Ref 6). Obscuration effects in battlefield environments are also reported (Refs 7 and 8, and references therein). However, few experiments have been published, to the author's knowledge, on the particular problem mentioned above (Refs 9 and 10).

Modelling of this problem seems to be out of range, considering the complexity of the phenomena involved. Gun blast comprises shock waves, muzzle flash, unsteady turbulent flow of hot, partially reactive gaseous combustion products, mixed with aerosols like particles of unreactivated propellant, metal wear, soot, and droplets of condensing water vapour. The characteristic properties of a laser beam traversing this chaotic medium are degraded significantly by absorption and scattering generating intensity attenuation, intensity fluctuations, beam broadening, and beam wander, all of these depending on the time after firing.

This investigation is confined to the particular effects caused by expanding gun blast. Experimental data are provided which may be taken into account in intended feasibility studies. First results have been reported elsewhere (Ref 11).
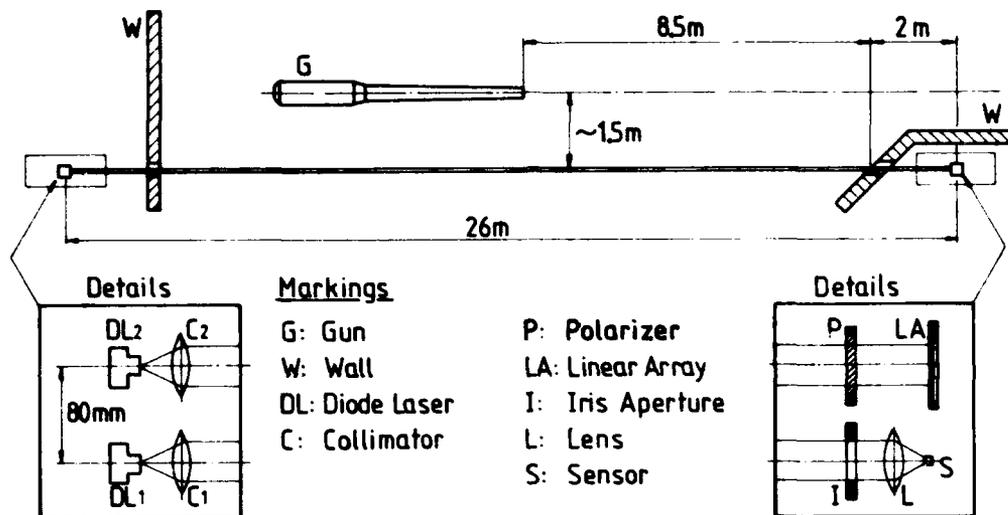
Fig. 1 Experimental configuration (schematic ground plan - not to scale) with details of sources and receivers

2. EXPERIMENTAL ARRANGEMENT

The experimental configuration sketched in Fig. 1 results from a compromise between the expected situation on a mobile launching system, e.g. a tank, and the technical restrictions given on the firing range. Two laser beams, only 8 cm apart from each other, are aligned parallel to the barrel axis of a 40 mm-bore powder gun, at a horizontal distance of about 1.5 m. A smaller space would have been preferable. The heights above the ground level are 1.4 m for the laser beams and 1.2 m for the barrel axis. The gun accelerates sub-calibre projectiles to a velocity of about 1800 m/s, using 430 g of nitrocellulose propellant and releasing 0.4 m^3 of gaseous combustion products. For all experiments, the gun was operated by a pyrotechnical team.

The lasers and two corresponding receivers are mounted on optical tables (see Fig. 1). Protective walls, vibration isolation by means of pneumatic springs with elastomeric damping pads and sound absorbing casings proved to be absolutely necessary in order to avoid the transfer of ground borne and acoustical shock waves from the gun to the optical equipment. Principally, the number of optical elements was kept as small as possible to prevent sources of optical interference and other beam quality degradation.

The interaction zone of the expanding gun blast with the laser beams is estimated at an effective length of roughly 8.5 m, extending between two planes normal to the laser beams: the first one at the muzzle, the

other one at the orifice in the protective wall in front of the receivers. The centre of this span is defined to be the "scattering centre" of deflected irradiance contributions.

Though diode lasers radiating in the near infrared region will probably be employed in future real systems, diode lasers emitting visible radiation (Toshiba TOLD9215s, wavelength 670 nm, maximum output power 10 mW) have been utilized in this study so far, to make handling easier. The effects to be examined should not differ essentially from those expected of laser radiation in the near infrared, first, because interactions with aerosols and turbulent gas flow structures are predominating over molecular absorption and scattering in gun blast, and, secondly, because any wavelength dependence (e.g. Mie scattering) will be compensated by the extended size distributions of particles and refractive structures in the expanding exhaust.The following coordinates will be used: z for the direction of the laser propagation, x for the vertical axis, and y for the horizontal axis.

The linearly polarized diode lasers, DL1 and DL2 in Fig. 1, are mounted with their electrical field vectors oriented in the y - direction. The beams are shaped by collimators, C1 and C2, resulting in the full cone angles of the beam divergencies, Θ_x and Θ_y, and the mean full widths of the elliptical beam spots inside the interaction zone, w_x and w_y, which are shown in Table 1 (measured at e^{-2}-intensity levels). The spot sizes at the iris aperture and at the linear array are given in

brackets, accordingly. These dimensions are important for estimating averaging effects over turbulent structures in the expanding gun blast.

Laser	Θ_x	Θ_y	w_x	w_y
DL1	0.18	0.4	6.5 (7.5)	10.5 (13.0)
DL2	0.13	0.7	6.5 (7.3)	14.5 (19.0)
	mrad		mm	

Table 1

Two different detector units are installed (see Fig. 1). The first one comprises an iris aperture and a lens focussing the transmitted and the forward scattered irradiance contributions on a single element photovoltaic sensor, the signal of which will be called "measured intensity" in this paper (lens diameter 20 mm; half cone acceptance angle 5°). By decreasing the free aperture of the diaphra··· a sensor may be simulated which is situated at a more distant position according to geometrical affinity.

The second detector consists of a charge-coupled device (CCD) linear array with high spatial resolution, oriented vertically. Covering the small principal axis of the elliptical spot of the second laser beam, it allows to measure beam profiles, i.e. irradiance distributions averaged over its integration time. Technical details will follow in section 3. A polarizer in front of the linear array ensures an appropriate intensity attenuation. Due to the small gap between the two laser beams, the signals of the two receivers, when affected by expanding gun blast, are expected to be correlated.

3. DATA ACQUISITION AND EXPLOITATION

All controlling and recording devices, connected to the receivers by shielded cables of 15 m length, are arranged protected in a bunker. The zero time of all recording devices is related to the same trigger signal originating from a pressure probe mounted in the combustion chamber of the gun (trigger threshold set to 200 MPa). This time scale will be called "time after firing" in the diagrams, though it still lasts 3.6 ms until the projectile leaves the muzzle (velocity 1800 m/s). However, this time difference is negligible in all diagrams, with the exception of Fig. 10, as indicated.

3.1 Measured Intensity

The signal of the photovoltaic sensor is fed to transient recorders (4 channels of 8 kbytes each, digital resolution 8 bits). The bandwidth of this detection unit as a whole amounts to 50 kHz. The sampling rates of the transient recorders were chosen appropriately, either to

cover the wanted time interval after firing or to ensure that the expected highest frequencies in the registered intensity fluctuations are resolved with sufficient accuracy. For instance, the intensity modulated laser signals were sampled at the rates $f_s = 100\ f$, with f being the modulation frequency. Frequency spectra of these "measured intensities" were computed, for selected time intervals, using a standard FFT (Fast Fourier Transform) routine.

3.2 Beam Profiles

The CCD linear array mentioned in section 2 consists of 1754 diode cells extending vertically over a length of $x \approx 17.5$ mm (Thomson-CSF TH7803A, pixel width $\Delta x = 10\ \mu m$). 1728 diodes are actively sensing, whereas a few of them at the extremities of the array are inactivated or covered, thus yielding a zero reference signal and an equivalent signal to the dark current, respectively, the latter being subtracted from the output signals of the active cells after the preset integration time during the readout cycle. Therefore, the signal of each active cell is proportional to the local radiant energy received, i.e. the integral of the irradiance over the diode area and over the integration time. The shortest integration time possible, $t_I = 2$ ms, is applied throughout this paper.

The linear array is connected to a special controlling and recording device which was developed at ISL (Ref 12). After the arrival of an external trigger signal, a series of up to 15 consecutive beam profiles can be stored in the memory of this instrument (digital resolution 8 bits), with the integration time interval t_I between consecutive profiles. Since the external trigger event and the internal clock with period t_I of the controlling unit are totally independent of each other, there results a systematic time ambiguity of $\pm\ t_I/2$ relative to the trigger event for each series of stored profiles. This should be taken into account when comparing profiles of various shots with one another or with recorded signals of the photovoltaic sensor. The registered signals of both receivers are transferred to a personal computer for durable storage and data processing.

A typical initial profile covering the small principal axis of the elliptical spot of the second diode laser beam is demonstrated in Fig. 2. At both extremities the zero reference level can be recognized. The observed noise is generated by optical interference mainly inside the protective window in front of the linear array chip.

3.3 Matching of Model Function

The solid curve is the result of data processing: a least-squares fit of a gaussian normal distribution g(N) with four parameters, A_1 to A_4, to the experimental data of the active diodes. The gaussian curve is described by the equation

$$g(N) = A_1 + A_2 \cdot e^{-4(\ln 2)((N-A_4)/A_3)^2} \quad (1)$$

where N : diode number
A_1 : bias level
A_2 : peak amplitude
A_3 : width (FWHM)
A_4 : peak position
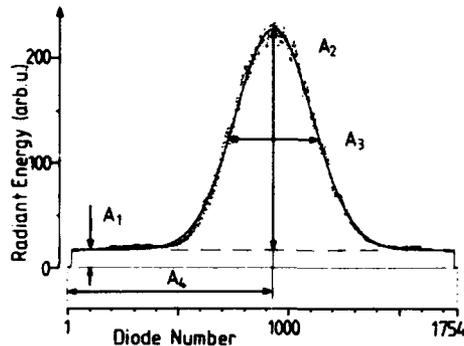
<u>Fig. 2</u> Laser beam profile and best fit of gaussian curve with 4 parameters

The radiant background in Fig. 2 was increased "artificially" by additional homogeneous irradiation of the array. As the diode cell width amounts to $\Delta x = 10$ μm, the diode number N may be replaced by the linear dimension $x/\mu m = 10$ N; A_3 and A_4 should be transformed adequately. The full width at e^{-2}-intensity level exceeds the full width at half-maximum (FWHM) by the factor $(2/\ln 2)^{-0.5} \approx 1.7$.

Though diode lasers do not provide exact gaussian intensity distributions, the agreement is sufficiently good, which is also confirmed by linear-correlation coefficients r > 0.993 for the initial profiles. In this way, a data reduction has been achieved down to four parameter values which now represent the beam profile.

The same model function g(N) is also applied to the beam profiles distorted by expanding gun blast, though there arises a principal discrepancy between model and reality. The disturbed beam profiles generally consist of at least two contributions. The first one is a gaussian profile of the initial width, attenuated by absorption and scattering. The second contribution is produced by scattering processes which cause a broadening as compared with the initial profile; its deteriorated shape cannot be predicted easily. Local focussing effects may give rise to additional contributions. Nevertheless, this matching procedure allows a kind of classification of the distortions, even in those "worst cases", when several small peaks and asymmetry appear in the intensity distributions. The linear-correlation coefficients generally remain r > 0.92, but may fall down to 0.8 in rare extreme cases.

Before each shot, 10 initial beam profiles were registered. The mean values of the fitted gaussian curves' parameters yield four reference quantities, termed A_{10} to A_{40} (standard deviation normally < 1%).

The parameters of best fits to the beam profiles registered after interaction with gun blast, at definite times after firing, are called $A_1(t)$ to $A_4(t)$. From these, the following four reduced parameters will be determined (in relation to the initial mean parameters), which facilitates the comparison of the results from various shots:

$$
\begin{aligned}
\Delta a_1(t) &= (A_1(t) - A_{10})/A_{20} \quad (2)\\
a_2(t) &= A_2(t)/A_{20}\\
a_3(t) &= A_3(t)/A_{30}\\
\Delta a_4(t) &= (A_4(t) - A_{40})/A_{30}
\end{aligned}
$$

After each shot, 10 additional profiles were taken as a stability test of the alignment.

4. RESULTS AND DISCUSSION

It should be first mentioned that the expansion behaviour of gun blast generally shows a large variation from shot to shot, even with identical shot parameters and under constant environmental conditions. One of the reasons could be identified, but not influenced: the *guiding petals of the subcalibre projectiles discard in different ways with changing spatial orientations* causing various preferential directions of gas flow. However, the random behaviour remains a principal feature of the chaotic process. Therefore, a large number of experiments is necessary to eliminate the statistical uncertainty.

Unless otherwise stated, the diagrams show records or results of continuous wave (cw) laser radiation.

4.1 Measured Intensity and Fluctuations

The time dependence of the "measured intensity" I(t), defined in section 2, is depicted in Fig. 3 for the first 0.8 s after firing. The signal I(t) represents the integral of the transmitted and scattered contributions of the first laser beam, which pass the free aperture in front of the photovoltaic sensor (see Fig. 1). I(t) is normalized by the initial intensity I_0. The first intensity spikes originate from shock waves (down) and the muzzle flash (up). These phenomena are illustrated in detail in Fig. 10 and will be discussed later. A sudden intensity fall occurs at about 100 ms after firing, when the main extinction effects by the muzzle exhaust start. Afterwards, the mean intensity gradually approaches its
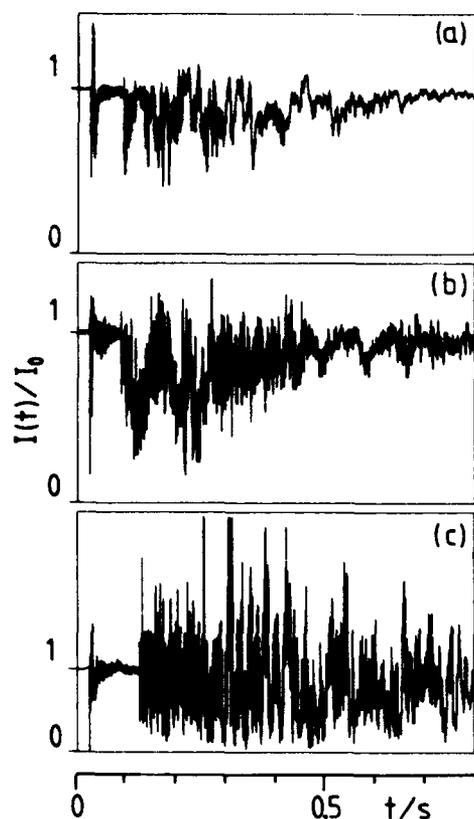
Fig. 3 Measured intensity vs. time after firing, for three different aperture diameters d/mm : (a) 20, (b) 10, (c) 5

Fig. 4 Frequency spectra determined for the three records of Fig. 3 (for t from 0.4 s to 0.8 s)

initial level; this may last up to 5 s, mainly depending on the cross-wind speed.

One essential phenomenon is demonstrated in the three parts of Fig. 3. With decreasing diameter d of the free aperture, I_0 diminishes and averaging effects over absorbing and scattering structures within the beam spot dimensions along the interaction zone become less significant, as can be concluded from the growing intensity fluctuations which temporarily even exceed the initial intensity level. In a rough approximation, the two lower of the three diameter values d/mm = (20; 10; 5) correspond to the simulation of a sensor with maximum aperture which is placed at elongated distance D from the "scattering centre" (defined in section 2): D/m = (actually 6.3; 12.5; 25).

Frequency spectra of the "measured intensities" I(t) were determined for the period of time 0.4 s to 0.8 s after firing, which is dominated by intensity fluctuations, while the mean intensity remains almost constant (Fig. 4). The amplitude A(f) is assumed to be nondimensional; it is proportional to the spectral density, normalized appropriately, of the signal I(t). The large contributions to frequencies f < 50 Hz have been

omitted. As expected, the three spectra reflect the tendency of increasing frequency contributions, i.e. fluctuations, with decreasing diameter d. The insertion in Fig. 4(c) is to be compared to the other two spectra. Fortunately, the magnitude of A(f) decays rapidly for frequencies greater than about 2 kHz. This finding suggests using higher frequencies for the transmission of pulsed or intensity modulated laser radiation.

4.2 Modulated Signals

In order to check this implication, measurements of sine-wave intensity modulated laser radiation were performed, using the same detecting method as described above. The free aperture in front of the sensor was set to d/mm = 5 and 2, simulating sensor distances D/m = 25 and 62.5, respectively. Five modulation frequencies f/kHz ranging between 1 and 40 were applied. A relatively high sampling rate of 100 data points per sine wave period was chosen.

Six selected records of "worst cases" found in the registered signals are represented in Figs. 5 and 7, showing 40 periods each. The records start at 0.5 s after firing; the period of time around this instant is supposed
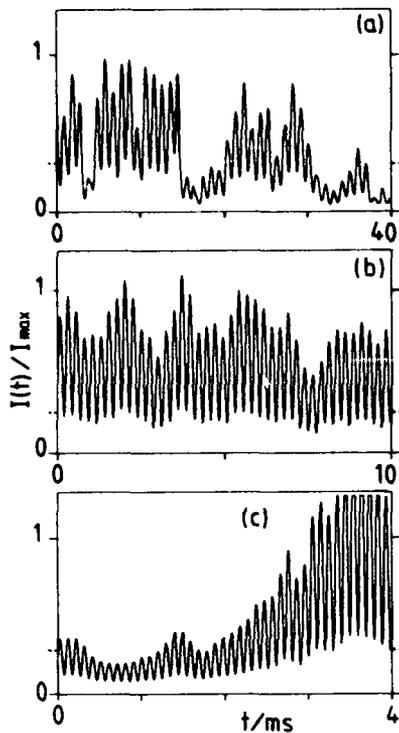
Fig. 5 Measured intensity vs. time, starting 0.5 s after
firing, for three different sine-wave modulation fre-
quencies f/kHz : (a) 1, (b) 4, (c) 10; (40 periods each;
aperture diameter d = 5 mm; --: I_{min}/I_{max})
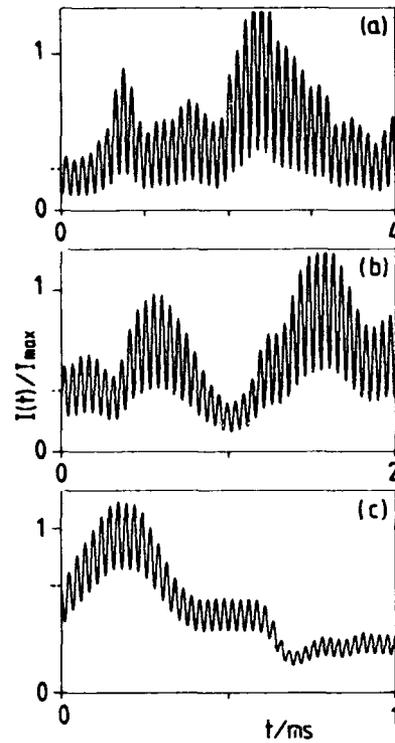
Fig. 7 Same as Fig. 5, but with d = 2 mm and in-
creased frequencies f/kHz : (a) 10, (b) 20, (c) 40
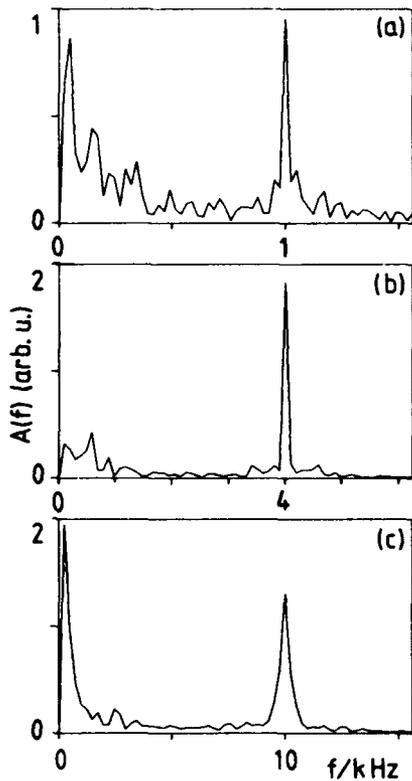
Fig. 6 Frequency spectra determined for the three
records of Fig. 5
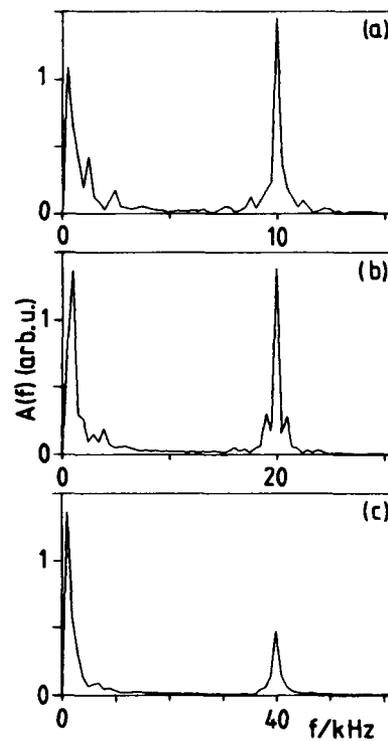
Fig. 8 Frequency spectra determined for the three
records of Fig. 7

to be relevant for the transmission of commands to a projectile in flight. The "measured intensity" I(t) is normalized by I_{max}, the maximum intensity of the modulated initial radiation. The corresponding minimum value is I_{min}. For most of the modulation frequencies the modulation degree $m = (I_{max} - I_{min})/I_{max}$ was 0.7, falling to 0.62 and 0.34 with f/kHz = 20 and 40, respectively (due to limitations of the diode driver unit).

Judging subjectively, the modulated signals can be "recognized" at any phase of the records, though the signal in Fig. 5(a) with f = 1 kHz is most affected by fluctuations and the low modulation degree with f = 40 kHz in Fig. 7(c) seems to be disadvantageous.

selected records were determined (Figs. 6 and 8), where all modulation frequencies appear as spikes. The digital frequency resolution amounts to $\Delta f = f/40$ (the amplitude A(0) is set to 0).

From these diagrams, the aspects mentioned before become more evident. The background noise of the spectral density is highest in the vicinity of the modulation frequency f = 1 kHz and decreases with increasing modulation frequency. The relatively small peak with f = 40 kHz is caused by the low modulation degree. Comparing the spectra of Figs. 6(c) and 8(a), both with f = 10 kHz, the reduction of the free aperture in this region does not seem to increase the noise substantially. Though the simulated distance is still far from the expected values in real applications, these findings imply positive predictions.

4.3 Comparison of Beam Profiles and Measured Intensities

The second detection method described in section 3.2, i.e. the registration of intensity profiles of the second laser beam, averaged over the integration time $t_I = 2$ ms of the linear array, may provide additional information about the kind of distortions observed with the first method which integrates spatially over the beam spot.

Fig. 9 Series of 15 beam profiles scanning the muzzle flash
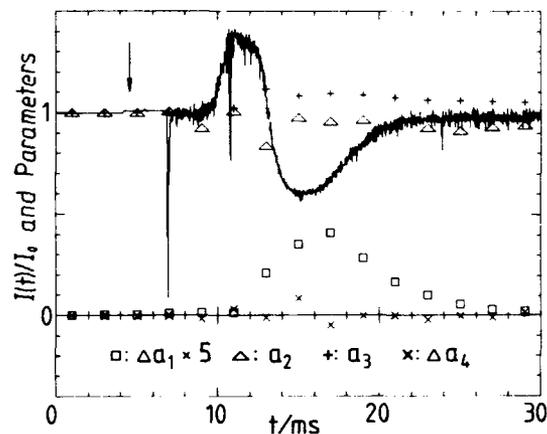
Fig. 10 Measured intensity and reduced parameters for the profiles of Fig. 9 vs. time (arrow indicating the time of the projectile's exit)

A series of 15 consecutive profiles is shown in Fig. 9 (high diode numbers represent the top of the vertically mounted linear array), extending over 30 ms after firing. During this period of time shock waves traverse the laser beams, and the muzzle flash lightens the scene. Nevertheless, the profiles appear to be identical, at first glance. Even the optical interference pattern remains unchanged. These findings demonstrate the stability of the optical alignment. Small alterations of the

As a more objective criterion for the recognizability of the modulated signals the frequency spectra of the six

profiles can be detected by thorough examination, e.g. at 12 ms and 14 ms, and 'he bias level reaches a maximum at 16 ms.

These small changes becc me evident by utilizing the reduced parameters defined in the equations (2), after matching of gaussian curves (equation (1)) to the individual profiles. The corresponding reduced parameters are illustrated in Fig. 10, together with the "measured intensity" of the first laser beam which was recorded simultaneously with the profiles (it is the very first section of the record in Fig. 3(a)).

After the muzzle exit, the front and rear shock waves of the projectile traverse the laser beams (two spikes down). The muzzle flash starts between the shock waves, but is soon superposed by a broad extinction zone between 12 ms and 20 ms which originates from the discarding guiding petals. However, in the variation of the reduced peak amplitude $a_2(t)$ this extinc-

tion zone does not exist, though the effects of the shock waves are visible at a delay of 2 ms relative to the spikes. This delay can be partially explained by the principal time ambiguity of the profiles, as mentioned in section 3.

One may conclude that the extinction zone is caused by phase fluctuations of the laser radiation which result in destructive interference in the signal of the photovoltaic sensor, averaged over the free aperture. The profiles of the linear array, however, are not affected by these random phase distributions, since the diode cell dimensions (≈ 10 μm) are sufficiently small.

The reduced bias level $\Delta a_1(t)$ clearly shows the radiant background produced by the muzzle flash, again at a time delay of about 2 ms. As the muzzle is situated off the field of view of the receivers, only an outer sector of the reacting gun blast (muzzle flash) contributes to the detected background.

A representation analogous to the two preceding diagrams is given in Figs. 11 and 12. Starting at 100 ms after firing, the shown period of time covers the moment when the front of the expanding gaseous products of combustion, loaden with particles of various kinds, passes the laser beams. After the first five profiles,


Fig. 11 Series of 15 beam profiles starting 0.1 s after firing, scanning the maximum extinction by the muzzle exhaust
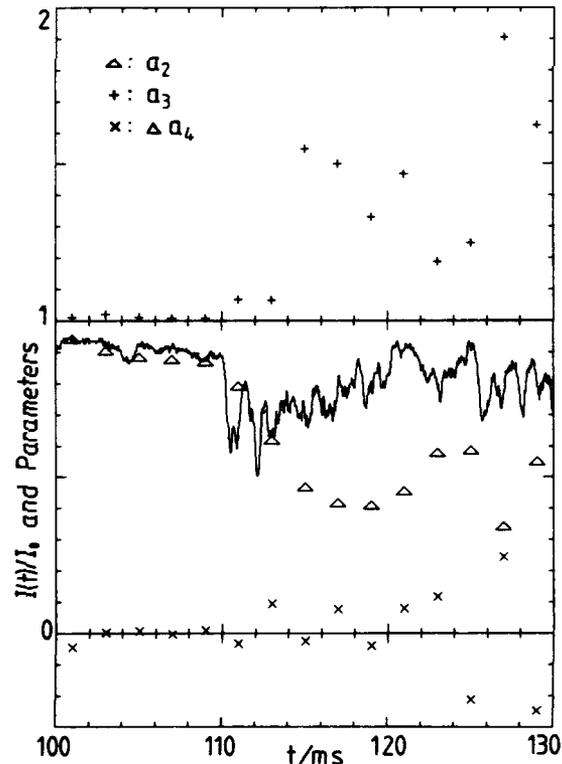

Fig. 12 Measured intensity and reduced parameters for the profiles of Fig. 11 vs. time after firing

which are comparatively unchanged, significant distortions of the profiles arise, showing the features of intensity attenuation, beam broadening, and beam wander. This behaviour is obvious in Fig. 11, and is reproduced by the corresponding reduced parameters in Fig. 12 (as $\Delta a_1(t) = 0$, it has been omitted). The "discontinuous" variation of the last four profiles in Fig. 11 suggests that the time resolution of $t_I = 2$ ms is too low to follow the rapid alterations during this phase of the gun blast expansion.

The shapes of the broadened profiles and the limited values of the reduced beam width $a_3(t)$ in Fig. 12 prove that, among the scattering processes, those contributing to the forward directions are predominant. The reduced peak amplitude $a_2(t)$ and the reduced beam width $a_3(t)$ behave in an opposite manner, following, very roughly, the relation

$$a_2(t)\, a_3(t) \approx I(t)/I_0. \qquad (3)$$

where $I(t)$: measured intensity
I_0 : initial intensity

This relation represents a conservation law for the radiant energy received by the linear array during a constant phase of $I(t)$. It is plausible for the orientation of the linear array, applied in this study, relative to the elliptical beam spot.

Finally, it is remarkable that an oscillation of the reduced peak position $\Delta a_4(t)$ is obviously stimulated by the front of the combustion products at 110 ms (see Fig. 12; period ≈ 4 ms, increasing amplitude). This beam deflection is supposed to be created by periodic eddies in the exhaust, and not to be due to mechanical vibrations with 250 Hz of any optical mounts.

As the period of time around 0.5 s after firing is assumed to be relevant for the transmission of corrective commands to the projectile in flight, a large number of beam profiles was taken in this particular time domain.

An example of 10 consecutive profiles is given in Fig. 13, together with one initial profile for comparison. The profiles still do show rapid alterations and all

Fig. 13 Series of 10 distorted beam profiles starting 0.5 s after firing and initial profile for comparison
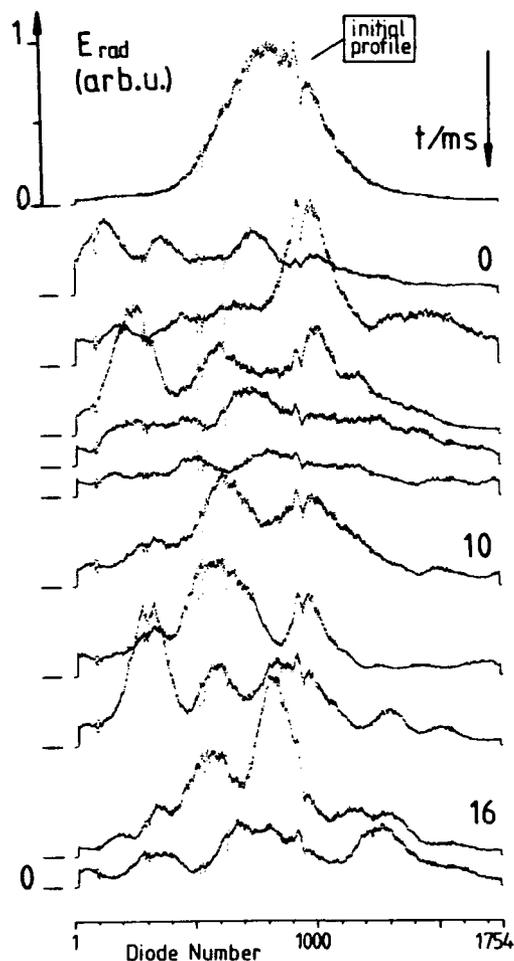

Fig. 14 Series of 10 distorted beam profiles produced by interaction with hot air turbulence - and initial profile for comparison

the features of distortions mentioned above. Additionally, a sharp peak due to local focussing by optically turbulent structures is observed with the profile at (500 + 14) ms. The persisting significant deteriorations should not be surprising, if one remembers the strong intensity fluctuations present in Fig. 3(c) at 0.5 s and later, measured with comparatively small free aperture, thus rendering averaging over turbulence elements less effective.

4.4 Simulation of Gun Blast Effects

The main cause of the distortions observed 0.5 s after firing can be demonstrated by a simple experimental setup. A fan producing a strong flow of turbulent hot air (pipe diameter 35 mm; flux rate 0.08 m^3/s; air temperature 800 K) was placed close to the "scattering centre" (the centre of the interaction zone) at an angle of 45° relative to the direction of the laser beams. The effects on the beam properties are illustrated in Fig. 14 with a series of 10 profiles. The achieved alterations even exceed those generated by the expanding gun blast in Fig. 13, especially considering beam broadening. Qualitatively, the features of the profiles in both figures look quite similar.

A frequency spectrum in Fig. 15, determined from a
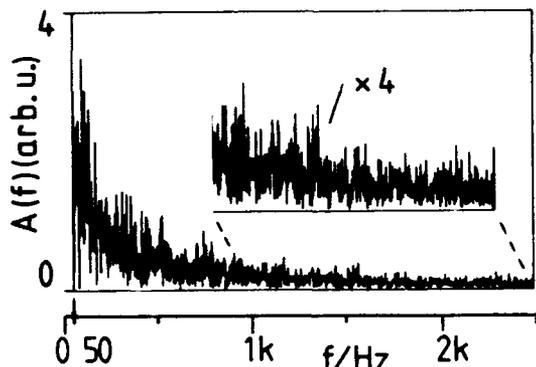
Fig. 15 Frequency spectrum of measured intensity transmitted through hot air turbulence

record of the measured intensity of 0.4 s duration (free aperture d = 20 mm) shows the same rapid decay of the spectral density with increasing frequency, as it is known from gun blast effects (Fig. 4(a)). Again, the turbulent hot air creates even stronger fluctuations than the gun blast.

From these similarities one may deduce that the observed gun blast effects at 0.5 s after firing are mainly caused by optical turbulence, i.e. by volume elements of gas with changing refractive indices. Thus, the described simple setup allows to perform adequate tests of the optical equipment in the laboratory.

4.5 Probability Distributions of Profile Parameters

No differences in the characteristic properties of the initial profiles integrated over t_i = 2 ms could be observed between cw and modulated laser radiation. Therefore, 150 profiles of modulated radiation, registered under identical shot and weather conditions about 0.5 s after firing, were analyzed in order to achieve probability distributions (normalized histograms; the sum of the cell probabilities P equals 1) of their reduced parameters according to equation (2). The results are depicted in Fig. 16. The reduced bias level
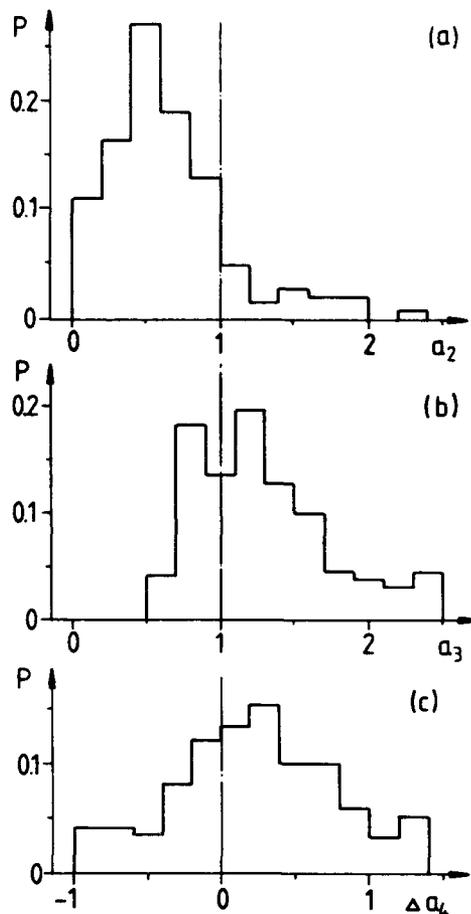

Fig. 16 Probability distributions of three reduced parameters (resulting from 150 beam profiles registered 0.5 s after firing)

$\Delta a_1(t)$ has been omitted, since it is negligibly small for all profiles. The relevant reference value, the average of the mean initial beam widths (FWHM), is A_{30} = 4.30 mm (± 4%).

The histogram of the reduced peak positions Δa_4 resembles a gaussian normal distribution with a width (FWHM) of 1.2 A_{30}, the centre of which is shifted by approximately 0.2 A_{30} ≈ 0.9 mm upwards on the vertically mounted linear array, relative to the initial peak position (Fig. 16(c)). The number of experiments is not sufficient, so far, to give a clear explanation of this

asymmetric displacement. The maximum beam deflections measured here range up to $\pm 1.1\ A_{30}$. Relative to the assumed "scattering centre", this corresponds to an angle of ± 0.75 mrad in the vertical direction. Extreme beam deflections found at earlier times after firing reach angles of up to 2 mrad.

The probability distribution of the reduced peak amplitudes a_2 in Fig. 16(a) shows a clear maximum at half the initial value, due to extinction processes. However, there exist small amounts of increased peak amplitudes $a_2 > 1$, up to more than twice the initial value. These result from local focussing effects by optically turbulent structures, the influence of which may also be observed in Fig. 16(b) at values of the reduced beam width $a_3 < 1$. The distributions of a_2 and a_3 are correlated, according to equation (3). Absorption as well as scattering give rise to a decrease of $a_2 < 1$, whereas only the scattering processes can cause beam broadening with an increase of $a_3 > 1$. Thus, the relative contributions of absorption and scattering should be reflected by the probability distributions.

The values of the peak intensity attenuation extend down to 0.1, while the maximum beam width (FWHM) amounts to 2.4 A_{30}, corresponding to a full-cone divergence angle (at e^{-2}-intensity level) of $\Theta_x \approx 1.8$ mrad, relative to the "scattering centre".

5. CONCLUSIONS

Some experimental data about the characteristic properties of diode laser radiation after interaction with expanding gun blast have been achieved. In this study, the priority was set to the period of time about 0.5 s after firing. Other time domains, relevant for the transmission of corrective commands to a projectile in flight, still remain to be examined, as well as the application of laser pulses. As a consequence of the reported findings, pulse rates of at least 10 kHz are recommended. Applying dimensional considerations to the gas expansion process, these results should be useful for estimating optical distortions also with guns of larger calibres.

REFERENCES

1. Andreas, E.L., Ed., "Selected Papers on Turbulence in a Refractive Medium", SPIE Vol. MS25, 1990

2. Bissonnette, L.R. and Miller, W.B., Eds., "Propagation Engineering: Fourth in a Series", SPIE Vol. 1487, 1991

3. Kohnle, A. and Miller, W.B., Eds., "Atmospheric Propagation and Remote Sensing", SPIE Vol. 1688, 1992

4. "Operational Decision Aids for Exploiting or Mitigating Electromagnetic Propagation Effects", AGARD-CP-453, 1989

5. "Atmospheric Propagation in the UV, Visible, IR and mm-Wave Region and Related Systems Aspects", AGARD-CP-454, 1990

6. Azoulay, E., "A Simple Code for Calculating Atmospheric Turbulence Effects on Laser Beam Propagation", Report FfO - 1989/71, Forschungsinstitut für Optik, Germany

7. Heaps, M.G. and Niles, F.E., "Battlefield Obscuration Factors", in Ref 4, pp 13/1-7

8. Niles, F.E., Heaps, M.G., Shirkey, R. C., Duncan, L.D., and Seagreaves, M.A., "Propagation Environments, Effects, and Decision Aids", in Ref 5, pp 14/18

9. Wegner, V., Schultze, G., Lentz, A., and Buderer, G., "Influence de la lueur de bouche d'un canon de 90 mm sur la propagation des faisceaux lasers dans le système TAPIR", Rapport S-RT 919/82, ISL, Saint-Louis, France

10. Fendt, D., "Infrarotoptische Transmissionsmessungen an der Mündungswolke des KPz's Leo 2", (Transl.: "Measurements of IR Transmission through the Muzzle Blast of the Tank Leo 2"), Report TN AE342-21/85, MBB, Ottobrunn, Germany

11. Kay, A.V., "Slow-Motion Acquisition of Laser Beam Profiles after Propagation through Gun Blast", pp 8-16, in Watkins, W.R. and Clement, D., Eds., "Characterization, Propagation, and Simulation of Sources and Backgrounds", SPIE Vol. 1486, 1991

12. König, M. and Baumann, G., "CCD-Bildsensor und Gerät zur Aufbereitung und Speicherung der Bildzeilensignale" (Transl.: "CCD Optical Sensor and Instrument for Treatment and Storage of the Signals of a Linear Diode Array"), Report RT 518/88, ISL, Saint-Louis, France

Discussion

Discussor's name :   D. Clement, GE

Comment/Question :

I assume that there may be potentially a tremendous acoustic interference between the firing gun and the measuring equipment. How did you cope with the problem? How did you make sure you succeeded in separating acoustic artifacts from measured data.

Author/Presenter's reply :

Protective walls, vibration isolation of the optical tables and sound absorbing casings were installed. In addition, tests were performed with a similar configuration where the lasers did not pass through the expanding gun blast. These tests proved sufficient stability of the intensity.

Discussor's name :   D. B. Webb, UK

Comment/Question :

Would the practical exploitation of optical command link to correct the projectile trajectory make use of more than one propagation path?

Author/Presenter's reply :

There are studies which suppose four pulse coded laser beams for the recognition of the trajectory error (e.g. "TAPIR").

INFRARED POLARIZATION SIGNATURES

D L Jordan, G Lewis
DRA (Malvern), St Andrews Road, Malvern, Worcs, WR14 3PS, UK

SUMMARY

Target detection using passive electro-optic devices operating in the 8-14μm band is often limited by background clutter. A possible method of overcoming this limitation may be to use the polarisation content of the image to discriminate between man-made targets and natural background. In this paper laboratory measurements are presented of the polarisation state of 10-6μm radiation reflected from, and emitted by, a range of materials. It is concluded that elliptical polarisation is not of primary importance and that measurements of the degree of linear polarisation appear to provide useful discrimination between man-made objects and 'natural' ones.

1. INTRODUCTION

The detection of targets by passive electro-optic devices such as thermal imagers operating in the 8-14μm band is often limited by scene clutter problems[1] rather than by more fundamental signal to noise effects. A possible method of increasing the signal to clutter ratio is to use the polarisation content of the image to discriminate between man-made targets and natural backgrounds [1,2]. Man-made targets generally consist of a series of regular facets which may be expected to give rise to significant polarisation signatures; in contrast, natural background would not be expected to exhibit preferred polarisation states. In the 8-14μm band the polarisation signature normally consists of both thermally emitted and reflected components, the balance between them depending upon a variety of factors.

In this paper the underlying theory is first outlined in Section 2. Laboratory measurements of the Stokes parameters of emitted and reflected radiation from a variety of materials are then described which support the contention that elliptically polarised radiation is not of significant importance; it is sufficient to study the degree of linear polarisation only. Finally measurements of the degree of linear polarisation arising from emission are described. All the measurements to be described have been carried out at a fixed wavelength of 10-6μm.

2. THEORY

For radiation that is polarised the end point of the electric (and magnetic) vector at each point in space moves periodically around an ellipse with increasing time (elliptically polarised). The ellipse reduces in special cases to a circle (circularly polarised) or a straight line (linearly polarised). By contrast, for unpolarised radiation the end point moves irregularly and the radiation shows no preferential directional properties when resolved in different directions at right angles to the direction of propagation. These cases represent two extremes. In general the variation of the field vectors is neither completely regular nor completely irregular, and the radiation is described as partially polarised.

The polarisation ellipse is conveniently described by the four Stokes parameters, given by [4,5]:

$$I = E_s^2 + E_p^2$$

$$M = E_s^2 - E_p^2$$

$$C = 2E_s E_p \cos \Delta \qquad (1)$$

$$S = 2E_s E_p \sin \Delta$$

where E_p and E_s are the two orthogonal field components and Δ is their phase difference. By convention E_p is in the plane of incidence. They can be directly related to the geometrical description of the polarisation ellipse as follows:[5]

Size: I (= total intensity of beam)

Azimuth Angle: C/M (= $\tan 2\psi$ where ψ is the azimuth angle)

Shape:

$$\frac{|S|}{(M^2+C^2+S^2)^{\frac{1}{2}}} \quad \left(= \frac{2\xi}{1+\xi^2} \quad : \quad \text{ellipticity} = 1-\xi \right)$$

Handedness: sign of S

The azimuth angle is the angle between the x-axis, which is the direction of the s-polarised component and the resultant electric vector. The semi-major axis of the ellipse is a and the semi-minor axis is b; $\xi = b/a$. The handedness describes whether the electric vector rotates clockwise or anti-clockwise around the polarization ellipse.

The Stokes parameters can be readily extended to deal with partially polarized radiation by decomposing it into an unpolarized and a polarized portion that are mutually independent. The degree of polarization P, which is the fraction of the intensity of the radiation that is contained in the polarized component is given by:

$$P = \frac{\left(M^2 + C^2 + S^2\right)^{\frac{1}{2}}}{I_{pol} + I_u} \qquad (2)$$

where $I_{pol} + I_u$ is the total intensity (I) and I_{pol} and I_u signify the polarized and unpolarised parts of it. In the case of partially linearly polarised radiation it is often more convenient to use a simpler expression for P. If the radiation is passed through a rotatable polarizer, then

$$P = \frac{I_{max} - I_{min}}{I_{max} + I_{min}} \qquad (3)$$

where I_{max} and I_{min} are the maximum and minimum values of the transmitted intensity.

The Stokes parameters can be determined by experiment[4]. If $I(\theta,\epsilon)$ describes the intensity of the radiation in the direction making an angle θ with the x-axis, when the y-component is subjected to a retardation of ϵ with respect to the x-component, then

$$I = I(0°,0) + I(90°,0)$$

$$M = I(0°,0) - I(90°,0)$$

$$C = I(45°0) - I(135°,0)$$

$$S = (45°,\Pi/2) - I(135°,\Pi/2)$$

(4)

When linearly polarized light is reflected at an oblique angle from a non absorbing dielectric the intensity is changed by an amount governed by the reflectivity of the surface and the azimuth angle or plane of polarization is rotated; the reflected radiation is still linearly polarized. This is a consequence of the phase difference Δ between the reflected p and s-polarized components being equal to zero or π. When however the perfect dielectric is replaced by a material with a complex dielectric constant, Δ is no longer either zero or π but exhibits a gradual transition between these two values. Consequently reflection of linearly (or partially linearly) polarized radiation from such a material results in the production of elliptically (or partially elliptically) polarized radiation. An example is shown if Figure 1 for sodalime glass; it has been calculated assuming a complex refractive index[6] of $\underline{n} = 2.4 - i0.49$. It can be seen that the angular range over which Δ is not close to zero or π is quite small. This is general for most materials in the 8-14 μm region; for metals it is even narrower. In general the width is of order 20° or less. This region however corresponds to that around the principal angle of incidence where the p-polarized reflectivity is a minimum. Consequently the resultant polarization ellipse even in the small angular range where Δ is not zero or π will be relatively narrow, the radiation approximating to some degree linear polarization.

For thermally emitted radiation

$$\rho(\theta) + \alpha(\theta) + \tau(\theta) = 1$$

(5)

where, referring to intensities, ρ is the reflectivity, α is the absorptivity and τ is the transmissivity of a body; θ is the angle between the surface normal and the line of sight. In thermal equilibrium it follows from Kirchoffs law that $\alpha(\theta) = \epsilon(\theta)$, where ϵ is the emissivity. Consequently for an opaque body

$$\epsilon(\theta) = 1 - \rho(\theta)$$

(6)

This expression is assumed to hold for both p and s-polarization. Because the two components are of unequal strength, the p-component being the stronger, and they are uncorrelated, the result is that the emitted radiation appears partially linearly polarized (p-polarized). Elliptical polarized radiation is not produced by emission. A more detailed description of emission polarization is given by Sandus[7] who includes a detailed discussion of the pioneering work of Millikan[8] carried out in 1895.

It is concluded from the above discussion that elliptically polarized radiation is only likely to occur as a result of the reflection of linearly (or partially linearly) polarized radiation from materials possessing a complex dielectric constant. Even from such materials elliptical radiation will only be produced over a relatively small range of angles. In addition, the p-polarized component is generally significantly smaller than the s-polarized one and so the reflected radiation will approximate,

at least to some degree, the linearly polarized case. Consequently it appears reasonable to assume that the use of the degree of linear polarization as a method for discriminating between man-made targets and natural backgrounds is a viable one.

3. EXPERIMENTAL MEASUREMENTS

The experimental arrangement used is shown in Figure 2. The target was mounted on a rotation stage and could either be heated to about 70°C for emission measurements or illuminated by a CO_2 laser for reflection measurements. For reflectivity studies the laser was operated at 10.6 μm and its plane of linear polarization changed by rotating the half-wave plate ($\lambda/2$). The signal emitted or reflected from the target was chopped and focused via a germanium telescope onto a 50 μm diameter cooled HgCdTe detector connected to a lock-in amplifier. The quarter wave plate, which is needed for the determination of the fourth Stokes parameter, and analysing polarizer were positioned as shown.

Measurements of the Stokes parameters of reflected linearly polarized radiation were made with the incident laser beam polarized at 45° to the plane of incidence, thereby ensuring equal p and s-polarized components. The targets were mounted vertically and the co-ordinate system used is shown in Figure 3. Typical results obtained for smooth (rms roughness = 0.02 μm) sodalime glass are shown for angles of incidence of 54° and 78° in Figure 4. For the 54° case the radiation appears almost linearly polarized with an azimuth angle of 24°. This is as expected from Figure 1 which shows that at 54° the p-polarized reflectivity is very small. The actual measured ratio of semi-minor (b) to semi-major axis (a) of the ellipse is 1/28. As may be anticipated from Figure 1, a somewhat more elliptically polarized beam was observed at 78°, the ratio b/a being approximately a quarter. Preliminary results suggest that increasing surface roughness does not significantly change the measured ellipticity.

A result for a smooth painted metal surface is shown in Figure 5, again for an angle of incidence of 78°. It appears almost linearly polarised, the ratio b/a being 1/44. Similar results were obtained from a range of commercial and military paints. The similarity is to be expected as different paints use similar binders that are infrared absorbing in the wavelength range greater than about 3 μm[9]. One coat of brush applied paint was sufficient to completely extinguish the effect of the substrate; the measured Stokes parameters were identical for wood, metal and glass substrates. For all the targets examined the emitted radiation was, as expected, either unpolarized or partially linearly polarized.

Figure 6 shows a plot of the measured reflectivity of smooth sodalime glass. Superimposed on it are curves calculated from Fresnels equations using the complex refractive index measured with the equipment shown in Figure 2 used as an ellipsometer. The measured refractive index ($\underline{n} = 2.17 - i0.32$) differs slightly from that given in Reference b ($\underline{n} = 2.4 - i0.49$) determined using the Kramers Kronig technique. The agreement between the measured and calculated curves is satisfactory. Figure 7 shows the measured emissivity from the same target, the values being normalised by comparison with a painted target of known emissivity ($\epsilon = 0.95$). Within the accuracy with which the absolute values of the emissivity and reflectivity are known, Figures 6 and 7 confirm the validity of Equation 6.

Figure 8 shows the measured degree of linear polarization P in emission from a variety of targets as a function of the viewing angle. In general, for man-made targets P increases with angle, reaching values of about 60% for sandblasted aluminium at 70°; values for glass and painted surfaces are somewhat lower. In contrast to these materials, natural objects such as wood only

display very low values of P, being less than 5% at 70°. The values for brick and grass were even lower.

4. CONCLUSION

Elliptically polarized radiation is generally only naturally produced via oblique reflection of linearly (or partially linearly) polarized radiation from objects possessing a complex dielectric constant; it is not produced by emission. If the thermal background is unpolarized, as is generally assumed[2], then elliptically polarized radiation should be relatively rare. Even in those situations where it may be more common, such as when hot parts of a complex shaped target emit partially linearly polarised radiation which is then reflected from surrounding metal or painted surfaces, the phase difference Δ between the reflected p and s-polarized components is only significantly different from zero or π over a small range of angles. In addition, within this range, the reflectivity of the p-polarized component is generally significantly smaller than the s-component. Consequently it appears that elliptical polarizatio n is of limited importance in the 8-14 μm band.

Measurements of the reflectivity and emissivity as a function of angles support the generally held view that $\epsilon_p(\theta) - 1 - \rho_p(\theta)$ and $\epsilon_s(\theta) = 1 - \rho_s(\theta)$. In addition, measurements of the degree of linear polarisation of emitted radiation as a function of viewing angle have been presented for a range of man-made and natural materials. They confirm that natural materials exhibit very low levels of polarization whereas man-made ones such as metal, glass and painted surfaces show quite high degrees of linear polarization. The reason for this difference is not entirely clear.

Figure 1. Calculated reflectivity and phase difference for soda lime glass 10.6μm
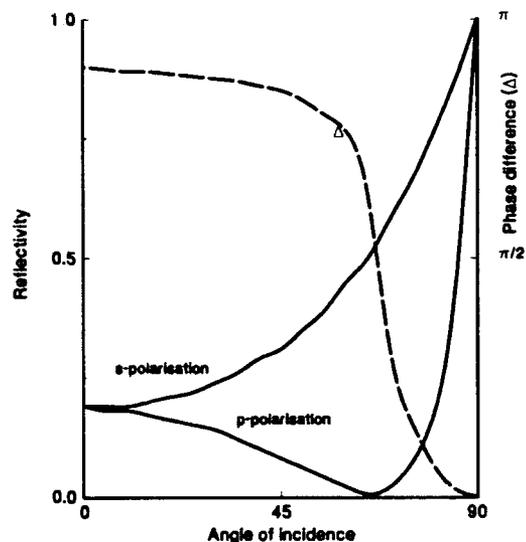
REFERENCES

1   Rogne, T.J., Smith, F.G., Rice, J.E., "Passive Target Detection using Polarized Components of Infrared Signatures", SPIE Vol. 1317, Polarimetry: Radar, Infrared, Visible, Ultraviolet and X-Ray (1990) 242-251.

2.   Tooley, R.D., "Man-made Target Detection using Infrared Polarization," SPIE Vol 1166 Polarization Considerations for Optical Systems II (1989) 52-58.

3.   Acquista, C., "Polarization Properties of Natural Background Materials in the IR," SPIE Vol 933 Multispectral Image Processing and Enhancement (1988) 155-158.

4.   Born, M., Wolf, E., "Principles of Optics", 5th Edition, Pergamon Press (1975).

5.   Clarke, D., Grainger, J.F., "Polarized Light and Optical Measurement," Pergamon Press (1971).

6.   Lane, D.W., "The Optical Properties and Laser Irradiation of Some Common Glasses", J-Phys. D.Appl. Phys. 23 (1990) 1727-1734.

7.   Sandus, O., "A Review of Emission Polarization," Appl. Optics 4 (1965) 1634-1642.

8.   Millikan, R.A., "A Study of the Polarization of the Light Emitted by Incandescent Solid and Liquid Surfaces II," Phys. Rev. 3 (1895) 177-192.

9.   Sandford, B.P., "Infrared Reflectance of Aircraft Paints," AFGL-TR-84-0307, (AD C001-133), Air Force Geophysics Laboratory, Hanscom AFB (1984).
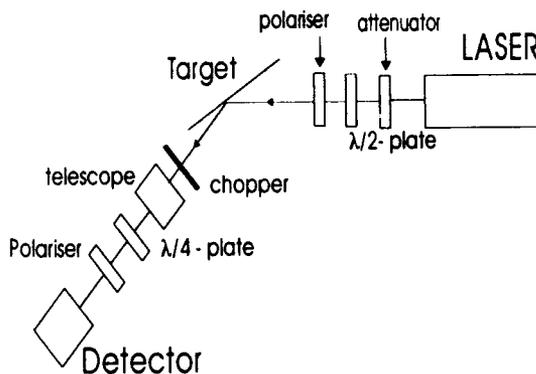

Figure 2   Experimental arrangement.
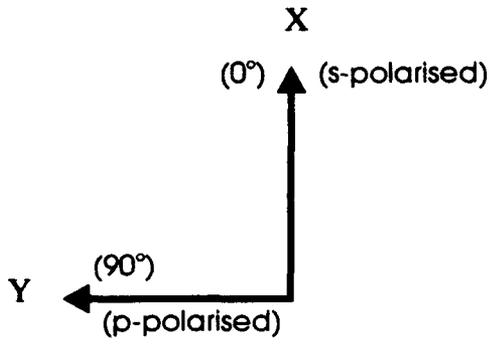
Figure 3   Coordinate system used.

Figure 4. Experimental result for soda lime glass,
for angles of incidence of 54° and 78°.

Figure 5. Experimental result for paint
at an angle of incidence of 78°.

Figure 6. Measured & calculated reflectivity of
sodalime glass.
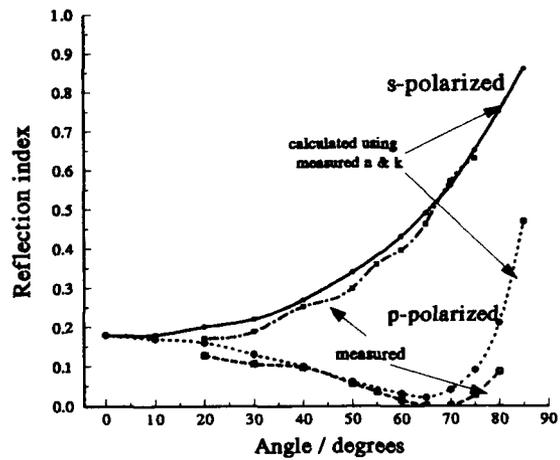
Figure 7. Measured emissivity of sodalime glass.
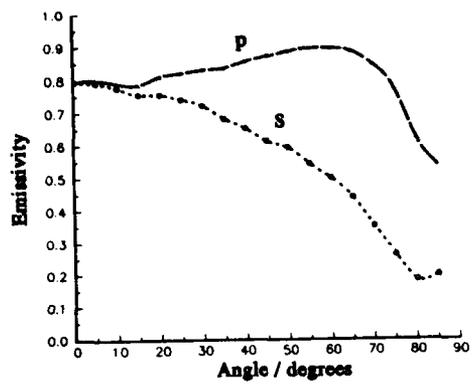
Figure 8. Measured degree of linear polarization from a range of materials.
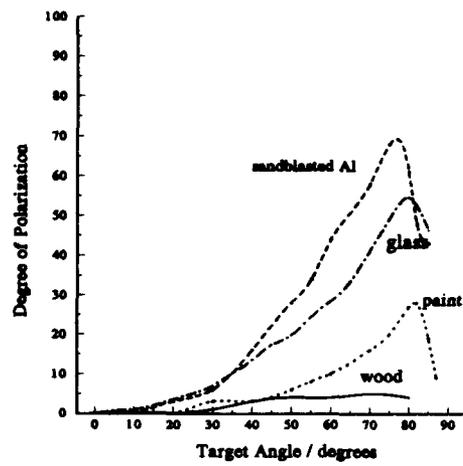
Discussion

Discussor's name :   B. Evain, FR

Comment/Question :

Did you study the influence of roughness on one particular material for example?

Author/Presenter's reply :

Yes. If for example the rms roughness of glass is increased from almost zero (0.02 μm) to several microns, the effective measured refractive index changes markedly and the measured value of the degree of linear polarization also shows a significant change.

Discussor's name :   E. Spitz, FR

Comment/Question :

Avez-vous developpé des modèles mathématiques plus compliqués tenant compte par exemple de la rugosité de la surface ?

Did you develop more complex mathematical models taking into account, for instance, the surface roughness?

Author/Presenter's reply :

We have not to date developed any theoretical or numerical model. This is because we want, first of all, to develop a better understanding of the physical processes that are occuring and to measure, using our IR ellipsometer, the complex refractive indices. This includes the effect of roughness or the effective refractive index.

MODEL FOR THE SIMULATION OF ATMOSPHERIC EFFECTS ON TARGETS TO BACKGROUND PASSIVE SIGNATURES

MODELE POUR LA SIMULATION DES EFFETS ATMOSPHERIQUES SUR LES SIGNATURES PASSIVES DE CIBLES DANS LEUR ENVIRONNEMENT

C. WALLEZ[1,2]   J. LEMORTON[1]   P.F. COMBES[2]   F. CHRISTOPHE[1]

1 : Centre d'Etudes et de Recherches de Toulouse (CERT/ONERA), 2, av. Edouard Belin, B.P. 4025
31055 TOULOUSE CEDEX   FRANCE
2 : Universite Paul SABATIER, 118, route de Narbonne 31062 TOULOUSE CEDEX   FRANCE

RESUME

Afin d'estimer de façon très précise les performances des systèmes imageurs passifs fonctionnant en ondes millimétriques, un logiciel de simulation facile d'emploi a été développé et a permis d'évaluer l'influence des conditions météorologiques sur les contrastes radiométriques.

L'action de plusieurs paramètres dont la fréquence, l'émissivité du sol et la position du radiomètre a été prise en compte. Un premier ensemble de simulations a été fait sous l'hypothèse d'une atmosphère non diffusante. Dans un deuxième temps, la diffusion par les hydrométéores a été prise en compte. Pour chaque cas, la possibilité de différencier les surfaces au sol par leur température radiométrique est étudiée.

ABSTRACT

In order to assess very accurately the performances of millimeter wave imaging passive systems, efforts have been made towards the development of a straightforward easy of use computer code. This simulation model has been used to evaluate the influence of meteorological conditions on radiometric contrasts.

In this paper, any parameters are studied : frequency, terrain emissivity and radiometer position. A first set of simulations is done in the scatter-free atmosphere assumption. Then scattering by hydrometeors is taken into account. In each case, ground surfaces discrimination by their radiometric temperature is discussed.

1. INTRODUCTION

Millimeter wave radiometry has been widely studied during the last twenty years. A lot of theoretical work has been done in order to understand and to represent mathematically radiative transfer phenomenas in the atmosphere and radiative properties of different types of surfaces or objects (ocean, terrains, vegetation ...) [1]. Extensive advances in hardware millimeter wave components and improved system understanding have also been achieved (better performances, higher reliability, lower weight and dimensions ...).

Today's sensors are mainly devoted to Earth and Atmosphere Remote Sensing. They are operating either from the ground or from airborne or satellite-borne platforms (SMMR, SSM/I, future AMSU, MIMR ...). Applications include determination of atmosphere profiles (temperature, water vapor ...), characterization of clouds and precipitations, evaluation of surfaces properties (soil moisture, vegetation ...) and oceanographic studies.

Concerning military applications, several reports have demonstrated excellent measurements results which could fill operational requirements for different kinds of systems. Good quality radiometric images have been obtained at 35 and 90 GHz, and also at 140 GHz, even in cloudy conditions from airborne or helicopter-borne radiometers [2]. Apart from cartographic applications or reconnaissance of specific terrains features (from aircrafts or drones), other fields of interest can be found in navigation or landing aid (for aircrafts), detection and guidance (millimeter wave seeker, smart weapons) and battlefield surveillance (from helicopters or ground vehicles).

For all these applications the advantages of millimeter wave radiometry are provided by its passive behaviour, less complexity than radar, smaller overall dimensions and easier images interpretation. Limitations come from poor geometrical resolution and reduced range. Future improvements could be brought by multireceiver techniques. Dual mode operation (passive/active, infrared/millimeter wave) is also considered using data fusion algorithms.

Anyway, for the design of these systems and for the evaluation of their performances, it is necessary to use simulation techniques. Since propagation and radiative transfer in the atmosphere have significant effects on millimeter wave imaging systems and depend on the frequency of operation and on meteorological conditions (presence of clouds, rainfall layers, fog ...), targets and background signatures, and therefore target to background contrasts, will be highly variable. These effects have to be evaluated very accurately.

The aim of this paper is to present a simulation code developed at CERT/ONERA as a useful tool for the

evaluation of performances of millimeter wave radiometer systems in various weather conditions. After a brief presentation of the general mathematical formulation, the principles of the simulation code concerning radiometric temperatures in a scatter-free atmosphere will be presented for an airborne and a satellite-borne radiometer. Then the simulation results at 35 GHz, 94 GHz and 140 GHz will be illustrated. Finally, some preliminary results will be discussed when scattering effects are taken into account.

2. THEORETICAL FORMULATION

In a medium containing a random distribution of particles, such as a cloudy or a rainy atmosphere, the electromagnetic radiation propagation is influenced by three phenomenas : absorption, emission and scattering. All these characteristics should be included in an appropriate equation.

Two distinct theories can be used : wave theory and radiative transfer theory.

The wave theory is directly based on Maxwell's equations. All multiple scattering and diffraction effects can be included. But many approximations have to be made before getting numerical solutions from these equations.

The radiative transfer theory is based on the radiative transfer equation that governs the variations of Stokes parameters of a wave which propagates in a scattering medium. This formulation can include all multiple volume scattering effects and seems interesting when scattering can be described globally. This is the case of a perturbated atmosphere.
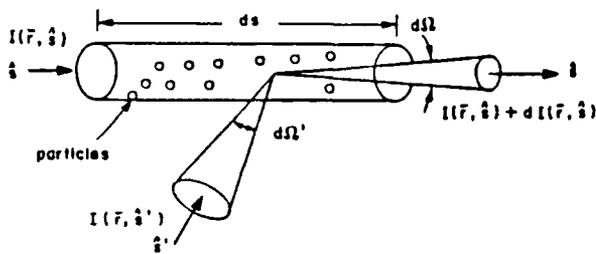
Inside the atmosphere, the radiative transfer equation takes the following form [3]

$$\frac{d\bar{I}(\bar{r},\hat{s})}{ds} = - \overline{\overline{Ke}}^{s}(\bar{r},\hat{s}) \, \bar{I}(\bar{r},\hat{s}) - Ka^{g}(\bar{r}) \, \bar{I}(\bar{r},\hat{s})$$

$$+ \overline{Je}(\bar{r}) + \int_{4\pi} d\Omega' \, \overline{\overline{P}}(\bar{r},\hat{s},\hat{s}') \, \bar{I}(\bar{r},\hat{s}')$$

I is a vector and represents the four Stokes parameters (Iv, Ih, U, V) of the electromagnetic radiation,
s is the observation direction,
s' is an incident direction,

r is the distance, referred to an arbitrary origin,
Ke^{s} is the extinction matrix which describes absorption and scattering by particles,
Ka^{g} is the scalar absorption coefficient of atmospheric gases,
Je is a four components vector describing emission by particles and gases,
P is the phase matrix which characterizes coupling of Stokes parameters of radiations in two directions due to scattering.

The left-handed term of the equation represents the variation of Stokes parameters across path ds from r in direction s.

The first two right-handed terms of the equation are characteristic of the extinction which describes attenuation of Stokes parameters due to absorption and scattering. The first term is the extinction due to particles. The second one is the extinction by gases. For gases, extinction means only absorption.

The third term is the emission vector which corresponds to the thermal emission source of the medium. The last term characterizes scattering and ⁻s contributions from directions s' into direction s.

2.1. Plane parallel and horizontally homogeneous atmosphere

As a simplification, a plane Earth assumption is made and the approximation of horizontal and homogeneous atmospheric stratification is used (specially for hydrometeors layers).

If direction s is written

$$\hat{s} = \sin\theta \cos\varphi \, \hat{x} + \sin\theta \sin\varphi \, \hat{y} + \cos\theta \, \hat{z}$$

with horizontal planes taken parallel to directions x and y, the radiative transfer equation becomes

$$\cos\theta \frac{d\bar{I}(\theta,\varphi,z)}{dz} = - \overline{\overline{Ke}}^{s}(\theta,\varphi,z) \, \bar{I}(\theta,\varphi,z)$$

$$- Ka^{g}(z) \, \bar{I}(\theta,\varphi,z) + \overline{Je}(z)$$

$$+ \int_{0}^{\pi} \int_{0}^{2\pi} d\theta' \, d\varphi' \, \sin\theta' \, \overline{\overline{P}}(\theta,\varphi,\theta',\varphi',z) \, \bar{I}(\theta',\varphi',z)$$

2.2. Scatter-free medium

When scattering can be neglected, the radiative transfer equation reduces to

$$\cos\theta \frac{d\bar{I}(z,\theta,\varphi)}{dz} = -Ka(z) \, \bar{I}(z,\theta,\varphi) + \overline{Je}(z)$$

where Ka(z) is the scalar total absorption coefficient due to particles and gases and

$$\overline{Je}(z) = Ka(z) \ \overline{I}^{*}(z)$$

where $I^{*}(z)$ is constituted by the Stokes parameters of a blackbody radiation $(I^{*}, I^{*}, 0, 0)$.

If boundary conditions do not introduce any coupling between the different Stokes parameters (azimuthal independence of ground surface), this vectorial equation can be reduced to four scalar equations which can be solved analytically. With the first two equations, we obtain [1]

$$I_p(z,\theta) = I_p(0,\theta) \exp\left(\frac{-\tau(0,z)}{\cos\theta}\right)$$

$$+ \frac{1}{\cos\theta} \int_0^z Ka(z') \ I^{*}(z') \exp\left(\frac{\tau(z',z)}{\cos\theta}\right) dz'$$

with $\quad \tau(z',z) = \int_{z'}^z Ka(z) \ dz$

where $\tau(z,z')$ is the optical thickness between height z and height z', p = v, h stands for respectively vertical and horizontal polarization and θ is the observation angle relative to the surface normal. Using Planck's law and Rayleigh-Jeans approximation, Stokes parameters can be proved proportional to the brightness temperature in the microwave region. Thus, the radiative transfer equation can be written

$$T_{Bp}(z,\theta) = T_{Bp}(0,\theta) \exp\left(\frac{-\tau(0,z)}{\cos\theta}\right)$$

$$+ \frac{1}{\cos\theta} \int_0^z Ka(z') \ T(z') \exp\left(\frac{-\tau(z',z)}{\cos\theta}\right) dz'$$

T(z) is the physical temperature at an altitude z and $T_{Bp}(z,\theta)$ is the p-polarized brightness temperature, at an altitude z and in a direction θ.

2.3. Validity domain of the scatter-free assumption

Since atmospheric gases are only absorbing at millimeter wave frequencies, the scatter-free assumption is valid under clear sky conditions. If there are hydrometeors layers in the atmosphere, the amount of scattering depends on the ratio of drop-radius to wavelength and on the permittivity of these hydrometeors. For a frequency below 35 GHz, scattering is negligible for most atmospheric weather conditions. Between 35 and 100 GHz, when rain is present, scattering must be taken into account. Above 100 GHz, scattering may be ignored only for some non-

precipitating clouds. With ice clouds, it is essential to take into consideration scattering because ice presents very light absorption but large scattering.

3. PRINCIPLES OF THE SIMULATION OF RADIOMETRIC TEMPERATURES IN A SCATTER-FREE ATMOSPHERE

3.1. Atmospheric model

A program calculating radiometric temperatures in a scatter-free atmosphere has been developed for a frequency range from 1 to 300 GHz. For this range of frequencies, the absorption by gases is only due to oxygen (two main absorption bands at 118.7 GHz and in the 50-70 GHz region) and to water vapor (22.2 and 183.3 GHz). The absorption lines of these two gases are described by Liebe [4], Water [5] and Rosenkranz [6] models.

In this calculation, pressure, temperature and water vapor density profiles are required. We have used the 1962 U.S. Standard Atmosphere. At sea level, pressure is equal to 101.3 kPa, temperature is 288.15 K and water vapor density is 7.72 g/m^3 and has an exponential decreasing with scale height equal to 2 km up to the tropopause. Above the tropopause, we have used the density water vapor profile described by Harries [7]. Radiosondes data or other standard profiles can be used as well.

Hydrometeors have been supposed spherical so Mie's theory and sometimes Rayleigh's approximation could be used to calculate the absorption coefficients. This calculation requires the knowledge of the complex refractive index of particles (Liebe's model [8]) and the drop size distribution. Deirmendjian's distribution for clouds and Marshall and Palmer's distribution for rain have been employed.

3.2. Apparent temperature of terrain observed through the atmosphere

In the case of an airborne or a satellite-borne radiometer, the brightness temperature $T_{Bp}(\theta,H)$ is constituted by the atmospheric upwelling temperature and by the contribution coming from the ground attenuated along the atmospheric path. This radiation is the sum of the self-emitted radiometric temperature of the terrain and of the sky brightness temperature reflected on the ground surface.

The radiometric temperature T_{Bp} obtained on a radiometer located at height H looking at observation angle θ is [1]

$$T_{Bp}(\theta,H) = \exp\left(\frac{-\tau(0,H)}{\cos\theta}\right) \cdot$$

$$\left(em_p(\theta) \ Tg + \left(1 - em_p(\theta)\right) Tsky(\theta)\right) + Tup(\theta)$$

where $em_p(\theta)$ is the p-polarized emissivity of the terrain seen by the radiometer,

Tg is the ground physical temperature,

Tsky is the sky brightness temperature,

$$Tsky(\theta) = Tdn(\theta) + Tcos \exp\left(\frac{-\tau(0,\infty)}{\cos\theta}\right)$$

Tcos is the cosmic temperature which is equal to 2.7 Kelvin,

Tdn(θ) is the downwelling atmospheric temperature,

$$Tdn(\theta) = \frac{1}{\cos\theta}\int_0^\infty Ka(z') \, T(z') \exp\left(\frac{-\tau(0,z')}{\cos\theta}\right) dz'$$

Tup(θ) is the upwelling atmospheric temperature.

$$Tup(\theta,H) = \frac{1}{\cos\theta}\int_0^H Ka(z') \, T(z') \exp\left(\frac{-\tau(z',H)}{\cos\theta}\right) dz'$$

4. NUMERICAL RESULTS
FOR A SCATTER-FREE ATMOSPHERE

After a validation phase with results from [1] [9], a great number of simulations have been done in many representative cases of typical weather conditions : haze, fog, clouds such as stratus, fair-weather cumulus, cumulus congestus and rain of rainfall rate between 1 and 25 mm/h. The program has been extensively used at the atmosphere window frequencies (35, 94 and 140 GHz).

A first set of simulations has been done for both low altitude airborne and satellite-borne radiometer. These simulations correspond to an observation angle equal to zero which eliminates the influence of polarization. In each case, various surface emissivities have been used in order to parameter each curve and to study the variations of contrasts between surfaces as a function of frequency and weather conditions.

Other radiometric temperature simulations have been conducted for a satellite-borne radiometer as a function of observation angle. In that case, the difference between a specular surface and a Lambertian surface will be shown.

In all these simulations the antenna pattern has not been taken into account. In a real case, when a radiometer observes a large ground scene, the radiation incoming on the receiver comes at the same time from several parcels of various emissivities through the instrument antenna pattern. A convolution has to be calculated between the radiometric temperature variations of the scene and the antenna pattern. So, observed contrasts measured by a radiometer would be worse than those simulated.

4.1. Numerical results for an airborne radiometer (altitude h = 100 meters)

Figures 1 to 3 give the radiometric temperatures of terrains of various emissivities em observed through different kinds of atmosphere.

As expected, it is shown that the more severe the atmospheric perturbation is, the smaller the radiometric contrast between terrains of various emissivities is. For surfaces with emissivity close to 1, the temperature remains at a high level in any weather condition. When emissivity is very low, the radiometric temperature increases a lot with the atmospheric perturbation. These effects are caused by the rising behaviour of Tsky(θ) and therefore of Tdn(θ). The brightness temperature reflected by low emissivity surfaces becomes warmer and warmer and its value approaches the brightness temperature emitted by high emissivity surfaces.

For example, at 35 GHz, the temperature contrast between the surfaces of uppest and lowest emissivities is 243.2 K under clear sky but is only 147.8 K in the presence of a 25 mm/h rain.

As expected, for a given meteorological condition, the contrast deterioration is all the more important as the window frequency is high. When a 5 mm/h rain occurs, the maximum contrast is 216.3 K at 35 GHz, 114.9 K at 94 GHz and only 104.2 K at 140 GHz.

However, with these values, it is still possible to discriminate a target or a specific feature in a map from other backgrounds, even if the limited geometrical resolution of the radiometer could conduct to a smoothing effect between surfaces. It has been proved experimentally, for example at JPL or DLR, that rivers, lakes or pools can be identified against fields or forests [10]. Small vehicles or ships can be detected against asphalt or water as well.

These performances can also be achieved for higher flight altitudes (for example h = 700 m [2]) but with a degraded pixel resolution. So, these contrasts could be of pratical use for mapping and navigation systems, detection and guidance systems either installed on a missile, smart ammunition, helicopter or aircraft.

4.2. Numerical results for a satellite-borne radiometer

Figures 4 to 6 are similar to the previous ones except that the radiometer is now located on satellite. The radiometric contrast globally has the same behaviour as a function of frequency and meteorological effects than for the airborne radiometer. However contrasts are worse because the atmospheric path is longer. For example, at 35 GHz, the maximum contrast between surfaces is 226.2 K under clear sky and 74.0 K for a 25 mm/h rain.

For a satellite-borne radiometer, the smoothing effect of the antenna pattern will be emphasized by the limited antenna size. So measured contrasts would be lower than those simulated.

Though radiometric resolution (minimum contrast that can be detected) on modern systems is less than some Kelvin depending on the integration time, it can be demonstrated that some weather conditions will prevent the discrimination between different surfaces.

This limitation will have higher probability of occurence when the radiometer is on satellite, particularly at 94 and 140 GHz. Only the 35 GHz frequency allows to measure detectable contrasts in almost any meteorological conditions. For example, it has been demonstrated with SSM/I satellite data that discrimination between large homogeneous surfaces can still be achieved (ocean, desert, forest ...).

Figures 7 to 12 give the variations of the radiometric temperature obtained on a satellite-borne radiometer as a function of the observation angle. The observed scene is a specular surface on figures 7 to 9. At each frequency, the permittivity of the surface corresponds to a smooth ocean. On figures 10 to 12, the terrain is modelised by a Lambertian surface of emissivity equal to 0.99.

Specular surface

Even under clear sky condition, the atmospheric path affects the brightness temperature emitted at ground level. On the three figures, the angular variation of the received radiation is altered under clear sky (gases absorption).

Since the atmosphere absorbs radiations and re-emits them at its own temperature, when the atmosphere becomes more absorbant (with frequency, meteorological condition or observation angle) the polarization dependence of radiometric temperature is weaker. This effect is obvious at 140 GHz in the presence of a 10 mm/h rain.

The angular variation of the radiometric temperature depends on the radiometric temperature at ground level and of course on the frequency and meteorological conditions. At large angle and at high frequency, atmospheric absorption is so important that the uppest atmospheric layers can hide the lowest ones so that the apparent temperature tends to decrease.

Lambertian surface

This kind of surface emits a radiation which does not depend on polarization and angle. The emissivity of such a surface is always near 1. In our simulation, this emissivity was equal to 0.99 with a physical temperature equal to 290 K. Simulations on figures 10 to 12 are related to the same cases as on figures 7 to 9 but with a Lambertian surface. The brightness temperature at ground level is high : 287.1 K.

Since there is no scattering in the atmosphere and terrain emission is here unpolarized, the apparent temperature observed by the radiometer does not depend on polarization. Radiometric temperature decreases with the observation angle because the atmospheric path through the uppest atmospheric layers becomes longer. The increase of atmospheric absorption tends to decrease the temperature measured on the radiometer.

If we compare results obtained in the case of a specular surface and a Lambertian one, when atmospheric absorption is weak, for example at 35 GHz, the discrimination between these surfaces is easy. When this absorption increases, with frequency and meteorological conditions, this discrimination becomes harder and is almost impossible in certain cases. At 140 GHz, with the presence of 10 mm/h rain, even an observation at different angles does not allow to differentiate these surfaces nevertheless very different.

Of course, most radiometric systems installed on satellite are multifrequency systems with a lot of microwave and millimeter wave channels, and sometimes infrared and visible channels. Dual polarization can also be added. So it is possible to associate several measurements and different kinds of inversion techniques to compensate meteorological effects and to get some classification among surfaces.

5. INFLUENCE OF SCATTERING

When scattering is taken into account, even under the approximations of stratified and parallel atmosphere, spherical particles and azimuthal independence, the vectorial radiative transfer equation cannot be solved analytically. Many numerical methods exist [3], [11], [12]. After an investigation on the advantages, drawbacks and validity domains of each technique, the method of invariant imbedding has been implemented in our simulation model.

In the method of invariant imbedding, the boundary value problem of the radiative transfer equation at the top of the atmosphere and at the ground surface is converted to an initial value problem starting at zero atmospheric thickness and solved with an iterative process on an increasing atmospheric thickness. In a first time, the continuum of propagation directions is discretized into a finite number of directions so that the integro-differential equations could be converted into a system of ordinary differential equations with constant coefficients. The reflectivity and the transmissivity of the whole atmosphere are calculated. Then the problem of thermal emission in passive remote sensing is studied and the radiometric temperature is expressed in terms of reflectivity and transmissivity.

Simulations with scattering are still in progress so only preliminary results will be shown here. Figure 13 shows the influence of scattering for a ground-based radiometer at 94 GHz and in the presence of a 25 mm/h rain layer. Curves A give the sky brightness temperature if rain scattering is neglected. With scattering, we obtain curves B. We consider the presence of an ice layer above the rain with no scattering in curves C and with scattering in curves D.

If we compare curves A and B, it becomes apparent that scattering decreases the gap between sky brightness temperatures at zenith and at large observation angles by mixing cold temperatures from small angles and warm temperatures from large angles. Even with spherical particles, scattering induces a polarization dependence because of the intrinsic properties of scattering and because of the polarization dependence of the terrain emissivity.

Ice particles are almost non-absorbant, so that curves C are very close to curves A. In another way, the ice layer is primarily a scattering medium and when scattering is taken into account, there is a big difference between the cases with or without ice layer (curves B and D).

Figures 14 and 15 are for a satellite-borne radiometer. The observed terrain is respectively a specular surface and a Lambertian one. Frequency is 94 GHz and meteorological conditions are clear sky (curves A) and rain of 10 mm/h rainfall rate with or without scattering (respectively curves B and C).

In figure 14, scattering causes coupling between polarizations so that the polarization dependence of radiometric temperatures is much weaker in curves B than in curves C. By coupling between different propagation angles and because particles scatter back a part of terrain emission, the angular dependence is weaker when scattering is taken into account and radiometric temperature is lower. With scattering, emission characteristics of terrain cannot be easily identified.

Figure 15 is for a Lambertian surface. Since terrain emission is unpolarized, scattering only causes a slight difference between polarizations. Particles scatter a part of terrain emission and terrain brightness temperature is high so that when scattering is taken into account, there is a darkening effect : apparent temperature on radiometer is lower in curves B with scattering than in curves C without scattering.

It is interesting to notice that there is a higher difference between curves A of both figures 14 and 15, when scattering is not taken into account, than in curves B when scattering is accounted for.

In certain cases the presence of scattering particles in the atmosphere will prevent the discriminations of various surfaces even if they are very different. The contrast between surfaces or the target to background contrast could be proved difficult.

Contamination of the temperature of the observed pixel by the temperature of adjacent pixels, caused by scattering in the atmosphere, is another problem to be studied but requires the cancellation of basic assumptions in the method.

One of the main interest in studying scattering is to evaluate the error made when scattering is not taken into account. This hypothesis is frequent in some applications. For example, most of the inversion techniques are based on radiative transfer theory and often neglects scattering in order to diminish computer time consumption, it is necessary to assess how severe the errors on the determination of useful parameters will be.

6. CONCLUSION

In this study about meteorological effects on millimeter wave passive systems, the influence of many parameters on surfaces contrasts has been accurately evaluated, especially the influence of frequency, radiometer position, weather condition and terrain emissivity.

A first aspect of this study has concerned a scatter-free atmosphere. It was confirmed how high frequency, high water content in the atmosphere and high radiometer altitude are restrictive factors in targets to background contrasts detection.

The nadir looking case was studied and angular dependent simulations were also done for a satellite-borne radiometer in order to have one more terrain parameter helping in surfaces discrimination. In some cases, when the atmosphere is very absorbant, this criterion does not help in the surfaces differentiation.

The second part of the study was about the influence of scattering by atmospheric hydrometeors. It was shown that scattering affects polarization and angular dependence of radiometric temperatures.

Simulations of radiometric temperatures obtained on a satellite-borne radiometer have proved that scattering shades off radiometric contrasts. In some cases, when scattering is important, the discrimination between two different surfaces such as specular and Lambertian surfaces becomes more difficult. The interest of taking into account scattering was obviously shown in the presence of ice clouds.

The computer code developed in this study could be a useful tool for the design and the evaluation of single or multifrequency millimeter wave radiometric systems which could be used for mapping and reconnaissance applications, detection and guidance systems, and battlefield surveillance.

REFERENCES

1. Ulaby F. T., Moore R. K. and Fung A. K., "Microwave Remote Sensing Active and Passive", vol. 1, Addison-Wesley Publishing Company, 1981 (ISBN 0 201 10759 7).

2. Süss H., Grüner K., Wilson W. J., "Passive Millimeter Wave Imaging : a Tool for Remote Sensing", Alta Frequenza, 58, 5-6, sept.-dec. 1989.

3. Tsang L., Kong J. A. and Shin R. T., "Theory of Microwave Remote Sensing", John Wiley and Sons, 1985 (ISBN 0 471 88860 5).

4. Liebe H. J., "Calculated Tropospheric Dispersion and Absorption Due to the 22 GHz Water Vapor Line", IEEE Trans. Ant. Prop., AP 17, 5 , sept. 1969, pp 621-627.

5. Waters J. W., "Absorption and Emission of Microwave Radiation by Atmospheric Gases", Methods of Experimental Physics, M. L. Meeks, ed. 12, part B, Radio Astronomy, Academic Press, Section 2.3, nov. 1976.

6. Rosenkranz P. W., "Shape of the 5 mm Oxygen Band in the Atmosphere", IEEE Trans. Ant. Prop, AP 23, 4, july 1975, pp 498-506.

7. Harries J. E.,"The Distribution of Water Vapor in the Stratosphere", Rev. Geophys. Space Phys., 17, nov. 1976, pp 565-575.

8. Liebe H. J., Manabe T., Hufford G. A., "Millimeter-Wave Attenuation and Delay Rates Due to Fog/Clouds Conditions", IEEE Trans. Ant. Prop., AP 37, 12, dec 1989, pp 1617-1623.

9. Ishimaru A. and Cheung R. L. -T., "Multiple-Scattering Effects on Radiometric Determination of Rain Attenuation at Millimeter Wavelengths", Radio Science, *15*, 3, May-June 1980, pp 507-516.

10. Wilson W. J. and Ibbott A. C., "Millimeter Wave Imaging Sensor Data Evaluation", JPL Publication 87-16, (NASA-CR-181159), May 1987.

11. Lenoble J., "Radiative Transfer in Scattering and Absorbing Atmospheres : Standard Computational Procedures", Hampton, Virginia USA, A. Deepak Publishing, 1985 (ISBN 0 937194 05 0).

12. Liou K. N., "An Introduction to Atmospheric Radiation", International Geophysics Series, *26*, Academic Press, 1980 (ISBN 0 12 451450 2).

	35 GHz	94 GHz
Forest	0.99	0.99
Grass	0.91	0.91
Asphalt	0.83	0.99
Concrete	0.76	0.91
Snow	0.60	0.78
Water	0.47	0.65
Dielectric coated metal	0.35	0.46
Painted metal	0.21	0.28
Metal	0.075	0.10

Table 2

Examples of emissivities at vertical incidence

APPENDIX

For each meteorological condition and frequency, the absorption coefficient is given in table1. Averages values are calculated in relation to the absorption coefficient variations along the thickness of the perturbation. Perturbation altitudes and drop size distribution coefficients were provided by [1].

	Ka (dB/km)		
	35 GHz	94 GHz	140 GHz
Haze	0.1	0.5	1.0
Fog	0.25	1.2	2.3
Stratus	0.29	1.4	2.45
Fair-weather cum.	0.5	2.55	4.35
Cumulus congestus	0.65	3.45	6.2
1 mm/h rain	0.22	0.9	1.6
5 mm/h rain	0.6	1.8	2.6
10 mm/h rain	1.0	2.6	3.4
25 mm/h rain	2.1	4.35	5.25

Table 1

Absorption coefficients
in presence of various weather conditions

At 35 and 94 GHz, emissivities were collected from open litterature or from measurements (table 1). Of course, these values are only given as examples for the simulation, since the emissivity of a medium (such as asphalt) is not unique and can vary with the specific properties of the medium and of its surface. At 140 GHz, through lack of data, emissivities were chosen more arbitrarily.
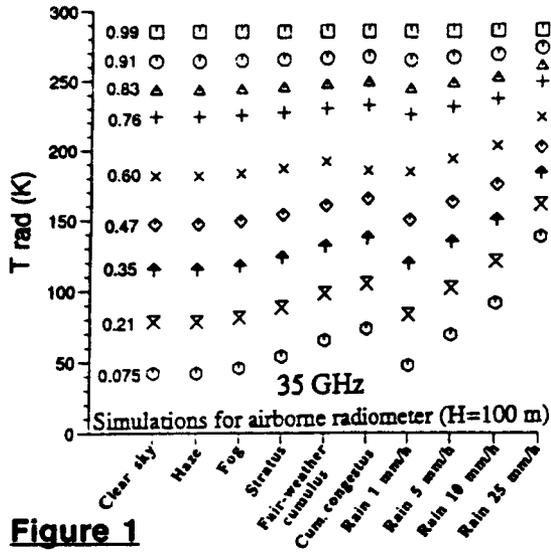
Figure 1

Figure 2

Figure 3

Figure 4

Figure 5

Figure 6

Satellite-borne radiometer
Specular surface
Surface rel. permit. : 18+28i
Surface temp. : 290 K

Figure 7

35 GHz

Satellite-borne radiometer
Specular surface
Surface rel. permit. : 7+13i
Surface temp. : 290 K

Figure 8

94 GHz

Satellite-borne radiometer
Specular surface
Surface rel. permit. : 6+9i
Surface temp. : 290 K
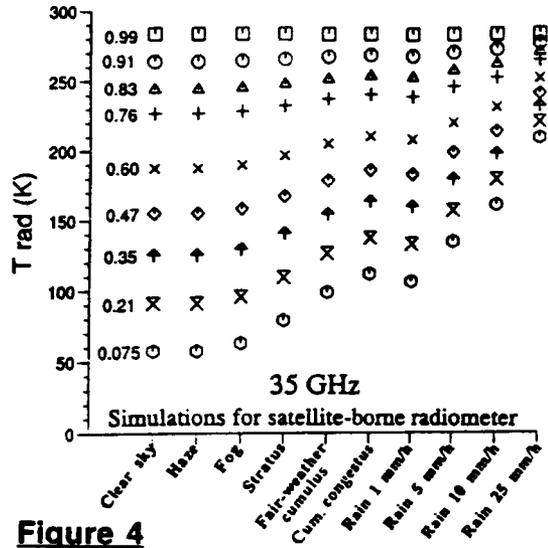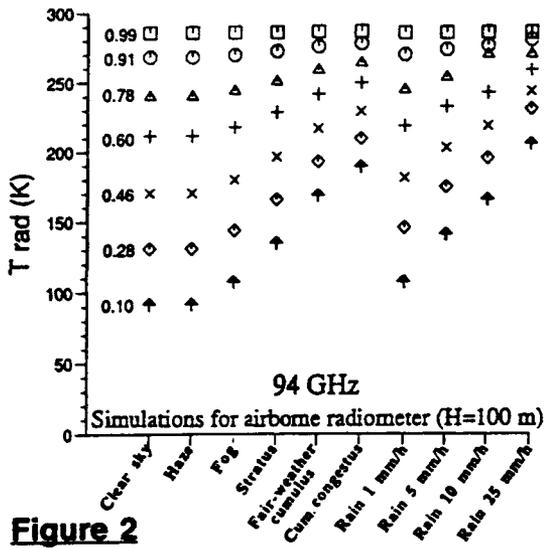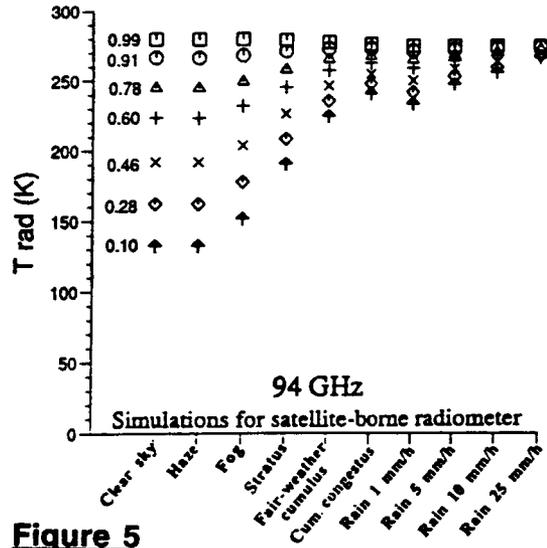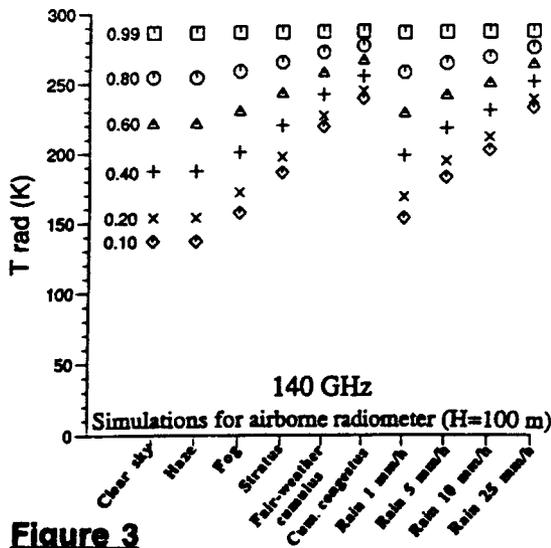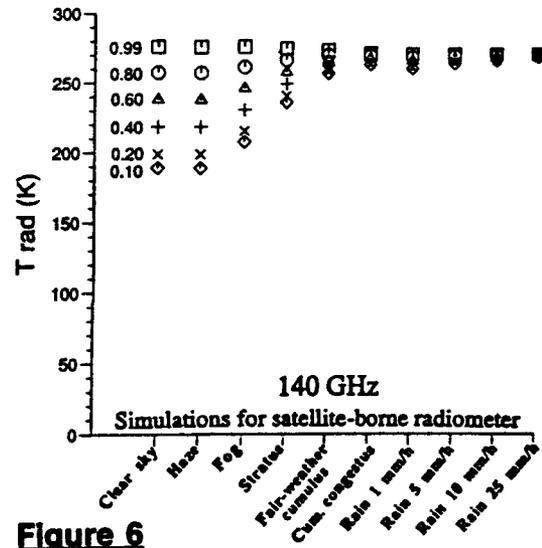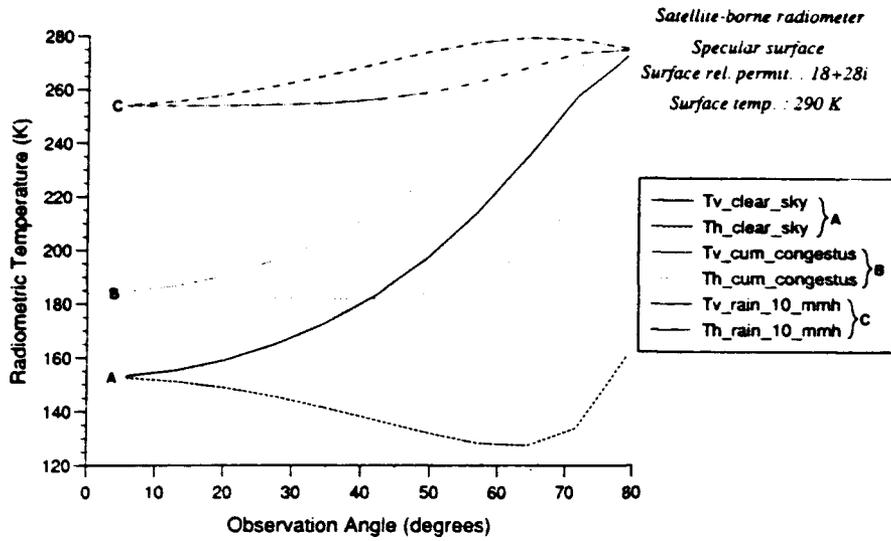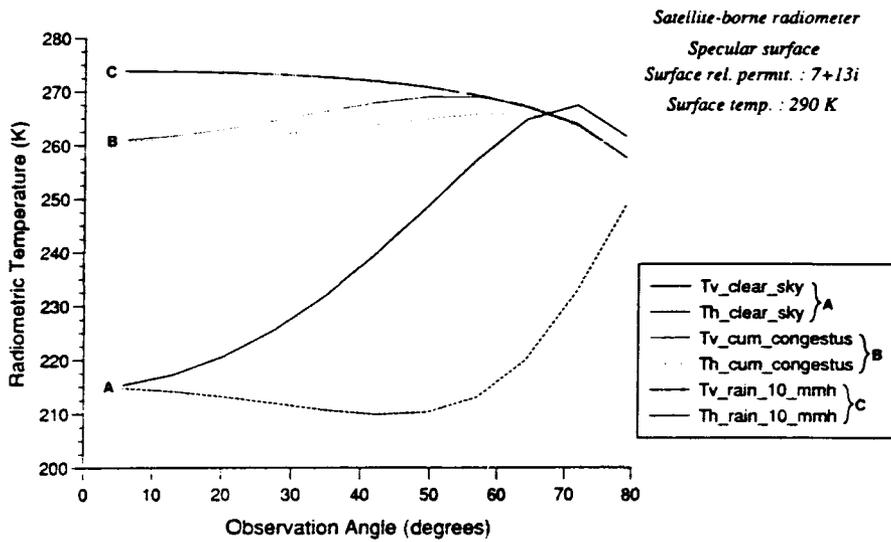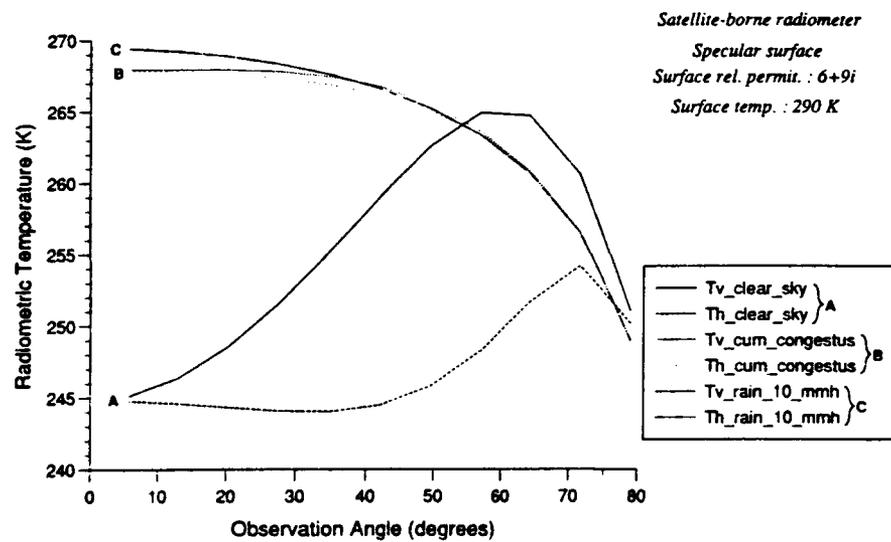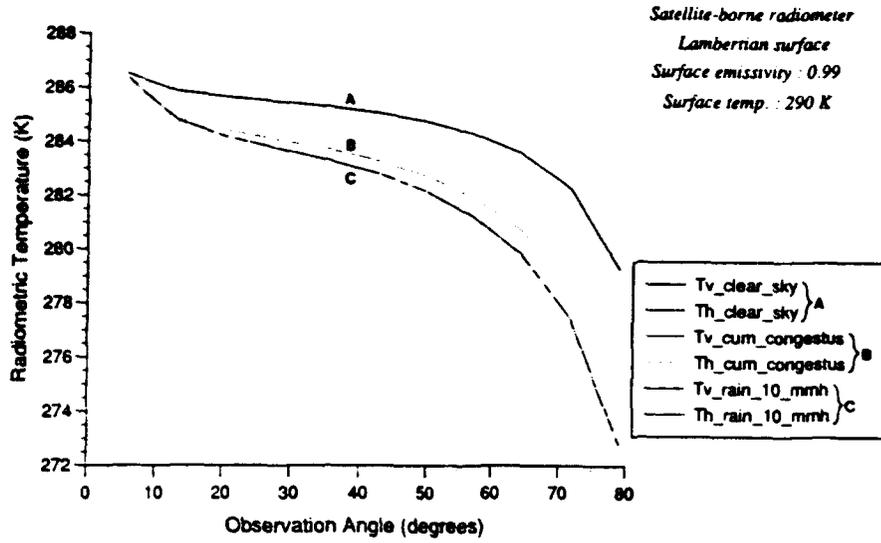
Figure 9

140 GHz

Figure 10

35 GHz
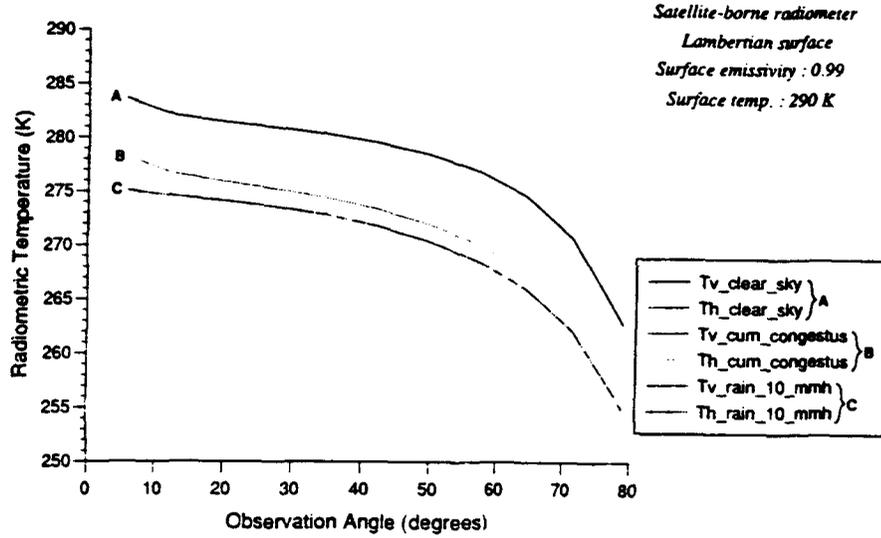
Figure 11

94 GHz

Figure 12

140 GHz

Ground-based radiometer
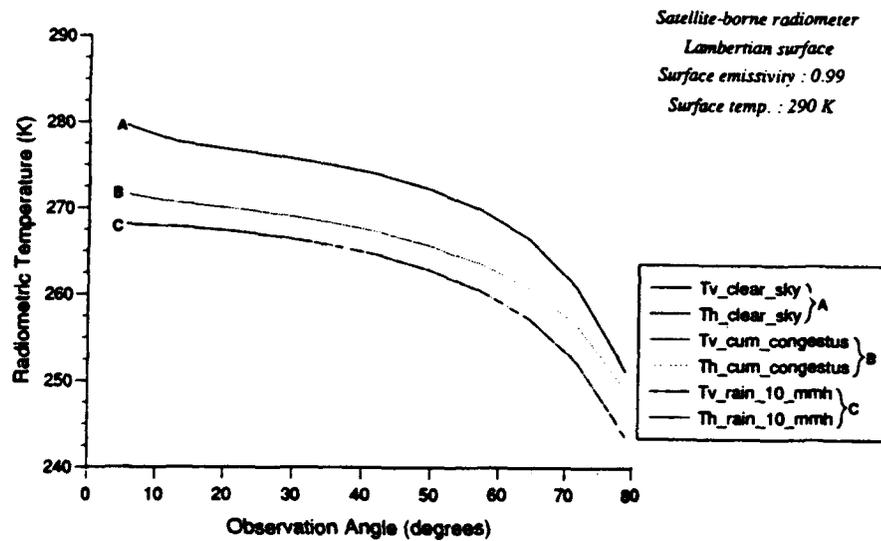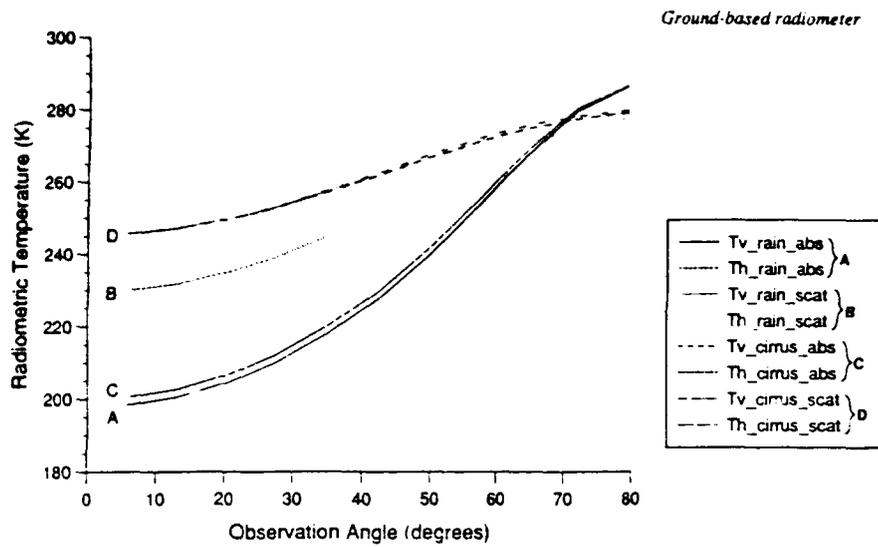
Figure 13

94 GHz
25 mm/h rain

Legend:
- Tv_rain_abs / Th_rain_abs — A
- Tv_rain_scat / Th_rain_scat — B
- Tv_cirrus_abs / Th_cirrus_abs — C
- Tv_cirrus_scat / Th_cirrus_scat — D

Satellite-borne radiometer
Specular surface
Surface rel. permit. : 7+13i
Surface temp. : 290 K
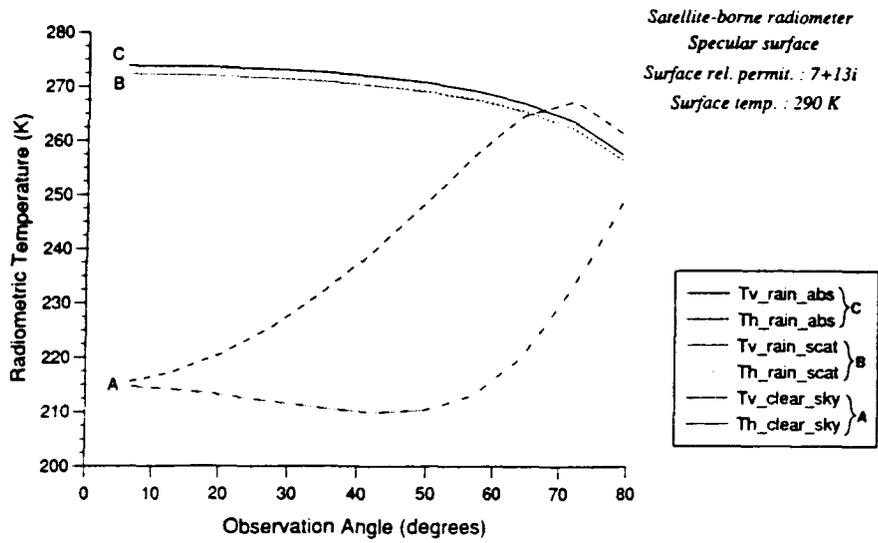
Figure 14

94 GHz
10 mm/h rain

Legend:
- Tv_rain_abs / Th_rain_abs — C
- Tv_rain_scat / Th_rain_scat — B
- Tv_clear_sky / Th_clear_sky — A

Satellite-borne radiometer
Lambertian surface
Surface emissivity : 0.99
Surface temp. : 290 K
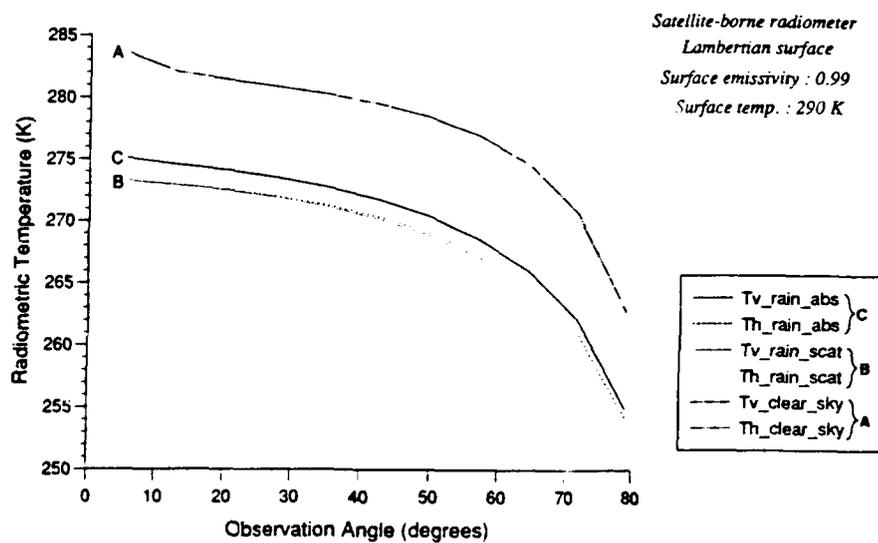
Figure 15

94 GHz
10 mm/h rain

Legend:
- Tv_rain_abs / Th_rain_abs — C
- Tv_rain_scat / Th_rain_scat — B
- Tv_clear_sky / Th_clear_sky — A

Discussion

Discussor's name :   F. Ulaby, US

Comment/Question :

1. Did you compare first-order solution for scattering with numerical results?

2. What did you use for dielectric constant of ice at millimeter wavelengths?

Author/Presenter's reply :

1. Nous n'avons pas comparé la solution numérique avec la solution du 1er ordre. Dans la méthode numérique que nous avons choisie, une fois que l'équation du transfert radiatif et les conditions aux limites ont été transformées en équations de l'invariant imbedding, la résolution numérique ne pose pas de problème et nous avons alors trouvé intéressant d'étudier une solution incluant toutes les diffusions plutot que de nous limiter au premier ordre de diffusion.

2. Nous avons utilisé un modèle développé par Liebe dans un artice de 1989. La partie réelle est proche de 3,15, la partie imaginaire est faible mais elle a été prise en compte.

THE EFFECT OF ENHANCED BACKSCATTERING ON TARGET DETECTION

E.Jakeman, J.P.Frank and G.J.Balmer

Defence Research Agency
St Andrews Road
Malvern, Worcestershire WR14 3PS
United Kingdom

1. SUMMARY

Error probabilities are calculated for the detection of a target illuminated through a random medium in the presence of ambient noise. Comparisons are made between monostatic operation, in which double passage of the radiation leads to an enhanced amplitude and fluctuation of the received signal and bistatic operation, where the outward and return radiation paths traverse uncorrelated regions of the intervening random medium. It is shown that although common transmit/receive optics are advantageous in the case of low signal-to-noise ratios, in normal regimes of operation a bistatic arrangement leads to lower total error probability, particularly when the scattering medium generates strong scintillation in the target plane.

2. INTRODUCTION

One of the simplest manifestations of multiple scattering is the phenomenon of enhanced-backscattering [1]. This coherent effect is due to constructive interference of radiation which has traversed reversible paths from the source through the scattering medium and back in the source direction. It results in an increased return, observed experimentally as a narrow peak of the scattered radiation in the backscattering direction whose magnitude is determined by the fraction of reversible paths and whose angular width is inversely proportional to the lateral scattering length within the medium. Several naturally occurring optical phenomena including the "glory" and the "opposition effect" [2] have been attributed to enhanced back-scattering and the analogous "weak Anderson-localisation" of electrons is familiar to the solid state physicist [3]. Closely related effects occur when radiation is back reflected through weakly scattering random media: a "double-passage" geometry commonly encountered in active remote sensing radars, lidars and sonars [4]. Recent optical frequency experiments have confirmed that enhanced backscattering is indeed a robust feature of the return in such geometries [5-7]. The effect has been observed in visible and infra-red experiments on systems ranging in scale from millimetres to kilometres and it is certain that active remote sensing at other electro-magnetic wavelengths [8] and using sound waves must be susceptible to the same phenomenon. This will generally not have been detected, however, since scanning the point of observation across a range of angles centred on the source direction is necessary to see the enhancement peak.

References in scientific publications to backscattering "amplification" can be traced back almost two decades and a review of Russian work on the subject appeared more than ten years ago [9]. Much of this early work was theoretical and little analysis of the implications of the results appeared in the open literature. The increased interest in multiple scattering phenomena in recent years has stimulated more experimental work, including that referred to above, and resulted in a better understanding of other special effects which can arise in double passage geometries [10]. For example, in addition to the coherent backscattering enhancement due to constructive interference, an incoherent, geometrical enhancement may occur due to lens-like focusing of rays on the target giving a "corner

reflector" or "cat's eye" effect [10]. Moreover, the fluctuations of the return signal may be enhanced, as well as its mean intensity. Several proposals have been made to exploit these effects so as to obtain improved resolution in imaging systems limited by the presence of refractive index fluctuations in the medium between the observer and object of interest [11-13]. However, there appears to have been relatively little analysis of how enhanced backscattering affects the performance of remote sensing systems [14]. It is the object of the work presented here to quantify the significance of the effect in this context by calculating detection probabilities for a simple radar system in a worst-case scenario.

The next section describes the scattering geometries to be investigated, summarises general results for the properties of the return signal in monostatic and bistatic operation and defines the measures of detection performance. In section 4 the statistical models used in the analysis will be discussed and formulae obtained for the detection probabilities. Numerical results are analysed and conclusions drawn in section 5.

3. THEORY

It will be assumed that radiation from the source reaches the target after being scattered by a random medium. This may fill the intervening propagation path as in laser beam propagation through the atmosphere, or occupy a concentrated layer as in radio wave propagation through the ionosphere, or redirect radiation from the source onto the target as in ionosphere mediated HF "over-the-horizon" radar. Radiation returned by the target is rescattered by the random medium and collected either using identical transmit/receive optics (monostatic configuration) or using spatially separated transmit and receive systems (bistatic configuration). It will be assumed that the scattering medium moves so slowly that it is essentially unchanged or "frozen" during the time taken for the radiation to propagate to the target and back. This ensures that in monostatic operation the radiation encounters exactly the same inhomogenieties on the outward and return paths. It will further be assumed that the spatial separation of the transmit and receive optics in the bistatic configuration is sufficiently large that there is no correlation between the inhomogeneities encountered on the outward and return path. According to previous theory, enhanced backscattering will occur in the monostatic case but not in the bistatic configuration. A simple direct detection radar system will therefore register a higher signal-to-noise ratio in monostatic operation. The overall detection performance will not necessarily be better, however, since the return signal will, in general, exhibit increased fluctuations or fading. This effect will be most severe when reflection from an element of the target much smaller than the coherence area of the incident radiation, dominates the return. In this worst-case scenario, when the target can be treated as a point, the scattering problem greatly simplifies if it is also assumed that the transmitter behaves as a point source (Fig 1). Reciprocity then demands statistically identical modification of the radiation in the outward and return paths.
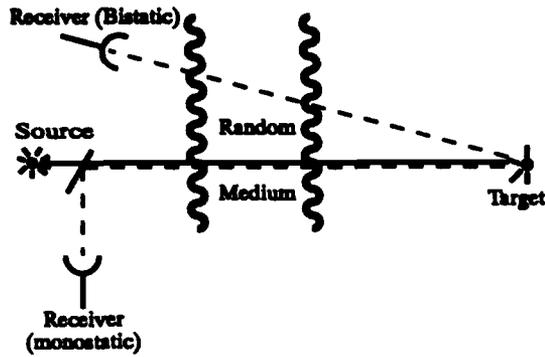
Fig 1 Scattering geometry

If the complex field amplitude, $\mathscr{E}$, and intensity, I, incident on the target are given by

$$\mathscr{E} = Af_0 \tag{1a}$$

and

$$I = |Af_0|^2 \tag{1b}$$

where the statistical variable f_0 characterises the effect of scattering and propagation on the outward path and A is constant, then the received signal field returned from the target can be expressed in the form

$$\mathscr{E}_S = Af_0f_r \tag{2}$$

where

$$f_r = f_0 \quad \text{for the monostatic case} \tag{3a}$$

and

$$\overline{f_0^m f_r^n} = \overline{f_0^m} \cdot \overline{f_0^n} \text{ for the bistatic case} \tag{3b}$$

The factorisation property (3b) simply expresses the statistical independence of the scattering on outward and return paths in the bistatic configuration. It is convenient, without losing generality to set A = 1 so that the received signal intensity may be written

$$S = I^2 \quad \text{for the monostatic case} \tag{4a}$$

$$= I_0 I_v \text{ with } \overline{I_0^n I_v^m} = \overline{I^n} . \overline{I^m} \text{ for the bistatic case} \tag{4b}$$

Equation (4) enables the signal statistics to be calculated given a statistical model for the intensity incident on the target. These can then be used in a standard threshold detection analysis assuming ambient noise, N, with probability density n(N), which

adds incoherently to the signal. In particular the false alarm and missed signal probabilities may be expressed in the following form:

$$P_F = 1 - \int_0^T n(N)dN \tag{5a}$$

$$P_M = \int_0^T n(N)dN \int_0^{T-N} \sigma(S)dS \tag{5b}$$

where T is the chosen threshold level, and σ is the probability density of the signal.

4. STATISTICAL MODELS
The gamma distribution

$$n(N) = \frac{\alpha}{N\Gamma(\alpha)} \left(\frac{\alpha N}{\overline{N}}\right)^{\alpha-1} \exp(-\alpha N/\overline{N}) \tag{6}$$

provides a suitably flexible model for the probability density of the ambient noise. The case $\alpha = 1$ corresponds to Gaussian speckle, whilst spatially or temporally averaged speckle can be represented by larger α values. More strongly scintillating noise can be modelled by choosing values of α smaller than unity since the scintillation index is equal to $\alpha^{-1/2}$.

Two models for the intensity statistics at the target will be investigated. In some situations of interest the scattering medium will generate a Gaussian speckle pattern in the target neighbourhood so that the intensity fluctuations will be governed by a negative exponential distribution

$$P(I) = \exp(-I/\overline{I})/\overline{I} \tag{7}$$

However, it is well known that propagation through random media can often lead to enhanced non-Gaussian fluctuations due to the presence of sharp features such as caustics in the scattered intensity pattern, or to clustering of scattering centres, invalidating application of the central theorem. A statistical model which has found increasing application in such situations is K-distributed noise characterised by the single interval density [15]:

$$p(I) = \frac{2}{\Gamma(\upsilon)} \sqrt{\frac{\upsilon}{I\overline{I}}} \left(\upsilon\frac{I}{\overline{I}}\right)^{\upsilon/2} K_{\upsilon-1}\left(2\sqrt{\frac{\upsilon I}{\overline{I}}}\right) \tag{8}$$

where $K_\upsilon(x)$ is a modified Bessel function of the second kind [16]. When υ is very large (8) reduces to (7). However, for finite values of υ the fluctuations governed by the density (8) exceed those of Gaussian speckle; indeed model (8) can be interpreted as Gaussian speckle with a locally varying mean which is gamma-distributed [17].

The false alarm probability based on model (6) for all situations is given in terms of the incomplete gamma function [16] by

$$P_F = 1 - \gamma(\alpha,\alpha\tau)/\Gamma(\alpha) \tag{9a}$$

where

$$\tau = T/\bar{N} \tag{9b}$$

is a normalised threshold parameter. The missed signal probability is calculated using relations (4) and models (7) or (8).

(a) Monostatic Case

The probability density of signal fluctuations obtained assuming relation (4a) with the Gaussian Speckle model (7) is

$$\sigma(S) = \exp(-\sqrt{S}/\bar{I})/2\,\bar{I}\sqrt{S} \tag{10}$$

Substituting this result into equation (5b) for the missed signal probability with gamma distributed noise, (6), gives

$$P_M = \frac{\alpha}{\Gamma(\alpha)} \int_0^{\tau} dt\,(\alpha t)^{\alpha-1} \exp(-\alpha t)\,x \tag{11}$$

$$x \left[1 - \exp\left(-\sqrt{\tau - t}/r\right) \right]$$

where

$$r = \bar{I}/\sqrt{\bar{N}} \tag{12}$$

is a measure of the received signal-to-noise ratio based on the intensity incident on the target, and is independent of scattering geometry.

In the case where the radiation falling on the target is K-distributed, model (8), the probability density of signal fluctuations assuming relation (4a), is

$$\sigma(S) = \frac{1}{\Gamma(\upsilon)} \left(\frac{\upsilon}{\bar{I}}\right)^{\frac{\upsilon+1}{2}} S^{\frac{\upsilon-3}{4}} K_{\upsilon-1}\left(2S^{\frac{1}{4}}\sqrt{\frac{\upsilon}{\bar{I}}}\right) \tag{13}$$

and the missed signal probability with gamma distributed noise (6) can be written as follows

$$P_M = \frac{\alpha}{\Gamma(\alpha)} \int_0^{\tau} dt\,(\alpha t)^{\alpha-1} e_{\wedge} p\,(-\alpha t)$$

$$x \left[1 - \frac{2}{\Gamma(\upsilon)} \left(\frac{\upsilon}{r}\right)^{\frac{\upsilon}{2}} (\tau - t)^{\frac{\upsilon}{4}} K_{\upsilon}\left(2\sqrt{\frac{\upsilon}{r}}\,(\tau - t)^{\frac{1}{4}}\right) \right] \tag{14a}$$

where r is defined by equation (12). This result will only be computed for two special cases: $\upsilon = \frac{1}{2}$, when, from (8), $\langle I^2\rangle/\langle I\rangle^2 = 6$ and $\upsilon = 3/2$ when $\langle I^2\rangle/\langle I\rangle^2 = 10/3$. Equation

(14a) reduces for these values of υ to

$$P_M = \frac{\alpha}{\Gamma(\alpha)} \int_0^{\tau} dt\,(\alpha t)^{\alpha-1} \exp(-\alpha t)\,x$$

$$x \left[1 - \exp\left(-\sqrt{\frac{2}{r}}\,(\tau - t)^{\frac{1}{4}}\right) \right]; \qquad \upsilon = \frac{1}{2} \tag{14b}$$

$$P_M = \frac{\alpha}{\Gamma(\alpha)} \int_0^{\tau} dt\,(\alpha t)^{\alpha-1} \exp(-\alpha t)\,x$$

$$x \left\{ 1 - \left[1 + 2\sqrt{\frac{3}{2r}}\,(\tau - t)^{\frac{1}{4}} \right] x \right.$$

$$\left. x \exp\left(-2\sqrt{\frac{3}{2r}}\,(\tau - t)^{\frac{1}{4}}\right) \right\}; \qquad \upsilon = 3/2 \tag{14c}$$

(b) Bistatic Case

The probability density of signal fluctuations obtained assuming relation (4b) with the Gaussian speckle model (7) is

$$\sigma(S) = 2K_0(2\sqrt{S}/\bar{I})/\bar{I}^2 \tag{15}$$

Substituting this result into equation (5b) for the missed signal probability with gamma distributed noise, (6), gives

$$P_M = \frac{\alpha}{\Gamma(\alpha)} \int_0^{\tau} dt\,(\alpha t)^{\alpha-1} \exp(-\alpha t)\,x \tag{16}$$

$$x \left[1 - \frac{2}{r}\sqrt{\tau - t}\, K_1\left(\frac{2}{r}\sqrt{\tau - t}\right) \right]$$

where r is given by equation (12) as before.

In the corresponding non-Gaussian case, model (8), the probability density of signal fluctuations takes the form

$$\sigma(S) = \frac{4}{\Gamma^2(\upsilon)} \left(\frac{\upsilon}{\bar{I}}\right)^{\upsilon+1} S^{\frac{\upsilon-1}{2}} x \tag{17a}$$

$$x \int_0^{\infty} \frac{dt}{t} \exp\left(-\frac{t}{2}\right) K_{\upsilon-1}\left(\frac{4\upsilon\sqrt{S}}{\bar{I}t}\right) K_0\left(\frac{4\upsilon\sqrt{S}}{\bar{I}t}\right)$$

The integral is in general not analytically tractable, but in the special cases of $\upsilon = \frac{1}{2}$ and $\upsilon = 3/2$ referred to above the following results may be obtained:

$$\sigma(S) = 2K_0 (2S^{\frac{1}{4}} \sqrt{2/\overline{I}}) / \overline{I} \sqrt{S} \quad ; \quad \upsilon = \frac{1}{2} \quad (17b)$$

$$\sigma(S) = 36K_0 (2S^{\frac{1}{4}} \sqrt{6/\overline{I}}) / \overline{I}^2 \quad ; \quad \upsilon = 3/2 \quad (17c)$$

The missed signal probability for these two cases, assuming the noise model (6) can be written as follows

$$P_M = \frac{\alpha}{\Gamma(\alpha)} \int_0^{\tau} dt \, (\alpha t)^{\alpha-1} \exp(-\alpha t) \, x$$

$$x \left[1 - 2 \sqrt{\frac{2}{r}} (\tau - t)^{\frac{1}{4}} K_1 \left(2 \sqrt{\frac{2}{r}} (\tau - t)^{\frac{1}{4}} \right) \right] ; \quad \upsilon = \frac{1}{2}$$

$$(18a)$$

$$P_M = \frac{\alpha}{\Gamma(\alpha)} \int_0^{\tau} dt \, (\alpha t)^{\alpha-1} \exp(-\alpha t) \, x$$

$$x \left\{ 1 - 2 \left[\sqrt{\frac{6}{r}} (\tau - t)^{\frac{1}{4}} \right]^3 K_1 \left(2 \sqrt{\frac{6}{r}} (\tau - t)^{\frac{1}{4}} \right) \right.$$

$$\left. - 2 \left(\frac{6}{r} \sqrt{\tau - t} \right) K_2 \left(2 \sqrt{\frac{6}{r}} (\tau - t)^{\frac{1}{4}} \right) \right\} ; \quad \upsilon = 3/2$$

$$(18b)$$

5.   RESULTS

Missed signal and false alarm probabilities have been computed using the formulae derived in the last section, as a function of the threshold parameter τ, for a range of signal to noise ratios and noise parameters. In addition, the total error probability, $P_F + P_M$, has been calculated and its minimum value determined as a function of threshold. This is used as a performance measure to enable comparison of monostatic and bistatic operation to be made for a range of typical signal and noise characteristics.

Fig 2 shows a typical plot of P_F against P_M. The general form of such plots is similar for both monostatic and bistatic operation with reasonable parameters governing signal and noise characteristics. Fig 3 shows a typical plot of the total error as a function of threshold level for various signal to noise ratios and a given value of the noise parameter α. Again, the general
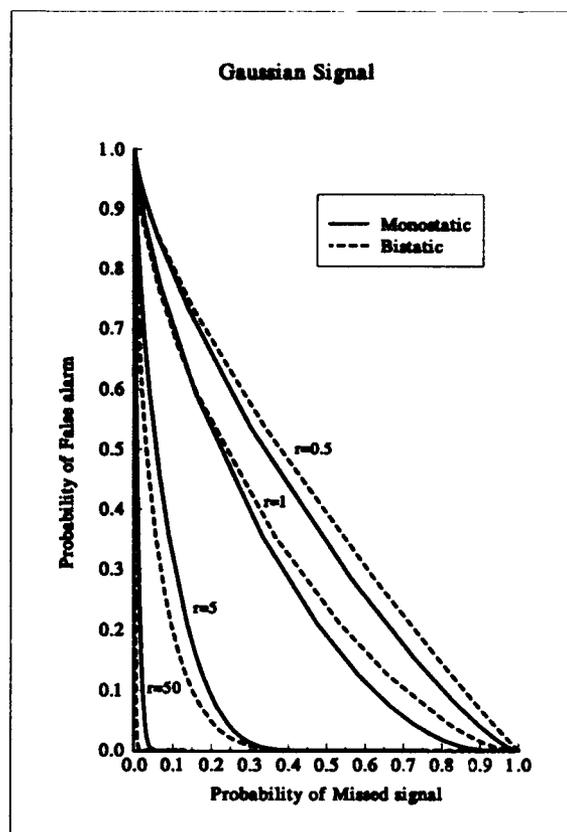

Fig 2 Error probabilities, target in Gaussian speckle pattern
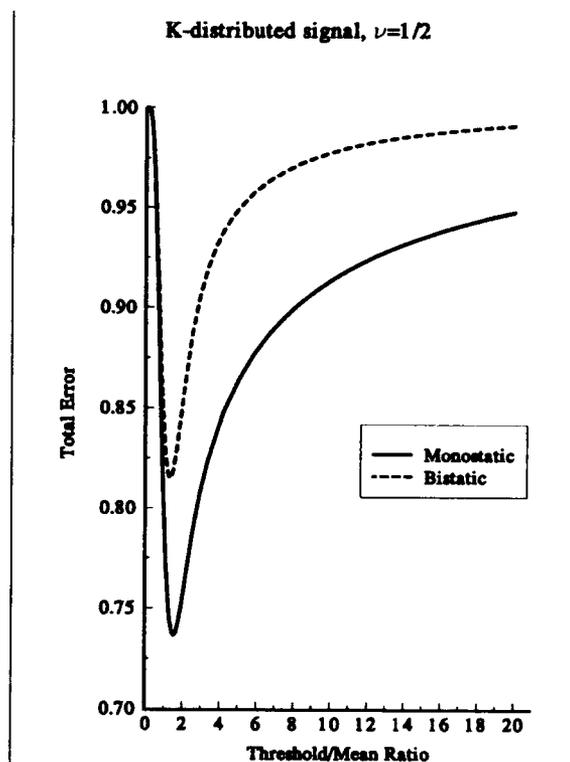
Fig 3   Total error vs τ, target in K-distributed noise, $\alpha = 5$, r = 2.

form of such plots is similar for all situations with reasonable signal and noise characteristics. The results shown in figures 4-6 compare the minimum total error probability for monostatic and bistatic operation as a function of the signal-to-noise characteristic, r, for Gaussian and non-Gaussian intensity illuminating the target and for various values of the noise parameter, α.

Inspection of Fig 4, corresponding to a target in Gaussian speckle, indicates that bistatic operation is advantageous except at small signal-to-noise ratios. As the ambient noise relative variance decreases (α large), enhanced signal fluctuations in the monostatic configuration become an increasingly dominant source of error as fading, or drop-out, increases the missed signal probability. This causes the advantage conferred on the monostatic configuration by enhanced mean signal to be confined to smaller and smaller signal-to-noise ratios. At high signal-to-noise ratios the dominant missed signal probability is reduced, for a given threshold but inspection of equations (11) and (16) shows that in the monostatic case $P_M \sim 1/r$ whilst in the bistatic case $P_M \sim \ln r/r^2$. This leads to the minimum total error in bistatic operation being smaller than in monostatic operation by a factor which increases with increasing r. As expected, the overall performance improves as fluctuations in the ambient noise decrease i.e as α becomes large.

Comparison of the results for the case of Gaussian speckle at the target with those for illumination in a non-Gaussian regime, figures 5 and 6, reveals a steadily deteriorating performance as the signal fluctuations increase. Moreover, the advantage of bistatic operation becomes greater. Investigation of formulae (14) and (18) indicates that the missed signal probability again falls off more rapidly with r at high signal to noise ratios in the case of bistatic operation than in the monostatic configuration.

Figures 7 and 8 compare detection performance assuming a low false alarm rate is required. The chosen value of $P_F = 10^{-6}$ ensures that the false alarm rate is much smaller than the missed signal probability over the range of signal-to-noise ratios shown. The errors are therefore coincident with those of figures 5 and 7 at high signal-to-noise ratios. The missed-signal probability is larger at lower values of r for the case of a small fixed false alarm rate as compared to the fully optimised case, however, and the region where improved performance can be achieved by monostatic operation is extended.

It may be concluded from the above analysis that in normal operating conditions (low error probabilities, high signal-to-noise ratios) bistatic operation, in which scattering in the forward and reverse paths to the target is uncorrelated, improves detection performance. The effect increases when the intensity fluctuations of the illuminating radiation at the target are larger. However, under conditions of sufficiently low signal-to-noise ratio, such as may be tolerated in covert systems, monostatic operation, in which scattering on the forward and reverse paths to the target is correlated, may significantly reduce the probability of error. The cross-over between these regimes occurs at error probability levels which are relatively model independent, but at signal-to-noise ratios which increase as the fluctuations in the radiation intensity incident on the target increase.

REFERENCES

1. Kuga Y and Ishimaru A, "Retroreflection from a dense distribution of spherical particles", J. Opt. Soc. Am. <u>A1</u> 831-835 (1984).

2. Gehrels T., Coffeen T. and Owings D., "Wavelength dependence of polarisation III: The lunar surface", Astron. J. <u>69</u>, 826-852 (1969).

3. Anderson P. W., "Absence of diffusion in certain random lattices", Phys. Rev. <u>109</u>, 1492-1505 (1958).

4. Banakh A. and Mironov V. L. "Lidar in a Turbulent Atmosphere", New York, Artech House, 1988.

5. Jakeman E., Tapster P. R. and Weeks A. R, "Enhanced backscattering through a deep random phase screen", J. Phys. D: Appl. Phys 432-536 (1968).

6. Tapster P. R., Weeks A. R. and Jakeman E., "Observation of backscattering enhancement through atmospheric phase screens", J. Opt. Soc. Am. <u>A6</u>, 517-522, 1989.

7. Balmer G. J., Jordan D L., Tapster P. R., Kent M. J. and Jakeman E. "Double passage wave propagation effects at infra-red and visible frequencies",. Opt. Commun. <u>88</u>, 6-12 (1992).

8. Knepp D. L. and Houpis H. L. F., "Altair VHF/UHF observations of multipath and backscatter enhancement", IEEE Trans. Ant. Propag. <u>AP-39</u> 598-534 (1991).

9. Kravtsov Yu. A. and Saichev A. I., "Effects of double passage of waves in randomly inhomogeneous media" Sov. Phys. Usp. <u>25</u> 494-508 (1983).

10. Jakeman E., "Enhanced backscattering through a deep random phase screen", J. Opt. Soc. Am. <u>A5</u>, 1638-1648 (1988).

11. Jakeman E., "Active imaging through a random phase screen" J. Phys. D: Appl. Phys., <u>24</u> 227-232 (1991).

12. Mavroidis T., Soloman C. J. and Dainty J. C., "Imaging a coherently illuminated object after double passage through a random screen", J. Opt. Soc. Am, <u>8</u> 1003-1013 (1991).

13. Jakeman E., "Statistical ray optics in double passage geometries", J. Opt. Soc. Am. <u>A10</u> 353-377 (1993).

14. Ishimaru A., "Backscattering enhancement: from radar cross sections to electrons and light localisations to rough surface scattering", IEEE Antennas and Propagation Magazine <u>33</u> 7-11 (1991).

15. Jakeman E. and Tough R. J. A, "Non-Gaussian models for the statistics of scattered waves" Adv. Phys. <u>37</u> 471-529 (1988).

16. Abramowitz M. and Stegun I. A., "Handbook of mathematical functions", New york, Dover Publications (1965).

17. Ward K. D., "Compound representations of high resolution sea clutter", Electron. Lett <u>17</u> 561-565 (1981).
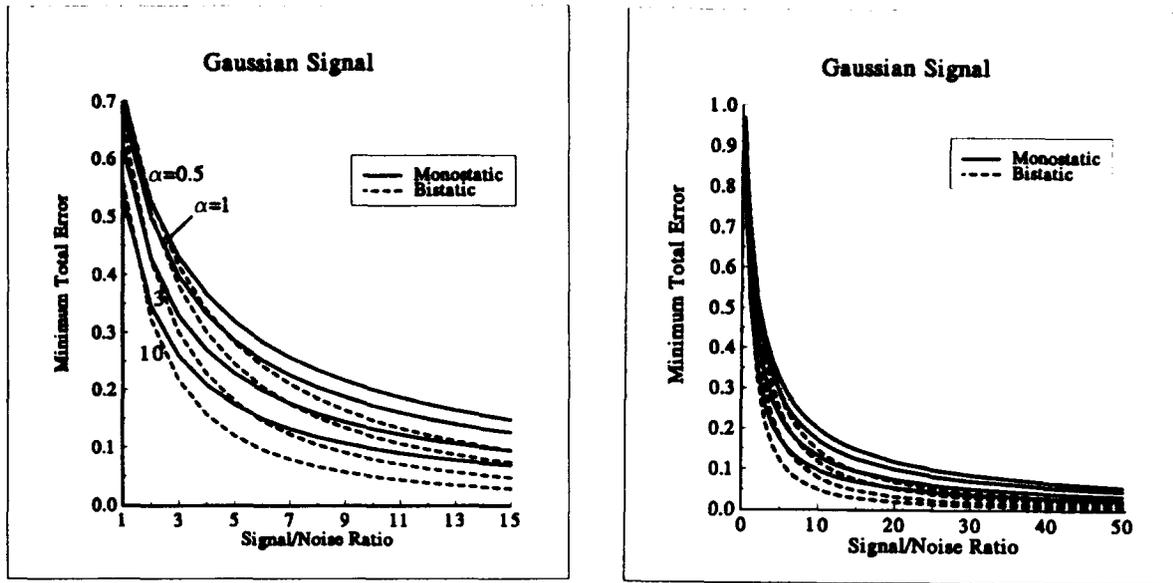
Figure 4   Minimum total error vs r, target in Gaussian speckle.
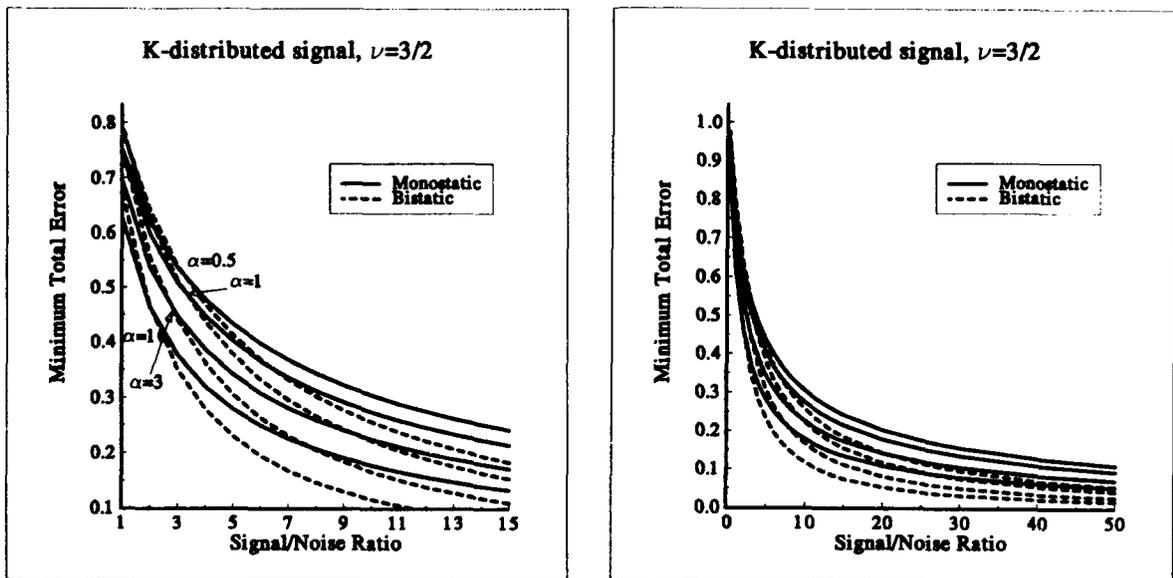
Figure 5   Minimum total error vs r. target in K-distributed noise
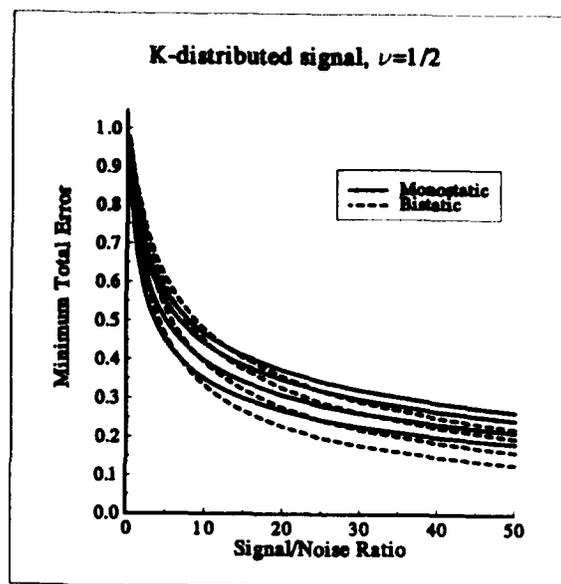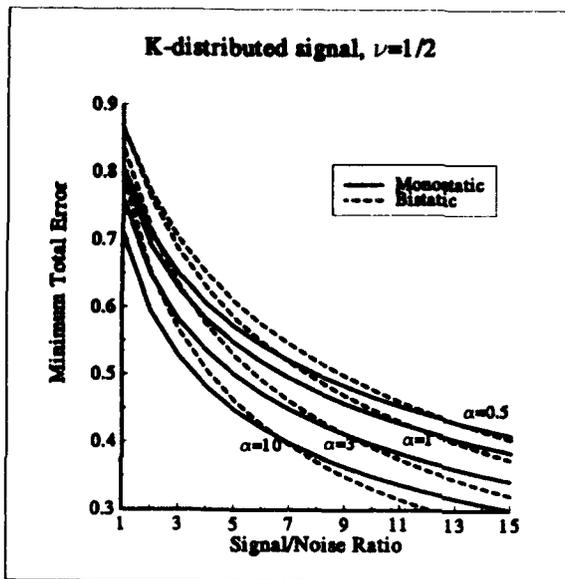
Figure 6   Minimum total error vs r, target in K-distributed noise
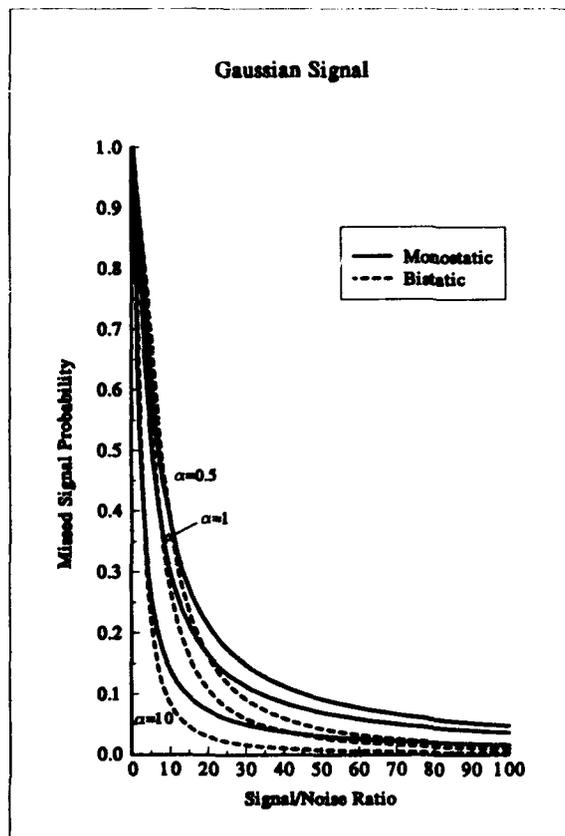
Figure 7   Missed signal probability vs r, $P_F = 10^{-6}$, target in Gaussian speckle
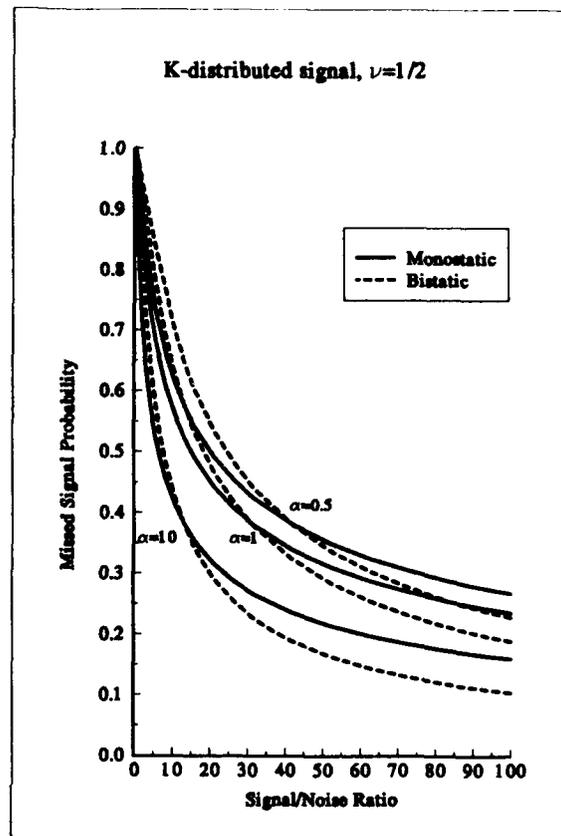
Figure 8   Missed Signal probability vs r, $P_F = 10^{-6}$, target in K-distributed noise

Discussion

Discussor's name :   B. Crosignani, IT

Comment/Question :

Can you comment on the polarization state of enhanced backscattering radiation? More precisely, will a polarization analyzer affect your detection scheme?

Author/Presenter's reply :

In the case of enhanced backscattering due to a rough surface, polarisation effects can be important. In our propagation experiments with reflection poor mirrors there are no polarisation effects as far as we know.

Discussor's name :   Ulaby, US

Comment/Question :

How large an enhancement effect did you measure?

Author/Presenter's reply :

In laboratory measurements we observed enhancements of the order of 3. For the scattering geometry of this presentation the enhancement is equal to the normalized second moment of the intensity scintillation at the target. In the case of atmospheric optical propagation this may be as much as a factor of 6.

Polarimetric Backscatter Measurements of Natural Surfaces at Millimeter Wavelengths

James Mead, Paul Chang and Robert McIntosh

University of Massachusetts
Microwave Remote Sensing Laboratory
Amherst, MA 01003, U.S.A.

1. SUMMARY

During the last four years the Microwave Remote Sensing Laboratory of the University of Massachusetts has studied the polarimetric backscatter response of natural and man-made surfaces at 35, 95 and 225 GHz. These surfaces include grass, asphalt, snowcover and trees. In addition, we have made ground-based and airborne backscatter measurements of clouds and precipitation at 95 GHz.

In this paper we summarize the results of these experiments, presenting histograms of normalized radar cross-section for trees, snowcover and clouds. The temporal dependence of the normalized radar cross-section for snowcover is also presented for 95 and 225 GHz which shows a strong diurnal variation due to melting and refreezing. We also present the angular dependence of backscatter from grass and asphalt at 35, 95 and 225 GHz, as well as volume backscattering coefficients for airborne measurements of clouds and precipitation at 95 GHz.

2. INTRODUCTION

The Microwave Remote Sensing Laboratory of the University of Massachusetts has developed several millimeter-wave radars for collecting backscatter data from natural and man-made targets. These radars include a 35 GHz FM-CW scatterometer, two 95 GHz polarimetric radars, a 215 GHz scatterometer, and a 225 GHz noncoherent polarimeter. Except for the FM-CW scatterometer, these radars employ relatively high-power Extended Interaction Klystron tubes, allowing distributed targets to be characterized at ranges between 50 m and several km. Table 1 provides a summary of the salient features of the 35, 95 and 225 GHz instruments. Further details on the design of these radar systems as well as measurement techniques may be found in the literature [1-5].

parameter	35 GHz	95 GHz	225 GHz
Transmitter:			
Frequency	34.82-35.12 GHz	94.92 GHz	225.63 GHz
Transmitter	Gunn Osc.	Klystron Amp.	Klystron Osc.
Peak Power	6 mW	1.5 kW	60 W
Modulation	FM-CW	Pulse	Pulse
Range Resolution	.5 m	30 m	30 m
Maximum PRF	n/a	80 KHz	20 KHz
Receiver:			
Front-End Mixer(s)	Balanced	Balanced	2nd harmonic
SSB Noise Figure	4.5 dB	9 dB	15 dB
Dynamic Range	60 dB	75 dB	70 dB
Antennas:			
Type	Dual Cassegrain	Rexolite lens	dual TPX lenses
Diameter	30 cm	30 cm	15 cm
3 dB beamwidth	1.8°	0.7°	0.6°
Transmit polarization	mechanically rotated, v and h	ferrite switch v and h	motor-controlled v,h,±45° RHCP,LHCP
Receiver polarization	mechanically rotated, v and h	dual v and h	dual v and h

Table 1   Summary of 35, 95 and 225 GHz radar parameters.

3. SUMMARY OF NORMALIZED RADAR CROSS-SECTION DATA AT 35, 95 AND 225 GHz

Backscatter measurements from snowcover and vegetation carried out by the Microwave Remote Sensing laboratory have been reported previously in the literature [6-11]. The following is a summary of normalized radar cross section measurements of trees, grass, asphalt, and snowcover.

3.1 Trees

Fig. 1 displays the range of observed radar cross sections, σ°_{vv}, for six tree species at 225 GHz. Fig. 2 presents σ°_{vv} for three of the six tree species at 95 GHz for comparison. These data were collected from ground level, with the radar beam pointed to the center of the tree canopy at ranges of between 100 and 300 m. All of the data presented are for fully foliated

trees, measured between June and October, 1990. σ°_{hh} was typically within $\pm$ 2 dB of σ°_{vv}. Coniferous trees with thin needles showed cross-polarized power approximately 6-9 dB below the copolarized signal. Deciduous trees with broad vertically hanging leaves (erectophil) showed cross-polarized power 11-13 dB below the copolarized signal. Decidous trees having horizontally oriented leaves (planophil) were slightly less polarized, with the cross-polarized signal 9-10 dB below the copolarized return. Planophil trees also showed slightly lower radar cross-sections than erectophil [11]. Observations of six deciduous tree species throughout the growing season at 215 GHz [9] indicate that σ° for bare trees drops by at least 7 dB and as much as 15 dB as compared to fully foliated trees. We note that the 95 GHz data was collected on the same individual trees as were the 225 GHz data, but were collected in Sept. 1992 and Sept. 1993.
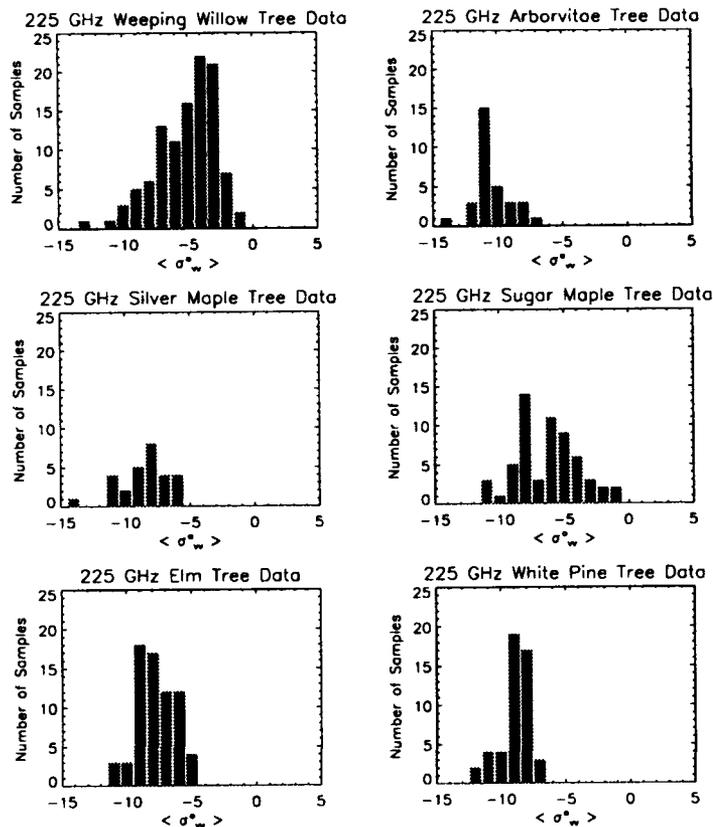
Figure 1   Histograms of σ°_{vv} for six tree species at 225 GHz.
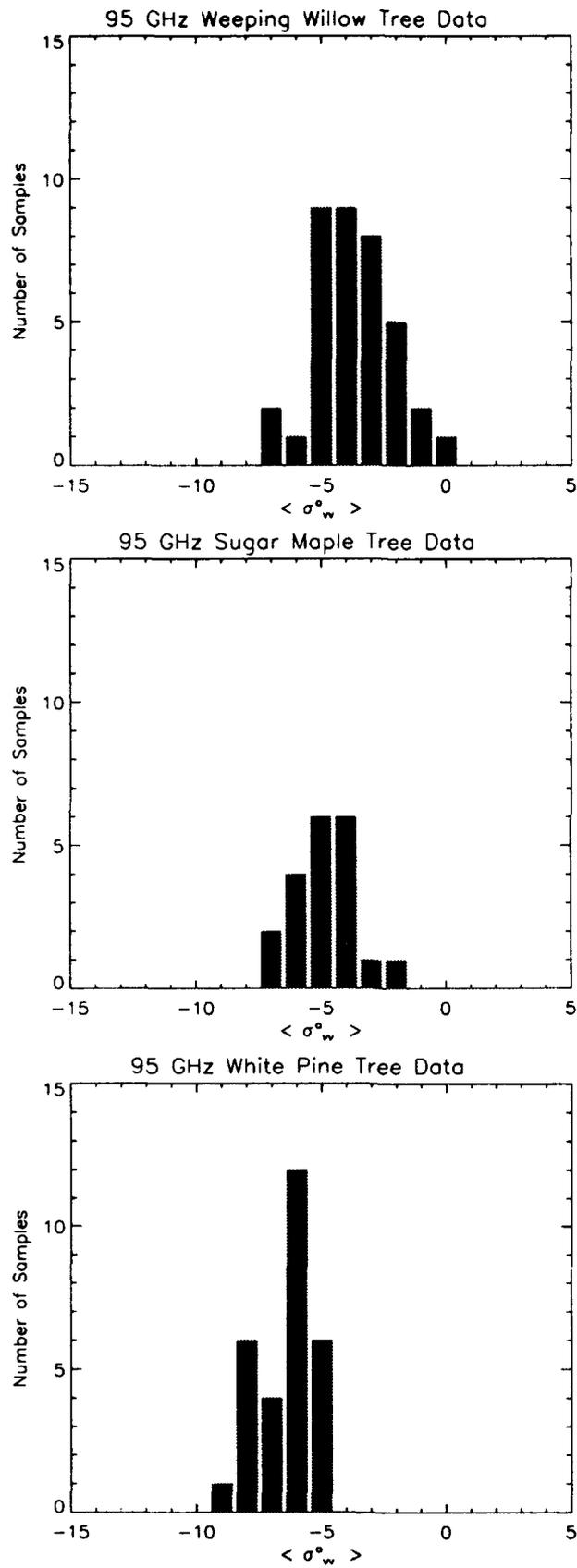
Figure 2   Histograms of σ°_{vv} for three tree species at 95 GHz.

3.2 Grass

Backscatter data for short grass is plotted versus incidence angle in Fig. 3a–5a. This data was collected from recreational and sports fields for grass heights of between 3 and 6 cm. Note that σ_{vv}° and σ_{hh}° track closely, while the cross-polarised signal is at least 8 dB below the copolarised terms.
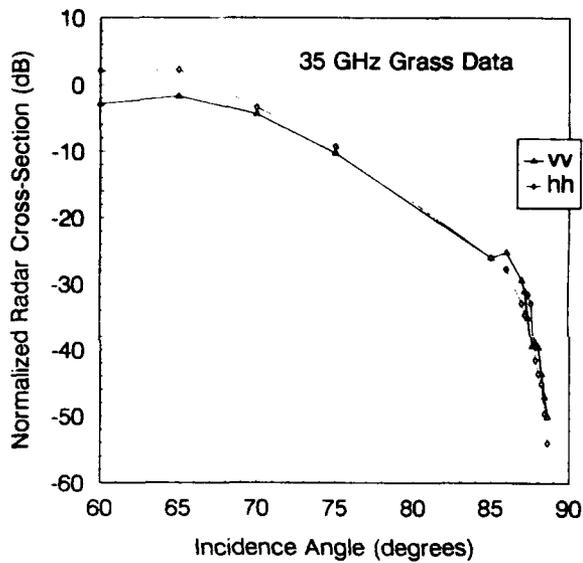
3.3 Asphalt

Backscatter data collected from asphalt is shown in Figs. 3b–5b. σ° is generally weaker for asphalt than grass, particularly for near-grazing incidence angles ($>$ 85°). Note that $\sigma_{hh} < \sigma_{vv}^\circ$ at 35 and 95 GHz, while 225 GHz exhibits $\sigma_{vv}^\circ < \sigma_{hh}^\circ$ for incidence angles greater than 85°. Depolarisation is seen to be quite severe between 85° and 88°.
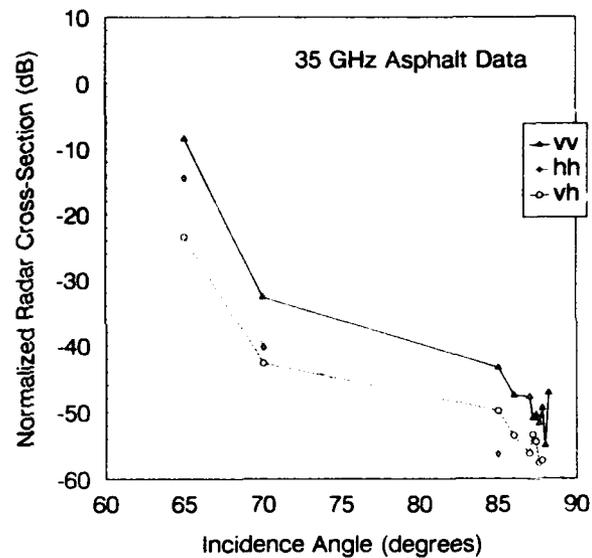
Figure 3 Normalized radar cross sections for (a) short grass (left figure) and (b) asphalt at 35 GHz.
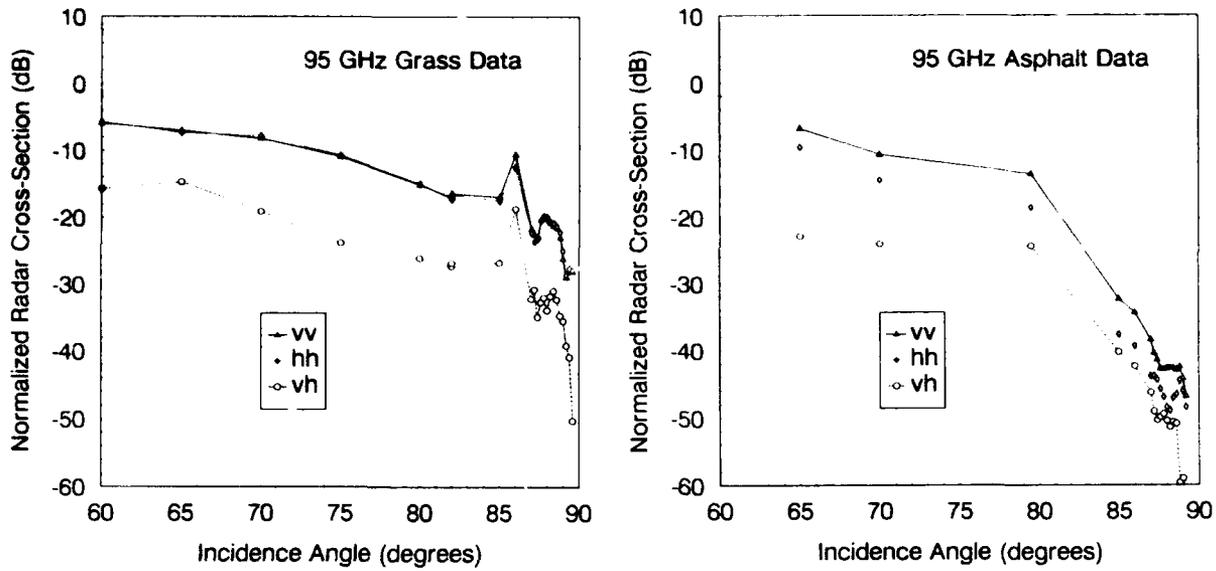
Figure 4   Normalized radar cross-sections for (a) short grass (left figure) and (b) asphalt at 95 GHz.
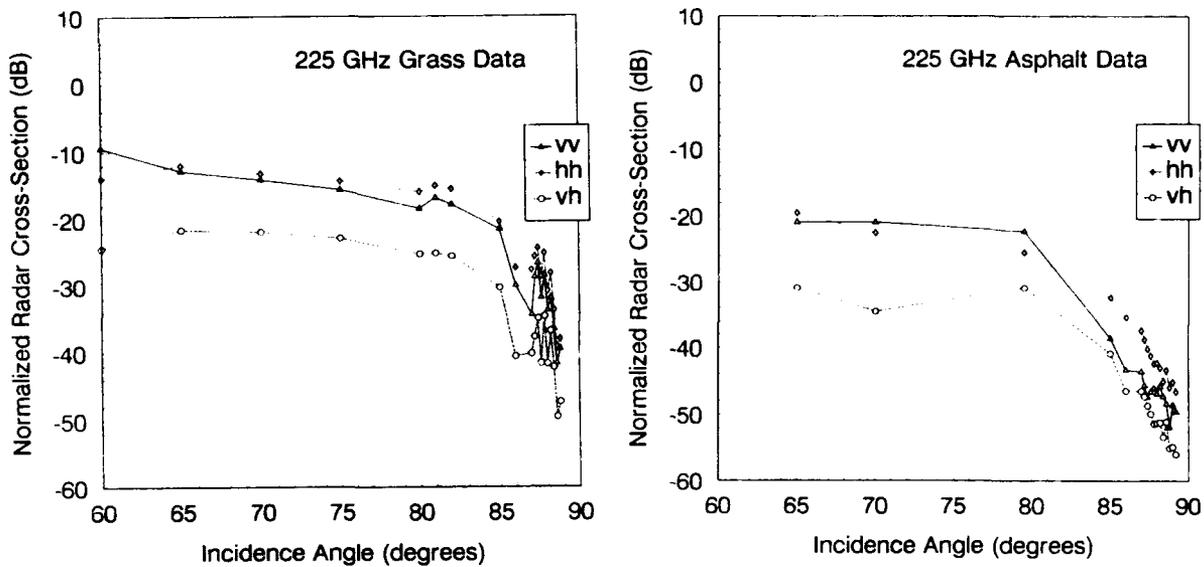
Figure 5   Normalized radar cross-sections for (a) short grass (left figure) and (b) asphalt at 225 GHz.

3.4 Snowcover

The Microwave Remote Sensing Laboratory has been collecting millimeter-wave backscatter data on snowcover since 1987, beginning with the 215 GHz scatterometer (1987-88) as summarized in [6]. Since then we have collected polarimetric data at 225 GHz (1990-93), 95 GHz (1991-93), and 35 GHz (1993). These measurements were carried out from the top of a 70 m building (1987-90, incidence angles 30-85°) and later from a 25 m building (1990-93, incidence angles 60-80°).

Diurnal variations in σ°_{vv} measured over a period of one week are shown in Fig. 6 at 95 GHz for 60° and 80° incidence. Nighttime is signified by the shaded regions. Variations of as much as 15 dB within a period of 1 hour can be seen, reflecting a rapid increase in snow wetness as the temperture rises in the morning. Similar diurnal variations were observed at both 35 and 225 GHz. Figs. 7 present histograms of σ°_{vv} versus incidence angle for a wide variety of dry and wet snowcover, collected throughout the winter of 1992-93 at 95 GHz for both 60° and 80° incidence.
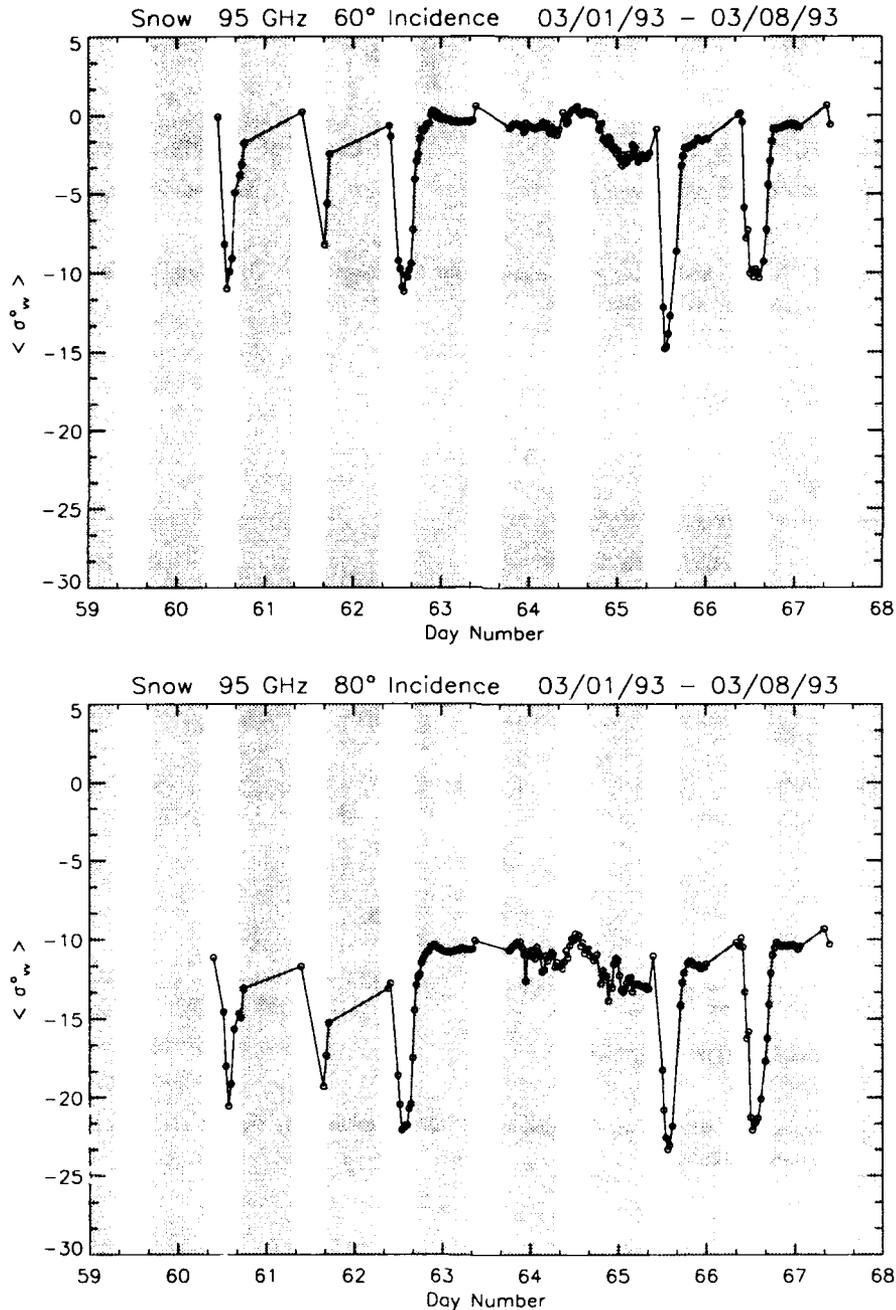
Figure 6   Diurnal variation of σ°_{vv} at 95 GHz at 60° (top) and 80° incidence angle.
Nighttime is signified by the shaded regions.

95 GHz Snowcover Data   60° incidence   1/12/93 – 3/20/93
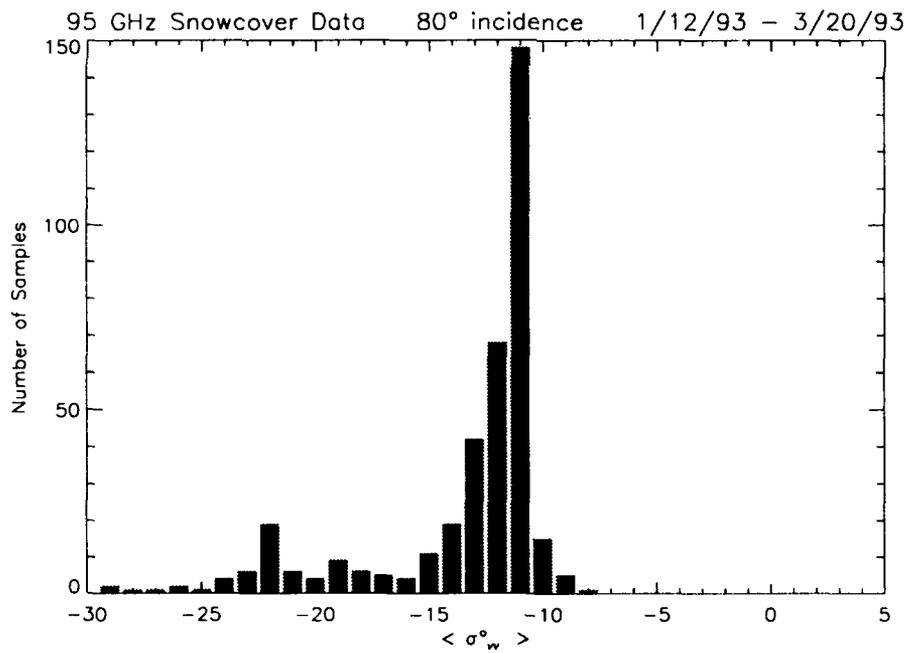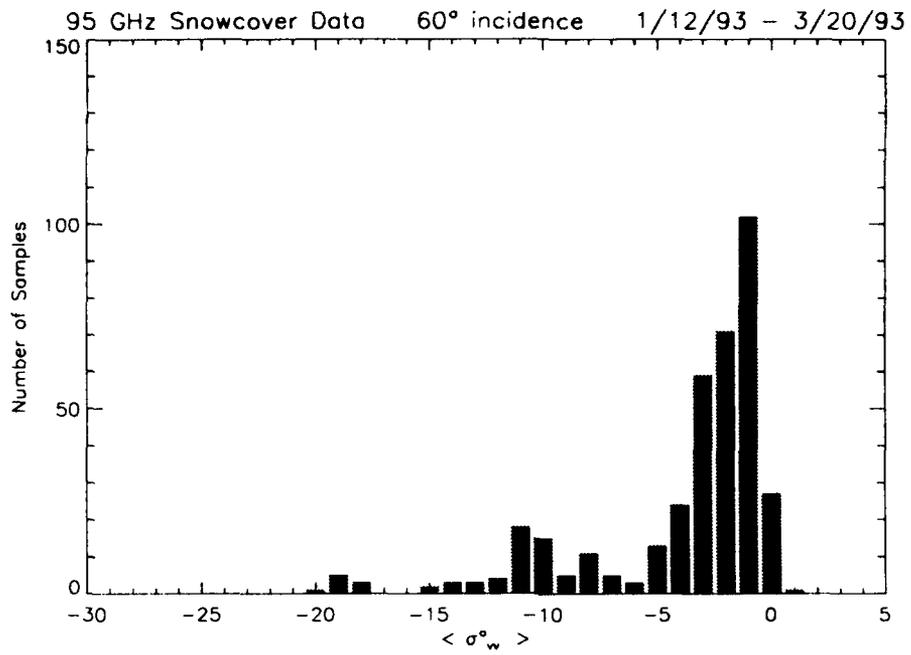
Figure 7   Histogram of σ°_{vv} at 95 GHz at 60° (top) and 80° incidence angle for winter of 1992-1993.

In Fig. 8 the diurnal variation in depolarisation ratio is plotted versus time for the same data set as in Fig. 6 at 80° incidence. Depolarisation ratio, χ, is defined as:

$$\chi = \frac{\sigma^{\circ}_{vh} + \sigma^{\circ}_{hv}}{\sigma^{\circ}_{hh} + \sigma^{\circ}_{vv}}$$

For this data set, the cross-polarised return from dry snowcover was between 3 and 8 dB below the copolarised return, while wet snowcover was generally between 8 and 13 dB below the copolarised return.

Using the fully polarimetric capability of the 95 and 225 GHz polarimeters, we observed significant phase shift between S_{vv} and S_{hh} for fresh snowcover at both 95 and 225 GHz [7], where S is the complex scattering coefficient. We attribute this differential phase shift to the anistropic nature of fresh snowcover, that often consists of non-spherical particles such as stellar dendrites, needles, and plates. Such particles usually fall with their broad faces parallel to the ground, resulting in preferred alignment in snowcover.
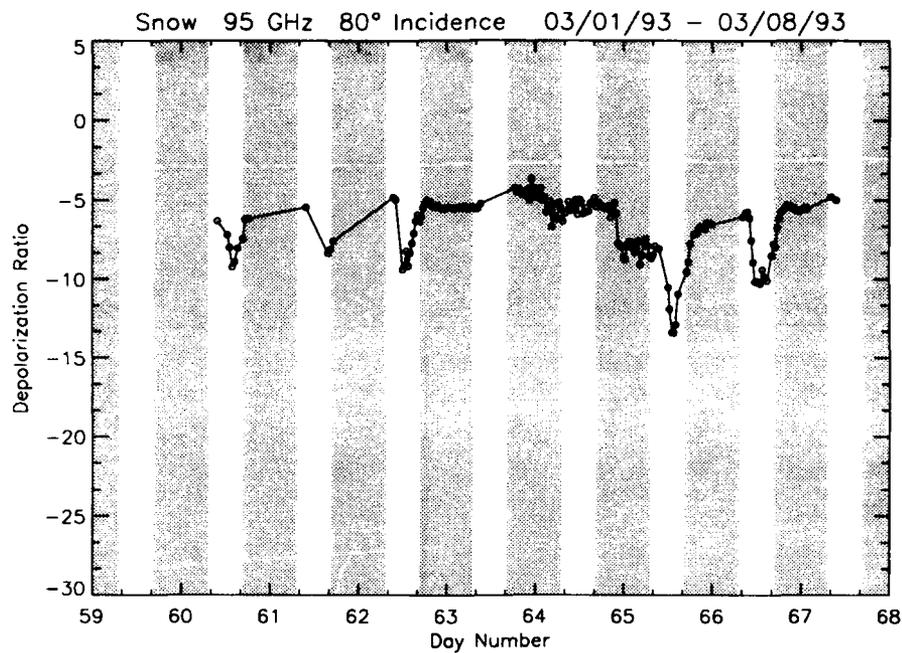

Figure 8   Diurnal variation of depolarization ratio, χ, at 95 GHz at 80° incidence angle.

4. SUMMARY OF REFLECTIVITIES OF CLOUDS AND PRECIPITATION AT 95 GHz

During the fall of 1992 we made airborne observations of clouds and precipitation at 95 GHz in cooperation with the Department of Atmospheric Sciences of the University of Wyoming. The 95 GHz radar was mounted in a twin engine aircraft from which both vertically and horizontally pointing observations were made. Observations of drizzle below the melting layer of nimbostratus clouds with concentrations of 5 particles per liter, mean diameter of 50 μm, with maximum diameters of 200 μm, showed reflectivities of $\eta=-72$ dB, where η is the volume backscattering coefficient, in m^{-1} [13], equal to the radar cross-section per unit volume. Wave clouds with individual stellar and broad-branched plates, and some small aggregates (up to 1 mm diameter) exhibited reflectivities of $\eta=-45$ dB. Precipitating graupel (up to 3 mm diameter) and light rain from small cumulonimbus exhibited reflectivities up to $\eta=-27$ dB. Fig. 9 presents a histogram of volume backscattering coefficient for vertically pointing observations of a convective cloud looking up through the melting band. Thus, this data set includes backscatter from rain, mixed phase (wet ice), graupel (ice), and aggregates (ice).

In general scattering from rain was found to be highly polarized with the cross-polarized signal weaker than the copolarized by >25 dB. For vertical pointing observations, the melting layer normally exhibited high levels of depolarization, with the cross-polarized power 10-15 dB below the copolarized return.
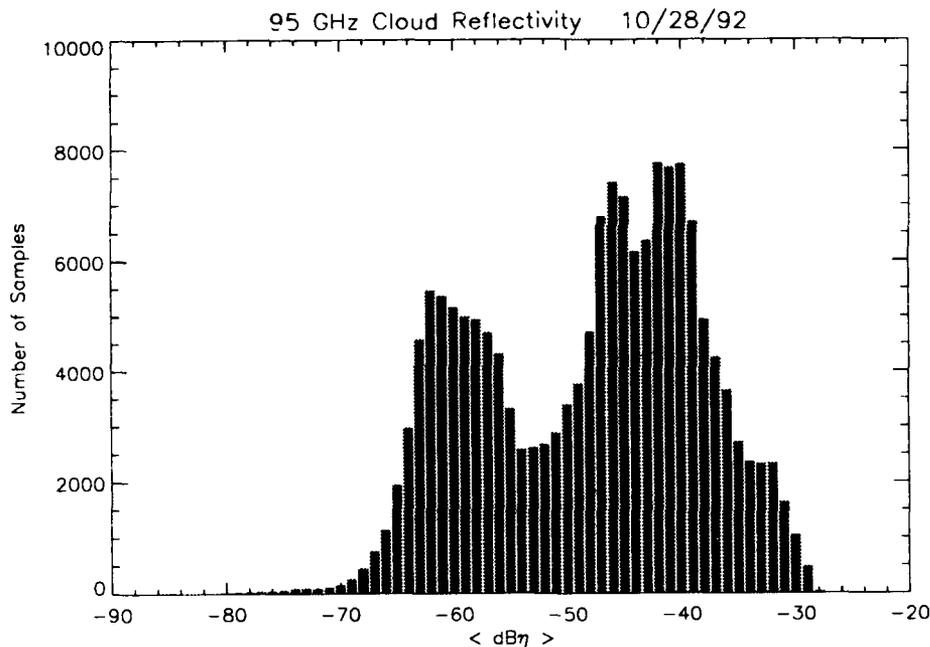

Figure 9   Histogram of copolarized volume backscattering coefficient for convective storm, vertically pointing observations (dB$\eta = 10\log\eta$).

REFERENCES

[1] R.E. McIntosh, R.M. Narayanan, J.B. Mead, and D.H. Schaubert, "Design and Performance of a 215 GHz Pulsed Radar System," *IEEE Trans. on Microwave Theory and Techniques*, vol. 36, June, 1988, pp. 994-1001.

[2] J.B. Mead and R.E. McIntosh, "A 225 GHz polarimetric radar," *IEEE Trans. on Microwave Theory and Techniques*, vol. 38, September, 1990, pp. 1252-1258.

[3] J.B. Mead and R.E. McIntosh, "Radar Scatterometry and Polarimetry at 220 GHz", *in* "Atmospheric Propagation in the UV, Visible, IR, and MM-Wave Region and Related Systems Aspects", AGARD CP 454, October, 1989, Paper 33.

[4] J. Mead, R. McIntosh, P. Langlois, and P. Chang, "Polarimetric Techniques and Measurements at 95 and 225 GHz", *in* "Target and Clutter Scattering and their Effects on Military Radar Performance", AGARD CP 501, May, 1991.

[5] P.B. Ferraro, "A KA-Band Stepped Frequency Scatterometer for the Measurement of Normalized Radar Cross Section", Master's Thesis, Dept. of Electrical and Computer Engineering, University of Massachusetts, Feb. 1992.

[6] R.M. Narayanan and R.E. McIntosh, "Millimeter-Wave Backscatter Characteristics of Multilayered Snow Surfaces," *IEEE Trans. Ant. Prop.*, vol. 38, May, 1990, pp. 693-703.

[7] J. Mead, P. Chang, S. Lohmeier, P. Langlois, R. McIntosh, 1993: Polarimetric observations and theory of millimeter-wave backscatter from snowcover, *IEEE Trans. Ant. Prop.*, 41, 38-46.

[8] R.M. Narayanan, C.C. Borel and R.E. McIntosh, "Radar Backscatter Characteristics of Trees at 215 GHz," IEEE Trans. Geoscience Remote Sensing, Vol. 26, May 1988, pp. 217-228.

[9] J.B. Mead and R.E. McIntosh, "Polarimetric backscatter measurements of deciduous and coniferous trees at 225 GHz," *IEEE Trans. on Geoscience and Remote Sensing*, vol. 29, No. 1., January, 1991, pp. 21-28.

[10] J.B. Mead, P.M. Langlois, P.S. Chang, R.E. McIntosh, 1991: Polarimetric scattering from natural surfaces at 225 GHz, *IEEE Trans. Ant. Prop.*, 39, 1405-1411.

[11] C.C. Borel and R.E. McIntosh, "Millimeterwave Backscatter from Deciduous Trees," *IEEE Trans. Ant. Prop.*, vol. 38, pp. 1391-1398, Sept. 1990.

[12] F.T. Ulaby, R.K. Moore, A.K. Fung, *Microwave Remote Sensing: Active and Passive*, Vol. 2, Artech House, Norwood, MA, 1982, p. 315.

Discussion

Discussor's name : P. Baars, GE

Comment/Question :

Do you have values for the penetration depth of mmWaves in snow and its dependence on Liquid Water content.

Author/Presenter's reply :

Although we did do some 'preliminary' transmission measurements at 35 and 95 GHz, I don't have any values at this time.

A HYBRID ELECTROMAGNETIC - STATISTICAL APPROACH FOR CHARACTERIZING MMW SCATTERING BY TERRAIN

Fawwaz T. Ulaby, Paul Siqueira, and Kamal Sarabandi
The Radiation Laboratory
Department of Electrical Engineering and Computer Science
The University of Michigan
Ann Arbor, MI 48109-2122
USA

SUMMARY

The performance of millimeter-wave (MMW) radar systems in target detection navigation and other applications depends in part on the scattering characteristics of the terrain background. Two different approaches have been pursued in the literature for characterizing MMW scattering by terrain. The first approach relies on the development of electromagnetic scattering models that relate the backscattering coefficient $\sigma°$ of a given terrain type (such as bare ground surfaces, snow cover, and vegetation) to the physical properties of the terrain target, and then verifying model predictions though experimental observations conducted under semi-controlled field conditions. The second approach is entirely empirical in nature; it relies on the acquisition of extensive radar data from which statistical distributions are generated. The University of Michigan has been involved in a research program, supported by the U.S. Army Research Office, whose goal is to pursue both approaches as well as to develop a hybrid approach that combines the strengths of both approaches. This paper provides an overview of how the hybrid approach can be used to simulate the statistical properties of terrain backscatter at millimeter wavelengths for several types of terrain, including bare soil surfaces, vegetation, and snow cover. The hybrid approach incorporates scintillation effects associated with coherent sensors together with information about the mix of terrain categories present in the scene. Two types of input data (or a merged set of both) can be used as input to the clutter simulation package: (a) measured data that is available in a University of Michigan data base, or (b) data generated by electromagnetic models. The data base is available in a University of Michigan Handbook that contains MMW scattering observations reported in the literature for certain terrain types and conditions. Alternatively, a set of electromagnetic models can be used for calculating the backscattering coefficient $\sigma°$ of the specified terrain type. These models, which are semi-empirical in form, are based on highly complicated theoretical models that had been tested against experimental observations. With this approach, it is possible to generate a probability density function for the backscatter from a certain type of terrain without the need for a measured clutter data base. This is particularly attractive at millimeter wavelengths bec   only a limited amount of terrain clutter data is currently available.

1 INTRODUCTION

By way of introducing the subject of terrain clutter at millimeter wavelengths, let us start by considering the case of a radar system designed to detect hard targets against the terrain background. Figure 1(a) depicts a radar beam with resolution area A illuminating a target with backscattering radar cross section (RCS) σ_t. The terrain background is a statistically homogeneous background with mean clutter RCS $\sigma_{c0} = \sigma°A$, where $\sigma°$ is the (average) backscattering coefficient of the terrain. In this case, the signal to noise ratio is given by:

$$\frac{S}{N} = \frac{\sigma_t}{\sigma_{c0}} = \frac{\sigma_t}{\sigma°A} . \tag{1}$$

Because terrain scattering is noise-like in character, its variability behaves according to Rayleigh fading statistics [1], which leads to the following expression for the probability density function (pdf) of the envelope voltage V_e at the output of the receiver's envelope detector:

$$p(V_e) = \frac{2V_e}{\sigma_{c0}} \exp\left[-\frac{(V_e^2 + \sigma_t)}{\sigma_{c0}}\right] I_0\left(\frac{2V_e\sqrt{\sigma_t}}{\sigma_{c0}}\right) \tag{2}$$

where $I_0(\ )$ is the zeroth-order Bessel function.
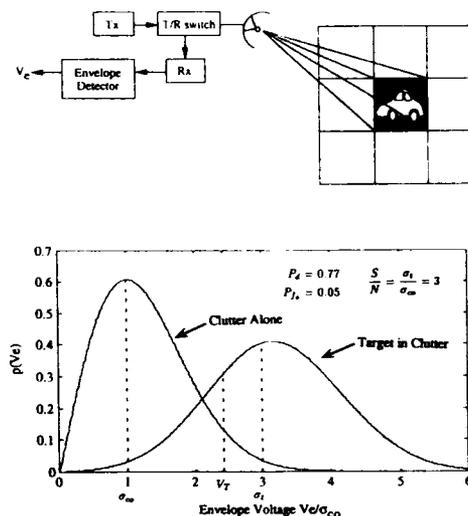

Figure 1. Probability density functions for clutter alone and clutter with a target with RCS = 5 dB above the average clutter cross section, σ_{co}.

34-2

If no target is present ($\sigma_t = 0$), Eq. (2) reduces to:

$$p(V_{e0}) = \frac{2V_{e0}}{\sigma_{c0}} \exp\left(-\frac{V_{e0}^2}{\sigma_{c0}}\right) , \qquad (3)$$

where V_{e0} denotes V_e with no target present. For a specified theshold voltage V_T, the false alarm probability P_{fa} is given by:

$$P_{fa} = \int_{V_T}^{\infty} p(V_{e0}) \, dV_{e0}$$
$$= \exp\left(-\frac{V_T^2}{\sigma_{c0}}\right) , \qquad (4).$$

and the corresponding detection probability P_d is obtained by integrating $p(V_e)$ over the limits V_T to ∞:

$$P_d = \int_{V_T}^{\infty} \frac{2V_e}{\sigma_{c0}} \exp\left[-\frac{(V_e^2 + \sigma_t)}{\sigma_{c0}}\right] I_0\left(\frac{2V_e\sqrt{\sigma_t}}{\sigma_{c0}}\right) dV_e \quad (5)$$

Figure 1(b) shows plots of $p(V_{e0})$ for $\sigma_{c0} = 1m^2$ and $p(V_e)$ for $S/N = \sigma_t/\sigma_{c0} = 3$ (5 dB). The indicated threshold voltage V_T was chosen to yield a probability of false alarm $P_{fa} = 0.05$; the corresponding value of P_d is 77%.

The preceding treatment, which describes the radar detection problem on the basis of a single pulse for statistically homogeneous clutter, is standard textbook material. Extensions include the integration of multiple pulses to increase P_d [2] and the use of frequency averaging [3] to decrease the variability of the clutter RCS (narrower $p(V_{e0})$), which also leads to improved P_d. Another extension relates to the nonuniform terrain situation for which the backscattering coefficient σ° is characterized by its own pdf $p(\sigma^\circ)$, rather than having a constant value as was assumed in the preceding expressions. Examples of such situations may include a background comprised of a single terrain type (such as vegetation cover) but with varying physical characteristics (height, moisture content, and geometry of vegetation elements) or a background comprised of a mixture of different types of terrain (vegetation, roads, water bodies, etc.). The methodology for characterizing the combined effects of fading variations and a non-constant σ° is described in [1].

For any radar-detection situation, regardless of whether or not multiple-pulse integration or frequency averaging is used, the two fundamental quantities governing the detection performance of the radar system are the target RCS (or $p(\sigma_t)$ if it is a fluctuating target), and the mean clutter RCS σ_{c0} (or $p(\sigma_{c0}) = \frac{1}{A}p(\sigma^\circ)$ for nonuniform terrain). Characterizing σ_t is outside the scope of this presentation, and therefore it will not be addressed. The remaining part of this paper will focus on two approaches for characterizing $\sigma^\circ = \sigma_{c0}/A$ and $p(\sigma^\circ)$, namely (a) the data-base approach, which relies on measured distributions of σ° for specific types of terrain, and (b) the electromagnetic model approach, which uses electromagnetic scattering models to compute $p(\sigma^\circ)$ for a given set of terrain conditions, specified in terms of the ranges of variability of pertinent physical parameters. Whereas either approach may be used at centimeter wavelengths, it is not possible to rely on the data-base approach alone at millimeter wavelengths because only a limited amount of terrain-specific clutter measurements is available at the present time. The next section describes a hybrid approach that utilizes both of the aforementioned approaches for characterizing terrain clutter. The sections that follow present electromagnetic models for snow cover and soil surfaces at 35 and 94 GHz. Models for other types of terrain are under development and will be presented in future publications.

2 HYBRID APPROACH FOR CHARACTERIZING CLUTTER

Figure 2 shows a simplified representation of the simulation package that uses the hybrid approach for evaluating the detection performance of a radar system. The radar system specifications include: (a) the operating frequency f, (b) the incidence angle θ (relative to nadir), (c) the receive / transmit antenna polarization configuration, (d) the number of pulses N_p available for integration, and (e) the spatial resolution area A. The terrain is specified as belonging to one of the categories / sub-categories given in Figure 3. The classification system depicted in Figure 3 forms the basis for the data base contained in the Handbook of Radar Scattering Statistics for Terrain [1], which exists in both hard-cover form and as a software package. The Handbook data base contains calibrated experimental measurements of σ° reported in the open literature, but it is not inclusive of all such data. Only data that had been judged as satisfying certain data-quality criteria were included in the data base. For each terrain category, the data are grouped into distinct frequency bands covering the range from 1 GHz to 100 GHz, but for most terrain categories, the number of data points at frequencies above 30 GHz is either very small or identically zero. This is precisely the motivation for proposing the use of electromagnetic (EM) models for generating a supplementary data base.

HYBRID APPROACH FOR CHARACTERIZING TERRAIN CLUTTER
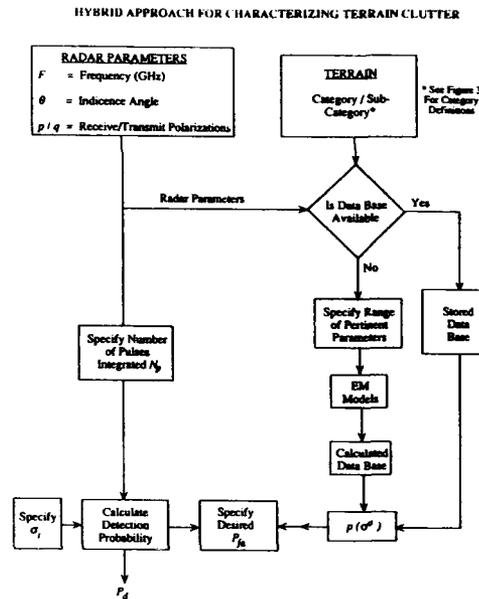
Figure 2. Flow-chart representation of the radar-detection performance simulation package.

In the flow chart given in Figure 2, this option follows from the response to the question: "Is a measured data base available (in the Handbook)?" The question refers to the category specified in the preceding step, subject to the radar parameters specified in the "Radar Parameters" block. If the answer to the question is negative, EM models of the form given in later sections are used to generate the supplementary data base. To do this, the user has to specify the range of pertinent parameters. For snow-covered terrain, for example, the user will be asked to specify the expected ranges of snow depth and air temperature. Similar specifications apply to other terrain categories. As a result of this process, a pdf for

σ°, $p(\sigma^\circ)$, is generated by merging the supplementary data base calculated from the EM models with whatever data base of measured data that happens to be available in the Handbook. The term "Handbook" refers to data in [1] as well as more recent MMW data given in [4].

RADAR TERRAIN CLASSIFICATION SYSTEM
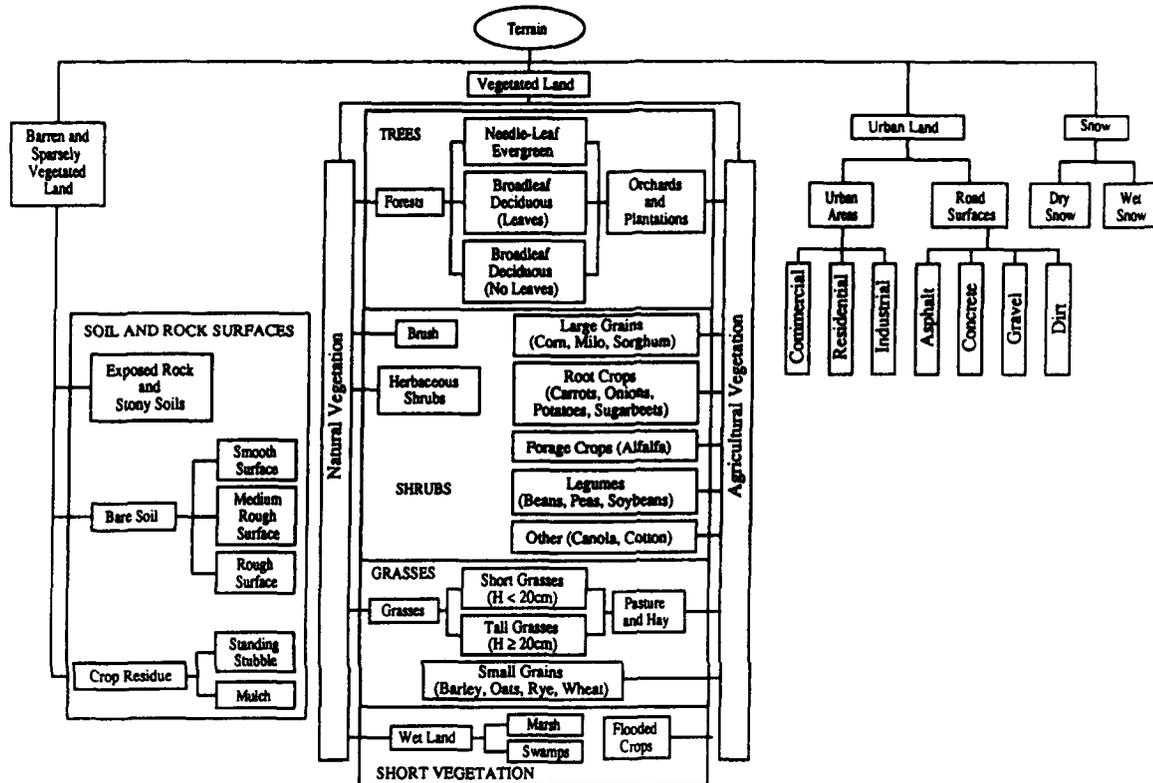
Figure 3. Radar terrain classification system.

With $p(\sigma^\circ)$ available, the pdf of the clutter cross section $p(\sigma_c)$ can be readily calculated by incorporating the variations due to signal fading fluctuations, as described in Section 3-5 of [1]. Upon additionally specifying the desired false alarm probability P_{fa} and the number of pulses used for incoherent integration, the program then calculates the expected detection probability P_d for a given hard-target cross section σ_t. This procedure can serve as an effective tool for evaluating the detection performance of MMW radar sensors.

3 EXAMPLES OF AVAILABLE MMW CLUTTER DATA

Most experimental measurements of radar backscatter reported in the literature, which are in the form of plots of σ° as a function of the incidence angle θ, pertain to a specific terrain type and condition. Data of this form are available in [4] for HH, HV, and VV polarizations at 35, 94, 140, and 215 GHz for various types of terrain including trees, grasses, road surfaces, dry snow, wet snow, and ice-covered ground. From this collection of data, histograms have been generated for specific combinations of frequency band, incidence angle, polarization configuration, and terrain type and condition. The histogram is an unnormalized pdf of σ°. An example is shown in Figure 4 for dry snow at 35 GHz for

$\theta = 50^\circ$. Because of the limited number of available data points, the histogram is not a smooth continuous function of σ°. Consequently, when such data is used in the radar detection- performance analysis, it is replaced with a Gaussian distribution having the same mean value and standard deviation as those calculated from the histogram. Analysis of the dependence of the mean value $\bar\sigma^\circ$ and the standard deviation $S(\text{of } \sigma^\circ)$ on the incidence angle θ led to the following functional form:

$$\bar\sigma^\circ_{dB} = P_1 + P_2\exp(-P_3\theta) + P_4\cos(P_5\theta + P_6) \quad (6)$$
$$S_{dB} = M_1 + M_2\exp(-M_3\theta) \quad (7)$$

where θ is the incidence angle in radians and the coefficients P_1 to P_6 and M_1 to M_3 assume fixed values for a specific terrain category and polarization configuration. The values of these coefficients are given in Table 1 for six terrain categories for which sufficient data exists to justify the curve fitting procedure. All the cases given in Table 1 are based on 35 GHz observations; insufficient data exists at the present time for higher MMW frequencies.

Histogram for Dry Snow
Ka Band, 50 Degree Incidence Angle

Figure 4. Histograms of $\sigma°$ for dry snow at 35 GHz.

Following the standard assumption that $\sigma°$ (dB) is a Gaussian-distributed variable, it follows that $\sigma°$, expressed in natural units of m^2/m^2, is log-normally distributed. That is, with

$$\sigma°_{dB} = 10 \log \sigma° , \qquad (8)$$

The pdf of $\sigma°$ is given by:

$$p(\sigma°) = \frac{4.34}{\sqrt{2\pi}\sigma°S_{dB}} \exp\left[-[10\log\sigma° - \bar{\sigma}°_{dB}]^2 / 2S^2_{dB}\right] \quad (9)$$

where $\bar{\sigma}°_{dB}$ and S_{dB} are the mean and standard derivations of $\sigma°$ in dB, as determined from the histogram of the experimental data. By way of illustration, Figure 5 shows plots of $p(\sigma°)$ for short vegetation, road surfaces, and dry snow cover, all for HH polarization at an incidence angle of 50°. These are the type of the probability density functions generated by the simulation package flow-charted in Figure 2.
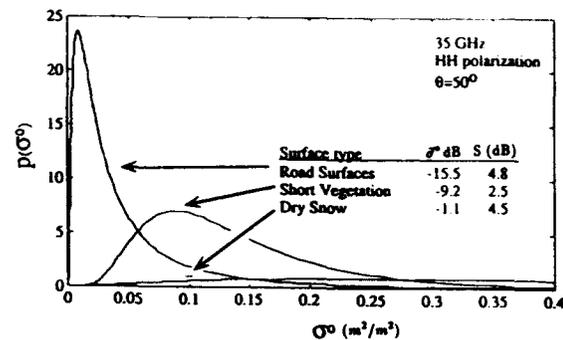

Figure 5. Probability density functions for short vegetation, road surfaces and dry snow cover at 35 GHz; $\bar{\sigma}°$ (dB) and 5 (dB) are the mean value and associated standard deviation, both in dB, of the measured $\sigma°$ (dB) distribution.

TABLE 1. Values of coefficients P_1 to P_6 and M_1 to M_3 associated with Equations (6) and (7), which characterize the angular dependence of the mean value $\bar{\sigma}°$ (dB) and standard deviation S(dB) for various types of terrain at 35 GHz.

Terrain	Pol.	Angular Range	$\bar{\sigma}°$(dB) Coefficients						S(dB) Coefficients		
			P_1	P_2	P_3	P_4	P_5	P_6	M_1	M_2	M_3
Grasses	HH	10-70	-99	92.4	0.04	1.17	5.0	-1.9	3.5	-1.1	1.6
	VV	10-70	-99	91.8	0.04	1.10	5.0	-2.1	3.0	-2.6	5.1
Shrubs	HH	20-70	-41	27.8	0.08	-8.7	0.9	3.1	2.2	4.4	4.6
	VV	20-70	-44	41.6	0.22	-0.8	5.0	-1.4	2.1	2.9	4.4
Short Vegetation	HH	10-80	-99	79.1	0.26	-30	0.7	2.1	2.8	3.1	15
	VV	10-80	-99	80.3	0.28	-30	0.8	2.0	2.7	0	0
Road Surfaces	HH	10-70	-95	99	0.69	30	1.3	-1.7	7.2	-5.2	0.8
	VV	10-70	-85	99	0.80	-30	1.6	1.1	3.2	0	0
Dry Snow	HH	0-75	-84	99	0.30	8.9	2.7	-3.1	-9	13.5	0.06
	VV	0-70	-88	99	0.22	7.4	2.8	-3.1	-9	13.8	0.06
Wet Snow	HH	0-70	44	-13	-0.86	29	1.1	2.8	-8.2	15	-0.08
	VV	0-70	-34	7.9	15	30	0.78	-0.4	5.5	1.4	0.55

4 ELECTROMAGNETIC MODELS FOR TERRAIN CLUTTER

As was stated in earlier section, radar clutter data currently available at millimeter wavelengths is deficient in the following ways: (1) most of the available data is at 35 GHz, with negligible amount of data available at the higher atmospheric window frequenies of 94, 140, and 215 GHz, (2) for some types of terrain, insufficient data exists even at 35 GHz, and (3) for those terrain types for which data is available at 35 GHz, the terrain conditions represented by the data may be too broad in comparison to terrain situations of interest, thereby resulting in $\sigma°$ distributions that cover a wider range of values than necessary, which in turn leads to poorer estimates of the false alarm and detection probabilities P_{fa} and P_d.

In principal, a possible solution to this problem is to develop a set of electromagnetic scattering models that can relate $\sigma°$ to the physical properties of the terrain. Using calibrated scatterometer systems, numerous experiments were conducted over the past several years to determine the dependence of $\sigma°$ on pertinent terrain parameters, and to serve as the basis for evaluating the applicability of theoretical models. Typical examples illustrating the agreement between experimental observations and theoretical predictions are shown in Figures 6 and 7 for snow. Figure 6 shows the angular dependence of $\sigma°$ at 95 GHz for snow cover with 5% liquid water content, and Figure 7 shows the diurnal variation of $\sigma°$ at 35, 95, and 140 GHz, which is in response
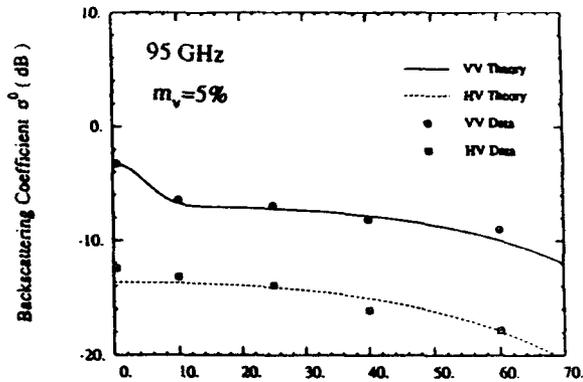
Figure 6. Measured and calculated angular variation of σ° for wet snow with 5% wetness at 95 GHz.

to variations in liquid water content. The theoretical model that was used in this case was a numerical radiative transfer model that accounts for multiple scattering in the snow volume [5,6]. Although the model provides good predictions of σ°, it is fairly complicated mathematically and its code is computationally intensive.
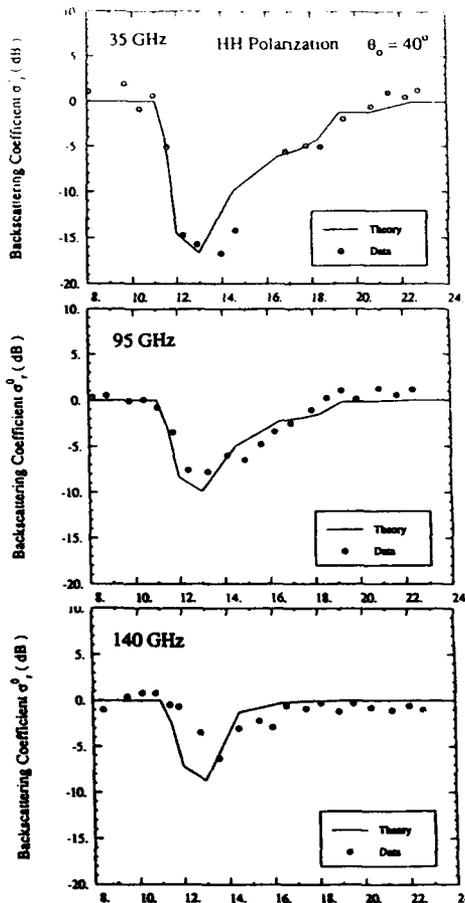

Figure 7. Comparison of measured and calculated diurnal response of σ° for snow at 35, 95, and 140 GHz. The incidence angle is 40°, snow density is 0.32 g/cm³, and the snow depth is 12 cm.

Similar models, with similarly good prediction capabilities but complicated mathematical formulations, have been developed for vegetation [7] and bare-ground surfaces. Unfortunately, because of their mathematically complicated form, these models are not being used by the radar community at large. To overcome this problem, we have developed relatively simple semi-empirical expressions that yield results within typically 1 dB of the values provided by the elaborate theoretical models. The next two sub-sections present these expressions, together with curves illustrating the behavior of σ°, for snow cover and bare-ground surfaces. Similar expressions are under development for other terrain types and will be presented in future publications.

4.1 Snow Cover

At millimeter wavelengths, the HH and VV polarized backscattering coefficients of snow-covered terrain are essentially identical in magnitude over the angular region between 10° and 70° from nadir. Hence, a single expression is used for both co-polarized backscattering coefficients. The parameters governing the magnitude of σ° are the incidence angle θ, the snow depth h (cm), and the volumetric liquid water content m_v (%). Secondary in importance are the snow density ρ and the ice crystal size distribution. The expressions given below were computed for a typical value of $\rho = 0.3$ g/cm³ and for a Gaussian distribution of ice particle diameters with a mean value of 1 mm and a standard deviation of 0.2 mm. Deviations from these conditions can lead to errors on the order of 1-3 dB.

For snow depth $h \geq 10$ cm, the following expression was found to provide excellent fits to experimental data as well as to values computed with the theoretical radiative transfer model:

$$\sigma^\circ(\theta, h, m_v) = \{A[1 - \exp(-B\,h\,\sec\theta')]\exp(-C\,m_v)\}$$
$$+ D\exp(-E\,m_v)\}\cos\theta + F \qquad (10)$$

with θ', the refraction angle in the snow medium, being related to the incidence angle θ by:

$$\theta' = \sin^{-1}\left[\frac{\sin\theta}{\sqrt{1.61 + 0.035m_v}}\right]. \qquad (11)$$

The constant coefficients A through F have the following values:

Coefficient	35 GHz	94 GHz
A	1.4	1.4
B	1.8×10^{-2}	5.6×10^{-2}
C	1.4	0.52
D	0.33	0.03
E	0.01	- 0.27
F	- 0.17	0.05

The variation of σ° with θ, h, and m_v is illustrated by the sets of curves shown in Figure 8 for 35 GHz and in Figure 9 for 94 GHz. The points denoted by stars in the figures represent the values of σ° calculated using the theoretical radiative transfer model [5,6], which are included in the figures for only a few cases in order to illustrate the magnitude of the error between the exact theoretical calculations and those calculated on the basis of the expression given by (10).
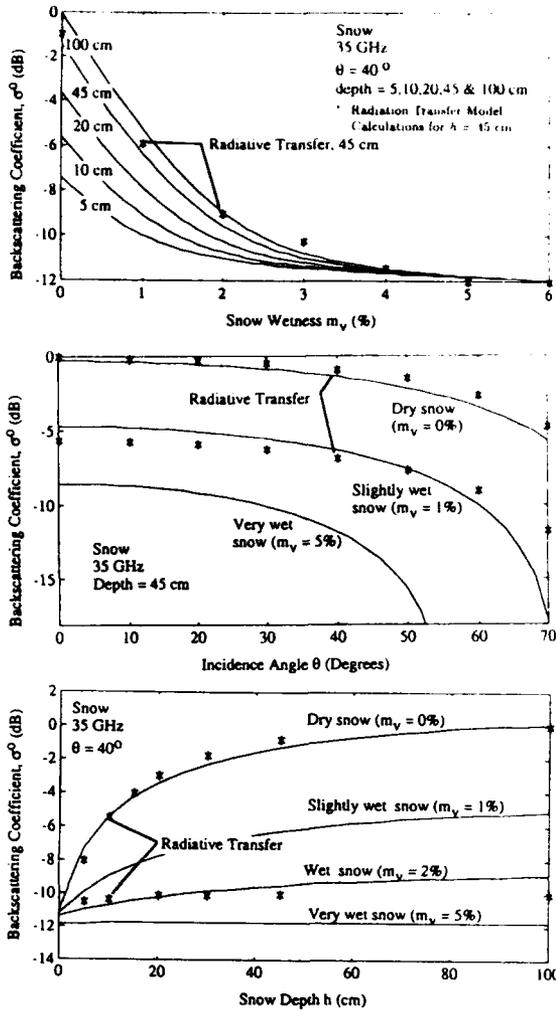
Figure 8. Variation of σ° with incidence angle θ, snow depth h and liquid water content m_v at 35 GHz.

Figure 9. Variations of co-polarized σ° with snow depth h and snow liquid water content m_v at 94 GHz.

4.2 Bare-Soil Surfaces

In general, scattering by a soil surface may contain two scattering components, one due to scattering by the surface itself and another due to particle scattering in the soil medium. Thus, the backscattering coefficient may be expressed as:

$$\sigma^\circ = \sigma^s + \sigma^v , \qquad (12)$$

where the superscripts s and v denote surface and volume scattering, respectively. The models given below for σ^s and σ^v are based on a combination of semi- empirical models and theoretical models that were generated through comparison with experimental data measured at 35 and 94 GHz.

Surface Scattering Component

The surface scattering component σ^s is a function of the incidence angle θ, the volumetic moisture content of the surface layer m_v, and the electromagnetic roughness of the surface ks, where $k = 2\pi/\lambda$ and s is the rms height of the surface. Based on experimental observaions made at 35 and 94 GHz for surfaces with various roughnesses and moisture contents, the following expressions were generated for the vv, hh, and hv polarization components of σ^s:

$$\sigma^s_{vv} = g\frac{\cos^x \theta}{\sqrt{P}} \left[\Gamma_v(\theta) + \Gamma_h(\theta) \right] \qquad (13)$$

$$\sigma^s_{hh} = P\sigma^s_v v \qquad (14)$$

$$\sigma^s_{hv} = q\sigma^s_v v \qquad (15)$$

where

$$q = \frac{\sigma^s_{hv}}{\sigma^s_{vv}} = 0.23\sqrt{\Gamma_0}\left[1 - \exp(-0.2ks)\right] \qquad (16)$$

$$P = \frac{\sigma^s_{hh}}{\sigma^s_{vv}} = \left[1 - \left(\frac{2\theta}{\pi}\right)^{1/(3\Gamma_0)} \cdot \exp(-0.4ks) \right]^2 \qquad (17)$$

$$g = 0.7\tau \left[1 - \exp\left(-0.65(ks)^{1.8}\right) \right]$$
$$+ 2.2(1 - \tau)\left[1 - \exp(-0.2ks)\right] \qquad (18)$$

$$x = 3.5 + \frac{1}{\pi} \tan^{-1}\left[10(1.65 - ks)\right] \qquad (19)$$

$$\tau = \frac{1}{2} + \frac{1}{\pi} \tan^{-1}\left[100(0.08 - m_v)\right] \qquad (20)$$

and $\Gamma_v(\theta)$ and $\Gamma_h(\theta)$ are the Fresnel reflectivities of the surface and θ is measured in radians.

Volume Scattering Component

The volume scattering component σ^v is a function of θ, the moisture content m_v and the mean particle diameter d_0. Comparison of the magnitude of σ^v to σ^s reveals that $\sigma^v \gg \sigma^s$ at 35 GHz, but at 94 GHz σ^v may be smaller than σ^s for wet soil or larger than σ^s for very dry soil. Hence, expressions for σ^v are given for 94 GHz only. With d_0 expressed in mm, the following expressions were established on the basis of matcyhing a radiative transfer model to experimental data:

$$\sigma^v_{vv} = [(11.75 - 0.8\cos\theta)d_0]^{2.73}\ e^{-0.6m_v} \qquad (21)$$

$$\sigma^v_{hh} = [(6.15 + 4.77\cos\theta)d_0]^{2.73}\ e^{-0.6m_v} \qquad (22)$$

The dependence of the total soil backscattering coefficient at 35 GHz on surface roughness ks and moisture content m_v is shown in Figure 10. The relative importance of the volume and surface components at 94 GHz is depicted in Figure 11 and the total backscattering coefficient is plotted in Figure 12 as a function of m_v for three different values of d_0. It is clear that if m_v exceeds 0.1, surface scattering becomes the dominant contribution.
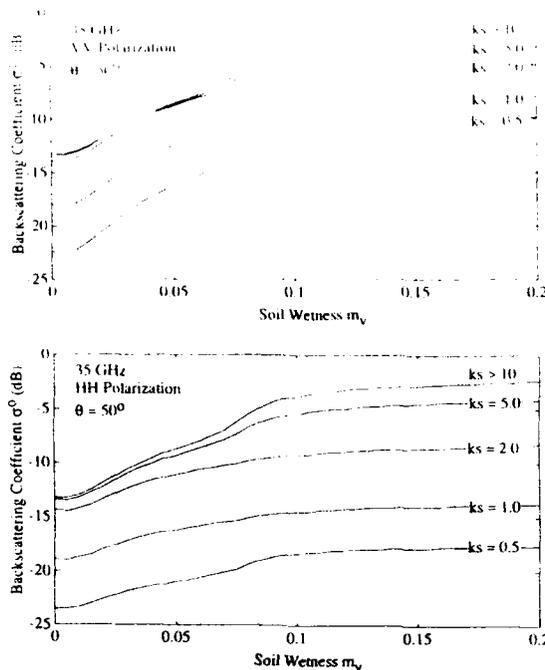
Figure 10. Dependence of σ^0 at 35 GHz on soil wetness and electromagnetic surfaced roughness ks for vv and hh polarizations.
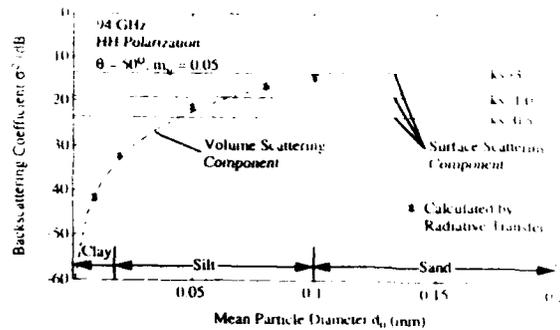
Figure 11. Variation of volume scattering component σ^v at 94 GHz with mean particle diameter d_0. The level of the surface scattering component is indicated for comparison for three roughnesses.
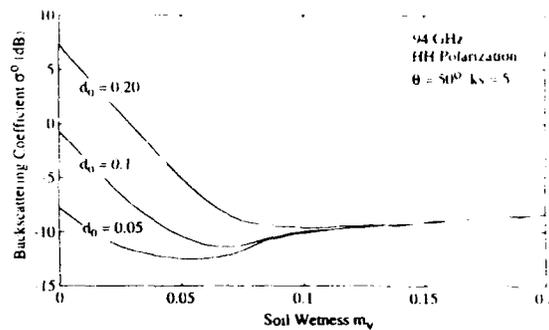

Figure 12. Variation of σ^0 at 94 GHz with m_v for moderately rough surface with $ks = 5$.

5 CONCLUSIONS

A hybrid model has been presented for evaluating the detection performance of a millimeter-wave radar against terrain clutter. In the case of terrain types and conditions for which sufficient experimental data exists to characterize the probability density function of the backscattering coefficient σ^0-which is limited to 35 GHz for a few types of terrain, the simulation model uses standard procedures for computing the false alarm and detection probabilities, P_{fa} and P_d.

For radars operating at 94 GHz, as well as for 35-GHz radars operating in terrain backgrounds for which sufficient experimental observatiosn are not available, the hybrid model generates the requisite clutter pdf on the basis of electromagnetic models that were developed through careful experimental investigations. In this paper, electromagnetic models are provided for snow cover and for bare soil surfaces. Similar models for vegetation cover and road surfaces are under development and will be presented in future publications.

References

[1] Ulaby, F.T., and M.C. Dobson, *Handbook of Radar Scattering Statistics for Terrain*, Artech House, Norwood, Massachusetts, 1989.

[2] Skolnik, M.I., *Introduction to Radar Systems*, McGraw Hill, New York, 1980, Chapter 2.

34-8

[3] Ulaby, F.T., T.F. Haddock, and R.T. Austin, "Fluctu-
ation Statistics of Millimeter-Wave Scattering for Dis-
tributed Targets," *IEEE Trans. Geosci. Remote Sens-
ing*, Vol. 26, No. 3, May 1988, pp. 268-281.

[4] Ulaby, F.T., and T.F. Haddock, "Millimeter-Wave Radar
Scattering From Terrain: Data Handbook, Version 2,
University of Michigan Radation Laboratory Technical
Report 026247-4-T, September 1990.

[5] Kuga, Y., F.T. Ulaby, T.F. Haddock, and R. DeRoo,
"Millimeter-Wave Radar Scattering From Snow: Part
I-Radiative Transfer Model with Quasi-Crystalline Ap-
proximation," *Radio Science*, Vol. 26, March 1991, pp.
329-341.

[6] Ulaby, F.T., T. Haddock, R. Austin and Y. Kuga,
"Millimeter-Wave Radar Scattering From Snow: Part
II-Comparison of Theory with Experimental Observa-
tions," *Radio Science*, Vol. 26, March 1991, pp. 343
351.

[7] Ulaby, F.T., T.H. Haddock, and Y. Kuga,
Measurement and Modeling of Millimeter-Wave Scat-
tering From Tree Foliage" *Radio Science*, Vol. 25, 1990,
pp. 193-203.

Discussion

Discussor's name :   E. Schweicher, BE

Comment/Question :

Is it true that the receiving antenna is a corrugated horn?

Author/Presenter's reply :

Yes it is for all four radar systems

Discussor's name :   H. B. Wallace, US

Comment/Question :

How do you relate the PdF of the clutter data to the instrumentation spatial resolution and
the postulated system resolution in your models?

Author/Presenter's reply :

For resolution cells containing several correlation lengths, Rayleigh statistics is applicable,
but for sub-correlation length size cells, we need to develop different statistical models. We
are working on that now.

GRANULOMETRIE DE MILIEUX A FAIBLE CONCENTRATION DE PARTICULES.

A. Delfour, B. Guillame
CERT/ONERA-DERO
2, Avenue Edouard Belin
31055 Toulouse Cedex, France

A. Junchat
CELAR/GEOS/SOP
35170 Bruz, France

RESUME
Le principe d'un système pour la granulométrie par diffusion de lumière des particules d'un milieu très faiblement concentré a été étudié. Le bilan de liaison a montré qu'il est possible de détecter des particules, à partir de $0,2\mu m$ de diamètre, avec un rapport signal à bruit acceptable, pour une concentration volumique au moins égale à 10^{-6} ppm.
Une maquette test a été dimensionnée et sa réponse à l'introduction de particules distribuées aléatoirement dans le volume de mesure, simulée numériquement. Des modèles atmosphériques urbain, rural ou maritime ont été utilisés dans une gamme de concentration étendue. Plusieurs longueurs d'onde d'éclairement ont été testées. La granulométrie d'aérosols atmosphériques est possible si la concentration volumique est supérieure ou égale à 10^{-5} ppm et la longueur d'onde d'éclairement de l'ordre de grandeur de la taille moyenne des particules.
La contribution des particules à la visibilité atmosphérique peut être mesurée moyennant un étalonnage préliminaire du système de détection.
Un montage de laboratoire a été réalisé en vue de valider la modélisation.
Afin de simuler des concentrations convenables de particules, une chambre de tests de $10\,dm^3$ a été construite.
Des expériences, à l'aide de poudres de licopodes (25 à 35 μm de diamètre) en concentration volumique connue, ont été reproduites correctement.

1. INTRODUCTION
La propagation des rayonnements électromagnétiques dans un milieu contenant des aérosols est d'autant plus perturbée que la distance parcourue est grande. L'influence du "canal atmosphérique" n'est donc pas négligeable sur la mesure des signatures optiques. L'exploitation de telles mesures sur sites terrestres et/ou maritimes, nécessite de pouvoir séparer, la partie due au rayonnement propre de la cible, de la contribution du "canal atmosphérique".

La modélisation de ce canal est fournie par des codes de calcul qui s'appuient sur des résultats théoriques et expérimentaux. Ainsi, certains paramètres caractéristiques du milieu peuvent être appréhendés par la mesure de la distribution en taille des aérosols atmosphériques.

Généralement, la distribution en taille d'aérosols par mesures de diffusion "in-situ" est obtenue en prenant en compte des hypothèses sur la nature physique et le nombre des particules composant l'aérosol.

En particulier, si une particule, sphérique, homogène, de diamètre a et d'indice de réfraction complexe n, est éclairée par une onde plane de longueur d'onde λ, la diffusion de la lumière par les particules peut être modélisée à l'aide du formalisme de Lorenz-Mie [1, 2, 3].

La section efficace de diffusion différentielle σ, dans une direction θ de l'espace est proportionnelle au rapport entre les vecteurs de Poynting diffusé N_{sc} et incident N_{in}, à la distance R entre l'observateur et la particule, et à l'angle solide d'observation $d\Omega$ [2] :

$$\sigma(n,a,\lambda,\theta) = \left| \frac{N_{sc}}{N_m} \right| R^2 \, d\Omega$$

Pour un nuage de distribution en taille $f(a)$, dont les particules ont un diamètre compris entre a_m et a_M:

- le nombre de particules par unité de volume d'aérosol est:

$$C_n = \int_{a_m}^{a_M} f(a)\, da$$

- la section efficace volumique de diffusion β du nuage dans la direction θ :

$$\beta(\theta) = \int_{a_m}^{a_M} \sigma(n,a,\lambda,\theta)\, f(a)\, da$$

- et la section efficace volumique d'extinction β_{ext} :

$$\beta_{ext} = \int_{a_m}^{a_M} \sigma_{ext}\, f(a)\, da$$

dans l'hypothèse que la lumière diffusée une première fois par une particule n'est pas rediffusée ensuite (diffusion simple).

Compte tenu de l'allure générale de la fonction de distribution en taille $f(a)$, il est plus judicieux de travailler en volume des particules.

- alors :

$$g(a) = \frac{6}{\pi a^3} f(a)$$

et le volume occupé par les particules par unité de volume d'aérosol (C_v : concentration volumique) est:

$$C_v = \int_{a_m}^{a_M} g(a)\, da$$

Si la concentration est trop élevée, la modélisation du phénomène est plus complexe.

Pour un volume éclairé de quelques cm^3, les mesures sont significatives si la concentration volumique est comprise entre 10^{-3} et 10 ppm.

Alors, moyennant un certain nombre de mesures de diffusion, la fonction de distribution des particules est obtenue. Une mesure complémentaire d'extinction pour une traversée D_d du nuage permet de connaître la concentration.

35-2

La plupart des appareils commerciaux répondent à ce besoin.

Le CERT/DERO a réalisé des systèmes basés sur le même principe, mais plus spécialement adaptés à des mesures "in-situ" dans des milieux hostiles [4]. La granulométrie est alors obtenue, à l'aide d'un logiciel original de traitement statistique: PSD.

Dans le cas de l'atmosphère, la concentration est très faible. La granulométrie est donnée par des compteurs qui mettent un temps prohibitif à identifier un nombre de particules statistiquement convenable.

Des mesures de diffusion, s'adressant à un volume suffisant pour la granulométrie d'aérosols moyennement concentrés, ne seraient pas significatives dans le cas d'une atmosphère classique, car le nombre de particules éclairées serait trop faible. Pour effectuer des mesures significatives, il faudrait augmenter le volume diffusant de manière prohibitive.

Un appareil, qui augmenterait artificiellement ce volume, permettrait de pallier à ce dernier inconvénient, tout en effectuant des mesures locales.

2. PRINCIPE DE MESURE

2.1 Schéma de principe.
Les appareils classiques étudiés au CERT/DERO mesurent la diffusion d'un nuage de particules traversé par un faisceau laser. Le volume diffusant est délimité par l'intersection du faisceau laser et du nuage de particules. Il est en général de faibles dimensions: 100 mm de long pour une section de 5 mm².

Pour que la mesure soit significative, dans le cas de milieux à faible concentration, le procédé devra créer un volume observé artificiellement plus grand, sinon, le faisceau laser induisant la diffusion aura une faible probabilité de rencontrer des particules, et le niveau du signal diffusé sera très bas.

D'autre part, le système ne devra pas agrandir de façon prohibitive les dimensions et donc l'encombrement de l'appareil.

Le principe retenu est le suivant:
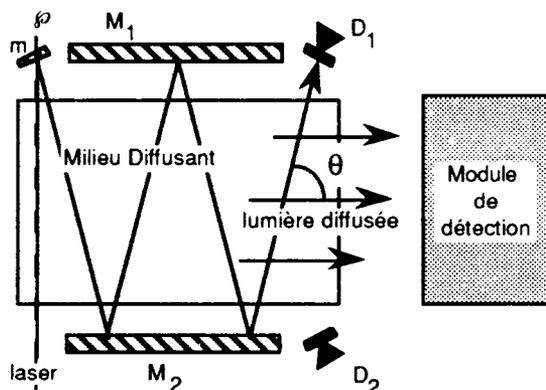
figure 1: Schéma de principe du dispositif de mesure

Le milieu diffusant est compris entre deux miroirs plans, parallèles entre eux M_1 et M_2.

Un petit miroir m, donne au faisceau incident une orientation variable, et le fait se propager entre ces deux derniers par réflexions successives. Le trajet parcouru par le faisceau incident peut ainsi être largement développé.

Ce miroir m est entraîné par un moteur dont la vitesse de rotation peut être choisie. Il est solidaire d'un codeur optique incrémental 1000 points/tour qui sera utilisé pour connaître avec précision la valeur de l'angle de diffusion.

Chaque particule qui se trouve sur ce trajet diffuse la lumière dans tout l'espace. Un détecteur placé dans une direction fixe parallèle aux miroirs M_1 et M_2, mesure l'intensité de lumière diffusée dans la direction θ relative à la direction du faisceau incident. A chaque tour du miroir m, une indicatrice de diffusion est ainsi obtenue.

Le bloc de détection est composé d'une optique permettant de limiter le champ entre les miroirs M_1 et M_2, en excluant les volumes voisins de leur surface. Cette optique dirige la lumière sur la surface sensible d'un photomultiplicateur qui lui-même est suivi d'une électronique de traitement.

Simultanément à la mesure de diffusion dans la direction θ le détecteur D_1 (ou D_2) mesure la puissance transmise par le nuage.

Afin d'obtenir des mesures complémentaires en rétrodiffusion, il suffit de compléter le schéma de principe de la figure 1, en ajoutant des miroirs M_3 et M_4 (et des détecteurs D_3 et D_4) symétriquement à M_1 et M_2 (D_1 et D_2) par rapport au plan $\wp$ contenant le faisceau laser et l'axe du miroir m.

Le problème fondamental d'un tel montage est la représentativité du phénomène de diffusion. Il est évident que le volume diffusant analysé diffère fortement suivant la direction d'éclairement. Les différences sont géographiques et dimensionnelles, et sont prises en compte dans la modélisation du procédé.

En contre-partie de cet inconvénient, le montage a des intérêts majeurs:

- Le trajet du faisceau laser dans le milieu est agrandi artificiellement par reflexions successives entre M_1 et M_2, le système global conservant un encombrement raisonnable.

- Le seul élément mobile est le miroir tournant m, de faibles dimensions.

2.2 Bilan de liaison.
Le milieu est composé de particules sphériques de diamètre a et de même indice de réfraction complexe n. Lorsqu'elles sont éclairées par une onde monochromatique de longueur d'onde λ, de densité de puissance J_0, elles présentent, observées dans la direction θ, une section efficace de diffusion différentielle σ.

Le but est d'exprimer la relation liant le signal lumineux de diffusion, somme des contributions élémentaires de chaque particule, avec la puissance incidente d'éclairement, et d'estimer le rapport signal à bruit S/B en sortie du module de détection.

Les paramètres du système sont répartis en trois postes:

La source
de puissance P_0, de diamètre d_s, éclairant le milieu dans une direction θ par rapport à la direction des miroirs M_1 et M_2, et présentant une densité de puissance J_0 à une distance d de l'axe de propagation.

Le milieu
caractérisé par:

- son volume diffusant V_{sc} fonction du diamètre du faisceau laser, de la direction d'éclairement et de la longueur L des miroirs M_1 et M_2:

$$V_{sc} = \pi d_s^2 \frac{L}{\cos\theta}$$

- sa concentration en particules C_n ou C_v. Le nombre de particules éclairées est :

$$N_p = C_n V_{sc}$$

Le bloc de détection
- en particulier, l'angle solide de détection Ω dépend de la surface du détecteur S_d, de la longueur des miroirs L et de la distance L_d entre le plan $\wp$ et le plan d'entrée du bloc de détection.

en diffusion avant:

$$\Omega = S_d \left(L_d - \frac{L}{2} \right)^{-2}$$

en rétrodiffusion:

$$\Omega = S_d \left(L_d + \frac{L}{2} \right)^{-2}$$

Pour une particule le bilan de liaison s'exprime par le schéma suivant:

```
┌─────────────────────────┐
│        Source:          │
│   Densité de puissance  │
│      J₀ (W.m⁻²)         │
└─────────────────────────┘
            │
            ▼
┌─────────────────────────┐
│       Particule:        │
│ Section efficace de     │
│       diffusion         │
│     σ (m².sr⁻¹)         │
└─────────────────────────┘
            │
            ▼
┌─────────────────────────┐
│       Réponse:          │
│ Angle solide dΩ -       │
│    Direction θ          │
│  J₀ σ(θ) dΩ (W)         │
└─────────────────────────┘
```
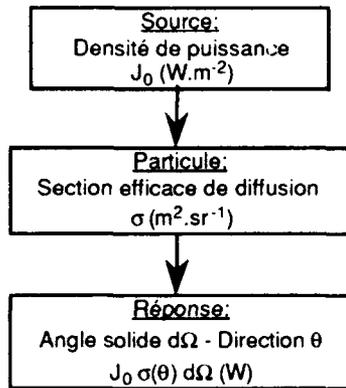
figure 2: Expression du bilan de liaison

Pour un nuage contenant C_n particules identiques par unité de volume, la puissance totale diffusée sera:

$$P_{sc} = J_0 \sigma(\theta) \Omega C_n V_{sc}$$

Si le détecteur est un photomultiplicateur et si le seul bruit pris en compte est le bruit de grenaille, le rapport S/B s'exprime ainsi:

$$\frac{S}{B} = \frac{S_a P_{sc}}{\sqrt{2 G e (S_a P_{sc} + I_{0s}) \Delta f}}$$

où :
S_a est la sensibilité typique de l'anode.
G le gain en courant entre photocathode et anode.
I_{0s} la valeur maximale du courant d'obscurité;
Δf la bande passante du PM (Δf_{PM} = 100 MHz) ou de son électronique associée (Δf_{PB} = 10 KHz).

La puissance diffusée et le rapport signal à bruit dans une direction quelconque de l'espace sont calculés à partir du formalisme de Lorenz-Mie, des caractéristiques typiques du P.M et d'un dimensionnement préliminaire du dispositif à évaluer.

Les résultats ont été obtenus à partir des caractéristiques suivantes:

- La source est un laser HeNe de puissance P_0 = 5 mW, de diamètre d_s = 1 mm, et de longueur d'onde λ = 632,8 nm.

- Le milieu compris entre deux miroirs M_1 et M_2 de longueur L = 150 mm, distants de h = 50 mm, est chargé de particules d'indice de réfraction n = 1,5 - 0,01 i, pour des concentrations volumiques inférieures à 10^{-3} ppm.

- Le bloc de détection est placé à une distance de $\wp$, égale à 250 mm

Le tableau suivant résume les résultats obtenus pour un angle moyen de diffusion de θ = 50° et une concentration volumique C_v = 10^{-3} ppm.

a(μm)	C_n(cm⁻³)	N_p	P_{sc}(W)	S/B(dB)	
				Δf_{PM}	Δf_{PB}
0,2	250000	45000	5.10^{-9}	3	23
1	2000	350	10^{-8}	4,5	24
5	15	3	8.10^{-10}	-1	20

Pour une concentration volumique C_v = 10^{-6} ppm.

a(μm)	C_n(cm⁻³)	N_p	P_{sc}(W)	S/B(dB)	
				Δf_{PM}	Δf_{PB}
0,2	250	45	5.10^{-12}	-3	8
1	2	0,35	10^{-11}	0	9,5

Il est possible de détecter des particules de 0,2 μm de diamètre pour une concentration volumique aussi faible que 10^{-6} ppm. Une seule particule est détectable si son diamètre est supérieur à 1 μm. Le rapport signal à bruit est toujours acceptable à condition d'associer au P.M un filtre passe-bas.

Il reste à évaluer les puissances lumineuses parasites susceptibles de détériorer ce rapport.

2.3 Puissance lumineuse parasite.
Le faisceau subit des pertes à chaque réflexion sur les miroirs M_1 et M_2. Elles sont de deux types:

- Les pertes par absorption et transmission qui sont négligeables.

- Les pertes par diffusion. Elles sont dues à des inhomogénéités sur les surfaces (défauts, présence de particules polluantes). Ces pertes sont beaucoup plus importantes que les précédentes, car elles engendrent de la lumière parasite se propageant dans toutes les directions, donc susceptible de parvenir jusqu'au détecteur.

Ces diffusions parasites sont éliminées en excluant les miroirs du champ du détecteur. Cependant, l'énergie diffusée par les surfaces rediffuse sur les particules du milieu conformément au schéma de la figure 3.

Si R_m est le coefficient de réflexion des miroirs, la puissance totale diffusée P_s dans le milieu après la ième reflexion:

$$P_s = (1 - R_m) P_i$$

La puissance utile provient d'une petite part du nombre total des particules, c'est-à-dire la part présente dans le faisceau laser. La puissance provenant de la diffusion des miroirs est supposée uniformément répartie dans un demi espace. La puissance sera issue de toutes les particules du milieu.
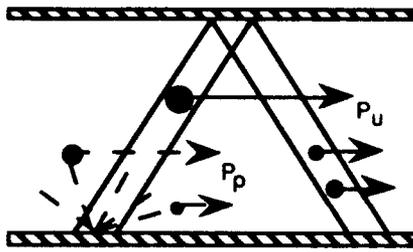
figure 3: Diffusion utile et diffusion parasite

Il s'ensuit que même si la diffusion à chaque réflexion sur un miroir est faible devant la puissance incidente, il est nécessaire de le justifier en ce qui concerne la diffusion secondaire par rapport à la diffusion utile. Il s'agit donc de comparer, après N réflexions sur les miroirs, la puissance utile P_u, incidente sur les particules se trouvant sur le trajet du faisceau laser:

$$P_u = \frac{k}{\sin\theta} \sum_{i=0}^{N} R_m^i$$

et la puissance parasite (issue des reflexions) P_p incidente sur les particules du milieu :

$$P_p = k(1 - R_m) \sum_{j=1}^{N} R_m^{j-1}$$

où k est un coefficient dépendant de la puissance incidente, de la taille et de la concentration des particules.

Si toutes les particules sont identiques, alors le rapport des puissances:

$$\varepsilon = \frac{P_p}{P_u} = K(N)(1 - R_m)\sin\theta$$

où:

$$K(N) = \frac{\sum_{j=1}^{N} R_m^{j-1}}{\sum_{i=0}^{N} R_m^i}$$

Suivant les valeurs de N et du coefficient de reflexion des miroirs, K est compris entre 0,5 et 1.

La limite inférieure de ε aura lieu pour N = 1, (20°< θ < 35°), et la limite supérieure quand N croît indéfiniment, soit quand θ approche de 90°.

En fonction du coefficient de réflexion R_m, les valeurs de ε se situeront dans les fourchettes [5] :

$R_m = 0,95$ $0,9\% < \varepsilon < 5\%$

$R_m = 0,99$ $0,2\% < \varepsilon < 1\%$

La puissance lumineuse parasite est toujours largement inférieure à la puissance utile.

Le bilan de liaison du système est satisfaisant. La simulation numérique du principe de mesure de diffusion pour la granulométrie de milieux faiblement concentrés doit permettre de confirmer les possibilités du procédé et de dimensionner une maquette de laboratoire.

3. SIMULATION

3.1 Caractéristiques du montage.

Le montage est conforme au descriptif présenté pour le calcul du bilan de liaison.

La dimension L des miroirs est égale à 150 mm, mais leur bord se situe à d_0 = 10 mm du plan $\wp$. La distance entre M_1 et M_2 est h = 80 mm. La distance entre le centre des détecteurs D_1 et D_2 et la deuxième extrémité des miroirs est aussi égale à d_0. Le plan d'entrée du bloc de détection est placé à L_d = 600 mm.

Compte-tenu de ces caractéristiques, la diffusion angulaire sera mesurée entre $\theta \approx 25°$ (impact du faisceau incident sur D_2 sans réflexion), et $\theta \approx 82°$ (impact du faisceau sur D_1 après 15 réflexions). L'agrandissement du trajet diffusant est compris entre 2,3 et 16.

En ce qui concerne la rétrodiffusion, la mesure est réalisable entre 97° et 153°.

3.2 Modélisation.

Modèle de référence

Il est possible de calculer simplement, à partir de formalismes de diffusion connus, la réponse angulaire d'un nuage de particules, tel que celui dont la distribution est représentée figure 4, s'il est éclairé entièrement par un faisceau de lumière monochromatique.
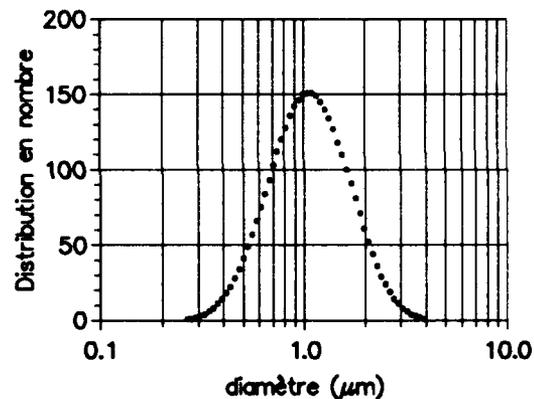

figure 4: Modèle de nuage.

Dans un premier temps, le formalisme choisi est un modèle de diffusion de Rayleigh qui offre l'avantage, par rapport au modèle de Lorenz-Mie plus général, de permettre le calcul des sections efficaces de manière quasi-instantanée. La validation définitive de la modélisation sera faite pour des distributions connues (modèles urbain, rural ou maritime) en utilisant le formalisme de Lorenz-Mie.

La longueur des miroirs M_1 et M_2 et la distance qui les sépare, imposent un volume de référence V_r, dont la base a les dimensions 500 mm × 100 mm. Pour une concentration volumique $C_v = 10^{-4}$ ppm, l'épaisseur est de 20 mm. V_r contient alors N_p = 65535 particules réparties suivant le modèle de la figure 4.

En supposant que tout le volume référence est éclairé par le faisceau laser, et par application du formalisme de Rayleigh à la distribution théorique des particules, une répartition théorique de l'intensité diffusée est calculée. L'indicatrice de diffusion ainsi obtenue sert de base de comparaison pour la validation du modèle.

Pour des concentrations volumiques différentes, le volume V_r est modifié en conséquence.

Modélisation de la réponse angulaire.

Pour la modélisation du procédé de mesure, les mêmes particules constituant la distribution sont réparties dans le volume référence à l'aide d'un programme basé sur la génération de nombres aléatoires.

Pour un angle θ défini, chaque particule de la distribution est positionnée dans l'espace V_r. Les coordonnées de la particule p_i sont alors x_i, y_i, z_i. L'équation de propagation de l'axe du faisceau laser après N réflexions sur les miroirs M_1 et M_2 est égale à:

$$y = (-1)^N \left[x \, tg\theta + (2N+1)\frac{h}{2} \right]$$

La projection, dans le plan du faisceau laser, de la particule p_i d'abscisse x_i, va se situer entre les réflexions:

$$N = Int\left(\frac{x \, tg\theta}{h}\right)$$

et N+1.

Si la distance entre la position (dans l'espace) de la particule et l'axe du faisceau est supérieure au rayon du faisceau, alors la particule est rejetée.

Dans le cas contraire, la particule est validée. Sa position est parfaitement connue et la puissance diffusée qui va parvenir sur l'ensemble de détection peut être calculée.

$$\beta = J_N \, \sigma(n,a,\lambda,\theta) \, \Omega$$

Cette puissance est fonction:
- de la densité de puissance incidente sur la particule (position dans le faisceau et pertes par réflexion sur les miroirs)
- de la taille de la particule.
- de l'angle solide du détecteur.

Simulation de l'acquisition.

A chaque instant, le volume réellement éclairé par le faisceau laser est une petite partie du volume V_r (1/1000 à 1/50 suivant l'angle de mesure).

La probabilité pour que le faisceau intercepte un nombre significatif de particules dans une position particulière du miroir tournant est faible.

Si le miroir m effectue un nombre de tours suffisant ($N_t = 100$ par exemple) et si les particules se déplacent aléatoirement dans le volume, le nombre de particules éclairées peut statistiquement devenir représentatif.

La simulation du processus d'acquisition est effectuée conformément à l'organigramme de la figure 5 et au descriptif suivant de la procédure SMD:

La procédure d'initialisation DMDD définit le modèle de distribution:
- Nombre de tours N_t de m concernés par l'acquisition.
- Angles de mesure ($\theta = \theta_{min}$, θ_{max}).
- Nombre N_p et taille des particules (a_i, $i = 1, N_p$)
- Concentration volumique (définition du volume).

A partir de ces définitions, le programme effectue une première boucle sur le nombre de tours de m ($k = 1, N_t$).

A chaque tour k, tous les valeurs de θ sont analysées séquentiellement.

Pour un angle θ :
- La procédure CCVR calcule le nombre de réflexions maximum entre M_1 et M_2 ainsi que le volume réellement éclairé et définit ainsi les coefficients correctifs relatifs au volume et aux pertes sur les miroirs.
- La procédure GPPA distribue aléatoirement les particules

dans le volume référence.
- La puissance détectée est initialisée ($P_{sc} = 0$)

Les particules sont observées une à une ($i = 1, N_p$).
- PP/L analyse les coordonnées de la particule p_i et détermine sa position par rapport au faisceau laser. Si elle est extérieure au faisceau, le programme incrémente sur la particule suivante.
- Si la particule se trouve dans le faisceau, elle est validée. La puissance β_i diffusée dans la direction θ est calculée en fonction de la densité de puissance incidente J_N, de la section efficace de diffusion σ et de l'angle solide du détecteur Ω. J_N va dépendre de la position de la particule et du nombre de réflexions que celui-ci a subi avant de la rencontrer.
- Cette puissance β_i est ensuite ajoutée à P_{sc}, somme des puissances discrètes diffusées par toutes les autres particules rencontrées par le faisceau dans cette même direction θ.

Quand toutes les particules ont été testées, P_{sc} représente la puissance détectée (au tour de miroir considéré et pour l'angle θ donné) provenant de la diffusion de toutes les particules contenues dans le volume éclairé à l'instant considéré.
- ACVR applique les coefficients rectificatifs.

Lorsque tous les angles ont été analysés, une indicatrice de diffusion du nuage est obtenue, qui n'est pas, en général, représentative de la distribution globale.

Le programme boucle et l'analyse recommence au tour de miroir suivant.

Les moyennes et écarts-types des niveaux angulaires de puissance détectée sont ensuite calculés.
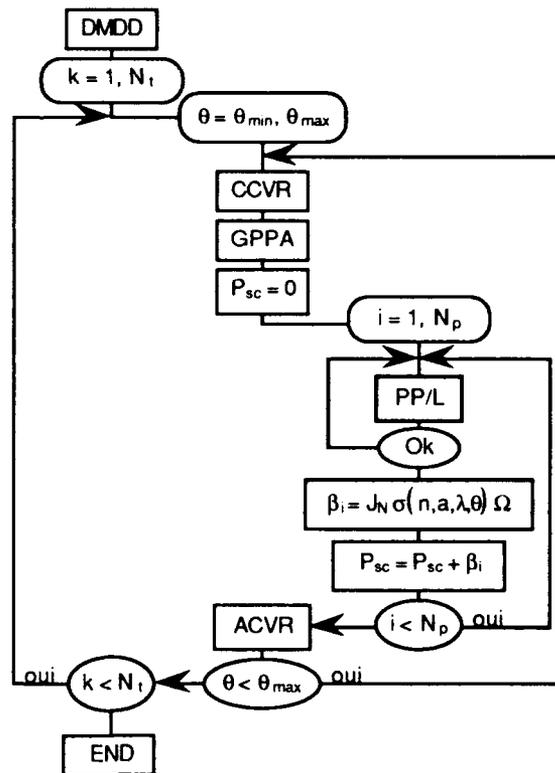
figure 5: Processus d'acquisition (SMD)

Validation du modèle.
Le modèle du procédé de mesure est validé en comparant pour une concentration élevée (1 ppm par exemple) les indicatrices de diffusion:

- d'une part, la réponse réelle de l'appareil quand les particules sont distribuées aléatoirement dans le volume référence (l'indicatrice est acquise à l'aide de la procédure SMD).
- et la réponse du nuage référence supposé entièrement éclairé par le faisceau laser. Le volume diffusant est alors V_r. Les valeurs acquises sont pondérées en leur appliquant des coefficients rectificatifs tenant compte, dans chaque direction, du volume réellement éclairé et de la perte moyenne de puissance par réflexions sur les miroirs M_1 et M_2.

Sur les figures suivantes, la réponse du nuage référence est représentée par le signe (•) et la réponse de l'appareil par le signe (!) représentant alors l'écart-type de l'ensemble des valeurs acquises sur 100 tours du miroir m.

La figure 6 illustre, pour une concentration volumique $C_v = 1$ ppm et un coefficient de réflexion des miroirs $R_m = 0,95$, la comparaison entre l'indicatrice de diffusion du nuage référence et l'ensemble des valeurs obtenues à l'aide de la simulation SMD.
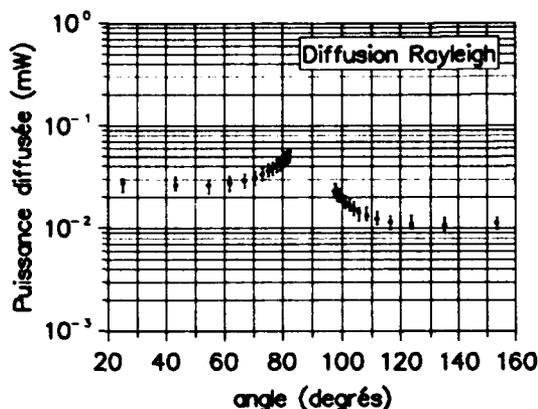
figure 6: Validation de la procédure de simulation
($C_v = 1$ ppm)

Les deux représentations sont parfaitement comparables, la procédure SMD est validée pour la concentration donnée.

Les données statistiques obtenues à l'aide de cette procédure peuvent être introduites dans le logiciel PSD pour obtenir la granulométrie du nuage. Les résultats présentés figure 6 et notre expérience de l'utilisation de ce logiciel permettent de conclure que la granulométrie est possible à l'aide d'un moyen basé sur le principe présenté.

Validation de la méthode.
La diffusion de lumière par un nuage de concentration volumique moyenne est correctement représentée par la procédure SMD.

Ce procédé est basé sur le principe d'un agrandissement artificiel du volume diffusant afin de pouvoir obtenir la granulométrie de nuages faiblement concentrés. Le bilan de liaison a montré que la détection des particules est possible si la concentration volumique des particules est au moins égale à 10^{-6} ppm. La simulation au moyen de SMD de telles concentrations doit permettre de spécifier la limite inférieure de validité du procédé.

Les figures 7 et 8 illustrent, pour des concentrations volumiques respectivement égales à 10^{-4} et 10^{-5} ppm, la même comparaison entre l'indicatrice de diffusion référence et les résultats de la procédure SMD que pour la simulation représentée figure 6 ($R_m = 0,95$).

Ces deux figures montrent que la simulation du procédé de mesure représente correctement le phénomène global d'un

nuage de volume important dont la concentration volumique est supérieure à 10^{-5} ppm.
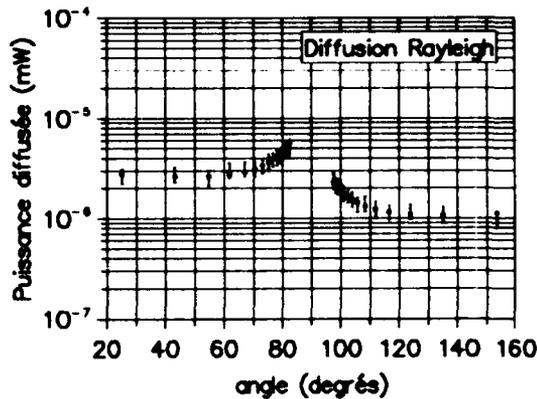
figure 7: Validation du procédé de mesure.
($C_v = 10^{-4}$ ppm)
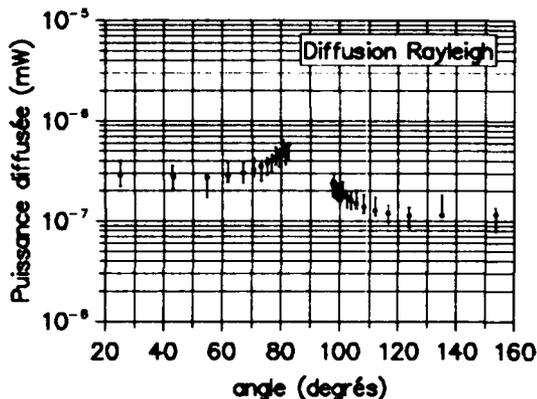
figure 8: Validation du procédé de mesure.
($C_v = 10^{-5}$ ppm)
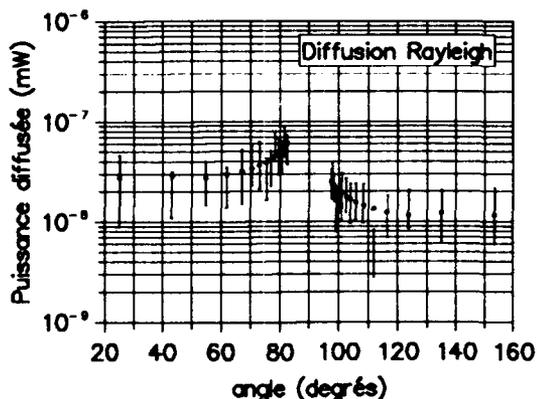
figure 9: Validation du procédé de mesure.
($C_v = 10^{-6}$ ppm)

Pour une concentration de 10^{-6} ppm l'illustration de la figure 9 montre que la maquette ne permet plus une représentation correcte. Le volume analysé est trop faible.

3.3 Résultats des simulations.

A partir du formalisme de diffusion de Rayleigh, la procédure de simulation SMD a été validée. Le procédé de mesure est correct si la concentration volumique du nuage est supérieure à 10^{-5} ppm.

Une maquette a été dimensionnée conformément aux caractéristiques présentées au chapitre 3.1 qui tiennent compte des impératifs de sa construction. Cette maquette doit permettre:
- d'acquérir un certain nombre d'indicatrices de diffusion pour des milieux de conditions urbaine, rurale ou maritime.
- de mesurer la visibilité.
- d'obtenir à partir des mesures la granulométrie du milieu.

Les modèles de distribution sont extraits de la littérature. Le formalisme de Lorenz-Mie est utilisé pour le calcul des sections efficaces de diffusion et d'extinction en s'appuyant sur des indices de réfraction communément admis [6].

La puissance diffusée par le nuage a été calculée en fonction des angles de diffusion compatibles avec le montage pour des modèles de distribution rural, urbain et maritime. Pour chaque modèle, deux concentrations volumiques ont été testées ($C_v = 10^{-4}$ et 10^{-5} ppm) et trois longueurs d'onde d'éclairement ($\lambda = 632,8$ nm; 1,06 et 10,6 µm).

Quelques résultats sont présentés sur les figures 10 à 13.

figure 12: Puissance diffusée.
(Modèle urbain, $C_v = 10^{-5}$ ppm, $\lambda = 632,8$ nm)
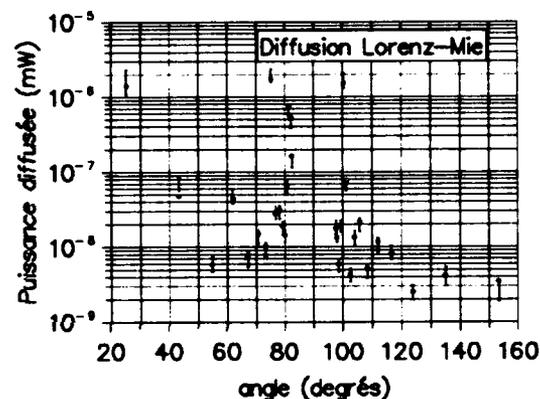
figure 13: Puissance diffusée.
(Modèle maritime, $C_v = 10^{-5}$ ppm, $\lambda = 632,8$ nm)

figure 10: Puissance diffusée.
(Modèle rural, $C_v = 10^{-4}$ ppm, $\lambda = 632,8$ nm)

Quelque soit le modèle de nuage, les niveaux de diffusion obtenus sont suffisants pour être détectés par le PM. La représentativité est très correcte et l'application du logiciel PSD à ces mesures donnera la granulométrie du milieu.


figure 11: Puissance diffusée.
(Modèle rural, $C_v = 10^{-5}$ ppm, $\lambda = 632,8$ nm)
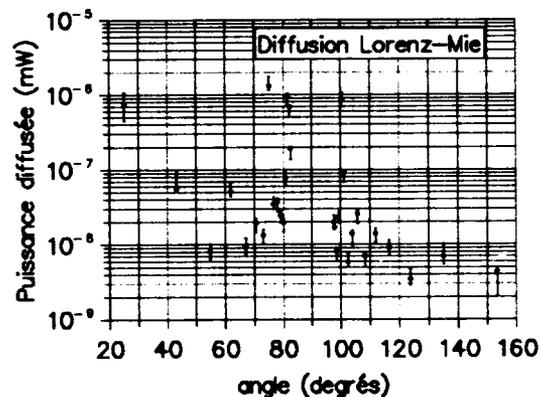
figure 14: Puissance diffusée.
(Modèle rural, $C_v = 10^{-5}$ ppm, $\lambda = 1,06$ µm)
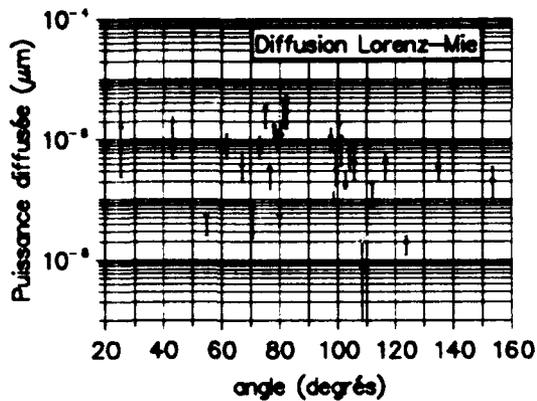
figure 15: Puissance diffusée.
(Modèle rural, $C_v = 10^{-5}$ ppm, $\lambda = 10,6$ μm)

Les figures 14 et 15 présentent des simulations de mesure sur modèle rural pour des longueurs d'onde d'éclairement de 1,06 et 10,6 μm. La représentativité de la diffusion est bonne dans le premier cas, mais il y a dégradation pour 10,6 μm.

La granulométrie semble correctement réalisable avec un tel système pour une longueur d'onde d'éclairement voisine de la taille moyenne des particules et des concentrations volumiques jusqu'à 10^{-5} ppm.

L'introduction dans le montage des détecteurs D_1, D_2... permet de mesurer le coefficient de transmission T du nuage, fonction directe de la section efficace volumique d'extinction β_{ext} :

$$T = \exp\left(-\beta_{ext}\, D_d\right)$$

où D_d est la longueur de la traversée de nuage correspondant.

L'obscuration du nuage est égale à 1-T.
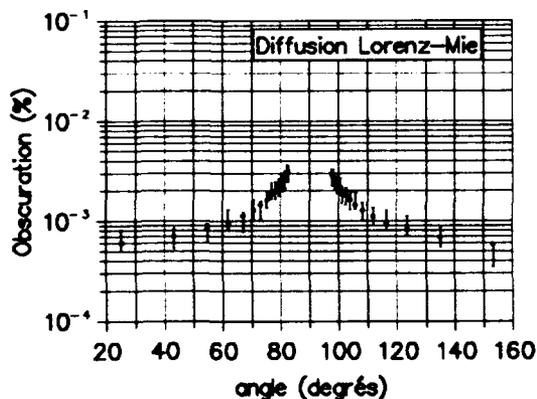
figure 16: Obscuration
(Modèle rural, $C_v = 10^{-5}$ ppm, $\lambda = 632,8$ nm)

La simulation d'une atmosphère rurale, de concentration $C_v = 10^{-5}$ ppm, montre (figure 16) que la mesure de l'obscuration par le procédé étudié n'est pas réalisable directement. L'atténuation de la puissance incidente n'est pas détectable.

Dans les conditions de la figure 17, la valeur théorique de la contribution des aérosols à la visibilité atmosphérique est

de 164 km.[7]:

$$V = \frac{3.912}{\beta_{ext}}$$

La référence d'atmosphère claire donnée par la littérature (23 km) permet de penser que la concentration volumique minimum rencontrée ne sera jamais inférieure à 10^{-4} ppm.
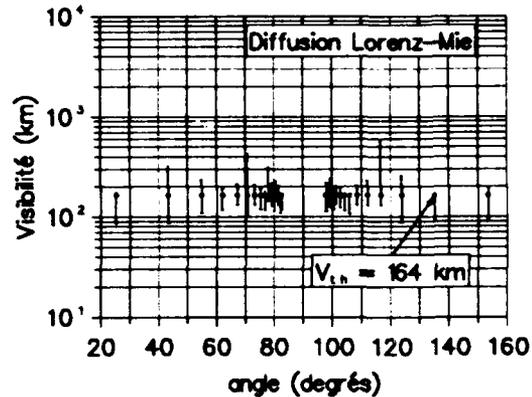

figure 17: Visibilité.
(Modèle rural, $C_v = 10^{-5}$ ppm, $\lambda = 632,8$ nm)

La visibilité ne peut pas être obtenue par la mesure d'atténuation. Cependant, un calibrage préliminaire de la réponse du module de détection, à partir d'une source étalon, permet la mesure absolue de $\beta(\theta)$. La fonction de distribution des particules f(a) est ensuite calculée à l'aide de PSD. β_{ext} et la visibilité sont alors obtenus.

4. DISPOSITIF EXPERIMENTAL

4.1 Chambre de tests.
La chambre de tests est conforme au schéma suivant:
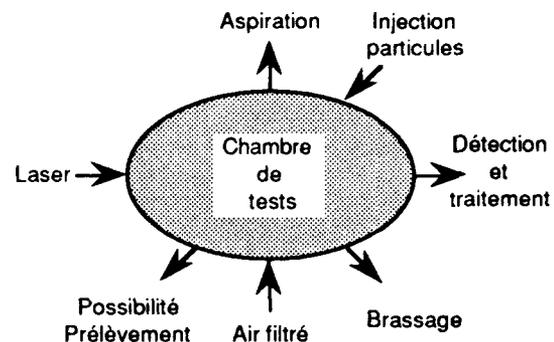
figure 18: Schéma du dispositif de qualification

Elle se présente sous la forme d'un parallélépipède de dimensions 600 mm × 400 mm × 400 mm. Les différentes pièces sont collées ou assemblées à l'aide de joints. L'intérieur est ainsi isolé de la poussière ambiante du laboratoire.

Afin d'évaluer la réponse de la maquette sans particules, un aspirateur permet d'extraire les poussières présentes. L'air propre est renouvelé à travers un filtre.

L'injection de particules test est effectuée par un petit orifice situé au niveau supérieur de la chambre. En fonction de la concentration volumique souhaitée, un volume
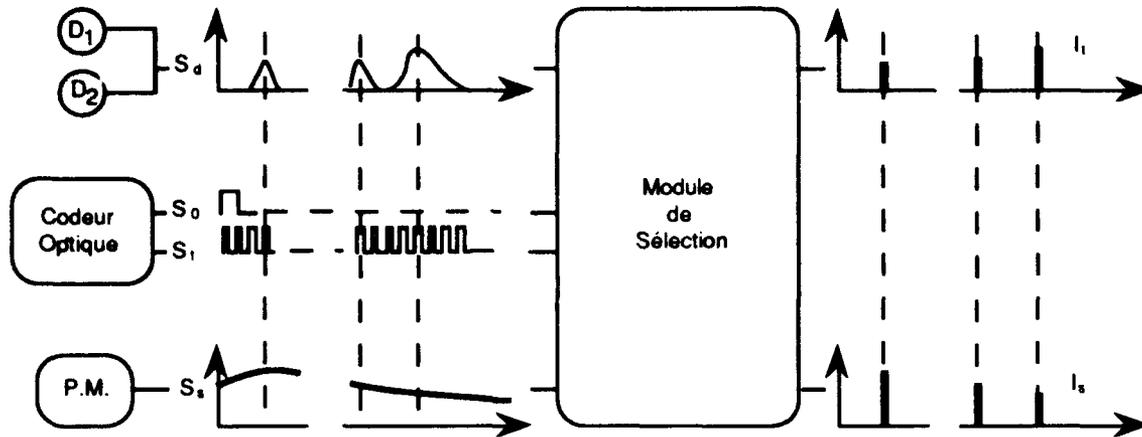
figure 19: Sélection des signaux utiles

convenable de particules est introduit dans la canalisation et injecté dans la chambre par un jet de gaz comprimé propre. (Par exemple une concentration volumique de 1 ppm sera obtenue avec 100 mm³ de poudre)

Un brassage de l'air ambiant de la chambre permet d'agiter les particules présentes et de les maintenir en suspension pendant un temps suffisant pour l'analyse.

Un laser HeNe est placé à l'extérieur de la chambre et le faisceau pénètre à l'intérieur par un hublot de bonne qualité optique.

4.2 Maquette de laboratoire.
La maquette d'évaluation a été élaborée conformément au dimensionnement défini au chapitre précédent.

Pour l'évaluation pratique du procédé, la partie de système permettant de mesurer la rétrodiffusion n'a pas été développée.

Comme il apparaît sur le schéma de la figure 19, quatre signaux utiles sont obtenus:

Le codeur optique délivre deux signaux permettant d'identifier avec précision l'angle d'incidence du faisceau laser sur les miroirs M_1 et M_2.
- S_0 est un signal TTL périodique délivré par le codeur optique, une fois par tour. Il permet d'identifier le passage à l'origine du miroir tournant m.
- S_t est aussi un signal TTL périodique, mais sa période est 1000 fois plus faible que la période de S_0. Il permet par comparaison avec S_0 de reconnaître la position instantanée du miroir m.

Les signaux issus des détecteurs D_1 et D_2 sont sommés. Le signal S_d résultant présente une série de pics correspondant chacun à un passage du faisceau laser devant l'un des détecteurs.

En sortie du photomultiplicateur, S_s est le signal continu de diffusion du nuage de particules éclairé par le faisceau laser en fonction du temps.

Le module de sélection permet d'éliminer tous les signaux inutiles issus du PM. (ou des détecteurs) afin de ne pas surcharger la mémoire de stockage du micro-calculateur.

La procédure de sélection est la suivante:
- Si le premier pic du signal S_d correspond à la ième impulsion de S_t après le top 0 de S_0, le numéro i est mis en mémoire dans le module de sélection. Si le deuxième pic de S_d correspond à la jième impulsion de S_t, le numéro j est mis en mémoire et ainsi de suite pour tous les angles sélectionnés.

- Quand le miroir tournant m renvoie le faisceau dans la direction incidente, l'angle de diffusion θ est égal à 90° (kième impulsion).

La connaissance de ces adresses permet d'associer à chaque impulsion sélectionnée la valeur correspondante de l'angle θ avec une précision de ±0,36°.

5. ESSAIS PRATIQUES DE FAISABILITE
Les simulations numériques ont montré la validité théorique des concepts. Le programme d'essais a été établi dans le but de confirmer pratiquement la faisabilité du procédé de mesure.

La première phase de ce programme a été la mise au point du processus (choix des particules tests, injection, temps d'établissement du nuage, acquisition...).

Pour cette mise au point, des poudres de licopodes (pollens) ont été sélectionnées. Malgré leur taille un peu élevée (25 à 35 μm), ces poudres sont parfaitement sphériques, légères, disponibles en très grande quantité et d'un coût très faible.

Dans un premier temps, les essais ont été réalisés en introduisant dans la chambre une quantité de poudre suffisante (environ 100 mm³) pour obtenir - si la répartition dans la chambre est uniforme - une concentration volumique de l'ordre de 1 ppm. Pour une telle concentration, environ 650000 particules sont distribuées dans la chambre. Le même nombre de particules de 1 μm de diamètre aurait donné une concentration volumique de 10^{-5} ppm

La réponse I_s du système, suivant chaque direction d'observation, a été analysée. Les conclusions suivantes peuvent être tirées:
- Le niveau de lumière parasite est très important et il semble inconcevable que le signal diffusé, dans le cas de concentrations volumiques plus faibles, puisse être extrait du bruit.
- L'injection de particules dans la chambre modifie le niveau de lumière parasite.

Le deuxième test effectué concerne l'observation de la stabilité du nuage dans la chambre.

Le signal diffusé a été enregistré sur 100 tours (2,5 s) et pour 8 angles de mesure. Le fichier a été divisé en cinq parties (0 à 0,5 s ; 0,5 a 1 s ; 1 à 1,5 s ; 1,5 à 2 s ; 2 à 2,5 s). Chaque partie a été traitée séparément (moyenne + écart-type) pour permettre la visualisation d'une évolution possible du nuage en fonction du temps.

Ces cinq parties sont juxtaposées pour chaque angle de mesure sur la figure 20.
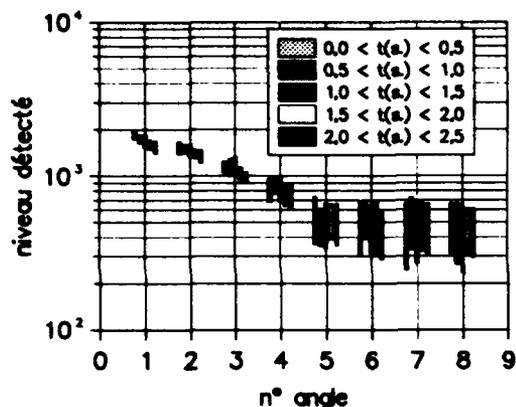
figure 20: Evolution en cours d'essai.
(Poudre de licopode, $C_v = 1$ ppm, $\lambda = 632,8$ nm)

Le nuage ne semble pas évoluer de manière significative au cours du temps.

Enfin, un processus de contrôle de la répétabilité des essais a été mis en place suivant les étapes suivantes :
- Dépoussiérage de la chambre par aspiration.
- Enregistrement du niveau de lumière parasite.
- Injection d'un volume contrôlé de particules.
- Attente 5 s.
- Enregistrement du niveau diffusé.

Un certain nombre d'essais ont été réalisés.

Les résultats concernant les essais 1 à 4 sont représentés sur la figure 21. Comme pour la représentation de la figure 20, les quatre essais sont juxtaposés pour chaque angle de mesure.
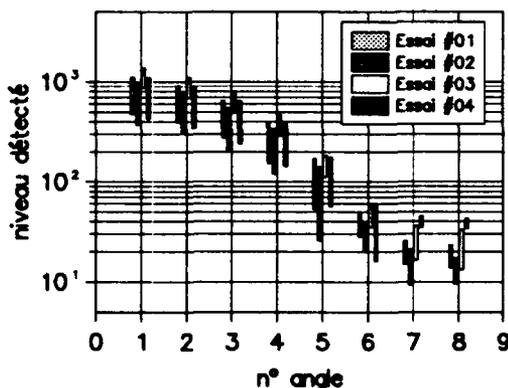
figure 21: Répétabilité des essais.
(Poudre de licopode, $C_v = 1$ ppm, $\lambda = 632,8$ nm)

La reproductibilité des essais 1, 2 et 4 est très bonne.

L'essai 3 présente une indicatrice de diffusion d'un niveau moyen supérieur d'environ 30 % à la moyenne des essais 1, 2 et 4. Sa forme est cependant comparable.

CONCLUSION
L'étude d'un appareil de granulométrie pour des nuages de particules en concentration très faible a été réalisée.

Le bilan de liaison a montré qu'il est possible de détecter des particules avec un rapport signal à bruit acceptable dans un domaine de concentration aussi faible que 10^{-6} ppm.

La maquette test, dont le principe est basé sur l'augmentation artificielle du volume à analyser par le jeu de réflexions multiples entre deux miroirs plans parallèles, a été modélisée. Le modèle a été validé par comparaison entre la réponse du système à une distribution aléatoire de particules dans le volume de mesure et la diffusion qui serait provoquée par la même distribution si toutes les particules étaient "vues" simultanément par le faisceau laser.

Les diverses simulations numériques ont montré que la granulométrie du nuage (urbain, rural ou maritime) était possible si la concentration volumique est au moins égale à 10^{-5} ppm. La limite supérieure se situe au-delà de 1 ppm.

La longueur d'onde d'éclairement doit être du même ordre de grandeur que le diamètre moyen des particules de la distribution.

La visibilité pourra être obtenue grâce à un étalonnage préliminaire du bloc de détection.

Les premiers essais de validation pratique ont souligné les imperfections du système, dues essentiellement au niveau élevé de lumière parasite.

Les résultats théoriques n'ont pas été confirmés à ce jour, malgré quelques points positifs : relative stabilité du nuage et répétabilité acceptable.

Le système de mesure ne paraît pas en cause, car les problèmes rencontrés semblent venir de la chambre de tests qui pourrait être améliorée.

La maquette de laboratoire paraît correctement dimensionnée, mais une étape complémentaire s'avère nécessaire avant d'envisager la conception d'un appareil de terrain.

REMERCIEMENTS

BIBLIOGRAPHIE
[1] H.C. Van de HULST, Light Scattering by Small Particles, John Wiley and Sons Inc., New York, 1957

[2] D. DEIRMENDJIAN, Electromagnetic Scattering on Spherical Polydispersions, American Elsevier Publishing Company Inc., New York, 1969.

[3] M. KERKER, The Scattering of Light and Other Electromagnétic Radiation, Academic Press Inc., New York, 1969.

[4] J.C. TRAINEAU, P. KUENTZMANN, M. PREVOST, P. TARRIN, A. DELFOUR, "Particle Size Distribution Measurements in a Subscale Motor for the Ariane 5 Solid Rocket Booster", AIAA/SAE/ASME/ASEE, 28th Joint Propulsion Conference and Exhibit, Nashville, TN(USA), July 1992.

[5] O. GRIMAL, "Etude d'un projet de diffusiomètre pour milieux très dilués", Rapport de projet CERT/ONERA, Toulouse, 1990.

[6] G.S. KENT, G.K. YUE, U.C. FARRUKH, A. DEEPAK, "Modeling Atmospheric Aerosol Backscatter at CO_2 Laser Wavelengths. 1: Aerosol Properties, Modeling Techniques, and Associated Problems.", Applied Optics, Vol. 22 n°11, p1655, June 1983.

[7] W. EPPERS, "Atmospheric Transmission", Handbook of Lasers with Selected Data on Optical Technology, R.J. Pressley Editor, CRC, USA, 1971.

RADAR CROSS SECTIONS OF GROUND CLUTTER
AT 95 GHz FOR SUMMER AND FALL CONDITIONS

R. J. Wellman, D. R. Hutchins, J. L. Silvious, H. Dropkin,
G. Goldman, J. Nemarich, D. A. Wikner, and R. K. Dahlstrom
US Army Research Laboratory
Adelphi, MD 20783-1197, USA

Summary
This paper describes radar cross section (RCS) measurements made on an extensively instrumented ground-clutter patch over a period of one month from late summer to early fall. The instrumentation allowed collection of a full set of data on meteorological conditions, solar flux, and soil moisture content. The RCS measurements were made using a 95-GHz, polarimetric, monopulse instrumentation radar. The radar is all-solid-state, coherent, frequency steppable over a 640-MHz bandwidth, and completely polarimetric for linearly or circularly polarized radiation. The clutter area measured was located in Grayling, Michigan, and consisted of a rectangular patch of ground, 50 by 100 m in area, at a range of about 100 to 250 m from the radar. The clutter patch included areas of bare sandy ground, short grass, low shrubs, evergreen trees, and deciduous trees and was similar to a NATO European environment. A wide range of atmospheric conditions were observed over the measurement period, including a few days of measurable snowfall. The paper describes analysis of the effects of different clutter types and different atmospheric conditions on the measured RCS of the clutter patch.

1. Introduction
Sensor systems operating at about 95 GHz are being investigated for use in smart munitions designed to defeat armored vehicles.[1] These systems require specific information on the clutter background that could be encountered in order to determine their target detection performance in a real clutter environment. The data presented in this paper were taken to assist in the validation of a millimeter wave clutter model for the Smart Weapons Operability Enhancement (SWOE) program managed by the US Army Cold Regions Research and Engineering Laboratory. The aim of the SWOE program is to produce validated models for simulating real-world environments for both the IR and MMW regions of the spectrum. The data described summarize 72 individual measurements of the entire clutter patch for circular polarization and 22 measurements for linear polarization. After a brief description of the

95-GHz polarimetric monopulse instrumentation radar used to acquire the data, the paper concentrates on the analysis of the variations in the measured RCS of the clutter patch versus environmental conditions.

Section 2 of this report describes the basic characteristics of the radar while Section 3 gives a brief discussion of the procedures used for calibration of the radar. Section 4 discusses the clutter measurement procedure and Section 5 presents samples of the measured data for selected clutter cells. Conclusions about the data and the measurement methods employed are given in Section 6.

2. Description of the Radar System
The radar used for these measurements has been discussed in detail previously.[2,3] Only a brief description of the radar as configured for this test will be presented. The radar was designed for obtaining 95-GHz target and background signature data, with the radar located on a tower and with computer-controlled operation from a remote ground station. Figure 1 shows the radar and the computer-controlled pedestal set up for this field test. A video camera that is boresighted with the radar records the radar scene through the glass window at the upper right corner of the metallic cover. The radar power supply and air conditioner for temperature control are also shown in the photograph. The radar is protected from rain or snow by the tent during operation and storage. Data recording and control of the radar are performed at a ground station located in an 11-m long semi-trailer. Data from the target platform and a meteorological station also may be recorded at that location.

The basic characteristics of the radar are summarized in Table 1. The radar is a completely polarimetric, two-coordinate, amplitude-comparison monopulse system. It is a fully coherent, dual polarization, pulsed radar that operates in a frequency-stepped mode between 95.00 and 95.64 GHz. For this application, the system was operated with 64 10-MHz steps and a transmit PRF of 10 kHz. The peak power of the all-solid-state transmitter is 45 W, the pulse width is 100 ns, and the

location of the end of the 15-m-long range gate was swept sequentially from 105 to 255 m. The polarization was switched from pulse to pulse and both linear and circular data were obtained. The primary emphasis was on the collection of circular polarization data, so there is three times as much data for circular than for linear polarization. The radar used a 15-cm-diameter lens antenna with a one-way beamwidth of 1.5 degrees.

The radar Data Acquisition System (DAS) has six I/Q detectors for the monopulse sum and difference signals. The relative phase of the two sum channels and their log amplitudes also are processed in the DAS. For each transmitted pulse the signals received in each of the 16 channels are sampled, multiplexed, and digitized by two 12-bit A/D's. The multiplexed data are transmitted from the radar via a fiber-optic data link to the remote computer control/recording system at a rate of 240 Kbytes/s. The latter is a PC that includes an 80486 33-MHz processor, 8-Mbytes of memory, and a 1-Gbyte disc drive. Data are magnetically recorded on 2-Gbyte 8mm cassette tapes.

The radar is mounted on a pedestal that can be computer controlled locally or from a remote station to scan the radar or to orient it to a fixed position. The pedestal is an elevation-over-azimuth type with 0.01-deg pointing accuracy and scanning rates between 0.1 and 10 deg/s. In addition, a co-boresighted video camera mounted on the radar head provides a video record of the clutter as the radar is scanned.

3. Radar Calibration Procedures
The radar calibration procedure is complicated due to the number and types of data channels. The entire procedure has been reported in detail previously,[2,3] and only a brief outline of the calibration procedure that is specific to these measurements will be discussed. Preliminary calibrations were performed in the laboratory before the radar was taken to the field measurement site at Grayling, Michigan, and a series of pre-measurement checks and calibrations were done at the field test site. The basic features of these checks and calibrations[4] include taking proper account of gain imbalances in I/Q detectors and nonlinear responses in detectors and amplifiers.

The radar calibrations at the field measurement site were performed using the reflectors listed in the calibration target array of Table 2. The range and the RCS of reflectors 3,4, and 5 were chosen so that the received signal levels from the reflectors were approximately equal and in the linear range of the receivers

(about 6 dB below A/D saturation). Reflectors 1 and 2 were used for determining a sign in the polarization distortion matrix (PDM) calibration described below, for circular and linear polarization, respectively.

The PDM calibration technique[5] was used to compensate for the effects of imperfect cross-polarization isolation in the radar. This calibration method is intended to remove the effects of the radar system parameters from the data so that the target polarization scattering matrix can be determined without degradation due to the system. It can be used for both linear and circular polarization by making measurements of the five reflectors listed in Table 2. For this report, the PDM calibration technique was carried out separately for both circular and linear polarization.

For PDM calibration purposes, depending on the polarization, four of the five reflectors were selected and 200 ramps of data were taken. A ramp of data consists of 64 pulses separated in frequency by 10 Mhz that are transmitted with one polarization and 64 pulses transmitted with the orthogonal polarization. The first step in processing the PDM data is to perform the I/Q corrections. We generated the I/Q corrections by characterizing each I/Q detector at four different amplitude levels at 22.5-deg phase intervals from 0 to 360 deg. This I/Q correction reduced the residual amplitude error due to I/Q imbalance to 40 dB below the signal level and the maximum required phase correction was 3 deg. The 200 ramps of data were averaged before calculating the PDM coefficients. To properly average the coherent channels in the PDM data, a constant phase for each frequency is required to calculate the correct average amplitude and phase. A motion-compensating algorithm was applied to the data before averaging to minimize any phase variations due to motion of the calibration reflectors during the acquisition of 200 ramps of data. The PDM correction parameters for each frequency and for each polarization were then calculated from the averaged data. This calibration procedure was carried out before and after all data runs, and the average of these calibrations was used for calibrating the data.

The cross-polarization isolation of the radar was between 25 and 30 dB across the frequency band, and the improvement in the cross-polarization isolation using the PDM calibration technique is between 5 and 10 dB, depending on the frequency. The improvement due to the PDM calibration technique is limited by the sidelobe clutter and any returns from the poles on which the reflectors are mounted. The resulting

cross-polarization isolation of the system was improved to about 35 dB, which is more than adequate for measuring clutter, since the cross-polarization ratio for most clutter was found to be less than 10 dB.

Antenna radiation patterns were obtained at the test site using the various reflectors. The approximate two-way sum channel beamwidth for the 15-cm lens used for the clutter measurements reported here was 1.2 deg and the two-way sidelobe levels were less than 40 dB. The radar monopulse boresight angle was determined for each polarization channel using the appropriate reflector. The boresights for the different polarizations combinations were found to vary slightly, with most of the variations being in the azimuth. The overall boresight angle difference for the RR and RL channels, for example, was about 0.1 deg with most of the difference being in azimuth. The optical boresight on the video camera was set to coincide with the center of the individual boresights.

4. Clutter Measurement Procedure
The clutter measurements were made at Camp Grayling in Grayling, Michigan, during September and October 1992. The measurement area was instrumented for the SWOE program by other laboratories with a full array of meteorological equipment to characterize the environment during the measurement periods. Standard meteorological data were obtained as well as measurements of solar radiance, soil moisture, soil temperature, and cloud conditions. In addition, snow depth and snow density were also measured when appropriate. The measurement area was 50-m wide by 100-m long and located at the bottom of a small valley as shown in figure 2. The radar was positioned on top of a hill overlooking the valley so that the measurement area could be scanned effectively.

The radar raster scan pattern covered an azimuth angle of 36 deg in 1.2-deg increments and an depression angle of -5 to -1 deg in 1.0-deg increments, and a range interval of 150 m in 15-m increments. For each azimuth, elevation, and range gate, 32 ramps of data were recorded. As discussed previously, each ramp consists of 128 transmitted pulses. At each angular position, the radar range gate was swept through the range interval, and then the azimuth angle was incremented. When all azimuth angles had been measured at one elevation angle, the elevation position was incremented. This process continued until the entire scan pattern had been measured.

The MMW measurements were made over 25 two-hour time periods randomly selected

from the time periods of 19 to 23 Sept. and 17 to 23 Oct. During the two hours, three complete scans (or data runs) were made with circular polarization and one data run with linear polarization. Each run produced a raw data file of 125 Mbytes. The raw data file included the six coherent I/Q monopulse data channels, the two logarithmic sum channels and the relative polarimetric phase I/Q channel. The final calibrated data set includes that for 72 circular and 22 linear polarization runs. Since the exact same clutter cells were measured over and over again for different environmental conditions and times, the data provide a good basis for validation of a SWOE MMW clutter model.

5. Data Discussion
In order to evaluate the effects of different environmental conditions on the clutter RCS, a small subset of approximately 1200 clutter cells was selected for analysis. These clutter cells were selected so that each one contained only one type of clutter. The types of clutter in the selected cells were grass and bushes, dirt and grass, evergreen trees, and deciduous trees. The measured RCS, in square meters, at each frequency was averaged over all ramps of data for all the clutter cells to compute the cell average for each run. The overall average in dBsm and the standard deviation of the individual averages in dB over all data runs for the selected cells were then computed. Tables 3 and 4 give the composite RCS statistics and standard deviation in dBsm for both circular and linear polarization, respectively. Table 3 shows that the RCS's for LR and RL are about equal and that the RCS's for RR and LL are about equal. Also, the LR RCS is about 4 dB larger than the RR RCS for all the cells except the deciduous tree cell where this ratio is almost 7 dB. For linear polarization, the RCS's for VV and HH are about equal and the RCS's for HV and VH are almost identical. In addition, the VV RCS is about 8 dB larger than the HV RCS for the grass cells, 7 dB larger for the evergreen tree cells, and 9.5 dB larger for the deciduous tree cells.

The standard deviation values in the tables indicate that the RCS for the deciduous tree cells had the largest variation over the measurement period. However, this variation is due almost entirely to a 6-dB decrease in the average RCS of these deciduous tree cells from the beginning of the test to the end. The grass cells actually had the largest variation in RCS due to changing weather conditions, while the evergreen tree cells had the smallest dependency on weather. This behavior is seen in figure 3, in which the average RCS for each data run for each clutter type is plotted versus run number. The run

numbers are sequential in time from the beginning to the end of the measurements.

The weather conditions present during the data runs are given in table 5. Upon comparison of figure 3 with table 5, it is apparent that the major variations of the grass cells are primarily due to the presence of water, frost, or snow on the ground. In fact, the largest variation in the RCS for these cells is due to the refrozen snow condition observed for run number 53. The RCS's for the evergreen trees was somewhat less sensitive to these conditions, but these effects are still evident. The RCS's for the deciduous trees seemed to be less sensitive to the weather, but the RCS's decreased as the leaves changed color and lost moisture. The results for linear polarization are similar and will not be discussed here.

The data were used to determine how well the polarimetric RCS's of individual clutter cells correlated with each other for the same clutter type. Linear correlations were calculated within and between clutter types using the average RCS values for the individual data runs for the polarization combinations of RR, LR, VV, and HV. The results of these calculations are shown in table 6. As shown in the table, the correlation between the different grass cells is very high for all polarizations, whereas the correlation between the different evergreen tree cells is lower. The correlation between different deciduous trees is very similar to that for the evergreen trees, with the exception of between cells 705 and 716, which give a very high correlation. These latter two cells are adjacent and encompass the same large tree, so this is not unexpected. This was the only tree of sufficient size to fill more than one complete cell. Upon examination of the last three lines in the table, it is obvious that there is very little correlation between cells of different clutter types.

The data also were used to generate histograms of a sample of the RCS data for each type of clutter cell for RR and RL polarization. Figures 4 and 5 show these histograms of the RCS's compiled for over 1800 individual measurements for particular cells. The data plotted are RCS values for the various frequencies over the 640 MHz bandwidth taken from a data file at the beginning of the test. This file was chosen to give a representative comparison of distributions for the different clutter types. The histograms plot the number of measurements occurring in a 1-dB bin, versus the measured RCS per unit area (sigma zero) of the bin for the indicated type of clutter cell. It is apparent that each type of clutter cell has about the same distribution

function for both polarizations with a slight difference in the mean value of the distribution, and that all the cells have a very similar distribution. The distribution function that best fits the data is currently being investigated and an expanded set of clutter cells is also being evaluated. Since the grass cells seem to exhibit the most variation due to changing weather conditions, comparison histograms were generated for a dirt and grass cell for different weather conditions. These are shown in figures 6 and 7 for RR and RL polarizations, respectively. The figures show the distributions at the beginning of the measurements and at the end, and for frost, and the refrozen snow condition observed during the test. The histograms for this particular cell were essentially the same for the beginning and the end of the test, while the frost condition modified the distributions only slightly. However, for the refrozen snow condition the distributions for both polarizations became more irregular with large peaks compared to the beginning distributions. The distribution for both polarizations was almost the same for this case as well. Analyses of the histograms for the other cell types indicated that the distributions did not change significantly during the test. These results suggest that a single type of distribution function should be able to describe the clutter for all conditions with the exception of refrozen snow. Further analysis is needed to determine the appropriate functions for describing the statistics of individual clutter cells and for determining a distribution function that best describes the entire clutter area.

6. Conclusions

We have described in detail the 95-Ghz clutter measurements taken on an extensively instrumented clutter patch. The clutter measurements were made during the summer-to-fall weather transition period for Grayling, Michigan. The area measured was similar to a European environment and consisted of short grass, bushes, evergreen trees, and deciduous trees. During the measurement period, the same exact clutter area was measured 72 times in circular polarization and 22 times in linear polarization.

The average RCS for the entire time period for some selected clutter cells has been presented. The cross-polarized return RCS's for both circular and linear polarization for the clutter are virtually the same while the co-polarized returns for both circular and linear polarization are very similar. The results for the cross-polarized radar returns are therefore in excellent agreement with scattering theory, and those for the co-polarized returns are similar to measurements made previously for hard targets. [2,3]

The measured RCS has been shown to vary greatly for grass cells during the measurement period due to changing conditions such as frost and snow, while the RCS change for evergreen tree cells due to these changing conditions was not as significant. It was also shown that the deciduous tree cells are more sensitive to the change in leaf condition than to the change in the weather. An attempt to correlate the change in the measured RCS's to other environmental conditions such as soil moisture, relative humidity, and temperature that were measured during the test was not successful.

An analysis of the correlation between the RCS's for various clutter cells indicates that those for grass cells are very well correlated, while those for evergreen trees and those for deciduous trees are not as well correlated. It was shown that different clutter types generally did not correlate well with each other. It was also shown that the histograms for each clutter type were very similar. These histograms were only slightly sensitive to changes in weather conditions, which primarily shifted the mean values of the distribution.

In conclusion, the polarimetric RCS values measured for this terrain and during this time period will provide an extensive data base for model evaluation and for analysis of MMW system performance.

References
1. N. C. Currie and C. E. Brown (Editors), "Principles and Applications of Millimeter-Wave Radar," Artech House, Norwood, MA, 1987.
2. R. J. Wellman, J. Nemarich, H. Dropkin, D. R. Hutchins, J. L. Silvious, and D. A. Wikner, "Polarimetric Monopulse Radar Scattering Measurements of Targets at 95 GHz," AGARD Conference Proceeding 501 Ottawa, Canada, May 1991.
3. R. J. Wellman, J. Nemarich, H. Dropkin, D. R. Hutchins, J. L. Silvious, and D. A. Wikner," Comparison of MMW Radar Signatures of Soviet-Built Military Vehicles," Proceedings, Precision Munitions Signatures and Simulators Conference, Eglin AFB, Florida, May 1992.
4. N. C. Currie (Editor), "Radar Reflectivity Measurement: Techniques and Applications," Artech House, Norwood, MA, 1989.
5. R. M. Barnes, MIT Lincoln Laboratory, "Polarimetric Calibration Using In-Scene Reflectors," 1986, MIT Lincoln Laboratory Project Report TT-65 on Contract F19628-85-C-0002.

Figure 1. Photograph showing radar set up at Grayling, Michigan.

Figure 2. Photograph of instrumented clutter area.
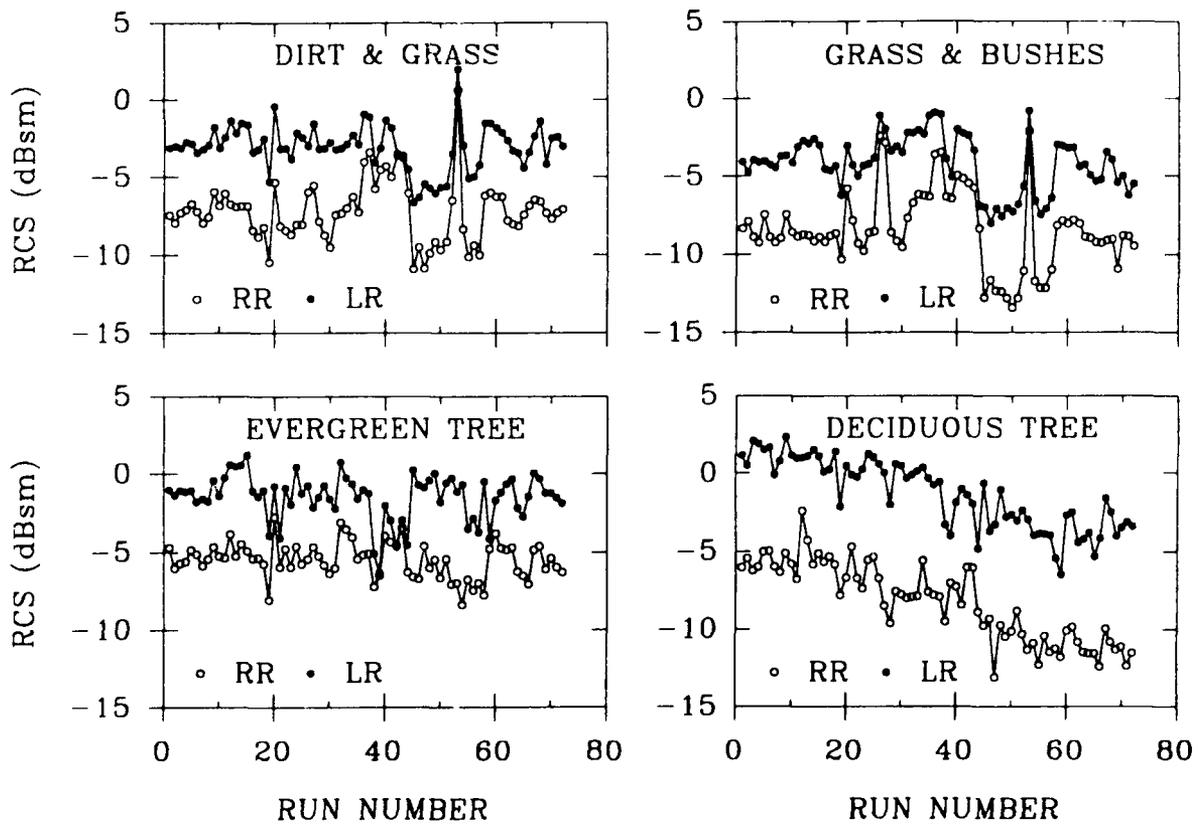
Figure 3. Measured circular polarization average RCS versus run number for a
selected set of sample cells.
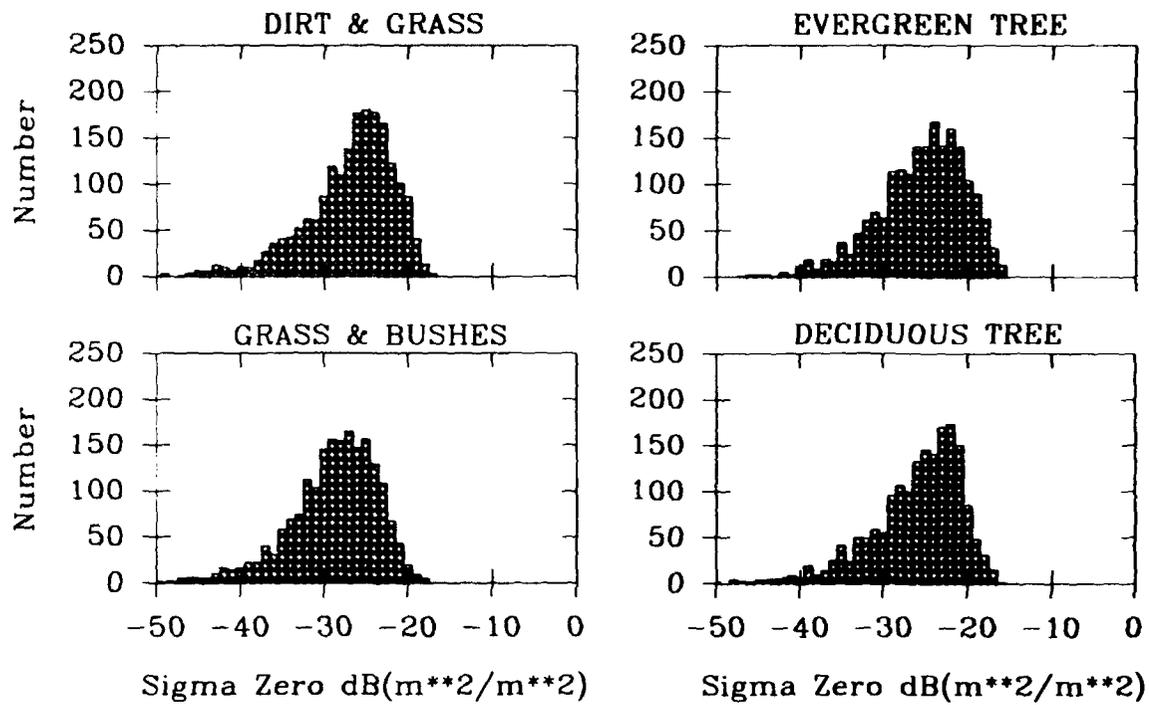
Figure 4. Histogram of RR polarization RCS per unit area (sigma 0) for four clutter cell types.
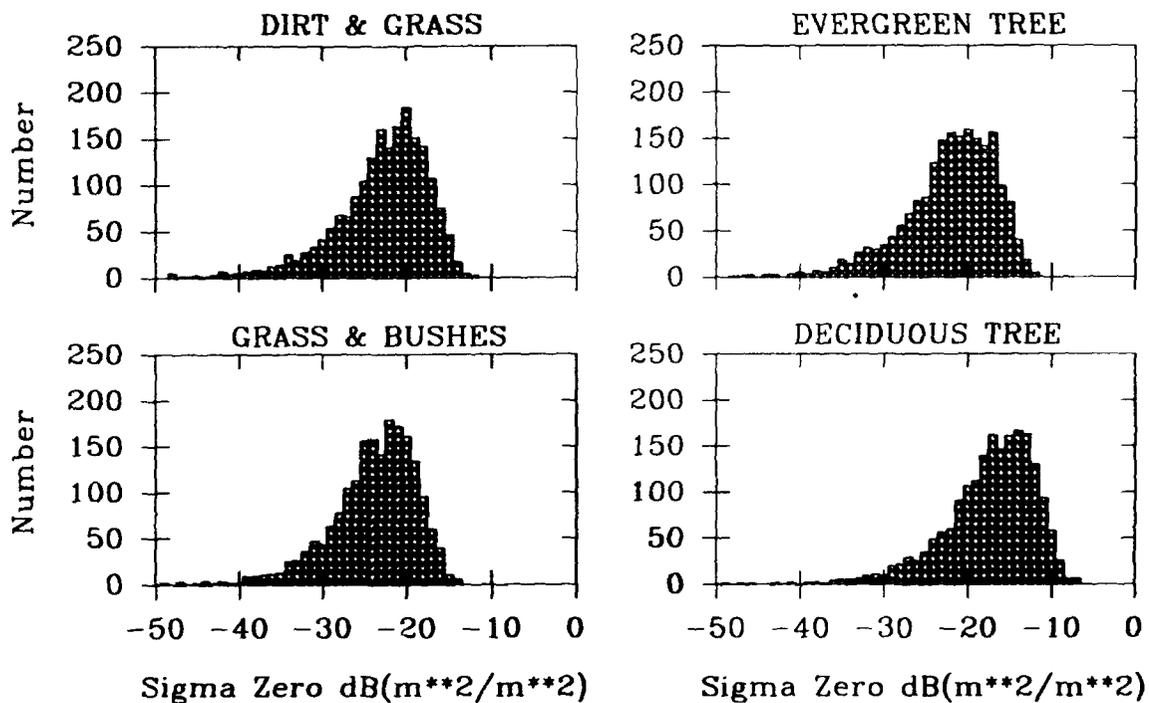
Figure 5. Histogram of RL polarization RCS per unit area (sigma 0) for four clutter cell types.
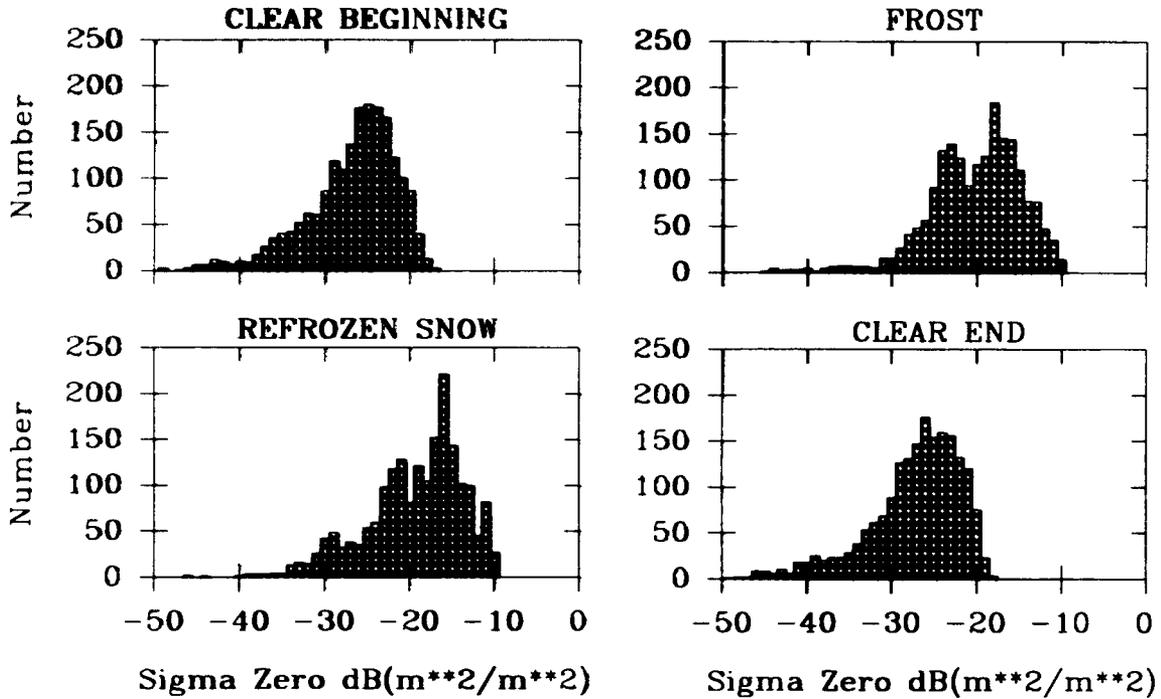
**Figure 6.** Histogram of RR polarization RCS per unit area (sigma 0) for dirt & grass cell for different environmental conditions.
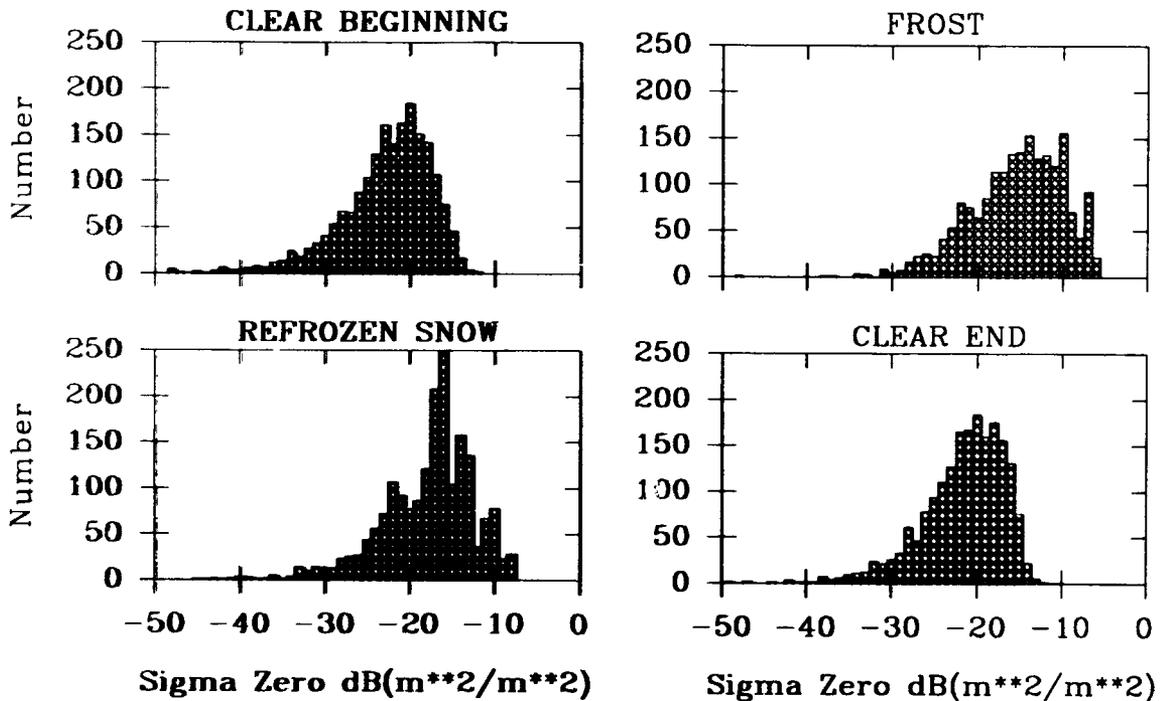
Figure 7. Histogram of RL polarization RCS per unit area (sigma 0) for dirt & grass cell for different environmental conditions.

Table 1.   Basic features of the radar system.

- Frequency: 95.0 GHz
- Two-coordinate amplitude-comparison monopulse
- Polarization agile: RHCP/LHCP or V/H (selectable)
- Coherent and wide bandwidth
- Frequency steppable: 64 10-MHz steps
- Peak power: 45 W
- Pulse width: 100 ns
- Pulse repetition frequency: 10 kHz
- Antenna beamwidth (one way): 1.5 degrees
- Receiver IF bandwidth: 30 MHz
- Receiver noise figure: 8 dB
- Dynamic range (amplitude): $\geq$66 dB
- Data recording: 16 channels for each pulse

Table 2:   Calibration Reflector Array

Reflector No.	Reflector Type	RCS(dBsm)	Range(m)
1	Gridded Trihedral	14	160
2	Dihedral 22.5°	18	189
3	Trihedral	23	218
4	Dihedral 0°	26	248
5	Dihedral 45°	26	280

Table 3:   Mean RCS (dBsm) and Standard Deviations for Selected Cells
for Circular Polarization

RCS (dBsm)

Cell Type	Cell#	RR	LL	LR	RL
Dirt and Grass	288	-7.3±1.7	-7.0±1.6	-3.0±1.3	-2.9±1.3
Dirt and Grass	299	-7.2±1.9	-7.1±1.9	-3.1±1.4	-3.0±1.5
Grass and Bushes	520	-8.5±2.4	-8.6±2.5	-4.2±1.8	-4.3±1.8
Grass and Bushes	542	-9.0±2.2	-9.4±2.3	-5.3±1.6	-5.4±1.6
Evergreen Tree	552	-5.5±1.1	-5.1±1.1	-1.5±1.4	-1.6±1.2
Evergreen Tree	574	-4.8±1.2	-5.0±1.4	-1.4±1.3	-1.5±1.2
Deciduous Tree	705	-8.2±2.5	-7.9±2.3	-1.3±2.2	-1.8±2.3
Deciduous Tree	716	-9.4±2.8	-9.7±3.0	-2.5±2.8	-3.0±3.0

Table 4:   Mean RCS (dBsm) and Standard Deviations for Selected Cells
for Linear Polarization

RCS (dBsm)

Cell Type	Cell#	VV	HH	HV	VH
Dirt and Grass	288	-2.2±1.3	-1.7±1.4	-10.2±1.9	-10.1±2.0
Dirt and Grass	299	-2.2±1.6	-1.9±1.7	-10.2±2.2	-10.2±2.2
Grass and Bushes	520	-3.0±1.9	-3.3±1.8	-11.4±2.5	-11.5±2.6
Grass and Bushes	542	-3.8±1.7	-4.6±1.8	-12.3±2.7	-12.4±2.6
Evergreen Tree	552	-1.0±0.9	-0.1±0.9	-8.1±0.9	-8.3±0.9
Evergreen Tree	574	-0.4±1.4	-0.3±1.0	-7.5±1.0	-7.6±0.9
Deciduous Tree	705	-1.1±2.2	-0.6±2.4	-10.6±2.3	-10.7±2.4
Deciduous Tree	716	-2.3±3.1	-2.2±3.5	-11.9±3.0	-12.3±3.0

Table 5:   Weather Conditions Observed During SWOE Test

Run Number	Weather Conditions
1-6	Clear, Dry, Temp 5-13° C
7-10	Clear, Dew for Runs 7 and 8, Temp 9-16° C
11-15	Cloudy, Wet, Temp 13° C, RH 98%
16-19	Wet, Temp 9° C. Rain Before Runs 18 and 19
20-23	Frost for 20, Temp -4° C, Clear
24-25	Clear and Dry, Temp 11 ° C
26-27	Dry Snow, -1° C, Cloudy
28-30	Cloudy, 2° C, Melting Snow
31-33	Cloudy, -4 to -5° C, Refreezing
34-44	Dry Snow, Cloudy -4 to -2.5° C
45-52	Wet Snow on Ground, Light Rain, Temp -.2 to 4° C
53	Refrozen Snow, Temp 0° C, Cloudy
54-57	Melting Snow, Temp 2-3° C, Cloudy
58-60	Temp -4° C, Clear
61-66	Temp 12° C, Cloudy
67-72	Dry, Partly Cloudy, 10-20° C

Table 6:   Calculated Correlation Coefficients Between Cells of Same Type
             for the Same Polarization

Cell Type	Cell#	RR	LR	VV	HV
Dirt and Grass	288/299	0.88	0.82	0.87	0.90
Grass and Bushes	520/531	0.96	0.92	0.95	0.95
Grass and Bushes	520/542	0.96	0.91	0.92	0.94
Evergreen Tree	552/574	0.45	0.67	0.64	0.24
Evergreen Tree	574/583	0.56	0.42	0.48	0.36
Evergreen Tree	683/696	0.45	0.64	0.12	0.48
Deciduous Tree	582/593	0.53	0.59	0.48	0.78
Deciduous Tree	593/705	0.51	0.46	0.41	0.61
Deciduous Tree	705/716	0.93	0.94	0.92	0.95
Grass/Evergreen	288/574	0.38	0.26	0.44	0.49
Evergreen/Deciduous	574/716	0.09	0.20	0.42	0.35
Deciduous/Grass	716/288	0.09	0.02	-0.01	0.07

Discussion

Discussor's name :   P. Baars, US

Comment/Question :

You showed high cell to cell correlation. Can you please comment on your correlation method.

Author/Presenter's reply :

The data were first averaged across the bandwidth and the number of observations for each clutter cell. This corresponds to an average of 64 frequencies and 32 observations for each cell. This produced 72 values for each polarization combination for the circular data runs for each cell. Linear correlations were made between cells and between polarization combinations versus run number. In other words, for circular polarization, 72 pairs of data values were used to calculate the linear correlation between the values.

Discussor's name :   F. Ulaby, US

Comment/Question :

One tabular data you showed indicate a standard deviation-to-mean ratio of unity, which implies that your individual measurements represent single independent samples. Do you agree?

Author/Presenter's reply :

The table you are referring to showed averages of 64 frequencies separated in time by 0.2ms, then averaged over 32 sets with a total time period of 0.4 seconds. We have not examined the frequency to frequency or ramp to ramp correlations, but a preliminary look at the data indicated some correlation. I do not believe that the data represent independent samples. We will be doing a more in depth analysis of the data in the future, and we will determine whether this is true or not.

Knowledge Combination and Data Fusion with application to Recognition Systems

Christiaan Perneel,* Michel de Mathelin,† and Marc Acheroy*

* Electrical Engineering Department, Royal Military Academy, 30 Renaissance avenue, 1040 Brussels, Belgium.

† Electrical & Computer Engineering Department, Carnegie Mellon University, Pittsburgh, PA 15213-3890.

1 Summary

In this paper, the fuzzy logic theory is used to derive knowledge combination rules for heuristic search algorithms and data fusion problems. Heuristic search algorithms are especially designed for expert systems which have to explore a large solution space in a limited amount of time. Therefore, search algorithms using heuristic knowledge are designed to limit the exploration of the solution space while preserving some quality in the results. An automatic target recognition expert system was designed using this approach. However, the fuzzy logic approach could be applied to other type of expert systems and to data fusion problems.

2 Introduction

Expert systems are usually designed to solve complex problems with numerous candidate solutions. Generally, the brute force approach consisting in exploring all the possible solutions to the problem is unpractical. Further, *uninformed* search methods like depth-first or breadth-first (cf. Nilsson [1], chapter 2) which are exhaustive methods for finding a solution are also often infeasible. Typically, the knowledge of an expert is required in order to guide the search toward the solution in a more efficient manner. This knowledge take the form of heuristics and a search procedure using information of this sort is called heuristic search. At any given time in the search process all the possible paths are evaluated with the help of the heuristics and the most promising path according to the heuristics is selected. The heuristics are designed based on the knowledge and the experience of the expert. The main difficulty in this approach resides in finding an appropriate way to combine the knowledge coming from the heuristics into a unique evaluation function. Furthermore, as the search of the solution progresses, new paths must be compared with paths abondonned earlier. However, new paths are usually much more advanced in the building of a solution than old paths and it might become very difficult to find a common ground for comparison. There has been a lot of research in this area. To mention a few interesting contributions, *e.g.*, Shafer [2] which

introduced the concept of belief functions, Bellman & Zadeh [3] and Zadeh [4] which introduced the fuzzy logics approach, and the paper by Kosko [5] about fuzzy knowledge combination. Note also the survey made by Prade [6] in this field. These approaches are criticized by Lindley [7] from a probabilisic view point. However, a defense of the fuzzy logic approach is made in the book by Kosko [8].

The aim of this paper is to study a fuzzy logics approach to the design of an evaluation function for heuristic searchs. In other words, fuzzy logics are used to combine knowledge used in decision algorithms for expert systems. The method developped in this paper could be used also to solve data fusion problems where information coming from different sources must be combined together.

The paper is divided in five sections. The first section presents the general assumptions made about the expert systems considered in this paper. The second section defines the search method used by the expert system. The fuzzy logics approach is presented in the third section. An automatic target recognition expert system is presented as example in the fourth section. In the last section, the fuzzy logic approach is tested on the target recognition expert system and the results are presented.

3 General assumptions

The following assumptions are made about the expert systems considered in this paper

- A solution to the problems solved by the expert system is made of N different levels of increasing knowledge. Level 1 is the initial level of knowledge of the solution in the search process. When the expert system reaches the next level in the search process, some more information about a candidate solution is generated. A candidate solution consists in values for N predefined characteristics or sets of characteristics (one per level). A candidate partial solution up to level i consists in values for i predefined characteristics or sets of characteristics. Level N is the last level of knowledge in the search process where a possible solution to the problem can be proposed.

- At each level i, at most n_i new possible partial solutions or, equivalently, new branches in the search tree are proposed. The n_i new candidate partial solutions consist in a candidate partial solution up to level $(i-1)$ combined with some incremental knowledge under the form of a possible value for one or more predefined characteristics of the solution. Consequently, the size of the candidate solution space $S \leq \prod_{i=1}^{N} n_i$.

- At each level i, m_i different heuristics give a rating to the n_i new candidate partial solutions of level i. These ratings must be combined to give a global rating to the partial solutions. The rating functions of the heuristics return a rating for each partial solution based on some measurement or observation made on the data of the problem.

4 Search algorithm

The expert system must be able to search through a solution space which can be too large to be fully explored. As the expert often do in front of a very complex problem, the problem is decomposed in simpler problems which are tackled one at a time. Then, the expert system starts searching in one direction making measurements, observations, and computations along the way. When the partial results obtained along the way are satisfaying (according to some heuristic rules), the exploration is continued in that direction. When suddently, the observations stop to be satisfaying according to some heuristics, the expert goes back where the partial solution is still the most satisfying and explores a new direction. This is called heuristic search. For an expert system to accomplish a heuristic search, it is necessary to evaluate all the possible paths at a given instant then choose the best according to some predefined criterion. Therefore, a global rating function will be defined to evaluate all the candidate partial solutions and candidate solutions.

Let R be the rating returned by this global rating function in the previous step of the search and let k be the level of the previous step, then

- If $a_k < R < b_k$, choose the highest rated candidate partial solution or path available.

- If $R \leq a_k$, change path but take the highest rated path available different from the current path.

- If $R \geq b_k$, stay on the current path.

Obviously, if $a_k = R_{\min}$ and $b_k = R_{\max}$, then a heuristic search strategy is implemented. The expert system chooses always the highest rated path even if it has to change path very often. If $a_k = b_k = R_{\min}$,

$k \neq N$, then a depth-first search strategy is implemented. If $a_k = b_k = R_{\max}$ then a complete exploration of the solution space is implemented. Therefore, by playing with the parameters $\{a_k\}$, $\{b_k\}$, the behavior of the expert system may vary greatly. How these parameters must be selected will depend on the usual trade-off speed of the search vs quality of the solution. If the quality of the solution is most important without any speed constraints then an exhaustive exploration of the solution space is called for. However, if speed is most important, then no backtracking between levels will be allowed.

5 Fuzzy reasoning

The heuristics rate the candidate solutions based on some measurements or observations. Very often, the range of the measured variable is more important than its exact value. The measurement can be often classified in simple categories describing how well it fits the hypothesis that the candidate is the solution to the problem. For example, **Good**, **Average**, and **Bad** could be the categories or linguistic terms describing how the observation fits the hypothesis. Furthermore, the transitions between these categories (*i.e.*, **Good** and **Average** or **Average** and **Bad**) are often blurred. Therefore, there must be also a smooth transition in the rating of the different candidate solutions. Logically, fuzzy logics seem to be a promising approach for handling this type of uncertainty and fuzziness.

5.1 Modelization

The following assumptions are made for modelling uncertainty and fuzziness (based on the terminology used in, *e.g.*, Bellman & Zadeh [3], Mamdani [9], King & Mamdani [10], or Mamdani *et al* [11])

- The values which define uniquely a solution (cf. section 3) belong to nonfuzzy support sets of universes of discourse like, for example, the k-th characteristic or set of characteristics of the solution . Let X_k be the set of possible values for the characteristics of the solution receiving a value at level k. Then, the X_k's are the nonfuzzy support sets, having a finite number, S_k where $S_k \leq \prod_{i=1}^{k} n_i$, of elements, of the universes of discourse "k-th characteristic or set of characteristics of the solution". Based on these definitions, the characteristics defining a candidate partial solution up to level k will be represented by the nonfuzzy support set

$$Y_k = (\ X_1, \ \ldots, \ X_k \ )$$

Therefore, a partial solution up to level i will be an element of Y_i and a complete solution will be an element of Y_N.

- Suppose that the n_i values $\{x_{ik}(y_{i-1})\}$, $k = 1, \ldots, n_i$, are all the elements depending on y_{i-1} which belongs to the nonfuzzy support set X_i, where y_{i-1} is an element selected in the previous levels nonfuzzy support set, Y_{i-1}. Suppose that there exist M different categories or linguistic terms (e.g., **Good, Average** and **Bad**, $M = 3$), for describing to what degree x_{ik} fits the characteristics of the solution represented by X_i. These linguistic terms define fuzzy subsets of the universes of discourse "i-th characteristic or set of characteristics of the solution". Then, for each level i, there exists M membership functions (one per linguistic term)

$$f_i^l(x_{ik}, y_{i-1}) \quad : \quad X_i \times Y_{i-1} \to [0,1] \; k = 1, \ldots, n_i$$
$$x_{ik} = x_{ik}(y_{i-1})$$

which define fuzzy subsets associated to the linguistic terms, l, describing to what degree the values $\{x_{ik}(y_{i-1})\}$ belongs or fits *a priori* the i-th characteristic or set of characteristics of the solution represented by X_i. Let's define the vector f_i as the combination of these M membership functions, $\{f_i^l\}$, in one vector. For example, if the linguistic terms are (**Good, Average, Bad**), the fuzzy subset $[x_1, x_2, x_3] = f_i(x_{ik})$ expresses that x_{ik} belongs *a priori* to the **Good** fit category with a factor x_1, to the **Average** fit category with a factor x_2, and to the **Bad** fit category with a factor x_3, for the characteristics of the solution represented by X_i.

Without loss of generality, it can be assumed that the membership functions, f_i^l, are normalized, so that

$$\text{Normality rule:} \qquad \max_x f_i^l(x) = 1$$

Furthermore, to minimize the number of linguistic terms and avoid redundant categories, it is assumed that the M linguistic terms describe different (but possibly overlapping) degrees of fit. Consequently, if the degree of fit of one category is 1, then the degree of fit of the others must be 0. This translates into the following rule

$$\text{Economy rule:} \qquad \sum_l f_i^l(x_{ik}) \leq 1 \qquad \forall \, i, k$$

Furthermore, if it is assumed that the linguistic terms span all the possible degrees of fit, then the following rule applies

$$\text{Completeness rule:} \qquad \sum_l f_i^l(x_{ik}) \geq 1 \quad \forall \, i, k$$

Consequently, if the three rules apply

$$\sum_l f_i^l(x_{ik}) = 1 \qquad \forall \, i, k$$

Finally, by default if the *a priori* degree of fit is unknown, a constant membership function will be assumed, i.e.,

$$f_i^{\text{Good}}(x_{ik}, y_{i-1}) = 1$$
$$f_i^{\text{Average}}(x_{ik}, y_{i-1}) = 0$$
$$f_i^{\text{Bad}}(x_{ik}, y_{i-1}) = 0$$

$$f_i(x_{ik}, y_{i-1}) = [\; 1, \quad 0, \quad 0, \;]$$

- There are m_i different rating functions at level i (one per heuristic). Let $h_{ij}^l(p_{ij})$ be the j-th membership function of level i associated to the linguistic term l, where p_{ij} is an observation depending on the characteristics described by Y_i. Let $h_{ij}(p_{ij})$ be the vector of M membership functions $h_{ij}^l(p_{ij})$. Given a candidate partial solution up to level i, $y_i \in Y_i$, an observation $p_{ij}(y_i)$ is made and the j-th heuristic returns a fuzzy subset, $h_{ij}(p_{ij})$, describing how the observation $p_{ij}(y_i)$ fits the hypothesis that y_i is the solution up to level i.

Without loss of generality, it can be assumed that the membership functions, h_{ij}^l, are normalized, so that

$$\max_p h_{ij}^l(p) = 1$$

Furthermore, it is assumed that the Economy rule applies

$$\sum_l h_{ij}^l(p) \leq 1 \qquad \forall \, i, j \text{ and } \forall \, p$$

Given a measurement p and assuming that $M = 3$, with linguistic terms (**Good, Average, Bad**), a typical heuristic membership function, $h(p)$, with an overlapping factor of 50%, may look like in Figure 1, where The observation p belongs to the **Good**
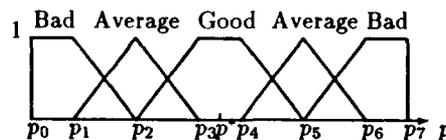

Figure 1: Heuristic fuzzy membership function, $h(p)$

fit category with a factor 1 around a reference value,

p^*, then slowly starts to belong to the **Average** category and finally to the **Bad** category outside this area. Finally, note that the overlapping factor between the different categories should be proportional to the fuzziness of the boundaries between categories. In his book, Kosko [8] recommends an overlapping factor of 25%. We use ourselves an overlapping factor of 50% in our application.

5.2 Rating function

A global rating function must be defined to follow an opportunistic search strategy. This global rating function should logically reinforce candidate partial solutions whose heuristics give mostly a **Good** rating and should disadvantage candidate partial solutions whose heuristics give mostly a **Bad** rating.

5.2.1 Heuristics rating functions

Each heuristics return a fuzzy vector of size M, the number of different linguistic terms. This fuzzy vector is made of the membership values for each of the M different linguistic terms. Now, these M different values must be combined in one unique value which is the rating given by the heuristic. This operation of transforming the fuzzy vector $h(p)$ in a unique non-fuzzy rating value is called defuzzification. This is usually done by assigning to each linguistic term, l, a rating membership function, $g^l(r)$, where r is the nonfuzzy rating value, obeying to the following rules

- $g^l \colon \Re \to [0,1]$.

- $\forall\, r$, the rating must increase when the linguistic term expresses an improvement and must decrease when the linguistic term expresses a worsening. For example,

$$g^{\text{Good}}(r) \geq g^{\text{Average}}(r) \geq g^{\text{Bad}}(r) \quad \forall\, r$$

- Assuming that the rating values must belong to the interval $[K_{\min}, K_{\max}]$ then $g^l(K_{\min}) = 1$ if l is the "worst degree of fit" linguistic term and $g^l(K_{\max}) = 1$ if l is the "best degree of fit" linguistic term.

For example, suppose that $M = 3$ and the linguistics terms are (**Good**, **Average**, **Bad**) and assume that the minimum rating is $R_{\min}$ and the maximum rating $R_{\max}$, then typical rating membership functions g^l are like in Fig. 2. Once the rating membership function have been defined, given an observation, p, given a heuristic with heuristic membership functions, $h^l(p)$, where l spans all the possible linguistic
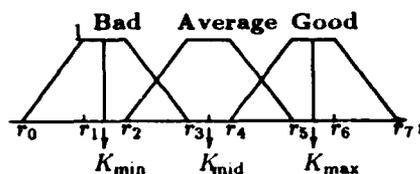
Figure 2: Rating membership functions

terms, we can define the cumulated rating membership function, $g_c(r)$, as

$$g_c(r) = \sum_l g^l(r) h^l(p) \qquad \text{product inference}$$

$$g_c(r) = \sum_l \min(g^l(r), h^l(p)) \quad \text{minimum inference}$$

For example, suppose that the the linguistics terms are (**Good**, **Average**, **Bad**), that $h(p)$ is defined as in Fig. 1, that the observation p is such that $h(p) = [4/5, 1/5, 0]$, and that the rating membership functions are defined as in Fig. 2, then if the minimum inference is used, $g_c(r)$ will look like in Fig. 3. Now, the simplest defuzzification scheme is the
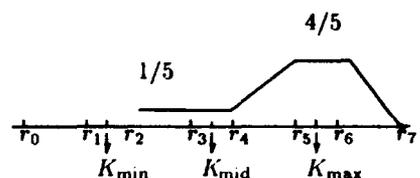

Figure 3: Cumulated rating membership functions

maximum-membership defuzzification scheme defined as

$$R = \arg\max_r g_c(r) = \begin{cases} \arg\max_r (\sum_l g^l(r) h^l(p)) \\[4pt] \text{product inference} \\[8pt] \arg\max_r (\sum_l \min(g^l(r), h^l(p))) \\[4pt] \text{minimum inference} \end{cases}$$

However, this scheme has two important imperfections. First, R is not always unique (see for example, Fig. 3). Second, most of the information in the shape of the rating membership functions, g^l, is lost. A better alternative is the well known *fuzzy centroid*

defuzzification scheme defined as

$$R = \frac{\int_{-\infty}^{+\infty} r g_c(r)\, dr}{\int_{-\infty}^{+\infty} g_c(r)\, dr} = \begin{cases} \dfrac{\sum_i h^i(p) \int_{-\infty}^{+\infty} r g^i(r)\, dr}{\sum_i h^i(p) \int_{-\infty}^{+\infty} g^i(r)\, dr} \\ \quad \text{product inference} \\[2ex] \dfrac{\sum_i \int_{-\infty}^{+\infty} r \min(g^i(r), h^i(p))\, dr}{\sum_i \int_{-\infty}^{+\infty} \min(g^i(r), h^i(p))\, dr} \\ \quad \text{minimum inference} \end{cases}$$

For the example in Fig. 3, the fuzzy centroid defuzzifier returns

$$R = \frac{K_{\text{mid}} \int_{-\infty}^{+\infty} \min(g^{\text{Average}}(r), 0.2)\, dr + K_{\text{max}} \int_{-\infty}^{+\infty} \min(g^{\text{Good}}(r), 0.8)\, dr}{\int_{-\infty}^{+\infty} \min(g^{\text{Average}}(r), 0.2)\, dr + \int_{-\infty}^{+\infty} \min(g^{\text{Good}}(r), 0.8)\, dr}$$

5.2.2 Level rating function

Now, the individual heuristic ratings must be combined for each levels. Suppose that y_i is a candidate solution up to level i, the level rating function is the combination of the m_i heuristic rating functions h_{ij} and of the *a priori* rating function f_i where all these rating functions represents fuzzy subsets. A classical approach in fuzzy logics (see, *e.g.*, Bellman & Zadeh [3], Zadeh [4], and Mamdani [9]) consists in taking the minimum of the different membership functions, *i.e.*, if the fuzzy centroid defuzzification scheme is adopted

$$\tilde{R}_i(y_i) = \begin{cases} \dfrac{\sum_i \min(\min_j(h^i_{ij}(p_{ij}(y_i))), f^i_i(y_i)) \int_{-\infty}^{+\infty} r g^i(r)\, dr}{\sum_i \min(\min_j(h^i_{ij}(p_{ij}(y_i))), f^i_i(y_i)) \int_{-\infty}^{+\infty} g^i(r)\, dr} \\ \quad \text{product inference} \\[2ex] \dfrac{\sum_i \int_{-\infty}^{+\infty} r \min(\min_j(h^i_{ij}(p_{ij}(y_i))), f^i_i(y_i), g^i(r))\, dr}{\sum_i \int_{-\infty}^{+\infty} \min(\min_j(h^i_{ij}(p_{ij}(y_i))), f^i_i(y_i), g^i(r))\, dr} \\ \quad \text{minimum inference} \end{cases}$$

$i = 1, \ldots, N$. Unfortunately, as it was pointed out by Kosko in [5], this type of combination rule is often too pessimistic, since the rating is always based on the heuristic giving the worst rating, even when all the other heuristics give a good rating. Much better, in our opinion, is the weighted sum approach where a weight, w_{ij}, is given to each heuristics according to its realibility and where a weighted sum of all the

different membership functions is done

$$\tilde{R}_i(y_i) = \begin{cases} \dfrac{\sum_i (w_i f^i_i(y_i) + \sum_{j=1}^{m_i} w_{ij} h^i_{ij}(p_{ij}(y_i))) \int_{-\infty}^{+\infty} r g^i(r)\, dr}{\sum_i (w_i f^i_i(y_i) + \sum_{j=1}^{m_i} w_{ij} h^i_{ij}(p_{ij}(y_i))) \int_{-\infty}^{+\infty} g^i(r)\, dr} \\ \quad \text{product inference} \\[2ex] \dfrac{\sum_i \int_{-\infty}^{+\infty} r(w_i \min(f^i_i(y_i), g^i(r)) + \sum_{j=1}^{m_i} w_{ij} \min(h^i_{ij}(p_{ij}(y_i)), g^i(r)))\, dr}{\sum_i \int_{-\infty}^{+\infty} (w_i \min(f^i_i(y_i), g^i(r)) + \sum_{j=1}^{m_i} w_{ij} \min(h^i_{ij}(p_{ij}(y_i)), g^i(r)))\, dr} \\ \quad \text{minimum inference} \end{cases}$$

$i = 1, \ldots, N$. This rating function does not take into account the rating obtained at the previous levels ($< i$). Only the heuristics of the current level are combined in this manner. We propose different methods to take into account the ratings from the previous levels: either a weighted sum of the different level ratings, or a global centroid of all the different levels, or even the minimum of the different level ratings. Assuming that the minimum inference is used

1. Weighted sum level combination

$$R_i(y_i) = \sum_{k=1}^i \tilde{R}_k(y_k) =$$

$$\frac{K_k \sum_i \int_{-\infty}^{+\infty} r(w_k \min(f^i_k(y_k), g^i(r)) + \sum_{j=1}^{m_k} w_{kj} \min(h^i_{kj}(p_{kj}(y_k)), g^i(r)))\, dr}{\sum_{k=1}^i (\sum_{k=1}^i K_k) \sum_i \int_{-\infty}^{+\infty} (w_k \min(f^i_k(y_k), g^i(r)) + \sum_{j=1}^{m_k} w_{kj} \min(h^i_{kj}(p_{kj}(y_k)), g^i(r)))\, dr}$$

2. Centroid level combination

$$R_i(y_i) =$$

$$\frac{\sum_i \sum_{k=1}^i \int_{-\infty}^{+\infty} r(w_k \min(f^i_k(y_k), g^i(r)) + \sum_{j=1}^{m_k} w_{kj} \min(h^i_{kj}(p_{kj}(y_k)), g^i(r)))\, dr}{\sum_i \sum_{k=1}^i \int_{-\infty}^{+\infty} (w_k \min(f^i_k(y_k), g^i(r)) + \sum_{j=1}^{m_k} w_{kj} \min(h^i_{kj}(p_{kj}(y_k)), g^i(r)))\, dr}$$

3. Minimum level combination

$$R_i(y_i) = \min_{1 \le k \le i} (\tilde{R}_k(y_k)) =$$

$$\min_{1 \le k \le i} \left(\frac{\sum_i \int_{-\infty}^{+\infty} r(w_k \min(f^i_k(y_k), g^i(r)) + \sum_{j=1}^{m_k} w_{kj} \min(h^i_{kj}(p_{kj}(y_k)), g^i(r)))\, dr}{\sum_i \int_{-\infty}^{+\infty} (w_k \min(f^i_k(y_k), g^i(r)) + \sum_{j=1}^{m_k} w_{kj} \min(h^i_{kj}(p_{kj}(y_k)), g^i(r)))\, dr} \right)$$

Which method should be selected depends on the application. For example, if it is critical to find the exact solution at each level and if the level have the same importance, the minimum combination is the most suitable method. However, if the different levels have different importance and if the different level characteristics X_i, $i = 1, \ldots, N$, are poorly related, it is much better to use the weighted sum method. Finally, if the

different level characteristics X_i, $i = 1, \ldots, N$ are very interdependent, then the centroid combination method is better. Finally, these level rating functions are unable to compare candidate partial solutions at different levels. To do so, a global rating function must be defined.

5.2.3 Global rating function

To compare two candidate partial solutions at different levels, the rating of the candidate at the lowest level should be extrapolated up to the highest level. In other words, an estimate of the rating that a candidate could possibly obtained at a higher level must be found. Therefore, to compare candidate solutions at every possible levels the rating of every candidates should be estimated up to the highest possible level, N. Assume that y_i is a candidate solution up to level i, then an estimate of

$$h_{kj}(p, (y_k)) \quad \text{and} \quad f_k(y_k) \quad k = i+1, \ldots, N$$
$$y_k = \begin{bmatrix} y_i^T & (\text{unknown subvector})^T \end{bmatrix}^T$$

must be found. Let's define $E\{h_{kj}\}(y_i)$ and $E\{f_k\}(y_i)$, $k = i+1, \ldots, N$ as these estimates. Then, they could be computed different ways depending on the type of behavior which is desired for the expert system.

(a) **Best case approach:** For each of the heuristics and *a priori* ratings to be estimated, the maximum value is always assumed. For example, if the linguistic terms are (**Good, Average, Bad**)

$$E\{h_{kj}\}(y_i) = \begin{bmatrix} 1, & 0, & 0, \end{bmatrix}$$
$$E\{f_k\}(y_i) = \begin{bmatrix} 1, & 0, & 0, \end{bmatrix}$$

This is a cautious approach. Indeed, the candidate partial solutions at the lower levels might be advantaged with respect to the candidates at the higer levels.

(b) **Arbitrary value approach:** If a less cautious approach is desired, expected values should be used. Estimates are selected arbitrarily and then later tuned for the application. For example, if the linguistic terms are (**Good, Average, Bad**)

$$E\{h_{kj}\}(y_i) = \begin{bmatrix} \bar{h}_{kj}^{Good}, & \bar{h}_{kj}^{Average}, & 0, \end{bmatrix}$$
$$E\{f_k\}(y_i) = \begin{bmatrix} \bar{f}_k^{Good}, & \bar{f}_k^{Average}, & 0, \end{bmatrix}$$

(c) **Expected value approach:** Ofcourse, if the probability distributions of the observations p_{kj}, $k = i+1, \ldots, N$, are known for a partial solution equal to y_i, then the expected values could be directly computed. So, let $d_{kj}(p)_{|y_i}$, $k = i+1, \ldots, N$, be the corresponding density of probability functions, then

$$E\{h_{kj}\}(y_i) =$$
$$\left[\int_{-\infty}^{+\infty} h_{kj}^{Good}(p) d_{kj}(p)_{|y_i} dp, \right.$$
$$\int_{-\infty}^{+\infty} h_{kj}^{Average}(p) d_{kj}(p)_{|y_i} dp,$$
$$\left. \int_{-\infty}^{+\infty} h_{kj}^{Bad}(p) d_{kj}(p)_{|y_i} dp \right]$$

This is basically equivalent to the computation of the probability of the fuzzy event: "observation p_{kj} is **Good**", as defined in Bellman & Zadeh [3].

Based on these estimates, the global rating function is defined the following way. Suppose that y_i is a candidate solution up to level i, and minimum inferences are used

Weighted sum level combination

$$R(y_i) =$$
$$\sum_{k=1}^{i} \frac{K_k}{\sum_{k=1}^{N} K_k} \frac{\sum_l \int_{-\infty}^{+\infty} r(w_k \min(f_k^l(y_k), g^l(r)) + \sum_{j=1}^{m_k} w_{kj} \min(h_{kj}^l(p_{kj}(y_k)), g^l(r))) dr}{\sum_l \int_{-\infty}^{+\infty} (w_k \min(f_k^l(y_k), g^l(r)) + \sum_{j=1}^{m_k} w_{kj} \min(h_{kj}^l(p_{kj}(y_k)), g^l(r))) dr}$$
$$\sum_{k=i+1}^{N} \frac{K_k}{\sum_{k=1}^{N} K_k} \frac{\sum_l \int_{-\infty}^{+\infty} r(w_k \min(E\{f_k^l\}(y_i), g^l(r)) + \sum_{j=1}^{m_k} w_{kj} \min(E\{h_{kj}^l\}(y_i), g^l(r))) dr}{\sum_l \int_{-\infty}^{+\infty} (w_k \min(E\{f_k^l\}(y_i), g^l(r)) + \sum_{j=1}^{m_k} w_{kj} \min(E\{h_{kj}^l\}(y_i), g^l(r))) dr}$$

Centroid level combination

$$R(y_i) =$$
$$\frac{\sum_l [\sum_{k=1}^{i} \int_{-\infty}^{+\infty} \frac{r(w_k \min(f_k^l(y_k), g^l(r)) +}{\sum_{j=1}^{m_k} w_{kj} \min(h_{kj}^l(p_{kj}(y_k)), g^l(r)))} dr + \sum_{k=i+1}^{N} \int_{-\infty}^{+\infty} \frac{r(w_k \min(E\{f_k^l\}(y_i), g^l(r)) +}{\sum_{j=1}^{m_k} w_{kj} \min(E\{h_{kj}^l\}(y_i), g^l(r)))} dr]}{\sum_l [\sum_{k=1}^{i} \int_{-\infty}^{+\infty} \frac{(w_k \min(f_k^l(y_k), g^l(r)) +}{\sum_{j=1}^{m_k} w_{kj} \min(h_{kj}^l(p_{kj}(y_k)), g^l(r)))} dr + \sum_{k=i+1}^{N} \int_{-\infty}^{+\infty} \frac{(w_k \min(E\{f_k^l\}(y_i), g^l(r)) +}{\sum_{j=1}^{m_k} w_{kj} \min(E\{h_{kj}^l\}(y_i), g^l(r)))} dr]}$$

Minimum level combination

$R(y_i) =$

$$\min\{\min_{1 \le k \le i}(\frac{\sum_i \int_{-\infty}^{+\infty} r(w_k \min(f_k^i(y_k), g^i(r)) + \sum_{j=1}^{m_k} w_{kj} \min(h_{kj}^i(p_{kj}(y_k)), g^i(r)))d\tau}{\sum_i \int_{-\infty}^{+\infty}(w_k \min(f_k^i(y_k), g^i(r)) + \sum_{j=1}^{m_k} w_{kj} \min(h_{kj}^i(p_{kj}(y_k)), g^i(r)))d\tau}),$$

$$\min_{i+1 \le k \le N}(\frac{\sum_i \int_{-\infty}^{+\infty} r(w_k \min(E\{f_k^i\}(y_i), g^i(r)) + \sum_{j=1}^{m_k} w_{kj} \min(E\{h_{kj}^i\}(y_i), g^i(r)))d\tau}{\sum_i \int_{-\infty}^{+\infty}(w_k \min(E\{f_k^i\}(y_i), g^i(r)) + \sum_{j=1}^{m_k} w_{kj} \min(E\{h_{kj}^i\}(y_i), g^i(r)))d\tau})]$$

6 The automatic target recognition system IRES

The problem to solve consists in identifying armored vehicles based on short distance 2-D forward-looking infrared (FL'R) images. The major difficulty in identifying vehicles from short distance FLIR images, lies in the lack of knowledge of the position and orientation of the vehicle with respect to the camera. Indeed, it is completely unpractical to realize a close matching of the image of the vehicle with a template given all the possible positions and orientations of the vehicle, and also given all the possible vehicles. Therefore, the problem is divided in two subproblems where the first subproblem is the computation of the orientation and position of the vehicle based on a crude model of the vehicle and the second subproblem is the identification of the vehicle in a reference position and orientation.

We designed IRES, a blackboard type expert system (cf. Nii [12, 13] or Hayes-Roth [14] for a definition and Murdock & Hayes-Roth [15] for an example of application), to accomplish these two tasks. The first task, position and orientation detection, consists in putting a system of three axes, $\{X, Y, Z\}$, on the image of the vehicle according to predefined conventions. In our application, the conventions are the following:

- X **axis**: the line on the side of the vehicle between the train of wheels and the ground.

- Y **axis**: the line on the front or on the rear of the vehicle between, respectively, the front or the rear wheels on each side of the vehicle and the ground.

- origin: the origin of the system of axes is, by convention, at the extremity of the X axis on the engine side if the image gives a side view of the vehicle, on the left of the Y axis if the image gives a front or rear view of the vehicle but the engine is on the front of the image, or on the right of the Y axis if the image gives a front or rear view of the vehicle but the engine is on the rear of the image.

- Z axis: the vertical direction of the vehicle, normalized on the wheel train height if the image gives a side view of the vehicle or on the distance between the floor of the vehicle body and the ground if the image gives a front or rear view of the vehicle.

An illustration of these conventions can be found in Fig. 4. The position and orientation detection
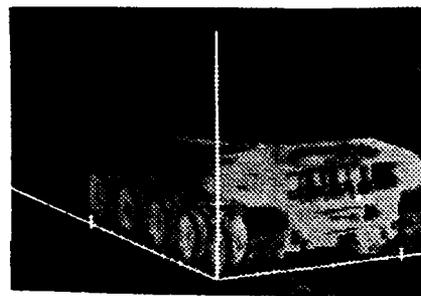
Figure 4: Axes conventions

is then divided into 5 subtasks to be executed by the expert system. These 5 subtasks correspond to 5 different levels of increasing knowledge of the position and orientation of the vehicle.

- **Level 1**: Determination of one principal direction, either the direction of the X axis if the image gives a side view, or the direction of the Y axis if the image gives a front or rear view. At this point, the view point is not yet determined.

- **Level 2**: Determination of the view point and of the line of the X axis if it is a side view or the line of the Y axis if it is a front or rear view.

- **Level 3**: Determination of the position of the origin.

AD-A276 919

ATMOSPHERIC PROPAGATION EFFECTS THROUGH NATURAL AND MAN-MADE OBSCURANTS F..(U) ADVISORY GROUP FOR AEROSPACE RESEARCH AND DEVELOPMENT NEUILLY.. NOV 93 AGARD-CP-542

UNCLASSIFIED   X5-XD   F/G 17/4   NL

END
FILMED

DTIC

AIIM

Association for Information and Image Management

1100 Wayne Avenue, Suite 1100
Silver Spring, Maryland 20910

301/587-8202

Centimeter

1 2 3 4 5 6 7 8 9 10 11 12 13 14 15 mm

1 2 3 4 5
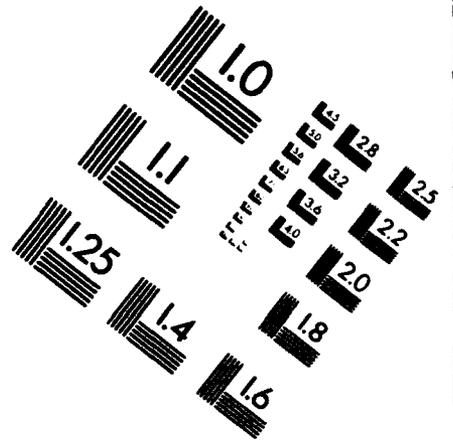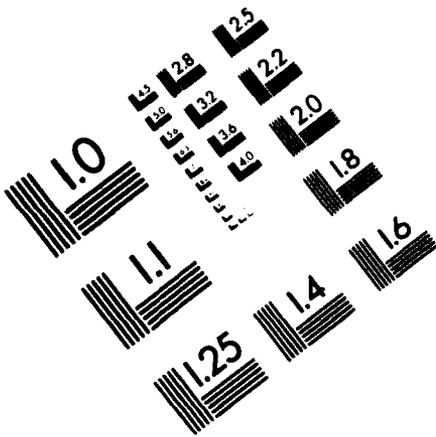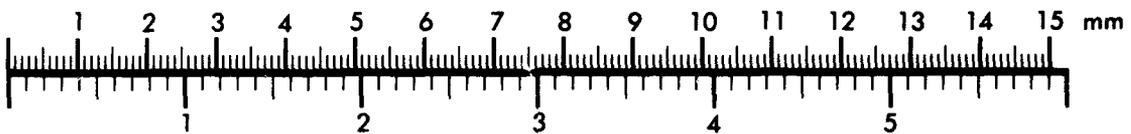
Inches
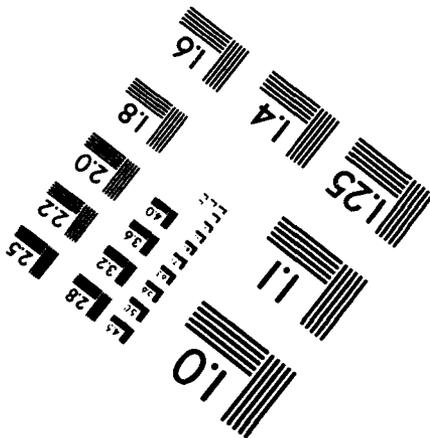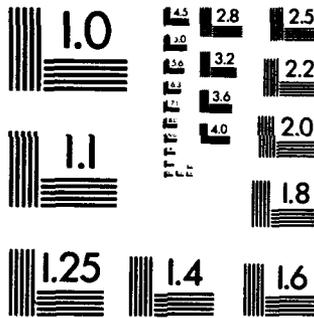
MANUFACTURED TO AIIM STANDARDS
BY APPLIED IMAGE, INC.
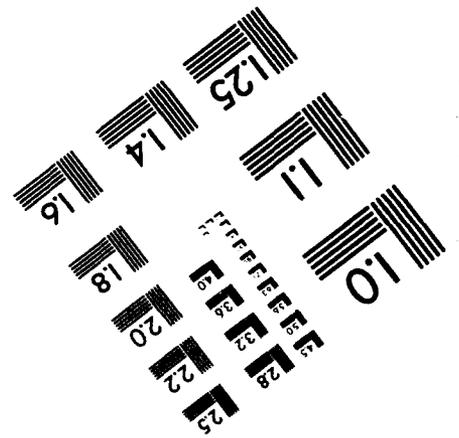
- **Level 4**: Determination of the Z axis.
- **Level 5**: Determination of the third axis, either the Y axis if it is a side view, or the X axis if it is a front or rear view.

Once the first task of detecting the position and orientation of the vehicle is accomplished, it remains to identify the type of vehicle. This is done by defining characteristic details, such as, *e.g.*, number of wheels, engine position, tracks size, exhaust system, for each vehicles to be recognized. The location and the shape of these characteristic details is known *a priori*. Therefore, templates can be created with their location on the vehicle specified in advance. Since the position and orientation of the vehicle is known, it is sufficient to verify that the templates match the corresponding areas on the image. This is done by using pattern recognition techniques as cross-correlation, or neural networks (cf. Duda & Hart [16] and Carpenter & Grossberg [17]).

7 Results

The reasoning method is implemented in IRES, our automatic target recognition system. In section 6, we divided the recognition problem in two tasks: detection of the position and orientation of the vehicle and template matching. The position and orientation detection was then divided into 5 subtasks, $N = 5$. The number of new partial solutions at each levels is $\{n_1 = 8, n_2 = 30, n_3 = 2, n_4 = 8, n_5 = 8\}$. Therefore, the size of the solution space, $S = 30720$ (for the first task). For the selection of the correct path in the solution space several heuristics are implemented at each levels. The number of heuristics is $\{m_1 = 3, m_2 = 12, m_3 = 2, m_4 = 3, m_5 = 6\}$. The image processing algorithms involved in the computation of the different candidates and in the different heuristics are too time consuming to make possible an exhaustive exploration of the solution space. Therefore, a heuristic search strategy is implemented. The Fuzzy logics approach is used for the implementation of the global rating function. Furthermore, trapezoidal type rating functions, as in Fig. 1, are used as rating functions. There are 3 different linguistic terms selected: **Good, Average, and Bad**. The overlapping factor is 50% for the heuristics and the rating membership functions.

The minimum inference is used, with the centroid defuzzifier for the level ratings, and the weighted sum level combination with the arbitrary value approach (for the estimation of the unknown ratings) for the global rating.

The results obtained for a database containing infrared images of 8 vehicles in 16 different positions are shown in Table 1. Perfect detection consists in finding the exact system of 3 axes. Almost perfect detection consists in finding the 3 axes directions, with small normalization or position errors. Sufficient detection consists in finding at least 2 axes (this is, in fact, sufficient for the vehicle identification). Partial detection consists in finding at least the direction of 2 axes. Even if this is not enough to identify directly the vehicle, the correct two axes are among the limited number, (< 240), of candidates having these same 2 directions.

Detection results	Fuzzy
Perfect	83.6 %
Almost perfect	88.8 %
Sufficient	94.0 %
Partial	94.8 %

Table 1: Position and orientation detection results

Once the first task of detecting the position and orientation of the vehicle is accomplished, it remains to identify the type of vehicle. This is done by defining characteristic details, such as, *e.g.*, number of wheels, engine position, tracks size, exhaust system, for each vehicle to be recognized. The location and the shape of these characteristic details is known *a priori*. Therefore, templates can be created with their location on the vehicle specified. Since the position and orientation of the vehicle is known, it is sufficient to verify that the templates match the corresponding areas on the image. Then, a final rating is given to the proposed solution based on the number of matching details and on the quality of this match. If the final rating is not judged sufficiently large, the expert system backtracks to the position and orientation task to propose another candidate solution.

8 Acknowledgement

References

[1] N. J. Nilsson, *Principles of artificial intelligence*. San Mateo, CA: Morgan Kaufmann Publishers, 1980.

[2] G. Shafer, "Probability judgment in artificial intelligence and expert systems," *Statistical Science*, vol. 2, no. 1, pp. 3-16, 1987.

[3] R. E. Bellman and L. A. Zadeh, "Decision making in a fuzzy environment," *Management Science*, vol. 17, pp. 141-164, 1970.

[4] L. A. Zadeh, "Outline of a new approach to the analysis of complex systems and decision processes," *IEEE Trans. Systs., Man, Cybern.*, vol. SMC-3, pp. 28-44, 1973.

[5] B. Kosko, "Fuzzy knowledge combination," *Int. J. of Intelligent Systems*, vol. I, pp. 293-320, 1986.

[6] H. Prade, "A computational approach to approximate and plausible reasoning with applications to expert systems," *Trans. Patt. Anal. Machine Intell.*, vol. PAMI-7, pp. 260-283, 1985.

[7] D. V. Lindley, "The probability approach to the treatment of uncertainty in artificial intelligence and expert systems," *Statistical Science*, vol. 2, no. 1, pp. 17-24, 1987.

[8] B. Kosko, *Neural networks and fuzzy systems*. Englewood Cliffs, NJ: Prentice-Hall, 1992.

[9] E. H. Mamdani, "Aplication of fuzzy logic to approximate reasoning using linguistic synthesis," *IEEE Trans. on Computers*, vol. C-26, pp. 1182-1191, 1977.

[10] P. J. King and E. H. Mamdani, "The aplication of fuzzy control systems to industrial processes," *Automatica*, vol. 13, pp. 235-242, 1977.

[11] E. H. Mamdani, J. J. Østergaard, and E. Lembessis, "Use of fuzzy logic for implementing rule-based control of industrial processes," *TIMS/Studies in the management Sciences*, vol. 20, pp. 429-445, 1984.

[12] H. P. Nii, "Blackboard systems: the blackboard model of problem solving and the evolution of blackboard architectures," *The AI Magazine*, pp. 38-53, Summer 1986.

[13] H. P. Nii, "Blackboard systems: blackboard application systems, blackboard systems from a knowledge engineering perspective," *The AI Magazine*, pp. 82-91, August 1986.

[14] B. Hayes-Roth, "A blackboard architecture for control," *Artificial Intelligence*, vol. 26, no. 3, pp. 251-321, 1985.

[15] J. L. Murdock and B. Hayes-Roth, "Intelligent monitoring and control of semiconductor manufacturing equipment," *IEEE Expert*, vol. 6, no. 6, pp. 19-31, 1991.

[16] R. O. Duda and P. E. Hart, *Pattern classification and scene analysis*. New-York, NY: John Wiley & Sons, 1973.

[17] G. A. Carpenter and S. Grossberg, "The art of adaptive pattern recognition by a self-organizing neural network," *Computer*, vol. 21, pp. 77-88, 1988.

Discussion

Discussor's name :   J. M. Colin, FR

Comment/Question :

Avez-vous analysé le nombre minimum de pixels, la définition minimale de l'image, pour pouvoir au moins définir les axes, donc l'orientation du véhicule?

Author/Presenter's reply :

La méthode peut uniquement etre utilisée à courte distance. La taille des cibles doit etre assez grande. On a testé uniquement des images dont la taille était 250x250 pixels.

Discussor's name :   Pfeifer, ISL, FR

Comment/Question :

Could the application of neuronal networks (NN) improve your results?

Author/Presenter's reply :

Using NN without precautions (when you apply the original image to a NN) will not be very usefull, because NN are not invariant for translation, rotation and scale variations.
Neural Networks can be used for the identification phase, to look if a certain detail is present, because the exact position and the scale of this detail is known once the coordinate system has been found.

Calculation of Turbulence Degraded Point Spread Function of an Imaging System

G. Saplakoglu, F. Erden and A. Altıntaş
Bilkent University,
Department of Electrical and Electronics Engineering
Bilkent 06533,
Ankara, Turkey.

Summary

In this paper the point spread function (PSF) of a turbulence degraded imaging system is statistically characterized. In particular sufficient data and functional fits are given for the calculation of long exposure average PSF and optical transfer function (OTF). Methods are presented for the calculation of second order statistics of PSF, however specific results pertaining to this case are beyond the scope of this paper and are not presented here.

1 Introduction

Effects of atmospheric turbulence on the propagation of optical waves is an extensively studied topic. There are several excellent works that summarize the research done in this area [see for example [1], [2], [3]]. However the results presented in these and related works usually involve fairly complicated expressions most of which can not be evaluated analytically. Hence the reader has to content with either tabulated or plotted results presented for specific atmospheric conditions.

Our aim in this work is twofold. First, at the conclusion of this paper we will point out to our main results in a manner such that they will be accessible to those professionals that are not directly involved in investigating the effects of turbulence on the propagation of optical fields, but require a suitable characterization of such effects in their research. A good example to this category is the signal processing community who work in the restoration of turbulence degraded images. Second, we will introduce some new tools whereby higher statistical order characterization of turbulence degraded images can be numerically evaluated. However the detailed treatment of this latter subject is beyond the scope of this paper and will be published elsewhere.

We will start our treatment in section 2 by stating the turbulence and propagation models that will be used. In section 3 we will formulate the problem that will be dealt with, and sketch the method of analysis. We will conclude in section 4, emphasizing our main results.

2 Modeling The Turbulent Atmosphere

Intuitively, the turbulent atmosphere can be thought of as a collection of random air packets [referred to as eddies] with varying refraction indices $n(r)$. Such variations in the index of refraction cause optical path differences for beams propagating in different parts of the atmosphere. Consequently when these beams are collected by an imaging system a degraded image is obtained.

In this work we will need the power spectral density of the refractive index variations. For this purpose the well known von Karman spectrum[4] will be used;

$$\Phi_n(\kappa) = \frac{0.033C_n^2}{(\kappa^2 + \kappa_0^2)^{11/6}} e^{-(\kappa^2/\kappa_m^2)} \qquad (2.1)$$

In 2.1 C_N^2 (meter$^{-2/3}$) is called the structure constant and is directly related to the strength of the turbulence. Its magnitude can range between 10^{-17} (weak turbulence) to 10^{-13} (strong turbulence). The wavenumber κ (1/meter) is a quantity that is inversely proportional to the size of the turbulent eddies. At a particular κ, $\Phi_n(\kappa)$ represents the relative amount of eddies with sizes $2\pi/\kappa$. The numerical values of the constants κ_m and κ_0 are given by; $\kappa_m \simeq 5.92/l_0$ and $\kappa_0 = 2\pi/L_0$ respectively where l_0 and L_0 are the inner and outer scales of the turbulence respectively [minimum and maximum sizes of turbulent eddies]. Near the ground l_0 is typically a few millimeters and $L_0 \simeq h/2$ where h is the height above ground.

Since we will be dealing with extended objects as opposed to simple plane waves, Gaussian beams or point sources, we will use extended Huygens-Fresnel

principle[5] which is a modified version of Huygens-Fresnel principle that takes into account the effects of the turbulent medium. In its paraxial form, extended Huygens-Fresnel principle specifies the complex field distribution g_0 [at plane $z = 0$] in terms of the complex field distribution g_{-d} at plane $z = -d$ taking into account the diffraction and turbulence effects over the propagation path via,

$$g_0(p) = \int_{S_{OBJECT}} dp' \; g_{-d_1}(p') e^{jk\frac{|p-p'|^2}{2d_1}+\psi(p,p')}$$

(2.2)

where $k = 2\pi/\lambda$, $\psi(p, p')$ is a complex function that represents the turbulence induced phase and amplitude perturbations [at $(p, 0)$] of the field of a point source located at $(p', -d_1)$. The statistics of $\psi(p, p')$ is readily available in the literature which we will refer to when necessary.

In our notation we will use p to indicate transverse coordinates (x, y) and r to indicate 3 dimensions (x, y, z). We will use paraxial approximation throughout this work, hence the propagation will be assumed to be taking predominantly along the z axis. Consequently objects and images will be assumed to be planar and will be represented by functions defined over the transverse coordinate p.

3   Imaging Extended Objects Through the Turbulent Atmosphere

The basic imaging system that will be analyzed is shown in figure 1. The object is located at $z = -d_1$ plane. The medium between $z = -d_1$ and $z = 0$ planes represent the turbulent medium that the rays have to propagate before reaching the lens. It is assumed that the distance d_1 is sufficiently large so that paraxial approximations can be used. Note that this condition is easily met in practice since the effects of turbulence is a major problem only for those optical systems that perform imaging over fairly long propagation paths.

At $z = 0$ plane we have a thin lens of focal length F with pupil function $a(p)$. There is no generality lost in representing an imaging system with a thin lens of finite size since a well corrected diffraction limited imaging system mimics a simple thin lens. The medium between the lens and the image plane located at $z = d_2$ is assumed to be turbulence free. The object distance, image distance and the focal length of the lens are related by the well known imaging condition $1/d_1 + 1/d_2 = 1/F$.

Our main goal in this work is to statistically characterize the long exposure point spread function (PSF) of the optical system shown in figure 1.

Using standard Fourier optics techniques the intensity of the image produced by the optical system in figure 1 is given by[6],

$$I_{d_2}(p) = \int dp' \; I^{(g)}_{-d_1}(p') \mid h(p, p') \mid^2$$

(3.3)

where $I_{d_2}(p)$ is the intensity distribution of the final image, $I^{(g)}_{-d_1}(p)$ is the geometrical image of the object and $\mid h(p, p') \mid^2$ is the point spread function that represent the combined effects of turbulence and diffraction,

$$\mid h(p, p') \mid^2 = \int dp''_\alpha \int dp''_\beta \; a(p''_\alpha)a^*(p''_\beta)$$

$$e^{-j\frac{k}{d_2}(p-p')\cdot(p''_\alpha - p''_\beta)+\psi(p''_\alpha, -\frac{p'}{m})+\psi^*(p''_\beta, -\frac{p'}{m})}$$

(3.4)

Note that the object coordinate p' is scaled by the magnification $m = d_2/d_1$ of the imaging system. In other words, $\mid h(p, p') \mid^2$ is the intensity at p in the image plane due to a point source whose image is located at p' also in the image plane.

In deriving 3.3 and 3.4 we have used the fact that for incoherent illumination,

$$< g_{-d_1}(p'_A)g^*_{-d_1}(p'_B) > = <\mid g_{-d_1}(p'_A) \mid^2 > \delta(p'_A - p'_B)$$

(3.5)

where $< \cdot >$ indicates time or ensemble averaging which are assumed to be interchangeable. That is, the final image is obtained by averaging several short exposure images, consequently, averages can be evaluated either by using time averaging [which is physically done when the exposure time T is much greater than about 1/100 seconds] or averaging individual members of an ensemble, each member of which represents a short exposure [$T \ll 1/100$ seconds] result.

Now that we have an expression for the PSF, we can obtain its statistics. The mean of PSF is given by,

$$E\{\mid h(p, p') \mid^2\} = \int dp''_\alpha \int dp''_\beta \; a(p''_\alpha)a^*(p''_\beta)$$

$$e^{-j\frac{k}{d_2}(p-p')\cdot(p''_\alpha - p''_\beta)}E\{e^{\psi(p''_\alpha, -\frac{p'}{m})+\psi^*(p''_\beta, -\frac{p'}{m})}\}$$

(3.6)

and its autocorrelation by,

$$E\{\mid h(p_A, p'_A) \mid^2 \mid h(p_B, p'_B) \mid^2\} =$$

$$\int dp''_\alpha \int dp''_\beta \int dp''_\gamma \int dp''_\delta \; a(p''_\alpha)a^*(p''_\beta)a(p''_\gamma)a^*(p''_\delta)$$

$$e^{-j\frac{k}{d_2}(p_A-p'_A)\cdot(p''_\alpha - p''_\beta)}e^{-j\frac{k}{d_2}(p_B-p'_B)\cdot(p''_\gamma - p''_\delta)}$$

$$E\{e^{\psi(p''_\alpha, -\frac{p'_A}{m})+\psi^*(p''_\beta, -\frac{p'_A}{m})+\psi(p''_\gamma, -\frac{p'_B}{m})+\psi^*(p''_\delta, -\frac{p'_B}{m})}\}$$

(3.7)

The problem now is to evaluate the expectations that appear inside the integrals of 3.6 and 3.7. In

reference [7], it is shown using first and second order Rytov approximations[8], and assuming a statistically stationary turbulence that,

$$E\{e^{\psi(p_A,p'_A)+\psi^*(p_B,p'_B)}\} =$$
$$e^{E\{\psi_1(p_A,p'_A)\psi_1^*(p_B,p'_B)\}-E\{|\psi_1|^2\}} \quad (3.8)$$

where $\psi_1(p, p')$ is the first order Rytov approximation. Note that the mean irradiance of ψ_1 is independent of spatial coordinates as implied by the stationarity assumption and is given by,

$$E\{|\psi_1|^2\} = (2\pi k)^2 d_1 \int_0^\infty d\kappa \, \Phi_n(\kappa)\kappa \quad (3.9)$$

Using similar methods, the expectation that appears in 3.7 can be written as,

$$E\{e^{\psi(p_A,p_A)+\psi^*(p_B,p'_B)+\psi(p_C,p'_C)+\psi^*(p_D,p'_D)}\} =$$
$$e^{E\{\psi_1(p_A,p'_A)\psi_1^*(p_B,p'_B)\}+E\{\psi_1(p_A,p'_A)\psi_1(p_C,p'_C)\}}$$
$$e^{E\{\psi_1(p_A,p'_A)\psi_1^*(p_D,p'_D)\}+E\{\psi_1^*(p_B,p'_B)\psi_1(p_C,p'_C)\}}$$
$$e^{E\{\psi_1^*(p_B,p'_B)\psi_1^*(p_D,p'_D)\}+E\{\psi_1(p_C,p'_C)\psi_1^*(p_D,p'_D)\}}$$
$$e^{-2E\{|\psi_1|^2\}} \quad (3.10)$$

The expectation $E\{\psi_1(p_A, p'_A)\psi_1^*(p_B, p'_B)\}$ is evaluated in [7],

$$E\{\psi_1(p_A, p'_A)\psi_1^*(p_B, p'_B)\} =$$
$$(2\pi k)^2 d_1 \int_0^\infty d\kappa \, \kappa \, \Phi_n(\kappa) \int_0^1 dt \, J_0(|\gamma| \kappa) \quad (3.11)$$

where

$$\gamma = t(p_A - p_B) + (1-t)(p'_A - p'_B) \quad (3.12)$$

Using similar methods the following expectation can be calculated as,

$$E\{\psi_1(p_A, p'_A)\psi_1(p_B, p'_B)\} = -(2\pi k)^2 L \cdot$$
$$\int_0^\infty d\kappa \, \kappa \Phi_n(\kappa) \int_0^1 dt \, J_0(|\gamma| \kappa)e^{-j\frac{4L}{k}(t-t^2)\kappa^2} \quad (3.13)$$

Consequently now we have all the necessary formulas to numerically calculate equations 3.6 and 3.7. Unfortunately the integrals that appear in 3.11 and 3.13 can not be evaluated analytically. For this purpose we will first present a functional fit to the integral expression,

$$g(\frac{\kappa_m}{\kappa_0}, \gamma) = \int_0^\infty d\kappa \, \frac{\kappa e^{-(\kappa_0/\kappa_m)^2\kappa^2}}{(1+\kappa^2)^{11/6}}[1 - J_0(|\gamma| \kappa)] \quad (3.14)$$

Note that with the above definition we have,

$$\int_0^1 dt \int_0^\infty d\kappa \, \kappa \Phi_n(\kappa)[1 - J_0(|\gamma| \kappa)] =$$
$$\frac{0.033 C_n^2}{\kappa_0^{5/3}} \int_0^1 dt \, g(\frac{\kappa_m}{\kappa_0}, \kappa_0 |\gamma|) \quad (3.15)$$

For a given κ_m/κ_0 in 3.14 we propose the following fit,

$$g_{fit}(|\gamma|) = a_1(1 - e^{-a_2|\gamma|^2}) + \sum_{i=1}^N b_i \frac{|\gamma|^2}{c_i + |\gamma|^2} \quad (3.16)$$

The values of the coefficients a_i, b_i and c_i are given in table 1. Maximum relative error, i.e. $|g(\gamma) - g_{fit}(\gamma)|/g(\gamma)$ is around 1%. Note that the functional form of g_{fit} is such that the t integral in 3.11 can be evaluated analytically.

Using the above functional fit, 3.6 and 3.7 can be evaluated. For example, for a circular pupil of diameter D, it is straight forward to show that 3.6 is shift invariant an is given by,

$$E\{|h(|p|)|^2\} = \int_0^D d\alpha \, \alpha \, J_0(2\pi \frac{|p|}{\lambda d_2}\alpha) \cdot$$
$$[\cos^{-1}(\frac{\alpha}{D}) - \frac{\alpha}{D}\sqrt{1 - (\frac{\alpha}{D})^2}]$$
$$e^{-0.033C_n^2 \frac{(2\pi k)^2 d_1}{\kappa_0^{5/3}} \int_0^1 dt \, g_{fit}(t\kappa_0\alpha)} \quad (3.17)$$

Similarly the average optical transfer function (OTF) can be written as,

$$OTF = cyl(\frac{|f|}{2D/\lambda d_2}) \cdot$$
$$[\cos^{-1}(\frac{|f|}{D/\lambda d_2}) - \frac{|f|}{D/\lambda d_2}\sqrt{1 - (\frac{|f|}{D/\lambda d_2})^2}]$$
$$e^{-0.033C_n^2 \frac{(2\pi k)^2 d_1}{\kappa_0^{5/3}} \int_0^1 dt \, g_{fit}(t\kappa_0\lambda d_2|f|)} \quad (3.18)$$

where

$$cyl(p) = \begin{cases} 1, & |p| \leq \frac{1}{2} \\ 0, & \text{otherwise} \end{cases} \quad (3.19)$$

Specific plots corresponding to the above two equations are rare in the literature. One such example is the OTF plots given in [9] which also refers to a series of reported experimental results. For easy comparison those plots are reproduced in fig 2 together with equation 3.18. It can be observed from the figure that our results are in very good agreement with the reported experiments.

4 Conclusion

The main results of this paper are equations 3.17 and 3.18 which can be easily evaluated using the function $g_{fit}(\cdot)$ defined in 3.14. As mentioned in the introduction, those readers that are not interested in the theory of propagation in turbulence can directly use the above equations in their work.

Although in this paper we have primarily dealt with long exposure characteristics of turbulence degraded

imaging system, it should be pointed out that the second order statistics of the PSF are related to the short exposure characteristics of the optical system. For example the variance of the PSF specifies an envelope around the mean PSF within which the majority of the particular realizations of the short exposure PSF's must lie. Such information can also be used in set membership based restoration algorithms[10]. However, as mentioned previously, the calculation and interpretation of higher order statistics, in particular the correlation function 3.7 is beyond the scope of this paper. Nevertheless sufficient material is presented here to enable interested readers to aid in calculating some second order statistics.

References

[1] J.W. Strohbehn, ed., *Laser Beam Propagation in the Atmosphere*, (Springer-Verlag, New York, 1978).

[2] A. Ishimaru, *Wave Propagation and Scattering in Random Media, Vols. 1 and 2*, (Academic Press, New York, 1978).

[3] R.M. Manning, *Stochastic Electromagnetic Image Propagation and Adaptive Compensation*, (McGraw-Hill, Inc., 1993).

[4] J.W. Goodman, *Statistical Optics*, (Wiley-Intersience, 1985).

[5] R.F. Lutomirski and H.T. Yura, *Propagation of a Finite Optical Beam in an Inhomogeneous Medium*, Applied Optics, Vol. 10, No. 7, July 1971, pp. 1652-1658.

[6] J.H. Shapiro, *Diffraction Limited Atmospheric Imaging of Extended Objects*, J. Opt. Soc. Am., Vol. 66, No. 5, May 1976, pp. 469-477.

[7] H.T. Yura, *Mutual Coherence Function of aFinite Cross Section Optical Beam Propagating in a Turbulent Medium*, Applied Optics, Vol. 11, No. 6, June 1972, pp. 1399 - 1406.

[8] H.T. Yura, *Optical Propagation Through a Turbulent Medium*, J. Opt. Soc. Am, Vol. 59, January 1969, pp. 111-112.

[9] R.E. Hufnagel and N.R. Stanley, *Modulation Transfer Function Associated with Image Transmission through Turbulent Media*, J. Opt. Soc. Am., Vol. 54, No. 1, January 1964, pp. 52-61.

[10] M.I. Sezan and H.J. Trussel, *Prototype Image Constraints for Set-Theoretic Image Restoration*, IEEE Trans. on Signal Proc., Vol. 39, No. 10, October 1991, pp. 2275-2285.
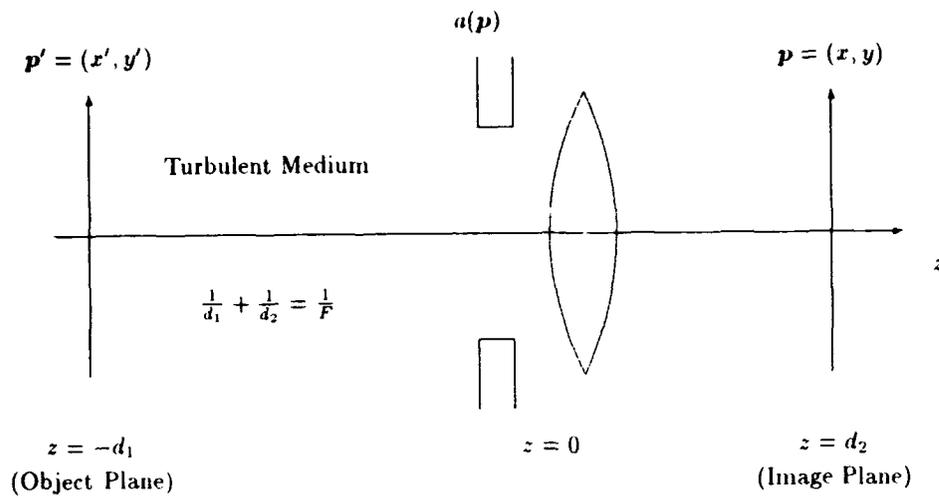
Figure 1: The imaging system analysed in text.

| | κ_m/κ_0 | |
	10^3	10^4
a_1	1.52587223557296e-01	1.69647810148367e-01
a_2	2.22140403416090e-01	2.65879456665575e-01
b_1	1.53560049849163e-04	4.12873188094264e-06
c_1	5.31100749264345e-05	6.31667100284521e-07
b_2	3.11912509978245e-03	3.51919439483754e-02
c_2	1.78898283405542e-03	3.56802359344083e-02
b_3	8.44468086599824e-02	1.07767909208223e-04
c_3	1.29122982863946e+00	2.79620878098983e-05
b_4	4.32127386703938e-02	2.24475783616493e-03
c_4	4.62634914234235e-02	1.12547486045722e-03
b_5	9.22111409451529e-03	2.37864517196957e-01
c_5	3.50105359537060e-01	1.35198669907389e+00
b_6	3.07229641581417e-01	1.54938390693092e-01
c_6	9.03728880407168e-01	4.93556986787747e-01

Table 1: Values of the coeeficients in 3.16
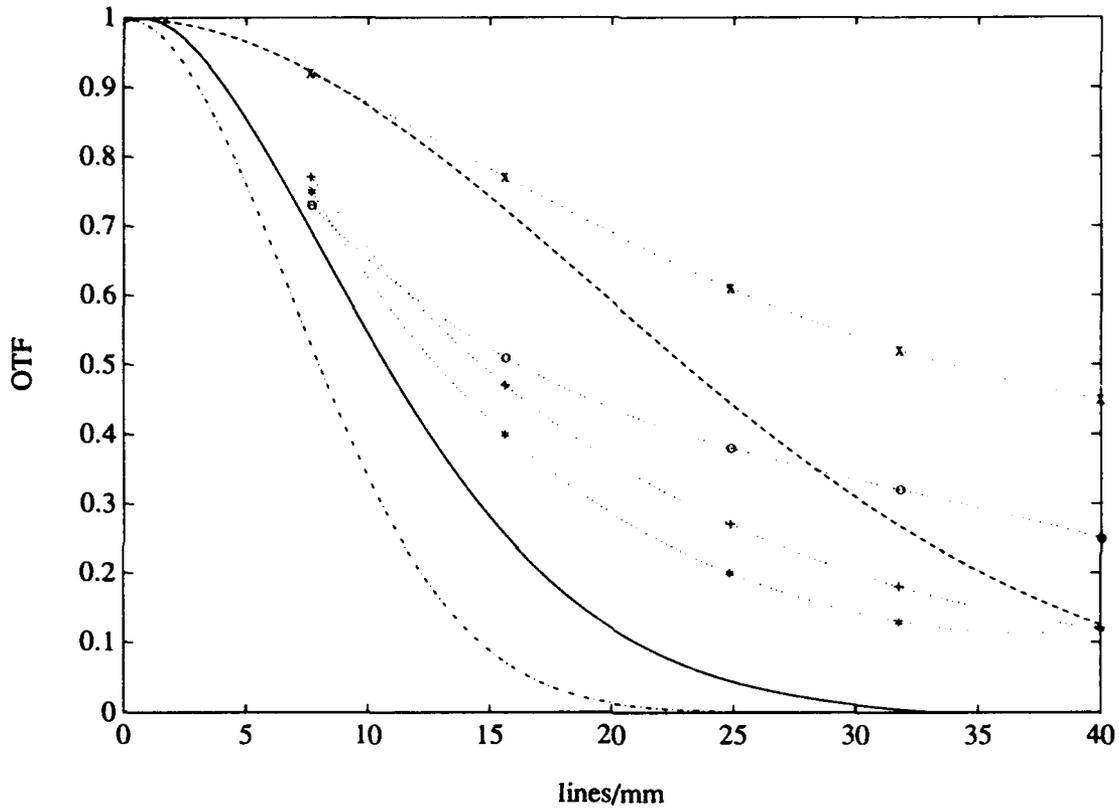
Figure 2: Theoretical and experimental OTF curves for $d_1 = 1.1 \times 10^4 m, F = 0.915m, \kappa_0 = 0.2513m^{-1}, \lambda = 0.55\mu m, C_n^2 = 4.85 \times 10^{-15}m^{-2/3}, D = 1m$. Solid curve is the theoretical OTF given in reference [9]. The dashed and dash-dotted curves are the OTF's calculated by the methods presented in this work for $\kappa_m/\kappa_0 = 10^3$ and 10^4 respectively. The remaining curves represent experimental data obtained at different dates as presented in [9].

Discussion

Discussor's name :   P. Fuerxer, FR

Comment/Question :

Do you lose information in the long time integration process of the image?

Author/Presenter's reply :

Indeed, information is lost when the integration time is extended. Averaging, which is the result of increasing the exposure time, is a low-pass operation that blurs the image, in fact reducing thereby the available information.

Discussor's name :   D. Höhn, GE

Comment/Question :

Does your model also offer information on a possible phase function of the atmospheric OTF?

Author/Presenter's reply :

Since long exposure imaging involves a significant amount of averaging, phase information is lost. Intuitively this is the reason behind the fact that equation (3-18) is a purely real function.

REPORT DOCUMENTATION PAGE

1. Recipient's Reference	2. Originator's Reference	3. Further Reference	4. Security Classification of Document
	AGARD-CP-542	ISBN 92-835-0727-4	UNCLASSIFIED/ UNLIMITED

5. Originator	Advisory Group for Aerospace Research and Development North Atlantic Treaty Organization 7 Rue Ancelle, 92200 Neuilly sur Seine, France

6. Title	ATMOSPHERIC PROPAGATION EFFECTS THROUGH NATURAL AND MAN-MADE OBSCURANTS FOR VISIBLE TO MM-WAVE RADIATION

7. Presented at	the Electromagnetic Wave Propagation Panel Symposium, held in Palma de Mallorca, Spain, 17th—20th May 1993.

8. Author(s)/Editor(s)	9. Date
Various	November 1993

10. Author's/Editor's Address	11. Pages
Various	208

12. Distribution Statement	There are no restrictions on the distribution of this document. Information about the availability of this and other AGARD unclassified publications is given on the back cover.

13. Keywords/Descriptors

Atmospheric propagation	Background discrimination
Smoke	Camouflage
Smoke screens	Clouds — meteorology
Light — visible radiation	Fog
Infrared radiation	Precipitation — meteorology
Millimeter waves	Data fusion
Signatures	Image processing

14. Abstract

This publication reports the papers presented to a specialists' meeting held by the Electromagnetic Wave Propagation Panel at its Spring 1993 meeting.

The topics covered on the occasion of that Symposium include:

Natural obscurants:
— The effects of natural obscurants (haze, clouds, fog, rain, snow and dust) on system performance.

Man-made obscurants and battlefield-induced phenomena:
— The effects of man-made smokes, battlefield-induced smokes and enhanced scintillation on system performance.

Target and background signatures:
— Atmospheric effects on target and background signatures, and target to background contrast.

Multispectral camouflage:
— Weather-related propagation effects on camouflage and obscurants effectiveness and contrast reduction.
— Theoretical and/or experimental evaluation of camouflage effectiveness.

System mitigation aspects:
— Methods to mitigate the above-mentioned factors e.g. image processing, sensor fusion, tactical weather intelligence, and tactical decision aids.

AGARD-CP-542

AGARD Conference Proceedings 542
Advisory Group for Aerospace Research and
Development, NATO
ATMOSPHERIC PROPAGATION EFFECTS
THROUGH NATURAL AND MAN-MADE
OBSCURANTS FOR VISIBLE TO MM-WAVE
RADIATION
Published November 1993
208 pages

This publication reports the papers presented to a
specialists' meeting held by the Electromagnetic Wave
Propagation Panel at its Spring 1993 meeting.

The topics covered on the occasion of that Symposium
include:

Natural obscurants:
— The effects of natural obscurants (haze, clouds, fog,
rain, snow and dust) on system performance.

P.T.O.

Atmospheric propagation
Smoke
Smoke screens
Light — visible radiation
Infrared radiation
Millimeter waves
Signatures
Background discrimination
Camouflage
Clouds — meteorology
Fog
Precipitation — meteorology
Data fusion
Image processing

AGARD-CP-542

AGARD Conference Proceedings 542
Advisory Group for Aerospace Research and
Development, NATO
ATMOSPHERIC PROPAGATION EFFECTS
THROUGH NATURAL AND MAN-MADE
OBSCURANTS FOR VISIBLE TO MM-WAVE
RADIATION
Published November 1993
208 pages

This publication reports the papers presented to a
specialists' meeting held by the Electromagnetic Wave
Propagation Panel at its Spring 1993 meeting.

The topics covered on the occasion of that Symposium
include:

Natural obscurants:
— The effects of natural obscurants (haze, clouds, fog,
rain, snow and dust) on system performance.

P.T.O.

Atmospheric propagation
Smoke
Smoke screens
Light — visible radiation
Infrared radiation
Millimeter waves
Signatures
Background discrimination
Camouflage
Clouds — meteorology
Fog
Precipitation — meteorology
Data fusion
Image processing

AGARD-CP-542

AGARD Conference Proceedings 542
Advisory Group for Aerospace Research and
Development, NATO
ATMOSPHERIC PROPAGATION EFFECTS
THROUGH NATURAL AND MAN-MADE
OBSCURANTS FOR VISIBLE TO MM-WAVE
RADIATION
Published November 1993
208 pages

This publication reports the papers presented to a
specialists' meeting held by the Electromagnetic Wave
Propagation Panel at its Spring 1993 meeting.

The topics covered on the occasion of that Symposium
include:

Natural obscurants:
— The effects of natural obscurants (haze, clouds, fog,
rain, snow and dust) on system performance.

P.T.O.

Atmospheric propagation
Smoke
Smoke screens
Light — visible radiation
Infrared radiation
Millimeter waves
Signatures
Background discrimination
Camouflage
Clouds — meteorology
Fog
Precipitation — meteorology
Data fusion
Image processing

AGARD-CP-542

AGARD Conference Proceedings 542
Advisory Group for Aerospace Research and
Development, NATO
ATMOSPHERIC PROPAGATION EFFECTS
THROUGH NATURAL AND MAN-MADE
OBSCURANTS FOR VISIBLE TO MM-WAVE
RADIATION
Published November 1993
208 pages

This publication reports the papers presented to a
specialists' meeting held by the Electromagnetic Wave
Propagation Panel at its Spring 1993 meeting.

The topics covered on the occasion of that Symposium
include:

Natural obscurants:
— The effects of natural obscurants (haze, clouds, fog,
rain, snow and dust) on system performance.

P.T.O.

Atmospheric propagation
Smoke
Smoke screens
Light — visible radiation
Infrared radiation
Millimeter waves
Signatures
Background discrimination
Camouflage
Clouds — meteorology
Fog
Precipitation — meteorology
Data fusion
Image processing

Man-made obscurants and battlefield-induced phenomena:
— The effects of man-made smokes, battlefield-induced smokes and enhanced scintillation on system performance.

Target and background signatures:
— Atmospheric effects on target and background signatures, and target to background contrast.

Multispectral camouflage:
— Weather-related propagation effects on camouflage and obscurants effectiveness and contrast reduction.
— Theoretical and/or experimental evaluation of camouflage effectiveness.

System mitigation aspects:
— Methods to mitigate the above-mentioned factors e.g. image processing, sensor fusion, tactical weather intelligence, and tactical decision aids.

ISBN 92-835-0727-4

NATO ⊕ OTAN
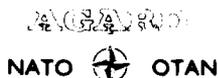
7 RUE ANCELLE · 92200 NEUILLY-SUR-SEINE

FRANCE

Télécopie (1)47.38.57.99 · Télex 610 176

DIFFUSION DES PUBLICATIONS

AGARD NON CLASSIFIEES

Aucun stock de publications n'a existé à AGARD. A partir de 1993, AGARD détiendra un stock limité des publications associées aux cycles de conférences et cours spéciaux ainsi que les AGARDographies et les rapports des groupes de travail, organisés et publiés à partir de 1993 inc. Les demandes de renseignements doivent être adressées à AGARD par lettre ou par fax à l'adresse indiquée ci-dessus. *Veuillez ne pas téléphoner.* La diffusion initiale de toutes les publications de l'AGARD est effectuée auprès des pays membres de l'OTAN par l'intermédiaire des centres de distribution nationaux indiqués ci-dessous. Des exemplaires supplémentaires peuvent parfois être obtenus auprès de ces centres (à l'exception des Etats-Unis). Si vous souhaitez recevoir toutes les publications de l'AGARD, ou simplement celles qui concernent certains Panels, vous pouvez demander à être inclu sur la liste d'envoi de l'un de ces centres. Les publications de l'AGARD sont en vente auprès des agences indiquées ci-dessous, sous forme de photocopie ou de microfiche.

CENTRES DE DIFFUSION NATIONAUX

ALLEMAGNE
Fachinformationszentrum,
Karlsruhe
D-7514 Eggenstein-Leopoldshafen 2

BELGIQUE
Coordonnateur AGARD-VSL
Etat-Major de la Force Aérienne
Quartier Reine Elisabeth
Rue d'Evere, 1140 Bruxelles

CANADA
Directeur du Service des Renseignements Scientifiques
Ministère de la Défense Nationale
Ottawa, Ontario K1A 0K2

DANEMARK
Danish Defence Research Establishment
Ryvangs Allé 1
P.O. Box 2715
DK-2100 Copenhagen Ø

ESPAGNE
INTA (AGARD Publications)
Pintor Rosales 34
28008 Madrid

ETATS-UNIS
National Aeronautics and Space Administration
Langley Research Center
M/S 180
Hampton, Virginia 23665

FRANCE
O.N.E.R.A. (Direction)
29, Avenue de la Division Leclerc
92322 Châtillon Cedex

GRECE
Hellenic Air Force
Air War College
Scientific and Technical Library
Dekelia Air Force Base
Dekelia, Athens TGA 1010

ISLANDE
Director of Aviation
c/o Flugrad
Reykjavik

ITALIE
Aeronautica Militare
Ufficio del Delegato Nazionale all'AGARD
Aeroporto Pratica di Mare
00040 Pomezia (Roma)

LUXEMBOURG
Voir Belgique

NORVEGE
Norwegian Defence Research Establishment
Attn: Biblioteket
P.O. Box 25
N-2007 Kjeller

PAYS-BAS
Netherlands Delegation to AGARD
National Aerospace Laboratory NLR
P.O. Box 90502
1006 BM Amsterdam

PORTUGAL
Força Aérea Portuguesa
Centro de Documentação e Informação
Alfragide
2700 Amadora

ROYAUME UNI
Defence Research Information Centre
Kentigern House
65 Brown Street
Glasgow G2 8EX

TURQUIE
Millî Savunma Başkanlığı (MSB)
ARGE Daire Başkanlığı (ARGE)
Ankara

Le centre de distribution national des Etats-Unis (NASA/Langley) ne détient PAS de stocks des publications de l'AGARD.
D'éventuelles demandes de photocopies doivent être formulées directement auprès du NASA Center for Aerospace Information
(CASI) à l'adresse suivante:

AGENCES DE VENTE

NASA Center for
 Aerospace Information (CASI)
800 Elkridge Landing Road
Linthicum Heights, MD 21090-2934
United States

ESA/Information Retrieval Service
European Space Agency
10, rue Mario Nikis
75015 Paris
France

The British Library
Document Supply Division
Boston Spa, Wetherby
West Yorkshire LS23 7BQ
Royaume Uni

Les demandes de microfiches ou de photocopies de documents AGARD (y compris les demandes faites auprès du CASI) doivent comporter la dénomination AGARD, ainsi que le numéro de série d'AGARD (par exemple AGARD-AG-315). Des informations analogues, telles que le titre et la date de publication sont souhaitables. Veuiller noter qu'il y a lieu de spécifier AGARD-R-nnn et AGARD-AR-nnn lors de la commande des rapports AGARD et des rapports consultatifs AGARD respectivement. Des références bibliographiques complètes ainsi que des résumés des publications AGARD figurent dans les journaux suivants:

Scientifique and Technical Aerospace Reports (STAR)
publié par la NASA Scientific and Technical
Information Program
NASA Headquarters (JTT)
Washington D.C. 20546
Etats-Unis

Government Reports Announcements and Index (GRA&I)
publié par le National Technical Information Service
Springfield
Virginia 22161
Etats-Unis
(accessible également en mode interactif dans la base de données bibliographiques en ligne du NTIS, et sur CD-ROM)

AGARD

NATO ⊕ OTAN

7 RUE ANCELLE · 92200 NEUILLY-SUR-SEINE

FRANCE

Telefax (1)47.38.57.99 · Telex 610 176

DISTRIBUTION OF UNCLASSIFIED
AGARD PUBLICATIONS

AGARD holds limited quantities of the publications that accompanied Lecture Series and Special Courses held in 1993 or later, and of AGARDographs and Working Group reports published from 1993 onward. For details, write or send a telefax to the address given above. *Please do not telephone.*

AGARD does not hold stocks of publications that accompanied earlier Lecture Series or Courses or of any other publications. Initial distribution of all AGARD publications is made to NATO nations through the National Distribution Centres listed below. Further copies are sometimes available from these centres (except in the United States). If you have a need to receive all AGARD publications, or just those relating to one or more specific AGARD Panels, they may be willing to include you (or your organisation) on their distribution list. AGARD publications may be purchased from the Sales Agencies listed below, in photocopy or microfiche form.

NATIONAL DISTRIBUTION CENTRES

BELGIUM
Coordonnateur AGARD — VSL
Etat-Major de la Force Aérienne
Quartier Reine Elisabeth
Rue d'Evere, 1140 Bruxelles

CANADA
Director Scientific Information Services
Dept of National Defence
Ottawa, Ontario K1A 0K2

DENMARK
Danish Defence Research Establishment
Ryvangs Allé 1
P.O. Box 2715
DK-2100 Copenhagen Ø

FRANCE
O.N.E.R.A. (Direction)
29 Avenue de la Division Leclerc
92322 Châtillon Cedex

GERMANY
Fachinformationszentrum
Karlsruhe
D-7514 Eggenstein-Leopoldshafen 2

GREECE
Hellenic Air Force
Air War College
Scientific and Technical Library
Dekelia Air Force Base
Dekelia, Athens TGA 1010

ICELAND
Director of Aviation
c/o Flugrad
Reykjavik ·

ITALY
Aeronautica Militare
Ufficio del Delegato Nazionale all'AGARD
Aeroporto Pratica di Mare
00040 Pomezia (Roma)

LUXEMBOURG
See Belgium

NETHERLANDS
Netherlands Delegation to AGARD
National Aerospace Laboratory, NLR
P.O. Box 90502
1006 BM Amsterdam

NORWAY
Norwegian Defence Research Establishment
Attn: Biblioteket
P.O. Box 25
N-2007 Kjeller

PORTUGAL
Força Aérea Portuguesa
Centro de Documentação e Informação
Alfragide
2700 Amadora

SPAIN
INTA (AGARD Publications)
Pintor Rosales 34
28008 Madrid

TURKEY
Milli Savunma Başkanlığı (MSB)
ARGE Daire Başkanlığı (ARGE)
Ankara

UNITED KINGDOM
Defence Research Information Centre
Kentigern House
65 Brown Street
Glasgow G2 8EX

UNITED STATES
National Aeronautics and Space Administration (NASA)
Langley Research Center
M/S 180
Hampton, Virginia 23665

The United States National Distribution Centre (NASA/Langley) does NOT hold stocks of AGARD publications.
Applications for copies should be made direct to the NASA Center for Aerospace Information (CASI) at the address below.

SALES AGENCIES

NASA Center for	ESA/Information Retrieval Service	The British Library
Aerospace Information (CASI)	European Space Agency	Document Supply Centre
800 Elkridge Landing Road	10, rue Mario Nikis	Boston Spa, Wetherby
Linthicum Heights, MD 21090-2934	75015 Paris	West Yorkshire LS23 7BQ
United States	France	United Kingdom

Requests for microfiches or photocopies of AGARD documents (including requests to CASI) should include the word 'AGARD' and the AGARD serial number (for example AGARD-AG-315). Collateral information such as title and publication date is desirable. Note that AGARD Reports and Advisory Reports should be specified as AGARD-R-nnn and AGARD-AR-nnn, respectively. Full bibliographical references and abstracts of AGARD publications are given in the following journals:

Scientific and Technical Aerospace Reports (STAR)
published by NASA Scientific and Technical
Information Program
NASA Headquarters (JTT)
Washington D.C. 20546
United States

Government Reports Announcements and Index (GRA&I)
published by the National Technical Information Service
Springfield
Virginia 22161
United States
(also available online in the NTIS Bibliographic
Database or on CD-ROM)